



## City Research Online

### City, University of London Institutional Repository

---

**Citation:** Leung, David (2013). Characterisation of silicon photonics devices. (Unpublished Doctoral thesis, City University London)

This is the unspecified version of the paper.

This version of the publication may differ from the final published version.

---

**Permanent repository link:** <https://openaccess.city.ac.uk/id/eprint/2135/>

**Link to published version:**

**Copyright:** City Research Online aims to make research outputs of City, University of London available to a wider audience. Copyright and Moral Rights remain with the author(s) and/or copyright holders. URLs from City Research Online may be freely distributed and linked to.

**Reuse:** Copies of full items can be used for personal research or study, educational, or not-for-profit purposes without prior permission or charge. Provided that the authors, title and full bibliographic details are credited, a hyperlink and/or URL is given for the original metadata page and the content is not changed in any way.



**CITY UNIVERSITY  
LONDON**

**CHARACTERISATION OF  
SILICON PHOTONICS  
DEVICES**

BY

**David M. H. LEUNG**

A THESIS SUBMITTED FOR THE  
DEGREE OF DOCTOR OF PHILOSOPHY  
AT

**CITY UNIVERSITY LONDON**

PHOTONICS MODELLING GROUP  
SCHOOL OF ENGINEERING AND MATHEMATICAL SCIENCES  
NORTHAMPTON SQUARE, LONDON EC1V 0HB  
UNITED KINGDOM

JANUARY 2013

# TABLE OF CONTENTS

List of Tables.....	v
List of Figures .....	vi
Symbols and Abbreviations .....	xi
Acknowledgements .....	xiii
Declaration.....	xiv
Abstract.....	xv

## **1 INTRODUCTION ..... 1**

1.1 Optics .....	1
1.2 Telecommunications .....	2
1.3 Photonics Integrated Circuits .....	5
1.4 Silicon Photonics .....	9
1.5 Aims and objectives of the thesis.....	16
1.6 Structure of the thesis.....	17

## **2 NUMERICAL METHODS ..... 20**

2.1 Introduction .....	20
2.2 Electromagnetic waveguide .....	20
2.3 Basic equations .....	21
2.3.1 Maxwell's equations .....	21
2.3.2 Interface and boundary conditions .....	22
2.4 Finite Element Method .....	25
2.4.1 Variational formulations .....	26
2.4.2 Scalar formulations .....	27
2.4.3 Different types of vector formulations .....	29
2.4.4 Natural boundary conditions .....	31
2.4.5 Spurious solutions .....	32

2.5	Formulation and implementation of the finite element method .....	33
2.5.1	Discretization of the problem .....	34
2.5.2	Shape functions .....	35
2.5.3	Formation of element and global matrices .....	37
2.6	Beam propagation method .....	40
2.6.1	Different types of propagation algorithms .....	41
2.6.2	Boundary conditions .....	45
2.6.3	Perfectly matched layer .....	46
2.6.4	Wave equations .....	49
2.7	BPM finite elements formulation .....	51
2.7.1	Wide angle approximation .....	56
2.8	BPM power formulations .....	58
2.9	Least square boundary residuals method .....	59
2.10	LSBR formulations .....	59
2.11	Application of LSBR method	
	by using finite element modal solution output .....	62
2.12	Formulation of losses in optical waveguides .....	63
2.13	Summary .....	65

### **3 ANALYSIS OF BENT WAVEGUIDES .....66**

3.1	Introduction .....	66
3.2	Analysis of rib waveguide .....	71
3.2.1	Numerical accuracy .....	71
3.2.2	Modal solution .....	73
3.2.3	Characteristics of rib waveguide.....	74
3.3	Features of bent rib waveguide .....	77
3.3.1	Leakage loss/propagation loss .....	80
3.3.2	Calculations of spot-size in BPM .....	81
3.3.3	Investigation of higher order modes .....	82
3.3.4	Polarized power .....	84
3.3.5	Bending loss analysis .....	85

---

3.3.6	Analysis of polarization conversion and crosstalk .....	87
3.3.7	Effects of lateral shift .....	89
3.4	Characteristics of slanted waveguide .....	93
3.4.1	Analysis of slant and bent slant waveguide .....	95
3.4.2	Effects of lateral offsets on loss .....	98
3.4.3	Effects of bending orientation on polarization conversions .....	100
3.5	Summary .....	102

## **4 SILICON PHOTONICS WAVEGUIDES .....104**

4.1	Introduction .....	104
4.2	Silicon slab solution .....	107
4.3	Analysis of strip waveguide .....	108
4.4	Modal fields analysis .....	109
4.4.1	Modal <b>H</b> -field profiles .....	110
4.4.2	Analysis of modal <b>E</b> -field profiles .....	111
4.4.3	Poynting vector profiles analysis .....	112
4.5	Effective index analysis .....	113
4.6	Hybridness analysis .....	115
4.7	Analysis of effective area .....	117
4.8	Calculation of power confinements .....	119
4.9	Birefringence analysis .....	121
4.10	Summary .....	124

## **5 SILICON POLARIZATION ROTATORS .....125**

5.1	Introduction.....	125
5.2	Numerical approach .....	128
5.3	Single section polarization rotator .....	129
5.3.1	Waveguide structure .....	130
5.3.2	Modal <b>H</b> -field analysis .....	131

5.4	Rotator simulation results .....	133
5.4.1	Characteristic of polarization rotator .....	133
5.4.2	Polarization conversion and cross-talk study .....	136
5.4.3	Lateral offset analysis .....	141
5.5	Summary .....	143
<b>6 SILICON SLOT WAVEGUIDES .....</b>		<b>144</b>
6.1	Introduction.....	144
6.2	Analysis of the vertical slot waveguide .....	146
6.2.1	Modal solution of vertical slot waveguide.....	146
6.2.2	Effects of effective index .....	149
6.2.3	Power confinement and density variations .....	150
6.3	Analysis of the horizontal slot waveguide .....	153
6.3.1	Modal analysis for quasi-TM mode.....	154
6.3.2	Effects of power confinement and density.....	156
6.4	Summary .....	159
<b>7 CONCLUSION AND SUGGESTIONS FOR FURTHER WORK.....</b>		<b>160</b>
7.1	Conclusion .....	160
7.2	Suggestions for future work.....	164
<b>Appendix A: Calculation of the element matrices in FEM.....</b>		<b>166</b>
<b>Appendix B: Calculation of the element matrices in BPM.....</b>		<b>168</b>
<b>Appendix C: Author’s Publications &amp; Conferences Proceedings .....</b>		<b>171</b>
<b>References .....</b>		<b>174</b>

# LIST OF TABLES

## Chapter 4

Table. 4.1	Numerical comparison of analytical results with FEM results.....	107
------------	--	-----

# LIST OF FIGURES

Fig. 1.1	Number of components per integrated function for minimum cost per component extrapolated against time.....	6
Fig. 1.2	Silicon photonics integrated circuit.....	11
Fig. 1.3	Schematic drawing of the hybrid laser structure with the optical mode superimposed.....	12
Fig. 1.4	Schematic cross-section of SOI strip waveguide for $\lambda=1.55 \mu\text{m}$ for plasma dispersion modulation.....	13
Fig. 1.5	Cross section of waveguide-based SiGe p-i-n PD. ....	14
Fig. 1.6	Typical fabrication process for silicon waveguides.....	15
Fig. 2.1	Classification of waveguides. (a) Planar waveguide. (b) Axially symmetric waveguide. (c) Strip cross-section waveguide.....	20
Fig. 2.2	Boundary on surface S between two different media.....	23
Fig. 2.3	Cross-section of the arbitrary waveguide subdivided into first-order triangular finite elements.....	34
Fig. 2.4	A typical first-order triangular element.....	35
Fig. 2.5	An arbitrarily shaped waveguide with different PML regions.....	47
Fig. 2.6	Shape functions and different cases of weighting functions for discretisation along the longitudinal z-axis.....	56
Fig. 2.7	Discontinuity at the junction of two dielectric waveguide. (a) Vertical section of the discontinuity between side I and side II. (b) Transverse cross section of the discontinuity between side I and side II.....	60
Fig. 3.1	Schematic cross-section of the bent optical waveguide.....	71
Fig. 3.2	(a) Schematic of the standard rib waveguide with a boundary condition at the left boundary, (b) the variations of $n_{eff}$ with and without Aitkens correction as mesh is increasing.....	72
Fig. 3.3	(a) The dominant $H_y$ field component and (b) the non-dominant $H_x$ field component of the quasi-TE mode, with $W = 3.0 \mu\text{m}$ and $H = 1.3 \mu\text{m}$ .....	73
Fig. 3.4	Variations of the $n_{eff}$ with $W$ for different $H$ for a straight waveguide.....	74
Fig. 3.5	Variations of the $\Gamma_{\text{InGaAsP}}$ with $W$ of quasi-TE and TM modes.....	75
Fig. 3.6	Variations of the modal birefringence with $W$ for different $H$ .....	76
Fig. 3.7	Variations of $\sigma$ with $W$ for different $H$ .....	76

Fig. 3.8	Bend Orientations for the rib waveguide - left facet at bend radius, $R$ .....	77
Fig. 3.9	(a) Refractive index profile of the straight waveguide (solid) and refractive index due to bending (dashed line). (b) Refractive index profile due to bending with different radii.....	78
Fig. 3.10	(a) The dominant $H_y$ field component and (b) the non-dominant $H_x$ field component of the quasi-TE mode of a bent waveguide with $R = 100 \mu\text{m}$ , $W = 3.0 \mu\text{m}$ and $H = 1.3 \mu\text{m}$ .....	79
Fig. 3.11	Variations of the $n_{eff}$ of quasi-TE and TM modes with the $W$ for a bent waveguide.....	80
Fig. 3.12	(a) Illustration of how the straight waveguide is coupled with a bent waveguide with core waveguide $W = 3.0 \mu\text{m}$ and $H = 1.3 \mu\text{m}$ . (b) Variation of power loss along the axial distance for a straight-to-bent waveguide with $W = 3.0 \mu\text{m}$ , $H = 1.3 \mu\text{m}$ and $R = 100 \mu\text{m}$ .....	81
Fig. 3.13	Variation of the $\sigma$ along the axial distance for a straight-to-bent waveguide with $W = 3.0 \mu\text{m}$ , $H = 1.3 \mu\text{m}$ and $R = 100 \mu\text{m}$ .....	82
Fig. 3.14	$H_y$ field profiles at two $z$ propagation locations with $W = 3.0 \mu\text{m}$ , $H = 1.3 \mu\text{m}$ and $R = 100 \mu\text{m}$ . (a) At $z = 1350 \mu\text{m}$ . (b) At $z = 1370 \mu\text{m}$ .....	83
Fig. 3.15	Difference between two $H_y$ field profiles at two locations with a phase reversal with $W = 3.0 \mu\text{m}$ , $H = 1.3 \mu\text{m}$ and $R = 100 \mu\text{m}$ .....	84
Fig. 3.16	Evolution of the $y$ and $x$ -polarized powers along the axial distance for straight-to-bent waveguide with $W=3.0 \mu\text{m}$ , $H = 1.3 \mu\text{m}$ and $R = 100 \mu\text{m}$ .....	84
Fig. 3.17	Variations of power losses along the axial distance for bent-to-bent and straight-to-bent with $W = 3.0 \mu\text{m}$ , $H = 1.2 \mu\text{m}$ and $R = 100 \mu\text{m}$ .....	85
Fig. 3.18	Variations of power losses with $R$ , for bent-to-bent and straight-to-bent waveguides with $W = 3.0 \mu\text{m}$ , $H = 1.3 \mu\text{m}$ .....	87
Fig. 3.19	Variations of the polarization conversions with $R$ , for bent-to-bent and straight-to-bent with $W = 3.0 \mu\text{m}$ and $H = 1.3 \mu\text{m}$ .....	88
Fig. 3.20	(a) Illustration of modal field profiles when a straight waveguide is coupled to a bent waveguide with an offset, $\Delta x$ , and (b) variations of the power loss for a straight-to-bent coupled waveguide with the waveguide offset, $\Delta x$ .....	89
Fig. 3.21	(a) Illustration of modal field profiles when a straight waveguide is coupled to a bent waveguide with an offset, $\Delta w$ , and (b) variations of the power loss for a straight-to-bent coupled waveguide with the $\Delta w$ when the waveguide widths are equal.....	90
Fig. 3.22	Variations of the $\sigma$ along the axial direction when an optimized value of $\Delta w$ is used.....	91
Fig. 3.23	$H_y$ field profiles at two $z$ propagation locations with $W = 3.0 \mu\text{m}$ , $H = 1.3 \mu\text{m}$ and $R = 100 \mu\text{m}$ . (a) At $z = 782 \mu\text{m}$ . (b) At $z = 802 \mu\text{m}$ .....	92

Fig. 3.24	Difference between two $H_y$ field profiles at two locations with a phase reversal with $W = 3.0 \mu\text{m}$ , $H = 1.3 \mu\text{m}$ and $R = 100 \mu\text{m}$ .....	93
Fig. 3.25	(a) Schematic cross-section of the slanted rib waveguide, and (b) example of how the slanted waveguide is discretized.....	94
Fig. 3.26	(a) Variations of the $n_{eff}$ of quasi-TE and TM modes with $W$ for a straight slant and Bent slant ( $R=100\mu\text{m}$ ) waveguide. (b) Variations of the $n_{eff}$ of quasi-modes with the bent radius of the slanted waveguide, $R$ for different $W$ .....	95
Fig. 3.27	(a) The dominant $H_y$ field component and (b) the non-dominant $H_x$ field component of quasi-TE mode of a slanted waveguide with $W = 1.2 \mu\text{m}$ and $H = 1.3 \mu\text{m}$ .....	96
Fig. 3.28	(a) The dominant $H_y$ field component and (b) the non-dominant $H_x$ field component of quasi-TE mode of a bent slanted waveguide with $R = 100 \mu\text{m}$ for $W = 3.0 \mu\text{m}$ and $H = 1.3 \mu\text{m}$ .....	96
Fig. 3.29	Variations of the $L_x$ of quasi- modes with the slanted waveguide $W$ for a straight and Bent ( $R=100\mu\text{m}$ ) waveguide.....	97
Fig. 3.30	(a) Butt-coupling of a rib waveguide with a bent slanted waveguide, and (b) the evolution of the power loss along the propagation direction of a butt-coupled straight waveguide to slant waveguide with bent ( $R = 100\mu\text{m}$ )with different $W$ .....	98
Fig. 3.31	(a) Butt-coupling of a (slanted) waveguide with a (bent) slanted waveguide, and (b) variations of the power loss with waveguide offset, $\Delta x$ ( $\mu\text{m}$ ) for both Slanted-to-Bent slanted ( $R=100\mu\text{m}$ ) and Bent slanted- to-Bent-slanted ( $R=100\mu\text{m}$ ) waveguide.....	99
Fig. 3.32	(a) Variations of the $n_{eff}$ of quasi-TE/TM modes for three different $W$ . (b) Variations of the Hybridness of quasi-TE/TM modes with the slanted waveguide $W$ for a straight and Bent ( $R = 200\mu\text{m}$ ) waveguide.....	100
Fig. 3.33	(a) Butt-coupling of a rib waveguide with a (bent) slanted waveguide, and (b) variations of the polarization rotation along the slanted waveguide with different $R$ when TE mode is incident.....	101
Fig. 4.1	Slab solutions for the variations of the $n_{eff}$ of TE and TM modes with $H$ for a Si slab waveguide.....	107
Fig. 4.2	Schematic cross-section of the Si strip waveguide.....	108
Fig. 4.3	Variations of the $n_{eff}$ with $W$ , for different quasi-TE modes.....	109
Fig. 4.4	(a) Variations of $H_y$ for the $H_y^{11}$ mode and (b) variations of $H_x$ for the $H_x^{11}$ mode along X-axis and Y-axis.....	110
Fig. 4.5	(a) Variations of the $E_x$ field for the $H_y^{11}$ mode and (b) variations of the $E_y$ field for the $H_x^{11}$ mode along the X and Y-axes.....	112
Fig. 4.6	(a) Variations of the $S_z$ intensity for the $H_y^{11}$ mode and (b) variations of the $S_z$ intensity for the $H_x^{11}$ mode along the X and Y-axes.....	113

Fig. 4.7	The variations of $n_{eff}$ with $W$ for the $H_y^{11}$ , $H_y^{21}$ , $H_y^{31}$ and $H_y^{41}$ modes.....	114
Fig. 4.8	The variations of $n_{eff}$ , (a) with $W$ for quasi-TE modes with different $H$ , (b) with $H$ for quasi-TE and TM modes.....	114
Fig. 4.9	The variations of hybridness with $W$ for the $H_y^{11}$ , $H_y^{21}$ , $H_y^{31}$ and $H_y^{41}$ modes.....	116
Fig. 4.10	The variations of hybridness, (a) with $W$ for quasi-TE modes with different $H$ , (b) with $H$ for quasi-TE and TM modes.....	116
Fig. 4.11	Variations of the $A_{eff}$ with $W$ for the $H_y^{11}$ , $H_y^{21}$ , $H_y^{31}$ and $H_y^{41}$ modes.....	117
Fig. 4.12	Variations of the $A_{eff}$ , (a) with $W$ , for quasi-TE modes with different $H$ , (b) with $H$ for quasi-TE and TM modes.....	118
Fig. 4.13	Variations of $\Gamma_{Si}$ with $W$ for the $H_y^{11}$ , $H_y^{21}$ , $H_y^{31}$ and $H_y^{41}$ modes.....	119
Fig. 4.14	Variations of the $\Gamma_{Si}$ , (a) with $W$ , for quasi-TE modes with different $H$ , (b) with $H$ for quasi-TE and TM modes.....	120
Fig. 4.15	Variations of the $n_{eff}$ of quasi-TE and TM modes and the birefringence with $W$ for an air-clad Si strip waveguide with $H = 300$ nm.....	121
Fig. 4.16	Variations of the modal birefringence with $W$ for different $H$ for an air-clad Si strip waveguide.....	122
Fig. 4.17	Variations of the $n_{eff}$ and $A_{eff}$ with the $W$ for $SiO_2$ or Air cladding for the $H_y^{11}$ mode.....	123
Fig. 4.18	Variations of the modal birefringence with the $W$ for the fundamental modes with $SiO_2$ or air cladding.....	123
Fig. 5.1	Schematic diagram of the asymmetric polarization rotator butt-coupled to input and output of a SOI strip waveguide with waveguide dimensions.....	129
Fig. 5.2	Illustration of Polarization Rotation.....	129
Fig. 5.3	Schematic diagram of the Si asymmetric strip rotator.....	130
Fig. 5.4	Field profile of the (a) dominant $H_y$ and (b) non-dominant $H_x$ of the $H_y^{11}$ mode with $W = 800$ nm, $H = 600$ nm, $t_w = 100$ nm and $t_h = 400$ nm.....	131
Fig. 5.5	(a) Variations of the $n_{eff}$ and (b) variations of the hybridness with $W$ for the quasi-TE and TM modes.....	133
Fig. 5.6	(a) Variations of $n_{eff}$ and $A_{eff}$ with $W$ and (b) variations of $\Gamma_{Si}$ and $\Gamma_{SiO_2}$ with $W$ for the fundamental TE mode.....	134
Fig. 5.7	Variations of $L_{\pi}$ , and birefringence with $W$ for the fundamental TE mode.....	135
Fig. 5.8	Schematic diagram of the asymmetric polarization rotator butt-coupled to input and output of a SOI strip waveguide.....	136
Fig. 5.9	Variations of the transmitted modal coefficients $C_x$ and $C_y$ , with $W$ , for the TE mode.....	137
Fig. 5.10	(a) Variations of the polarization conversion and (b) variations of polarization cross-talk and polarization conversion with $W$ .....	138
Fig. 5.11	Variations of the hybridness with $W$ , from 710 nm to 750 nm for the fundamental TE and TM modes.....	139

---

Fig. 5.12	(a) Variations of $n_{eff}$ , and hybridness and (b) variations of $A_{eff}$ , and $\Gamma_{Si}$ with $\lambda$ for quasi-TE mode.....	140
Fig. 5.13	Illustrations of the performance of the straight-to-polarization rotator coupled waveguide with offsets, $\Delta x = 100$ nm.....	141
Fig. 5.14	Illustrations of the performance of the straight-to-polarization rotator coupled waveguide with offsets, $\Delta w = 200$ nm.....	142
Fig. 6.1	2D Schematic cross-section of Si vertical slot nano-waveguide.....	146
Fig. 6.2	(a) The dominant $H_y$ field profile and (b) variations of the $E_x$ field along the X axis for the $H_y^{11}$ mode.....	147
Fig. 6.3	Variations of the $S_z$ field along the X axis for the $H_y^{11}$ mode.....	148
Fig. 6.4	(a) Variations of $n_{eff}$ , with $W$ for different $W_s$ for quasi-TE and TM modes. (b) Variations of $n_{eff}$ , with $W_s$ for different structure dimension for TE modes.....	149
Fig. 6.5	Variations of confinement factor in slot, $\Gamma_{slot\_SiO_2}$ , and power density, $D_{slot\_SiO_2}$ , with different scenarios for the vertical slot waveguide.....	150
Fig. 6.6	2D Schematic cross-section of Si horizontal slot nano-waveguide.....	153
Fig. 6.7	Variations of $E_y$ field along (a) X-axis or (b) Y-axis for the $H_x^{11}$ mode.....	154
Fig. 6.8	Variations of $S_z$ field profile along (a) X-axis or (b) Y-axis.....	155
Fig. 6.9	Variations of confinement factor in slot, $\Gamma_s$ , and power density, $D_s$ , with different scenarios for the horizontal slot waveguide.....	156

# LIST OF SYMBOLS AND ABBREVIATIONS

LED	Light Emitting Diode
WDM	Wavelength Division Multiplexing
IC	Integrated Circuit
PIC	Photonics Integrated Circuit
LiNbO <sub>3</sub>	Lithium Niobate
SiO <sub>2</sub>	Silica
Si	Silicon
InP	Indium Phosphide
GaAs	Gallium Arsenide
SOI	Silicon-On-Insulator
CMOS	Complementary Metal Oxide Semiconductor
FTTH	Fiber To The Home
VLSI	Very Large Scale Integration
CW	Continuous Wave
Ge	Germanium
EB	E-beam Lithography
DUV	Deep Ultra-Violet Lithography
ECR	Electron Cyclotron Resonance Plasma
ICP	Inductive Coupled Plasma
PECVD	Plasma Enhance Chemical Vapour Deposition
InGaAsP	Indium Gallium Arsenide Phosphide
LSBR	Least Square Boundary Residual
BPM	Beam Propagation Method
FEM	Finite Element Method
TE	Transverse Electric
TM	Transverse Magnetic
FFT-BPM	Fast Fourier Transform Beam Propagation Method
FD-BPM	Finite Difference Beam Propagation Method
FE-BPM	Finite Element Beam Propagation Method
PML	Perfectly Matched Layer

---

TBC	Transparent Boundary Condition
FDTD	Finite Difference Time Domain
VFEM	Vectorial H-Field Finite Element Method
WKB	Wentzel–Kramers–Brillouin
PMD	Polarization Mode Dispersion
OEIC	OptoElectronic Integrated Circuit
FWM	Four Wave Mixing
SSW	Silicon Slot Waveguide
NPD	Normalised Power Density
$n_{\text{eff}}$	Effective index
$A_{\text{eff}}$	Effective area
$\Gamma_{\text{Si}}$	Power confinement in silicon
$\Gamma_{\text{SiO}_2}$	Power confinement in silica
$S_z$	Poynting Vector
$L_{\pi}$	Half-beat length
$\lambda$	Wavelength

# ACKNOWLEDGEMENTS

First and foremost, I would like to express my deepest gratitude to my supervisor, Professor B. M. A. Rahman, for his assistance, guidance, inspiration, encouragement and support throughout my research project and the writing up of this thesis. I would also like to thank Professor K.T.V. Grattan for his valuable advice and influence throughout this research.

Secondly, I am much obliged to my family. I would like to thank my parents for their love, understanding, support, and encouragement to allow me to pursue my dream to work in the field of silicon photonics.

I would also like to sincerely thank all my colleagues at the Photonics Research Group and my friends at university for maintaining a friendly and joyful work atmosphere.

# DECLARATION

I grant powers of discretion to the University Librarian to allow this thesis to be copied in whole or in part without further reference to the author. The permission covers only single copies made for study purposes, subject to normal conditions of acknowledgement.

# ABSTRACT

Silicon based integrated circuits has been dominating the electronics technology industry in the last few decades. As the telecommunications and the computing industry slowly converges together, the need for a material to build photonics integrated circuits (PIC) that can be cost-effective and be produced in mass market has become very important.

This thesis describes and outlines the characteristics of high index contrast waveguides as a building blocks that can be designed, fabricated and employed on devices in silicon photonics. Initially in this work, a fully vectorial  $\mathbf{H}$ -field based finite element method has been used to obtain the modal characteristics of high index contrast bent waveguide to get a better understanding of the curved section. Through the beam propagation method, the propagation losses and the spot-size along the propagation distance are obtained when a mode from the straight guide is launched into a bent guide. It is also learnt that mode beating exists at the junction of a straight-to-bent waveguide, in which higher order modes will also be generated. It will be shown in this work that power do exchange between the two polarization states, therefore the polarization conversion, the power losses and the bending losses will be investigated. It will also shown in here that by applying lateral offsets with coupled waveguides of unequal widths, the insertion loss can be reduced.

Secondly, for a high index contrast waveguide such as the silicon strip waveguide with a nanoscale cross-section, modes in such waveguide are not purely TE or TM but hybrid in nature, with all the six components of their  $\mathbf{E}$  and  $\mathbf{H}$ -fields being present. Therefore a detail analysis of the modal field profiles along with the Poynting vector profile will be shown. The effects of waveguide's width and height on the effective indices, the hybridness, the modal effective area and the power confinement in the core or cladding has been studied. Furthermore the modal birefringence of such strip waveguide will be shown. It will be presented that for a strip waveguide with height of 260 nm, single mode exists in the region of the width being 200 nm to 400 nm and that the modal effective is at its minimum when width is around 320 nm for both polarization states.

Thirdly, a compact polarization rotator with an asymmetric waveguide structure design, suitable for fabrication that does not require a slanted side wall or curved waveguide is considered in this work. It will be shown in here that due to the hybrid nature of the asymmetric waveguide design, maximum polarization rotation (from TE to TM) will be achieve by enhancing the non-dominant field profile of both polarized fundamental mode. As the modal hybridness and the propagation constants of both polarized modes will be obtained, the half-beat length, polarization conversion and polarization cross-talk will be calculated by using the FEM and the least squares residual boundary method (LSBR). It is learnt that a compact single stage polarization rotator with a device length of 48  $\mu\text{m}$  with more than 99% of polarization conversion is achieved in this work.

Finally, a study of vertical and horizontal slot waveguide will be shown. Based on silicon strip waveguide, a detail modal characteristics of  $\mathbf{E}$  and  $\mathbf{H}$ -fields along with the Poynting vectors are presented. It will be shown that for slot waveguide, high power confinement and power density will be achieved in the slot area. It will be presented that by optimising the waveguide and slot dimension, the performance of the power confinement and power density in the slot region can be improved.

# 1

# Introduction

## 1.1 OPTICS

Light can be treated as wave phenomenon. It was described that light was identified as propagating wave in 1637 by Rene´ Descartes. Then the wave theory of light was developed by Christiaan Huygens in 1690, known as Huygens’ construction. However, Sir Issac Newton described light as a stream of particles in Opticks, published in 1704 and discouraged the wave theory. It was not until 1800s that the wave theory was firmly established. The double slit experiment in an opaque screen, creating interference fringes where the two beams overlapped demonstrated by Thomas Young, the effect of such experiment could only be explained in terms of waves. Then in 1821, Augustin-Jean Fresnel extended the work carried out by Young, and was able to show by mathematical methods that wave must be transverse oscillation. Then in 1873 James Clerk Maxwell contributed significantly to the field of optics with the Maxwell equations inspired by the electromagnetism work carried out earlier by Michael Faraday. Maxwell combined basic physics of electricity and magnetism into four partial differential equations, and realised that light is an electromagnetic disturbance propagated through the field at a speed according to electromagnetic laws. The discovery of electromagnetism, wave theory and Maxwell equations led directly to the development of wireless communications, modern radio, radar, television, electromagnetic imaging, and optical communications.

## **1.2 TELECOMMUNICATION**

Telecommunication has played a key role for the advanced development of optics. It is described that the system of telecommunication is to transmit information from one place to another through a medium or a channel. Normally a basic telecommunication system consists of three elements, a transmitter, a receiver and a transmission channel. The first optical transmission system to transmit voices over a short distance was developed by Alexander Graham Bell in 1880. Such invention was called the "photophone" and it was designed to use sunlight reflected off a vibrating mirror and a selenium photocell. However sending light signals through the air was not so reliable as severe weather would block the light path and interrupt communications. Moreover, such light beam communications required a clear line-of-sight path between the transmitter and the receiver. Therefore Bell decided to abandon such idea and concentrated more efforts to commercialising the telephone system where it uses electricity as transmission signal.

### **Optical Fibre**

The propagation of light in an optical system depends on the phenomenon of "total internal reflection", whereby light confines in a medium due to the differences in refractive indices of the two materials involved, such as glass in air. It can be described that optical fibres are essentially transparent rods of glass or plastic stretched into long and flexible wires. In the early researches, fibres were made with total internal reflection at a glass-air interface. Then in the early 1950s, van Heel developed a clad fibre, which basically covered the total-reflection surface with a transparent cladding of lower refractive index. Such development inspired Larry Curtiss to suggest making glass clad fibres by melting a tube onto a rod of higher-index glass.

The demonstration of semiconductor LASER in the early 60's by Maiman [Maiman, 1960] paved the way to develop a transmission medium capable for transmitting and processing large bandwidth of signals reliably. From previous researches, it had been known that light can be guided in thin fibres made of

transparent dielectric materials. Theoretically, fibre optics communications technology was known to be possible, however, such system did not emerge for several more years. It was not until the 1966 finding by Charles Kao and George A. Hockham [Kao and Hockham, 1966] at Standard Telephone Laboratories (STL) in Britain that a major breakthrough to communicating through glass was not the material itself but the impurities in it. At that time, the thought of light in a glass medium can carry more information over longer distances than electrical signals can carry in a copper or coaxial medium was thought to be possible. With the impurities removed, they calculated that fibre could carry light as far as one kilometre while retaining a small percentage of the light signal. Such small percentage of light sounds trivial, but if it could be achieved, it would be the same as the copper based telephone system which did not require repeated transmission over the same distance. Kao then had the intuition to show that an intractable form of pure glass called fused silica would have no attenuation at all. Kao's finding inspired the researchers at Corning to focus their attention on fused silica material. Later Maurer and his associates [Kapron *et al.*, 1970] created the first fibre with a completely new technology to fabricate the glass fibre that can reduce signal losses over any distance. By 1970, his team had produced a fibre with a measured attenuation of less than 20 dB/km. Soon Corning managed to create a next generation of fibre that could lower the attenuation level to 1.0 dB/km. In these early designs, fibres were multimode in which the fibre had larger core area and allowed different modes of light to propagate simultaneously.

In these early optical transmission systems, multimode fibres were used to transmit light from optical transmitter with LEDs (Light Emitting Diodes) sources operating at wavelength near 800 nm. It was found that with these systems, the fibre employed here has attenuation of 3 dB/km and it is much better than the coaxial cable which has attenuation of 10-20 dB/km. However, the fibres used in the optical transmission system suffers chromatic and modal dispersion in which such interferences would cut the distance the signals could travel. Maurer's team at Corning then made further development on the fibre. They proved that by reducing the size of the fibre to under 10 microns, they could restrict the light waves to a single mode travels down the fibre. With the single mode fibre, it would eliminate the modal dispersion; and around the same time a newer semiconductor laser was

also developed. This latest laser operated at an infrared wavelength at 1330 nm band and would reduce chromatic dispersion.

Single mode fibres operated at 1310 nm wavelength are designed to carry higher capacity over long distances with low intrinsic loss and zero modal dispersion. These types of fibre became the ideal transmission medium for longer distance and higher bandwidth. A laser operating at the 1550 nm band was developed afterwards and when signals were transmitted down the fibre, it was found that the attenuation of the fibre was at its minimum. However such 1550 nm laser was less effective than the 1330 nm laser for reducing dispersions in fibre. Nevertheless, with these developments and other advancement, liked dispersion compensating techniques and development in hardware, liked integrated circuit (IC) or optical electronics integrated circuits (OEIC), fibre optics telecommunications were now widely deployed.

### **Wavelength Division Multiplexing (WDM)**

As technology advances, the demand for bandwidths has surged due to the growth of internet. Such demand put substantial strains on the telecommunication network and to overcome this, the wavelength division multiplexing (WDM) transmission system was developed [Lin *et al.*, 1988]. In a pre-WDM telecommunication system era, light signal was carried in the fibre by one channel, but now the WDM system exploits the inadequate fibre bandwidth by introducing a technique that can sent many "colour" or infrared light down a single fibre at once. This was done by sending different wavelength of light, each bearing a different stream of information, hence, many channels simultaneously. However, all wavelengths used in fibre optics telecommunications are in the near infrared band, within the bandwidth of fibre amplifiers, therefore the number of channels transmits in the single optical fibre is finite. It should be noted that the narrower the spacing between channels, the larger the number of channels that can be transmitted. In order to make these systems, the optical components, electronics, and fibre coupling will need to be integrated onto a silicon or other substrate material and that is where

photonics integrated circuit will play a key role in the development of future optical systems.

## **1.3 PHOTONICS INTEGRATED CIRCUITS**

To understand photonics integrated circuits, we have to recognise what is "photonics" and what is "integrated circuits". Both of these terms will be explained in the following section.

Photonics is the technology associated with signal generation, processing, transmission and detection where the signal is carried by photons. The primary interest in the applications of photonic devices is in an even narrower range of visible and near infrared wavelengths.

### **Integrated Circuit**

Integrated Circuit (IC) or chip is basically an advanced electric circuit behind all electronics devices. An electric circuit normally consists of different electrical components such as transistors, resistors, capacitors, and diodes that are interconnected to each other. One of the components that is most important for the development of integrated circuit is the transistor. It was developed in 1947 [Bardeen and Brattain, 1948] and since then the smaller, faster and effective transistor allowed engineer to build more advanced circuits. However building advanced circuits required putting many individual components together and connecting them together with metal wires became a problem. Another problem would be the size of the circuit, with a complex circuit, the number of individual components increased and in turn the size of the circuit also increased. This made the electric signals could not travel fast enough through a large circuit. All these problem can be solved by integrated circuit. The first integrated circuit was created by Jack Kilby at Texas Instruments in 1958. He proposed to make all the components and the chip out of the same block of a thin substrate of semiconductor

material, normally the thin substrate is made from silicon. Such technology allowed rapid developments of electronics devices.

Gordon Moore [Moore, 1965] foresaw this exponential growth and predicted that the number of transistors that could be placed on a chip would roughly double every 18 months as illustrated in Fig.1.1.

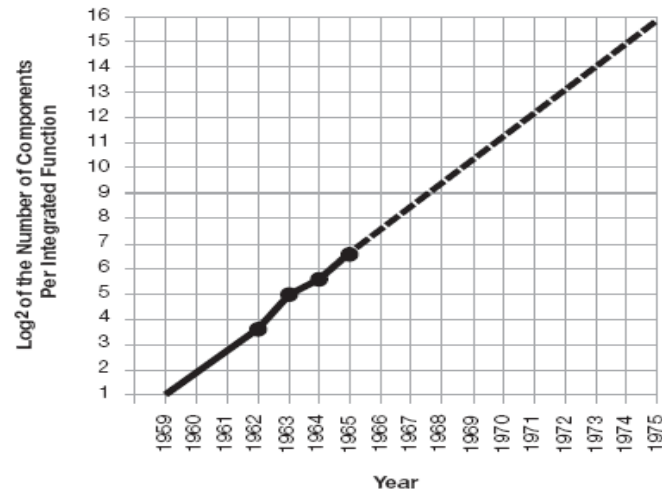


**Fig. 1.1** *Number of components per integrated function for minimum cost per component extrapolated against time. [Moore, 1965]*

From his review, it was said that more components enable higher performance, and this has been the basis of five decades of constantly improving system speeds. This Moore's Law has been upheld since the early prediction and with the latest technology of scaling down of the transistor size to achieve the exponential growth of transistor counts, experts believe that it will continue for some times. For instance, a Quad-Core Intel® Core™2 Extreme processor contains 820 million transistors.

Photonics Integrated Circuits (PIC) is described to be very similar to electronics integrated circuits. PIC integrates individual optical components such as laser, modulator, detectors, waveguides or optical amplifiers onto one optical circuit. PIC started after S.E. Miller [Miller, 1969] proposed to fabricate integrated optical circuits through a process in which passive and active guided optical components, were integrated onto a single substrate. The transmission medium that interconnect all these individual optical components is called waveguide, and instead of guiding

electricity liked in electronic IC, waveguide is used to guide light in the PIC. Waveguide is an important building block in PIC and it is usually made of silica, polymer, or semiconductors. Miller also suggested the term "integrated photonics" in which he emphasised the similarity between planar optical circuits technology and the well established electronic integrated circuits. By integrating multiple optical functions onto a single photonic device, the costs for building advanced optical devices will be lower and therefore driving the cost down for advanced optical systems. Therefore the main goal pursued by integrated photonics is to develop miniaturised optical circuits of high functionality on a common substrate, similar to the way in which electronic integrated circuits have shrunk electronic devices. Normally the sizes of the fabricated optical circuits and compact optical devices are in the order of micros because light that travels inside the waveguide has a short wavelength range (0.5 - 2.0  $\mu\text{m}$ ). In order to achieve the compact sizes of the optical circuits, planar lithographic fabrication technique has to be employed and in fact, it is quite similar to the electronic ICs fabrication, using the tools and techniques of the semiconductor industry. Similar to electronic ICs, PICs can include both monolithic and hybrid integration. In monolithic integration, all the optical components including light sources, light control, electronics and detectors are incorporated on a single substrate. However in hybrid integration technology, the optical chip fabricated on a single substrate controls the optical signals, while additional components such as lasers or detectors are built on different substrates and are directly attached to the integrated photonic device or interconnected by optical fibres.

The most commonly used of substrates for PIC are glassed, Lithium Niobate ( $\text{LiNbO}_3$ ), Silica on Silicon, Indium Phosphide (InP) and Gallium Arsenide (GaAs) and polymers. Each type of material has its own advantages and disadvantages, and the choice of a specific substrate depends on the particular application of the photonic device. Nowadays there exists a great variety of devices based on each of these materials. The most promising materials to achieve full monolithic integration are semiconductor materials, in particular InP and GaAs.

One of the materials used in the fabrication of integrated optical devices is  $\text{LiNbO}_3$ . This type of material shows very interesting physical properties which allows the fabrication of functional devices such as phase modulator, switches,

directional couplers and etc. However PIC based on  $\text{LiNbO}_3$  substrate would not be economically practical as it cannot be used to implement active optoelectronic components like lasers and detectors.

Silica-on-silicon is a waveguide platform that allows to fabricate very low loss optical filters, but due to the low refractive index contrast, the devices are large and the integration density is limited.

GaAs material can be the substrate for PIC as active optoelectronic device can be implemented. However it might not be widely used as the intrinsic band-gap of GaAs generally only operates in the 850 nm telecom band, therefore restricting its use to local area network applications and limiting its use in the much wide-area telecom networks.

It was found that the most promising material to use in PIC as a substrate is InP. It has been known that InP optical devices can be active and passive, operating in the 1310 nm or 1550 nm wavelength band. InP based PIC would be cost effective to fabricate as individual optical components such as, laser, optical modulator, light detector and optical amplifier can be integrated onto one single substrate. The development of InP based PIC would offer compact system design, improved performance characteristics, power consumption, reliability however costs can be quite high.

Silicon (Si) has attracted substantial interest to be the substrate platform for large scale fabrication of PIC. It has been suggested that Si has shown great promises for passive optical devices such as the arrayed waveguide gratings (AWG) and optical switches. Si PIC can also offers the ability to be build by using the standard Complementary Metal Oxide Semiconductor (CMOS) processing infrastructure, currently employed in the electronics world, and therefore Si PIC holds a potential to integrate both optical and electronic devices on a single substrate. However Si has problems implementing the high-performance active optoelectronic functions such as lasing, modulation and light detection. Nevertheless, Si PIC holds a great potential as the primary host material for PIC design.

Nowadays, photonic and optoelectronic devices based on PIC have grown in such a way that they have not only clearly dominate long-distance communications through optical fibres, but have also opened up new fields of application, such as sensor devices, and are also beginning to penetrate in the field of the information processing technology. In fact, the actual optoelectronic devices may be merely a transition to a future of all-optical computation and communication systems.

## 1.4 SILICON PHOTONICS

Currently most of the photonic devices are fabricated from InP, LiNbO<sub>3</sub>, and other exotic materials that are relatively expensive to make. However, this is not the case for silicon. It has been known that Si is the second most abundant element on earth, next to oxygen. Due to the stability of silicon oxide compounds, elemental silicon does not occur in its free state in nature, but occurs as oxide, i.e. sand, therefore this made Si as an inexpensive material. More recently, the applications for Si now include electronics in the form of electronic IC. A Si based device is found in almost every consumer product available in our world today. Si has been the dominated technology in electronics industry since the first IC was created and it is going to be dominance for the foreseeable future.

The concept of Si photonics was worked on by Soref [Soref and Lorenzo, 1986] extensively in the mid to late 1980s. One of the advantages to use Si for photonics components is because Si is transparent at the infrared wavelength at which optical communication systems normally operate (typically around 1.31 - 1.55  $\mu\text{m}$ ). Another advantage of Si photonics is the strong optical confinement offered by the high index contrast, such as between Si and SiO<sub>2</sub>. Such strong index contrast as Si ( $n = 3.45$ ) and SiO<sub>2</sub> ( $n = 1.45$ ) makes it possible to reduce the size of the photonics circuits or create a very compact and high density waveguide called, Si photonics wire. Si photonics can also be fabricated on a silicon-on-insulator (SOI) wafer scale using CMOS technology. Normally, a SOI wafer consists of a thin Si waveguide layer on top of a buried oxide (SiO<sub>2</sub>) layer on a Si substrate. The top Si layer is the

waveguide core and the oxide layer is the bottom cladding layer. The Si substrate itself has no optical functionality.

However there is one major limitation of Si as optical material for PIC because Si is an indirect band gap semiconductor therefore it leads to inefficient band to band light emission. Also due to the inversion symmetry of silicon's crystal structure, this leads to the absence of the linear electro-optic effect, a measure of how fast light can be controlled through the presence of an electrical field. That characteristic means it is not very good at modulating a laser beam. However these problems did not discourage researchers in the field of silicon photonics but in fact more researches had been done in this field which resulted in the demonstration of both passive and active components and system devices such as, modulator, laser, optical filter, silicon waveguide, silicon coupler and detector.

## **Applications**

There are numerous application that can be employed by Si photonics. One of the applications could be benefited is in fibre-optic telecommunication system. For instance, the extremely popular Fibre To The Home (FTTH) device which requires low cost of fabrication, makes it an ideal product for Si photonics mass production technology. Another application could be in optical interconnection between digital electronic chips [Miller, 2000] for example, chip-to-chip, board-to-board or rack-to-rack interconnections. The concept of optical interconnects was first introduced by Goodman in 1984 [Goodman *et al.*, 1984]. He described the possibility of using optics to replace the electrical interconnects for backplane-to-backplane and chip-to-chip communications in Very Large Scale Integration (VLSI) systems. The motivation for using optics to solve the electrical interconnect bottleneck comes from the widespread successes of optics in the telecommunication industry. It was suggested that by replacing the copper interconnect with optical interconnect, higher bandwidths can be achieved without the constraint of distance and still maintaining the tight power constraints of the optical interconnect system. Other application could be in the field of biosensing [Jokerst *et al.*, 2005], it was suggested that one

likely application area for Si photonics is the lab-on-chip [Saarinen *et al.* 2005] in which both reaction and analysis are performed in a single device.

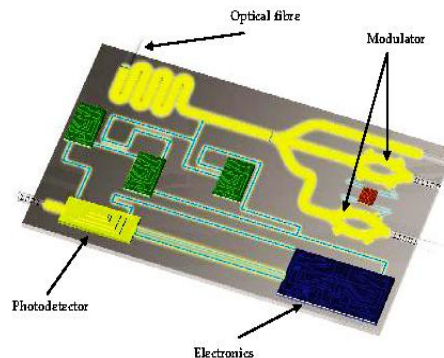


**Fig. 1.2** *Silicon photonics integrated circuit.*

It can be suggested that the goal of Si photonics is to integrate optical components such as, laser, modulator, photodetector and waveguides, onto a single chip as shown in Fig. 1.2 that can be mass manufactured using the standard semiconductor equipment like CMOS electronics.

## Silicon laser

Si has an indirect bandgap which means that it cannot amplify the light. There has been many approaches in emitting and amplifying light in silicon such as Raman laser [Boyraz and Jalali, 2004], nano-patterning [Cloutier *et al.*, 2005], nanocrystalline-Si structures [Pavesi *et al.*, 2000]. These approaches are found to be optically pumped by another laser source or operating at cryogenic temperatures. For the Si Raman laser approach, it was proposed in 2002 [Claps *et al.*, 2002] and soon led to the demonstration of the first Si laser [Boyraz and Jalali, 2004]. The pulsed laser demonstration was followed by demonstration of continuous wave (CW) lasing in 2005 [Rong *et al.*, 2005]. However the Si Raman laser needs to be optically pumped by another laser. This make it unsuitable and not economically viable to employ in Si photonics system. Another approach has been focused on developing hybrid platform that integrate communication wavelength bandgap-matched materials such as group III-V (GaAs or InP) or Germanium (Ge) material on Si waveguides. This is called hybrid integration. Such approach may be done using flip-chip bonding [Friedrich *et al.*, 1992] [Kato and Tohmori, 2000], self-assembly [Kato *et al.*, 2001] or vertical coupling of membrane type devices [Monat *et al.*,

2001]. However all these approaches have the same problem in which a pre-fabricated laser chip has to be aligned to the Si waveguide precisely, hence it will be time consuming, expensive and increase the cost of producing the optical device. Although the membrane III-V disc laser [Hattori *et al.*, 2006] can ease the alignment tolerance but coupling is still an issue due to the different materials used for the laser and the waveguide.

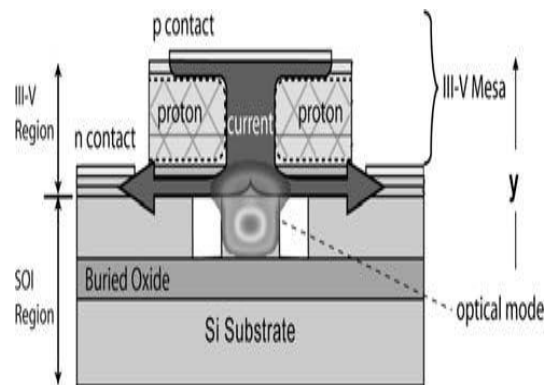


**Fig. 1.3** Schematic drawing of the hybrid laser structure with the optical mode superimposed. [Fang *et al.*, 2006]

One of the laser that can be electrically pumped is the III-V hybrid laser [Park *et al.*, 2005], sometimes called the Si evanescent device. This is a device with a hybrid structure that consists of an offset multiple quantum well region bonded to a Si waveguide which is fabricated on a SOI wafer, as illustrated in Fig. 1.3. It is found that optical mode can obtain electrically pumped gain from the III-V region with such architecture while being guided by the underlying Si waveguide region.

## Modulator

Optical modulator is a device to convert electrical signal into light signal. It was described [Reed 2010] that an optical modulator is a device that is used to modulate (to change the characteristic of) a light beam propagating either in free space or in an optical waveguide. These device can change different beam parameters in which it can be classified as either amplitude, phase or polarisation modulator. Also modulator can be known as either elector-refractive or electro-absorptive by applying an electric field to the real part and the imaginary part of the material's refractive indices, respectively. The primary electric field effects that are traditionally useful in semiconductor materials for causing either electro-absorption or electro-refraction

are the Pockels effect, the Kerr effect and the Franz–Keldysh effect. However, it has been shown that these are weak in pure Si at the telecommunications wavelengths of 1.3  $\mu\text{m}$  and 1.55  $\mu\text{m}$  [Reed and Knights, 2004], therefore modulation of light is not possible.

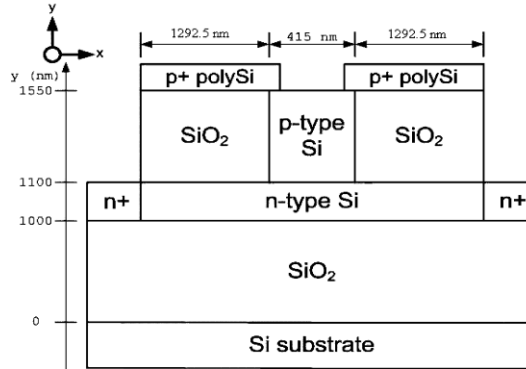


**Fig. 1.4** Schematic cross-section of SOI strip waveguide for  $\lambda=1.55 \mu\text{m}$  for plasma dispersion modulation. [Gardes *et al.* 2005]

To achieve modulation in Si, thermal modulation can be used due to the large thermo-optic coefficient of Si but such technique is too slow for the high frequencies required by telecommunication application. Another technique to achieve modulation in Si is to exploit the plasma dispersion effect, in which the concentration of free charges in silicon changes the real and imaginary parts of the refractive index. Such method has been investigated by Soref and Bennett [Soref and Bennett, 1987]. Most monolithic devices exploited carrier injection, using the plasma dispersion effect for modulating either the refractive index or the absorption coefficient of the material [Barrios *et al.*, 2003]. Carrier depletion is another technique that manipulates free-carrier densities in a modulator to avoid the speed limitation posed by the minority carrier lifetime. Devices based on carrier depletion like the one shown in Fig. 1.4 [Gardes *et al.*, 2005], operate by allowing the propagating light to interact with the junction region of a p–n diode operated at reverse bias. The diode's depletion width, and therefore the free-carrier density in the waveguide, varies with the applied reverse bias. Carrier-injection type optical modulators suffer from the static power dissipation, however the carrier depletion modulators will have negligible static power dissipation.

## Photodetector

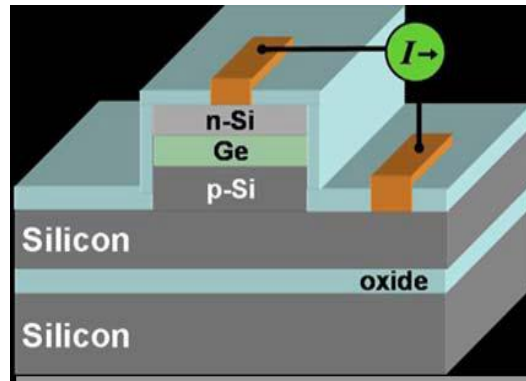


Fig. 1.5 Cross section of waveguide-based SiGe p-i-n PD. [Jalali et al. 2006]

The function of photodetector is to collect the photons travelling in the waveguide and convert them into electrical signals. Photodetector can also be used to monitor the optical beam's properties such as the power and the wavelength, these information are then fed back to the transmitter so that the optical beam can be optimized. Si based photodetectors are widely used in the visible spectrum however, for Si to detect light in the communication wavelength is not possible. Therefore Germanium (Ge) has been introduced to the Si based detectors (similar to the one shown in Fig. 1.5) to improve the detection. It is found that Ge absorbs infrared radiation at longer wavelengths than does Si. So implementing Ge in part of the Si waveguide creates a region where infrared photons can be absorbed. Recent research [Kang et al., 2009] has demonstrated a 340 GHz gain-bandwidth Ge-Si avalanche photodiode using CVD growth of Ge and Si layers at 850°C.

## Silicon optical waveguide

In PIC, individual optical components such as, laser, modulator and photodetector are integrated onto a single chip, however it is the purpose of a waveguide to connect or interconnect all of these individual components together to form a workable device. Therefore waveguide is the most essential building block of a photonic circuit. The main function of waveguide is to trap light locally and then guide it in a specific direction. Waveguide can be made from different optical materials depending on the applications. In Si photonics, Si waveguide will be used, the first Si waveguides were reported in the mid 1980s, in silicon on doped silicon [Soref and

Lorenzo, 1986], silicon on sapphire [Albares and Soref 1987], silicon germanium [Soref *et al.* 1990], and SOI [Cortesi *et al.* 1989].

Normally Si waveguide based on a SOI structure is a promising platform for highly integrated, ultra-small optical circuits or devices. In Si waveguide normally the strip [Vlasov and McNab, 2004] type waveguide with a rectangular core and a rib-type waveguide [Chan *et al.*, 2005] are used for Si photonics. The first Si waveguide was developed by Bookham Technology [Bestwick 1998], it was a rib waveguide with a large cross-section. In this waveguide, the loss was less and it was designed to couple to fibre easily as the waveguide spot-size was bigger but it was found that such waveguide has a large bending radius. However the Si strip waveguide consisting of a rectangular Si core and SiO<sub>2</sub> cladding has very high index core with a low index cladding, therefore it leads to extremely strong light confinement within a geometry that is several times smaller than the wavelength of light. In general the core size at 1.55  $\mu\text{m}$  wavelength is designed to be less than 1.0  $\mu\text{m}$ , and with a sharp bending radius of only a few micrometers. Since most of the waveguides considered in this thesis are for used in integrated optical devices, a brief discussion of the fabrication process of Si waveguide will be presented next.

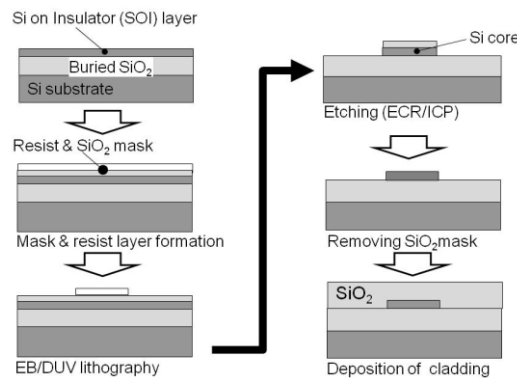


**Fig. 1.6** Typical fabrication process for silicon waveguides. [Tsuchizawa *et al.* 2008]

Figure 1.6 shown the typical fabrication process for the Si wire waveguide [Tsuchizawa *et al.* 2008]. First, the resist patterns that will become the Si core are formed on SOI wafer by E-beam (EB) lithography or deep ultraviolet (DUV) lithography, which can provide 100-nm-level patterns. Next, the Si core is formed with the dry etching based on the patterned resist using a low-pressure plasma, such as electron cyclotron resonance (ECR) plasma or inductive coupled plasma (ICP). Finally, the wafer is coated with another layer of polymer or SiO<sub>2</sub> for the over-

cladding. On formation of the over-cladding, a low temperature process is needed in order to avoid distortion of the Si core shape and to not destroy electronic devices integrated monolithically with the waveguide. The plasma enhanced chemical vapour deposition (PECVD) method is commonly used for the over-cladding film.

## **1.5 AIMS AND OBJECTIVES OF THE THESIS**

The discussion given so far provides an insight of the potential applications that can be offered by Si photonics technology. The primary aims and objectives of this research work can be summarized as follows:

1. To implement the rigorous, accurate and efficient finite element method (FEM) based on vector **H**-field variational formulation for the analysis of optical waveguides based on indium gallium arsenide phosphide (InGaAsP) material.
2. To implement the conformal transformation algorithm used to study arbitrary bends into the vector **H**-field FEM to determine the modal characteristics of a bent waveguide.
3. To implement the beam propagation method (BPM) to study the leakage loss of a straight waveguide coupled to a bend waveguide.
4. To implement the least squares boundary residual (LSBR) method together with the modal solutions obtained from the vector **H**-field FEM in order to achieve an accurate waveguide junction analysis and to account for power conversion phenomenon.
5. To study in depth of the Si strip waveguide by the use of vector **H**-field FEM and to implement the **E**-field formulations with Poynting vector into the FEM. The characteristics of the modal profiles of the **H**-field, the **E**-field and

Poynting vector will be study in detail, in doing so the critical size of such waveguide can be determined.

6. To design and characterise a novel Si rotator device by implementing the FEM and the LSBR to show that such device can achieve almost 100% polarisation conversion with a very short device lengths.
7. To characterise the Si slot waveguide with nano-cross section, and to enhance the power confinement and power density in the slot area by optimising the different design parameters of the waveguide.

## 1.6 STRUCTURE OF THE THESIS

The work presented in this thesis is based on the research carried out by the author in the use of the versatile FEM, the LSBR and the BPM in the analysis of Si photonics devices. The discussion given here is an outline of the structure of the thesis.

A general introduction is given in the first chapter, this chapter introduces the reader to a brief historical view of optics and telecommunication. This is followed by a review of photonics integrated circuits, in which different substrates materials are described for use in photonics integrated circuits. This is then lead to the topic of silicon photonics, where different applications and devices are discussed.

Chapter 2 presents the numerical methods used during the research. Firstly, the theoretical formulation of the FEM as a numerical tool in analysing optical waveguides is described. In here, a brief history of the FEM is presented focusing on their importance in analysing waveguide problems. The fundamental mathematical relations derived from Maxwells equations, for the application of this approach in the solution of optical waveguides problems are defined and examined. Furthermore, a comparison of several variation formulations is presented with an emphasis on the vector **H**-field FEM. The utilization of triangular elements, coordinates and the shape functions are studied to calculate the propagation constants and the field

profiles of various modes propagating through an uniform waveguide. The problem of spurious solutions is also investigated and the penalty function method is implemented to avoid the appearance of non-physical solutions. Secondly, the BPM based on the FEM is presented. An overview of different BPM formulations are reviewed and the mathematical derivation of the BPM is reported. The propagating beam power to determine how much power is transmitted by the unit length of the optical waveguide device is also presented. Then the theoretical foundation of a junction analysis approach called the LSBR method is presented. A brief introduction of waveguide discontinuity analysis is described. The use of the finite element output data in the LSBR approach is also explained. The insertion loss of optical waveguides which can be obtained by using the scattering coefficients calculated by employing the LSBR approach is also shown.

Chapter 3 provides a detailed analysis of bent waveguides based on indium gallium arsenide phosphide symmetric rib waveguide. Initially, the vectorial  $\mathbf{H}$ -field based FEM is used to simulate the rib waveguide with straight side walls to obtain the modal solutions, in which the modal field profiles are thoroughly examined. The characteristics of the rib waveguide, such as, the effective index, power confinement in core, spot size and the birefringence are considered. This is then followed by analysing the bent rib waveguide. In order to simulate such bent rib waveguide, a conformal transformation method has to be applied to the vectorial  $\mathbf{H}$ -field based FEM. The use of BPM to determine the leakage loss/propagation loss when a straight waveguide is butt-coupled to the bent waveguide is also presented. The least LSBR is also employed in here to determine the existence of higher order modes when straight and bent waveguides are butt-coupled together. The TE to TM power conversion, the bending loss and the power loss are also examined in here. It is also described in here that by using lateral offsets to butt-couple straight and bent waveguide together, the transition losses and polarization conversions can be reduced. The investigation of a slanted rib waveguide is also reported in this chapter. The effects of bending on polarization conversions when a straight waveguide is butt-coupled to a slanted bent waveguide is also examined.

Chapter 4 focuses on the Si photonics waveguides. In this chapter, a thorough investigation of a Si strip waveguide defining the modal characteristics

such as the effective index, the hybridness, the mode size effective area, the power confinement in Si core and the power confinement in SiO<sub>2</sub> substrate are examined with different dimensions of the waveguide. The modal profiles of the **H**-field, the **E**-field and the Poynting vector are analysed by the used of the vectorial **H**-field based FEM.

In Chapter 5, following the detailed investigation of a Si waveguide in Chapter 4, a polarization rotator based on the concept of a Si strip waveguide but with a trench section in the Si strip waveguide is proposed in here. The vectorial **H**-field based FEM is used to obtain the modal **H**-field profiles of the asymmetric trench polarization rotator waveguide. The rigorous LSBR method is employed to calculate the excited modal coefficients of the modes in the rotator for both TE and TM polarizations. The characteristics of the Si polarization rotator, such as the hybridness, the power confinement in core, the half-beat length and the birefringence are examined. When the asymmetric polarization rotator is butt-coupled to a straight strip waveguide, the study of polarization conversion and cross-talk are determined by the LSBR method. A lateral offset analysis to determine the minimum total power loss and polarization cross-talk is also studied.

Chapter 6 discusses the numerically simulated results by using the vectorial **H**-field based FEM on Si slots waveguides. It is described in here that an ultra high optical power density can be achieved in the low refractive index slot region that may be suitable for various device such as the four wave mixing or optical sensors. The modal **H**-field profiles, the modal **E**-field profiles along with the Poynting vector profiles for both the vertical and horizontal slot waveguide form the foundation for future researches. The characteristics such as the mode size effective area, power confinement in slot and power density in slot for both vertical and horizontal slot waveguide for quasi-TE and TM modes are thoroughly investigated.

Finally in Chapter 7, general conclusions gained from this research work are summarised and explores. Possible future research related to this research work are also suggested. The thesis also concludes with a list of relevant publications in the major international literature by the author followed by a list of references cited in this work.

# 2

# Numerical Methods

## 2.1 INTRODUCTION

Numerical methods have been widely used in science and engineering. This chapter explains the numerical methods used for optical waveguide problems. The finite element method, the beam propagation method and the least squares residual method, as they are used in this work, will be discussed in detail in the following sections.

## 2.2 ELECTROMAGNETIC WAVEGUIDE

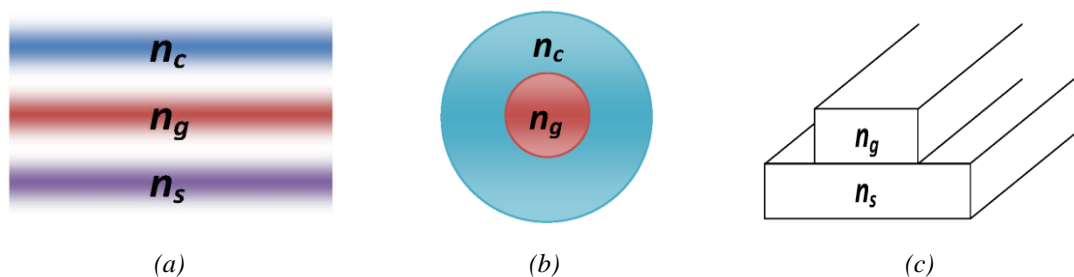


Fig. 2.1

*Classification of waveguides. (a) Planar waveguide. (b) Axially symmetric waveguide. (c) Strip cross-section waveguide.*

Electromagnetic waveguide problems can be grouped into two categories according to their cross-sectional shapes. Figure 2.1 (a), shows a planar waveguide and a

circular waveguide is shown in Fig. 2.1 (b), both of these waveguides can be treated as a one dimensional problem. Normally, a strip waveguide illustrated in Fig. 2.1 (c) is generally treated as a two dimensional problem.

## 2.3 BASIC EQUATIONS

The Maxwell's equations and boundary conditions are the fundamentals equations to consider first when applying the FEM.

### 2.3.1 MAXWELL'S EQUATIONS

Maxwell's equations are a set of equations that formed the foundation of the classical electromagnetic wave phenomena. The equations can be represented in both integral and differential form. However in the use of FEM, it is more convenient and necessary to consider these equations in differential form.

For the time-varying electromagnetic fields, the differential form of Maxwell's equations are written as:

$$\nabla \times \mathbf{E} = \frac{-\partial \mathbf{B}}{\partial t} \quad (\text{Faraday's law}) \quad (2.1)$$

$$\nabla \times \mathbf{H} = \frac{-\partial \mathbf{D}}{\partial t} + \mathbf{J} \quad (\text{Ampere's law}) \quad (2.2)$$

$$\nabla \cdot \mathbf{D} = \rho \quad (\text{Gauss's law}) \quad (2.3)$$

$$\nabla \cdot \mathbf{B} = 0 \quad (\text{Gauss's law of magnetism}) \quad (2.4)$$

<b>E</b>	=	electric field intensity ( $\text{Vm}^{-1}$ )
<b>H</b>	=	magnetic field intensity ( $\text{Am}^{-1}$ )
<b>D</b>	=	electric flux density ( $\text{Cm}^{-2}$ )
<b>B</b>	=	magnetic flux density ( $\text{Wbm}^{-2}$ )
<b>J</b>	=	electric current density ( $\text{Am}^{-2}$ )
$\rho$	=	electric charge density ( $\text{Cm}^{-3}$ )

The fundamental field vectors  $\mathbf{E}$  and  $\mathbf{H}$  are called the electric and magnetic field intensities, and the vectors functions  $\mathbf{D}$  and  $\mathbf{B}$  are called the electric flux density and the magnetic flux density, respectively.

The divergence conditions of (2.3) and (2.4) are consequences of the fundamental field equations, (2.1) and (2.2), provided charge is conserved. If charge is conserved, another fundamental equation which specifies the conservation of charge, called the continuity equation, can be written as:

$$\nabla \cdot \mathbf{J} = \frac{-\partial \rho}{\partial t} \quad (2.5)$$

The associated constitutive relations for the field and the medium can be written as:

$$\mathbf{D} = \varepsilon \mathbf{E} \quad (2.6)$$

$$\mathbf{B} = \mu \mathbf{H} \quad (2.7)$$

where  $\varepsilon$  is the permittivity and  $\mu$  is the permeability of the medium.

Currently all the equations are time dependent and it is necessary and more convenient to express the time derivatives to be  $\exp(j\omega t)$ , where  $j$  is the imaginary unit,  $\omega$  is the angular (radian) frequency and  $t$  is the time. As the factor  $\exp(j\omega t)$  is a common factor in all terms, it can be assumed that all the time derivatives in all the equations can be replaced by the term  $j\omega$ . Hence, the improved differential form of Maxwell's equations becomes:

$$\nabla \times \mathbf{E} = -j\omega \mathbf{B} \quad (2.8)$$

$$\nabla \times \mathbf{H} = -j\omega \mathbf{D} + \mathbf{J} \quad (2.9)$$

thus the continuity equation becomes:

$$\nabla \cdot \mathbf{J} = -j\omega \rho \quad (2.10)$$

### 2.3.2 INTERFACE AND BOUNDARY CONDITIONS

The Maxwell's equations considered so far are not a complete classical description of the electromagnetic field since these equations have not considered the abrupt changes between different materials (i.e. silica-air interface) at the boundary between

two interfaces. Therefore boundary conditions have to be enforced on the Maxwell's equations and boundary conditions are described in here as the conditions that must be met at the boundary of its domain where two different media come into contact.

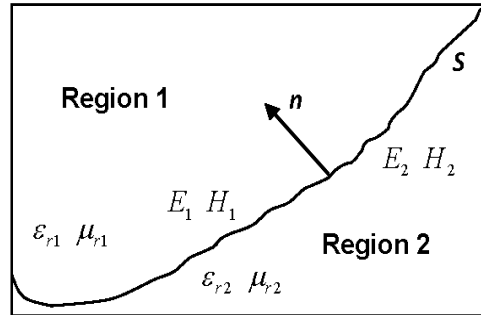


**Fig. 2.2** Boundary on surface  $S$  between two different media.

Figure 2.2 considers the case of two media with unit normal vector  $\mathbf{n}$  separated by a surface  $S$  and directed from region 2 to region 1. In the absence of surface charges ( $\rho = 0$ ) and surface currents ( $\mathbf{J} = 0$ ), the boundary conditions are given by:

1. The tangential components of the electric field must be continuous: i.e. the tangential components of the electric field to be continuous across  $S$  and so  $\mathbf{n} \times \mathbf{E}$  is continuous across  $S$ . Thus if  $\mathbf{E}_1$  denotes the limiting value of the electric field as  $S$  is approached from region 1 and  $\mathbf{E}_2$  denotes that the limit of the field from the other region, then

$$\mathbf{n} \times (\mathbf{E}_1 - \mathbf{E}_2) = 0 \quad \text{on } S \quad (2.11)$$

$$\therefore \mathbf{E}_{t1} = \mathbf{E}_{t2}$$

2. The tangential of the magnetic field must be continuous:

$$\mathbf{n} \times (\mathbf{H}_1 - \mathbf{H}_2) = 0 \quad \text{on } S \quad (2.12)$$

$$\therefore \mathbf{H}_{t1} = \mathbf{H}_{t2}$$

3. The normal components of the electric flux density must be continuous:

$$\mathbf{n} \cdot (\mathbf{D}_1 - \mathbf{D}_2) = 0 \quad \text{on } S \quad (2.13)$$

$$\therefore D_{n1} = D_{n2} \quad \Rightarrow \epsilon_1 E_{n1} = \epsilon_2 E_{n2} \quad \text{where } E_{n1} \neq E_{n2}$$

4. The normal components of the magnetic flux density must be continuous:

$$\mathbf{n} \cdot (\mathbf{B}_1 - \mathbf{B}_2) = 0 \quad \text{on } S \quad (2.14)$$

$$\therefore B_{n1} = B_{n2} \quad \Rightarrow \mu_1 H_{n1} = \mu_2 H_{n2}$$

For most of the optical waveguides, the relative permeabilities in region 1 and region 2 is equal to one ( $\mu_1 = \mu_2 = 1$ ), thus equation 2.14 becomes:

$$H_{n1} = H_{n2} \quad \text{on } S \quad (2.15)$$

which suggests that the magnetic field vector is continuous at the boundary.

For a perfectly electric conductor, the boundary condition is described as an “electric wall” with the following condition:

$$\mathbf{n} \times \mathbf{E} = 0 \quad \text{or} \quad \mathbf{n} \cdot \mathbf{H} = 0 \quad (2.16)$$

This boundary condition means that the magnetic field vector,  $\mathbf{H}$  is forced to disappear and therefore it remains the continuity of the electric field vector,  $\mathbf{E}$  at the boundary.

For a perfectly magnetic conductor, magnetic wall conduction is imposed as:

$$\mathbf{n} \times \mathbf{H} = 0 \quad \text{or} \quad \mathbf{n} \cdot \mathbf{E} = 0 \quad (2.17)$$

This boundary condition means that the continuity of the magnetic field component,  $\mathbf{H}$  at the boundary and its electric field vector  $\mathbf{E}$  is forced to disappear.

## 2.4 FINITE ELEMENT METHOD

The FEM is now widely accepted as one of the most powerful and versatile techniques for the numerical solution to solve complicated problems in science and engineering. This method originated during the 1940s in the work carried out by Courant [Courant, 1943] to study the torsion problem in structural mechanics, who used a collection of triangular elements to get approximate numerical solutions on the unknown function. It was not until the work by Clough, Turner, Martin and Topp at the Boeing Aircraft Company [Turner *et al*, 1956] in 1956 that this method was widely accepted to use for a variety of engineering applications. Clough then introduced the term 'finite element' in 1960 [Clough, 1960] to such method to describe the new technique for plane stress analysis. The method was then incorporated into the field of electromagnetic in 1969 by Ahmed [Ahmed, 1968], since then it has been applied to many other domains, such as, fluid mechanics, thermodynamics, semiconductor devices, optical waveguides, biomedical engineering, etc.

The fundamental purpose of the FEM is that it is a numerical technique to provide an approximate solution at a set of governing equations, normally in the forms of algebraic, differential, or integral equations through a discretization process of a problem domain. The principal characteristic of the FEM is the discretization of the problem domain into an equivalent set of smaller sub-domains (elements). Rather than solving the problem as a whole domain in one operation, the solutions are formulated by each element in a simplified manner expressed in terms of the values at several points of an element called element nodes and then combined to obtain the solution for the original whole domain.

The FEM is a systematic technique for generating the basic functions used in the variational method (Rayleigh-Ritz) and weighted residual method (Galerkin). In the variational technique, the differential equation is put into an equivalent variational form, and then the approximate solution is assumed to be a combination of given approximation functions called trial functions. On the other hand, the weighted residual method is in which the domain of the differential equation is discretized and the overall solution is obtained by minimising the error residual of

the differential equation. However for problems with arbitrary domains and irregular shaped boundaries, it is very difficult to impose the boundary conditions and to construct the approximation functions by employing such method.

As the FEM provides a more systematic approach to the derivation of the approximation functions, it reduces the difficulty encountered in the variational methods. It is said that there are two well-know features in FEM that would distinguish its superiority over other methods. Firstly, a geometrically complex domain of the problem is characterized as a collection of geometrically simple sub-domains, called 'finite element', which could be different shapes, such as, triangular or rectangular. Secondly, over each finite element the approximation functions are derived using the fundamental idea that any continuous function can be corresponded to by a linear combination of algebraic polynomials.

### 2.4.1 VARIATIONAL FORMULATIONS

As discussed earlier, in essence, the formulation of the FEM depends on either the variational method or the weighted residual approach. It is found that the weighted residual method like the Galerkin method is more straight forward to apply with the FEM, however, the variational approach is more advantageous as especially only one global parameter such as the propagation constant is needed to solve for the final solution. Therefore, in this thesis's work, only the variational method is considered here.

Once the variational method is chosen, it can be converted into a standard eigenvalue problem through the application of FEM in the form of:

$$[\mathbf{A}]\{x\} = \lambda [\mathbf{B}]\{x\} \quad (2.18)$$

where  $[\mathbf{A}]$  and  $[\mathbf{B}]$  are real symmetric sparse matrices, and  $[\mathbf{B}]$  is also the positive definite matrix.

Equation (2.18) can also be expressed as:

$$[\mathbf{A}]\{x\} - \lambda[\mathbf{B}]\{x\} = 0 \quad (2.19)$$

where the eigenvalue  $\lambda$  can be defined as  $k_0^2$  or  $\beta^2$  depending on the variational formulation, as  $k_0$  as the free space wavenumber and the eigenvectors  $\{x\}$  represent the unknown value of the nodal fields. Equation (2.19) is of canonical form, as it allows for a more efficient solution and useful to solve for, by employing one of the standard subroutines to obtain different eigenvectors and eigenvalues.

Normally scalar or vector formulations are used by the variational formulations in the finite element method. Both of these approaches will be studied and in particular the vector formulations will be discussed more in greater details.

## 2.4.2 SCALAR FORMULATIONS

The scalar formulation was first used in FEM in the 1960s for the analysis of electromagnetic waveguides problems. The simplest formulation of this kind can be used to describe the mode of the waveguide fields as either predominantly TE (transverse electric) or TM (transverse magnetic). There have been numerous variational scalar formulations used with FEM proposed in the past, like the analysis of anisotropic waveguides by Koshiha [Koshiha *et al.*, 1982]. The most notable approach of using scalar formulation of FEM was by Mabaya [Mabaya *et al.*, 1981] and the scalar variational expression was described as:

$$\mathbf{F}(\varphi) = \iint_{\Omega} m \left[ \left( \frac{\partial \varphi}{\partial x} \right)^2 + \left( \frac{\partial \varphi}{\partial y} \right)^2 + (\beta^2 - k_0^2 n^2) \varphi^2 \right] dx dy \quad (2.20)$$

where,  $\beta$  is propagation constant  
 $k_0$  is the free space wavenumber  
 $n$  is the refractive index

In the equation (2.20),  $\Omega$  represents the cross-sectional domain where the integration is carried out over the whole domain. For a FEM incorporated with the above mentioned  $\mathbf{F}$  functional yields that  $\beta^2$  as the eigenvalue of the matrix equation

for a given  $k_0$  and the eigenvector,  $\varphi$  is given as  $\varphi(x,y)$  as described as the transverse field distribution. As optical waveguide can be described as TE or TM, equation (2.20) can be re-written accordingly.

For the dominant quasi-TE modes,  $m$  is equal to 1,  $\varphi$  is given as  $\varphi(x,y)$  and for the case of TE modes,  $\mathbf{E}_x$  is the dominant fields component and the scalar formulation for the TE modes is then based on the following functional:

$$\mathbf{F}(\varphi) = \iint_{\Omega} \left[ \left( \frac{\partial \mathbf{E}_x}{\partial x} \right)^2 + \left( \frac{\partial \mathbf{E}_x}{\partial y} \right)^2 + \beta^2 \mathbf{E}_x^2 - k_0^2 n^2 \mathbf{E}_x^2 \right] dx dy \quad (2.21)$$

For the dominant quasi-TM mode,  $m$  is equal to  $1/n^2$ , and  $\mathbf{H}_x$  is the dominant fields component, the scalar formulation for the TM modes is expressed as:

$$\mathbf{F}(\varphi) = \iint_{\Omega} \frac{1}{n^2} \left[ \left( \frac{\partial \mathbf{H}_x}{\partial x} \right)^2 + \left( \frac{\partial \mathbf{H}_x}{\partial y} \right)^2 + \beta^2 \mathbf{H}_x^2 - k_0^2 n^2 \mathbf{H}_x^2 \right] dx dy \quad (2.22)$$

Although scalar formulation based FEM is sufficient for solving solutions on quasi-TE, quasi-TM or any one dimensional waveguide problems, it is however, inadequate to found solutions for hybrid modes of anisotropic or inhomogeneous or any two-dimensional optical waveguide problems. The vectorial based FEM formulations is more appropriate for the two-dimensional hybrid modes problems. Nevertheless, there are some advantages for employing the scalar formulations, such as that, the TE and TM scalar functionals are positive definite and therefore all the eigenvalues are positive and therefore there will not be any spurious modes or non-physical solutions. Spurious modes happen when numerical methods are introduced to the matrix eigenvalue equation and it will be explain in more details in a later Section. Apart from the non-existence of spurious modes, scalar formulations have also lowered the computational cost when compared to the vectorial formulations, in which the number of matrix elements to be solved are reduced.

### 2.4.3 DIFFERENT TYPES OF VECTOR FORMULATIONS

As discussed in section (2.4.2) that scalar formulation is inadequate to handle the hybrid modes of anisotropic or two dimensional, inhomogeneous optical waveguide problems. However a vectorial wave analysis with at least two field components is required to evaluate rigorously the propagation characteristics of these waveguide problems. The vectorial formulations also provide more accuracy on the solution of general waveguide problems when compared to the corresponding scalar formulations. There are several forms of the FEM that used the vector formulations depending on which electromagnetic field component is considered for formulation. These components are deemed as followed:

1. using the longitudinal (axial) components of  $E_z$  and  $H_z$  of the electromagnetic fields of  $\mathbf{E}$  and  $\mathbf{H}$ .
2. using the transverse electric field components,  $\mathbf{E}_t$ .
3. using the transverse magnetic field components,  $\mathbf{H}_t$ .
4. using the transverse components  $\mathbf{E}_t$  and  $\mathbf{H}_t$  of the fields.
5. using the both the full vector  $\mathbf{E}$  and  $\mathbf{H}$  fields (all six electromagnetic field components).
6. using the full vector electric field components,  $\mathbf{E}$ .
7. using the full vector magnetic field components,  $\mathbf{H}$ .

The FEM based vectorial formulations in terms of both the longitudinal electric and magnetic field components of  $E_z$  and  $H_z$  was one of several vector formulations used in finite element to solve many different types of guiding structures. This was primarily developed for microwave waveguides but later on extended to optical waveguide problems. This type of formulation can also analyse anisotropic waveguides, however such formulation will destroy the canonical form of the eigenvalue matrix problem in Equation (2.19). It is also found that it is significantly difficult for this method to enforce the boundary conditions on a waveguide with arbitrary dielectric distribution. The fundament drawback for such method is that it is based on the longitudinal components of the vector fields that are significantly less important when analysing with optical waveguide problems.

A variation formulations for the FEM in terms of the transverse electric (**E**) and magnetic (**H**) field component has been developed by Angkaew [Angkaew *et al.*, 1987]. Although such method discriminated the spurious solution but it has led to produce a large sparse, non-symmetric matrices in the eigenvalue equation, which would increase the computation time, therefore efforts have been made to the sparse matrix solvers [Fernandez *et al.*, 1991] in order to tackle such problems.

The total vector **E** and **H** formulation has been developed by Svedin [Svedin, 1989] and English and Young [English and Young, 1971]. These finite element formulations used all six components of the electric and magnetic fields and also based on variational principles or Galerkin approach, but such formulations created complicated problem when solving the matrix equations in which the matrix size double when compared to **E** or **H** field formulation and therefore does not appear to have much advantage.

A FEM based on vector **E**-field formulation has been applied to analyse cylindrical and anisotropy, but loss-less waveguide problems by English and Young [English and Young, 1971], Hano [Hano, 1984] and Koshiba [Koshiba *et al.*, 1985*b*; Koshiba *et al.*, 1986]. It is found that the natural boundary conditions satisfy only the magnetic wall condition, and therefore for the electric wall situation, ( $\mathbf{n} \times \mathbf{E} = 0$ ) needs to be implemented and imposed on any conducting boundaries. However such condition is difficult to implement for irregular shaped structures. Also the field is not continuous across dielectric interfaces.

The first vectorial formulations based on FEM in terms of the **H**-field, the **E**-field or both was derived by Berk [Berk, 1956] in 1956 for lossless anisotropic and resonators. This vector **H**-field formulation is further developed by Rahman and Davies [Rahman and Davies, 1984*a*; Rahman and Davies, 1984*b*] for general anisotropic problems with a non-diagonal permittivity tensor. For optical waveguide analysis, the magnetic field for this formulation is continuous everywhere and that for the natural boundary condition it corresponds to electric wall, in which it is relatively simple to enforce and that it can be left free for arbitrary shaped structures.

The full  $\mathbf{H}$ -field vector-formulation [Rahman and Davies, 1984c] can then be written as:

$$\omega^2 = \frac{\int (\nabla \times \mathbf{H})^* \cdot \varepsilon^{-1} \cdot (\nabla \times \mathbf{H}) d\Omega}{\int \mathbf{H}^* \cdot \mu \cdot \mathbf{H} d\Omega} \quad (2.23)$$

where,  $\varepsilon$  and  $\mu$  are the general anisotropic permittivity and permeability of the loss free medium, respectively. While,  $\omega$  is the radian frequency and  $\Omega$  is the integration carried over the whole domain (the waveguide cross-section).

For such formulation, by applying the Rayleigh-Ritz procedure equation (2.23), in which the solution is minimized with respect to each of the variables, which are the unknown nodal field components  $H_x$ ,  $H_y$  and  $H_z$  led to a matrix eigenvalue equation as stated in equation (2.19), where now  $[\mathbf{A}]$  is a complex Hermitian matrix which can be transformed to a real symmetric matrix for a loss-less problem and  $[\mathbf{B}]$  is a real symmetric and positive definite matrix because of the general  $90^\circ$  phase difference between the axial and transverse components of  $\mathbf{H}$  [Konrad, 1977]. The eigenvectors  $\{x\}$  represent the unknown field components at the nodal points for different modes with  $\omega^2$  corresponding eigenvalues. For mode analysis, for a given wavelength,  $\lambda$ , in which  $\lambda$  is proportional to  $\omega^2$ , the propagation constant,  $\beta$ , has to be changed iteratively until the output eigenvalue corresponds to the desired wavelength.

Unfortunately, most of these formulations suffered the possible appearance of spurious and non-physical solutions which will appear to mix up with correct solutions. Such spurious solutions will be discussed in section (2.4.5) and efforts on how to avoid spurious solutions will also be studied.

## 2.4.4 NATURAL BOUNDARY CONDITIONS

In variational approach, the boundary condition which is automatically satisfied is called the "*natural boundary condition*". Such condition can be set free and automatically satisfied if it is the same as the required boundary conditions in variational formulations.

For instance, in the scalar formulations equation (2.20), the functional has the continuity of  $m(\partial\phi/\partial n)$  where  $m = 1$  for TE and  $m = 1/n^2$  for TM, as the natural boundary condition, where  $\mathbf{n}$  is the outward normal unit vector. Whereas in the vector  $\mathbf{H}$ -field formulation given in equation (2.23), the natural boundary condition is of electric wall where,  $\mathbf{n} \cdot \mathbf{H} = 0$ , in which, there is no need to force any boundary condition on conducting guiding walls.

However, for optical waveguides analysis, the geometry of the waveguide problem can be symmetric and therefore sometimes it is necessary to enforce the boundary condition so that the size of the matrix problem can be greatly reduced and therefore significantly decreased the computational cost.

### 2.4.5 SPURIOUS SOLUTIONS

It is already mentioned earlier on that in using vector finite element formulations in optical waveguides analysis, non-physical and spurious solutions will appear along with the real solutions. The cause of this spurious modes has been known for sometimes and various methods have been developed to suppress such occurrences. Although a number of factors could cause the spurious solutions such as the enforcement of the boundary conditions or the non zero divergence of the trial fields [Rahman and Davies, 1984a; Rahman and Davies, 1984c], it has been found [Konrad, 1976; Mabaya *et al.*, 1981; Davies *et al.*, 1982] that spurious solution will not appear if the trial field precisely satisfies the condition of  $\text{div } \mathbf{B} = 0$ . However in the  $\mathbf{H}$ -field finite element formulation, the  $\nabla \cdot \mathbf{H}$  is not satisfied and caused the spurious solutions to occur. This is further observed by Rahman and Davies [Rahman and Davies, 1984a; Davies *et al.*, 1982] that when the divergence free condition ( $\text{div } \mathbf{H} = 0$ ) is neither implied or force, spurious mode will occur.

In order to remove the spurious solutions, it is essential to identify the solution as either a physical or spurious solutions. For a physical mode, the eigenvector has to satisfy the zero divergence condition, in which  $\text{div } \mathbf{H} = 0$ . To identify the spurious solutions of real modes,  $\nabla \cdot \mathbf{H}$  is calculated over the whole cross section of the waveguide for each solution and the real modes would be the lower

values of  $\nabla \cdot \mathbf{H}$  while those with higher values are the spurious modes. Based on this, the penalty function method [Rahman and Davies, 1984b; Koshiba *et al.*, 1984; Koshiba *et al.*, 1985a; Young, 1988] was applied to equation (2.23) by Rahman and Davies [Rahman and Davies, 1984b]. The penalty term approach has been used in structural engineering [Bathe, 1982] and by imposing certain constraints on solutions variables, spurious solution would be eliminated.

For optical waveguide analysis, Rahman and Davies [Rahman and Davies, 1984b] applied additional integral to the variational formulation in equation (2.23) which satisfied the zero divergence condition  $\nabla \cdot \mathbf{H}$ . Therefore the functional of the vectorial  $\mathbf{H}$ -field finite element formulation with the penalty term can be expressed as:

$$\omega^2 = \frac{\int \left[ (\nabla \times \mathbf{H})^* \cdot \varepsilon^{-1} \cdot (\nabla \times \mathbf{H}) d\Omega + \left( \frac{\alpha}{\varepsilon_0} \right) (\nabla \times \mathbf{H})^* \cdot (\nabla \times \mathbf{H}) \right] d\Omega}{\int \mathbf{H}^* \cdot \mu \cdot \mathbf{H} d\Omega} \quad (2.24)$$

where  $\alpha$  is the dimensionless penalty number. To implement the additional penalty term in equation (2.24), a separate subroutine in the finite element program has to be introduced. The value of the parameter  $\alpha$  can be estimated as  $1/\varepsilon_g$  where  $\varepsilon_g$  is the dielectric constant of the waveguide core. It is found that by increasing the value of the penalty coefficient term the more divergence-free constraint is imposed and further reduced the spurious modes on the solutions. The other advantage of applying the penalty function is that it does not increase the matrix order of the eigenvalue problem so that no additional memory usage is required.

## 2.5 FORMULATION AND IMPLEMENTATION OF THE FINITE ELEMENT METHOD

The finite element is based on the idea that the differential operator equations of the waveguide programs are replaced by an appropriate extremum functional  $\mathbf{F}$  in Euler density form and of variational for the desired quantity. The problem can be said to be as that of obtaining a solution surface  $\mathbf{H}$  over a specified region of the transverse plane so that the boundary conditions for such problem are satisfied and that the

extremum requirement of  $\mathbf{F}$  is met. It is assumed that most waveguides problems can be treated as two dimensional and that the axial dependence is in the form of  $\exp(-j\beta z)$ , and that the transverse plane is used for the discretization.

### 2.5.1 DISCRETIZATION OF THE PROBLEM

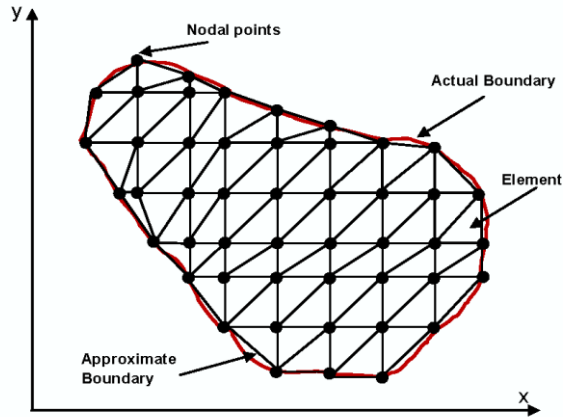


*Fig. 2.3 Cross-section of the arbitrary waveguide subdivided into first-order triangular finite elements.*

The first step in FEM is to sub-divide the problem region into a set finite polygonal sub-regions called 'finite element' as shown in Fig. 2.3. Such element can be of different shapes and different elements can be used in the same domain. Elements can be described as one, two or three dimensional. Most problems are in three dimensional but under certain assumptions it is possible to approximate certain problems in two dimensional format and these two dimensional elements are shown in Fig. 2.3. In this study a first-order triangular element is selected for two-dimensional analysis of waveguide problems. It is found that when the size of the element is small, the final solution is more accurate.

As the domain is sub-divided into smaller regions, the distribution of unknown  $\mathbf{H}$  is also discretized and therefore it is easier to examine the elements when compared to the whole domain. In Fig. 2.3, the intersections of the side of the triangular elements (normally the vertices or the corner points) are defined as nodes or nodal points and the interfaces between the elements are called nodal lines. Within the actual boundary of the problem, the elements are interconnected at a

discrete number of nodal points and that the values of  $\mathbf{H}$  at these nodal points are the unknown basic parameters needed to solve the functional  $\mathbf{F}$ .

### 2.5.2 SHAPE FUNCTIONS

Once the domain is discretized, the distribution of the unknown field  $\mathbf{H}$  at the vertices of the triangular shape element is approximated by a set of polynomials approximation called the 'shape function'. Polynomials are used because it can be easily manipulated both algebraically and computationally. Shape functions are also consider as continuous function within the element and across the element boundaries. A first degree polynomials are used in this study where there are three coefficients, in which it can be corresponded to the three nodal values at the triangular element vertices.

The continuous field function  $\Phi(x,y)$  in the problem domain may be replaced by a set of discrete values  $\{\Phi_e$ , where  $e = 1,2,3, \dots,m$ ), where  $m$  is the total number of nodes. Such function is going to be continuous across adjacent triangles. For these functions to be admissible, field across the elements boundaries must be continuous.

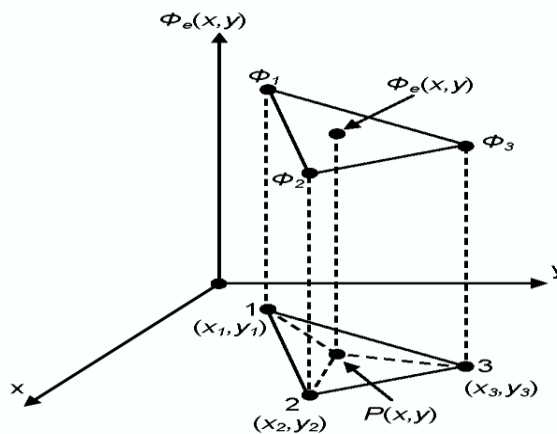


Fig. 2.4 A typical first-order triangular element.

A first order triangular element is shown in Fig. 2.4. In here, for each first order triangular element,  $\Phi$  is continuously interpolated. Such continuity can be achieved by introducing the nodal shape function  $N_i(x,y)$ . Therefore by incorporating

the interpolation functions for  $i = 3$ , the field  $\Phi_e(x,y)$  inside the element can be written as:

$$\Phi_e(x, y) = \sum_{i=1}^3 N_i(x, y) \cdot \Phi_i \quad (2.25)$$

where,  $\Phi_i$  are the nodal field values.

Equation (2.25) can also be expressed in the matrix form:

$$\Phi_e(x, y) = [N_1 \quad N_2 \quad N_3] \begin{Bmatrix} \Phi_1 \\ \Phi_2 \\ \Phi_3 \end{Bmatrix} \quad (2.26)$$

$$\Phi_e(x, y) = [N] \{\Phi_e\} \quad (2.27)$$

where  $[N]$  is the shape function matrix and the column vector  $\{\Phi_e\}$  is the vector corresponding to the element nodal field values.

The first-degree polynomial can be described as  $(a + bx + cy)$  and such polynomial is used for the first order triangular elements over each element.

It can be shown that the element shape functions can be written in the matrix notation form [Reddy, 1984; Davies, 1989] as:

$$\{N\}^T = \begin{bmatrix} N_1 \\ N_2 \\ N_3 \end{bmatrix} = \frac{1}{2A_e} \begin{bmatrix} x_2y_3 - x_3y_2 & y_2 - y_3 & x_3 - x_2 \\ x_3y_1 - x_1y_3 & y_3 - y_1 & x_1 - x_3 \\ x_1y_2 - x_2y_1 & y_1 - y_2 & x_2 - x_1 \end{bmatrix} \begin{bmatrix} 1 \\ x \\ y \end{bmatrix} \quad (2.28)$$

in which  $T$  denotes the transpose.  $A_e$  is the area of the triangle and  $x_1, x_2, x_3, y_1, y_2$  and  $y_3$  are the x,y coordinates of the three nodes of the triangle.  $A_e$  is also given by:

$$A_e = \frac{1}{2} \begin{vmatrix} 1 & x_1 & y_1 \\ 1 & x_2 & y_2 \\ 1 & x_3 & y_3 \end{vmatrix} = \frac{1}{2} (x_2y_3 - x_3y_2) + (x_3y_1 - x_1y_3) + (x_1y_2 - x_2y_1) \quad (2.29)$$

Such shape function can also be expressed as:

$$\{N\}^T = \begin{bmatrix} N_1 \\ N_2 \\ N_3 \end{bmatrix} = \begin{bmatrix} a_1 & b_1x & c_1y \\ a_2 & b_2x & c_2y \\ a_3 & b_3x & c_3y \end{bmatrix} \quad (2.30)$$

The coefficients of  $a_i$ ,  $b_i$  and  $c_i$  (for  $i = 1,2,3$ ) can be calculated as:

$$a_1 = \frac{x_2 y_3 - x_3 y_2}{2A_e} \quad (2.31)$$

$$b_1 = \frac{y_2 - y_3}{2A_e} \quad (2.32)$$

$$c_1 = \frac{x_3 - x_2}{2A_e} \quad (2.33)$$

For the value of  $a_2$ ,  $b_2$ ,  $c_2$ ,  $a_3$ ,  $b_3$  and  $c_3$ , it can be calculated by cyclic exchange of  $1 \rightarrow 2 \rightarrow 3$  in equations (2.31), (2.32) and (2.33) respectively.

The shape functions can be normalised in terms of  $x$  and  $y$  coordinates. By considering a typical point  $P(x,y)$  inside the triangular element as shown in Fig. 2.4. The shape functions  $N_i$  (for  $i = 1,2,3$ ) can be expressed by using the areas of the triangles as:

$$N_1 = \frac{\text{area of the sub-triangle } P-2-3}{\text{area of the full-triangle } 1-2-3} \quad (2.34)$$

where ( $P-2-3$ ) denotes the triangle with vertices, the nodes or nodal points are defined as  $P$ , 2 and 3, respectively.

For  $N_2$  and  $N_3$ , it can be defined similar to Equation (2.34). and it can be noted that from Fig. 2.4,  $N_1$  takes the value of 1 at node 1 and the value 0 at nodes 2 and 3 and at all points on the line passing through these nodes. Therefore it demonstrates that this is the unique interpolating first degree polynomial for node 1. For the shape functions of  $N_2$  and  $N_3$ , the value of 1 will be at nodes 2 and 3 respectively and 0 at any other nodes. Therefore the shape functions  $N_i$  ( $i = 1,2,3$ ) can also be defined as:

$$\sum_{i=1}^3 N_i = 1 \quad (2.35)$$

### 2.5.3 FORMATION OF ELEMENT & GLOBAL MATRICES

It was described earlier on that the solution of the optical waveguide problems by FEM can be defined as a standard eigenvalue equation as seen in Equation (2.20). In

here, matrices [A] and [B] are known as 'global matrices' and that such matrices are formed by adding all of the element matrices of each triangular element of the discretized domain of the optical waveguide.

The element matrices derived in this section are based on the full  $\mathbf{H}$ -field variational expression of Equation (2.23). It is found that within each triangular element, there are three unknown  $\mathbf{H}$ -field components and the magnetic field components of  $H_x$ ,  $H_y$  and  $H_z$  can be written as:

$$H_x(x, y) = [N_1 \quad N_2 \quad N_3] \begin{Bmatrix} H_{x1} \\ H_{x2} \\ H_{x3} \end{Bmatrix} \quad (2.36)$$

$$H_y(x, y) = [N_1 \quad N_2 \quad N_3] \begin{Bmatrix} H_{y1} \\ H_{y2} \\ H_{y3} \end{Bmatrix} \quad (2.37)$$

$$H_z(x, y) = [N_1 \quad N_2 \quad N_3] \begin{Bmatrix} H_{z1} \\ H_{z2} \\ H_{z3} \end{Bmatrix} \quad (2.38)$$

in which,  $H_{xi}$ ,  $H_{yi}$  and  $H_{zi}$  (for  $i = 1, 2, 3$ ) represents the  $x$ ,  $y$  and  $z$  components of the nodal magnetic fields.

Therefore the nodal magnetic field vector  $[H]_e$  can be defined as:

$$[H]_e = \begin{bmatrix} N_1 & N_2 & N_3 & 0 & 0 & 0 & 0 & 0 & 0 \\ 0 & 0 & 0 & N_1 & N_2 & N_3 & 0 & 0 & 0 \\ 0 & 0 & 0 & 0 & 0 & 0 & N_1 & N_2 & N_3 \end{bmatrix} \begin{Bmatrix} H_{x1} \\ H_{x2} \\ H_{x3} \\ H_{y1} \\ H_{y2} \\ H_{y3} \\ H_{z1} \\ H_{z2} \\ H_{z3} \end{Bmatrix} \quad (2.39)$$

Equation (2.39) can also be written as:

$$[H]_e = [N] \{H\}_e \quad (2.40)$$

where  $\{H\}_e$  is the column vector which consists the nodal field values of the three components in the element and [N] is the matrix of the shape function.

Also by taking the Curl  $\mathbf{H}$  within each element with the factor  $(\nabla \times \mathbf{H})_e$  in Equation (2.40), the equation can be written as:

$$(\nabla \times H)_e = \nabla \times [\mathbf{N}] \{H\}_e = \begin{bmatrix} 0 & -\frac{\partial}{\partial z} & \frac{\partial}{\partial y} \\ \frac{\partial}{\partial z} & 0 & -\frac{\partial}{\partial x} \\ -\frac{\partial}{\partial y} & \frac{\partial}{\partial x} & 0 \end{bmatrix} [\mathbf{N}] \{H\}_e = [Q] \{H\}_e \quad (2.41)$$

where the matrix  $[Q]$  can be defined as:

$$[Q] = \begin{bmatrix} [0] & -\frac{\partial[\mathbf{N}]}{\partial z} & \frac{\partial[\mathbf{N}]}{\partial y} \\ \frac{\partial[\mathbf{N}]}{\partial z} & [0] & -\frac{\partial[\mathbf{N}]}{\partial x} \\ -\frac{\partial[\mathbf{N}]}{\partial y} & \frac{\partial[\mathbf{N}]}{\partial x} & [0] \end{bmatrix} = \begin{bmatrix} [0] & -j\beta[\mathbf{N}] & \frac{\partial[\mathbf{N}]}{\partial y} \\ -j\beta[\mathbf{N}] & [0] & -\frac{\partial[\mathbf{N}]}{\partial x} \\ -\frac{\partial[\mathbf{N}]}{\partial y} & \frac{\partial[\mathbf{N}]}{\partial x} & [0] \end{bmatrix} \quad (2.42)$$

where,

$$[0] = [0 \ 0 \ 0] \quad (2.43)$$

$$[\mathbf{N}] = [N_1 \ N_2 \ N_3] \quad (2.44)$$

$$\frac{\partial[\mathbf{N}]}{\partial x} = [b_1 \ b_2 \ b_3] \quad (2.45)$$

$$\frac{\partial[\mathbf{N}]}{\partial y} = [c_1 \ c_2 \ c_3] \quad (2.46)$$

The coefficients of the shape functions  $b_1$ ,  $b_2$ ,  $b_3$ ,  $c_1$ ,  $c_2$  and  $c_3$  have been defined in Equations (2.45) and (2.46).

By substituting the Equations (2.40) and (2.41) into the variational expression Equation of (2.23) and assuming that the material is isotropic then the vector  $\mathbf{H}$ -field formulation for an element can be expressed as:

$$F_e = \int_{\Omega} \{H\}_e^T [Q]^* \varepsilon^{-1} [Q] \{H\}_e \partial\Omega - \omega^2 \int_{\Omega} \{H\}_e^T [N]^T \mu [N] \{H\}_e \partial\Omega \quad (2.47)$$

where  $\Omega$  is the integration over the triangular element domain,  $T$  denotes the transpose and  $*$  is the complex conjugate transpose.

The total function  $F$ , can be defined by adding all the individual  $F_e$  functions of all the elements across the whole area of the waveguide and it can be expressed as:

$$F = \sum_{e=1}^N F_e \quad (2.48)$$

where  $N$  is the number of elements.

By applying the Rayleigh-Ritz procedure in Equation (2.48), in which the equation is differentiated with respect to the field nodal values and equated to zero:

$$\frac{\partial F}{\partial \{H\}_e} = 0 \quad (2.49)$$

where  $e$  is the element number, in which  $e = 1, 2, \dots, n$ .

Such minimisation leads to following eigenvalue equation being achieved:

$$[\mathbf{A}]\{H\} - \omega^2 [\mathbf{B}]\{H\} = 0 \quad (2.50)$$

where

$$[\mathbf{A}] = \sum_{e=1}^n [\mathbf{A}]_e = \sum_{e=1}^n \int_{\Omega} \epsilon^{-1} [Q]^* [Q] \partial \Omega \quad (2.51)$$

$$[\mathbf{B}] = \sum_{e=1}^n [\mathbf{B}]_e = \sum_{e=1}^n \int_{\Omega} \mu [N]^T [N] \partial \Omega \quad (2.52)$$

where  $\{H\}$  is the column matrix in which it contains all the  $\mathbf{H}$ -field nodal values on the whole cross section of the waveguide.  $[\mathbf{A}]$  and  $[\mathbf{B}]$  are the global matrices of the eigenvalue equation while  $[\mathbf{A}]_e$  and  $[\mathbf{B}]_e$  are the element matrices. Appendix 1 shows the calculations and implementation of the element matrices of  $[\mathbf{A}]_e$  and  $[\mathbf{B}]_e$ .

## 2.6 BEAM PROPAGATION METHOD

In section (2.4) the fundamentals of vectorial  $\mathbf{H}$ -field base finite FEM is presented, in which it can be described as a versatile tool for the modal solution of optical waveguide problems. However in integrated optics, it is essential to analyse, model and simulate how electromagnetic wave is propagated through the optical waveguide device before such device is fabricated. Although the  $\mathbf{H}$ -field FEM can simulate the modal field in the device but such method does not simulate on how light is propagating and interacting with the medium in the longitudinally non-uniform

structures. For that reason various numerical methods have been developed and one of these is the beam propagation method (BPM), which will be the main focus of this chapter. The BPM is described as the propagation of light is simulated by taking a small longitudinal step (in  $z$ -direction) and calculating the relating input fields and output fields of the section. The calculations are repeated for each step in a manner of step like calculation of the propagating field.

The BPM has been first developed by Feit and Fleck [Feit and Fleck, 1978; Feit and Fleck, 1980] for the study of optical fibres to calculate the modal properties. Since then many other optical waveguide structures [Neyer *et al.*, 1985] such as taper [Hermansson *et al.*, 1983], bends [Baets *et al.*, 1983], gratings, [Yevick *et al.*, 1982] non-linear directional coupler [Thylen *et al.*, 1986] and waveguide modulator [Danielsen, 1984] have been analysed and evaluated by using the BPM.

## 2.6.1 DIFFERENT TYPES OF PROPAGATION ALGORITHMS

Various kinds of BPM have been developed for the analysis and simulation of a guided wave propagation in axially non-uniform structures, such as bends, tapers and directional couplers. The numerical algorithms of the BPM can be categorised into the following numerical approaches:

- Fast Fourier transform Method (FFT-BPM)
- Finite Difference Method (FD-BPM)
- Finite Element Method (FE-BPM)

All these numerical approaches will be discussed briefly in the following sections.

### FAST FOURIER TRANSFORM BPM (FFT-BPM)

The FFT-BPM [Feit and Fleck, 1978; Thylen *et al.*, 1983] was the first BPM algorithm to be used and it had been widely applied to design optical waveguides until the finite difference method BPM [Chung and Dagli, 1990; Yamauchi *et al.*, 1991; Liu and Li, 1991; Huang and Xu, 1993; Yamauchi *et al.*, 1995] was developed. The fundamental for this method is described as the wave propagation in the

inhomogeneous medium is modelled as a plane wave in the spectral domain and the effect of the medium inhomogeneity is treated as the phase correction in the spatial domain at each propagation step [Feit and Fleck, 1978]. Such method can be expressed as:

$$\psi(x, y, z + \Delta z) = PQP\psi(x, y, z) \quad (2.53)$$

where  $\psi(x, y, z)$  and  $\psi(x, y, z + \Delta z)$  are the field distributions at two subsequent propagation steps,  $P$  is a propagator which can be solved by FFT and  $Q$  is the phase correction.

The FFT-BPM has the following disadvantages due to the nature of the conventional FFT:

- For a modern optoelectronic device structure based on semiconductor materials, such structure has large index discontinuities. It is found that FFT-BPM formulation cannot be described for such discontinuities, due to the fact that FFT-BPM formulation is derived under the assumption that the refractive index difference in the transverse plane is very small, so that the phase error term can be expressed by the first term in a Taylor series.
- The FFT-BPM is only accurate when the beam propagates in the z-axis direction with a small angle due to the fact that a paraxial approximation has been applied to the derivation.
- The vectorial properties of polarization dependence and polarization coupling of the guided-wave devices cannot be treated as FFT-BPM can only work with the scalar wave propagation.

However FFT-BPM is historically important and there are still some advantages over such method:

- FFT-BPM can be applied to structure with arbitrary cross section.
- For the FFT-BPM, both the guided and radiation waves are included in the analysis.

## FINITE DIFFERENCE BPM (FD-BPM)

The FD-BPM is a very powerful tool and it has been extensively used for optical waveguide analysis. The FD-BPM [Lagasse and Baets, 1987; Rolland *et al.*, 1989; Yevick and Glasner, 1989a; Yevick and Hermansson, 1989b; Yevick and Hermansson, 1990; Splett *et al.*, 1991] is described as BPM that solves the paraxial form of the scalar wave equation by the FEM and such approach has been developed by Hendow and Shakir [Hendow and Shakir, 1986]. Initially, the FD-BPM has been developed for the cylindrically symmetric structures but the one developed by Chung and Dagli [Chung and Dagli, 1990] which introduced the FD-BPM to the Cartesian coordinate system is found to be most successful due to the fact that such method yields good accuracy, numerical efficiency and excellent stability. It is found that the FD-BPM has some numerical advantages over the conventional FFT-BPM and it is described as following:

- To analyse a given cross-section, the FD-BPM computation is proportional to the number of mesh points,  $N$ , compared to  $N \log N$  in FFT-BPM. Therefore the computational time in FD-BPM is better than FFT-BPM.
- The FD-BPM is more accurate especially in modelling structures with large refractive index discontinuities.
- The FD-BPM can also accommodate the wide-angle propagation and full vector algorithms [Hadley, 1992c; Huang and Xu, 1992c].

Research has also been carried out on developing the semi and full vectorial beam propagation algorithms based on the finite difference method [Huang *et al.*, 1991a; Huang *et al.*, 1991b; Liu and Li, 1992; Huang *et al.*, 1992a; Huang *et al.*, 1992b; Liu *et al.*, 1993]. Such method is found to be able to analysis the polarization dependence and polarization coupling of optical waveguide. However, the disadvantages for such method are described as following:

- The FD-BPM always discretized the cross-section with uniform grids, in which, it results in higher computational efforts and for curved boundaries, the FD-BPM present a very crude approximation.
- When an arbitrary input field is studied, FD-BPM will generate some unphysical gain (lossless structure is assumed) during the propagation

[Kriezis, 1997]. The reason for that is that the propagation matrices involved in the FD-BPM algorithms are complex non-Hermitian, which enhance the unphysical spurious mode to appear.

### **FINITE ELEMENT BPM (FE-BPM)**

The FE-BPM is described as one of the most versatile and powerful numerical algorithms for the beam propagation method. A method developed by Koch and Davies [Koch *et al.*, 1989; Koch *et al.*, 1991] seen that a variational method is employed to solve the scalar wave equation, under the paraxial approximation, with the finite element applied to the transverse cross section and the finite difference Crank-Nicolson method employed to the longitudinal axis of propagation. Another FE-BPM derived via the used of Galerkin's formulation to solve the scalar wave equation is developed by Koshihara [Hayata *et al.*, 1990; Tsuji *et al.*, 1996; Tsuji *et al.*, 1997a; Tsuji *et al.*, 1997b; Niiyama and Koshihara, 1998]. In this method, a wide angle Pade approximation has been employed to model the longitudinally non-uniform optical devices instead of the crude paraxial approximation. A transparent boundary condition needs to be satisfied to minimise the occurrence of the non-physical reflections from the edge of the computational domain. However all the FE-BPM described so far are solving scalar wave equation, which means that these methods cannot be solve for polarization properties and the power coupling of optical devices.

A vectorial approach by Montanari [Monanari *et al.*, 1997; Monanari *et al.*, 1998] was developed based on the paraxial approximation and did not have to satisfy the absorbing boundary condition. However, such method yields a large computational effort and storage requirements for solving three magnetic field components.

It is found that a full vectorial FE-BPM by Obayya [Obayya *et al.*, 2000a; Obayya *et al.*, 2000b] based on the two transverse components of the magnetic field was more versatile and efficient. Such method employed the robust perfectly matched layer (PML) boundary condition into the FE-BPM formulation to absorb the unwanted radiation out of the computational domain and the sparsity of the matrix

equation will not be destroyed. This FE-BPM has also certain advantages over the FD-BPM and FFT-BPM, such as the discretization of the domain, better approximation of curved structures and an efficient distribution of nodal points. The advantages of the vectorial FE-BPM considered in this work are described below:

- It uses wide angle approximation therefore it better to find waves propagating off the propagation axis
- Employed the perfectly matched layer (PML) as boundary condition.
- The computational time and the computational storage will be reduced and minimised as FE-BPM solve only the transverse components of the magnetic field.

In the following sections, the vectorial FE-BPM formulation will be discussed and presented, as this approach will be used in this project.

## **2.6.2 BOUNDARY CONDITIONS**

The computational domain window in BPM formulation is finite therefore it is fundamental to employ and specify the boundary condition when optical waveguide analysis is studied. It is essential to choose a correct boundary condition so that when analysing an optical waveguide, the effect of the boundaries does not introduce additional errors in the propagation of the optical field. These errors can occur when the boundary conditions are not set properly and that the radiation tends to reflect back to the region of interest from the boundaries of the computational window. Different types of BPM has different types of natural boundary conditions. Besides that they can consider different boundary conditions.

For instance, in the FFT-BPM, the boundary condition used is the 'absorbing boundary condition' [Feit and Fleck, 1978; Feit and Fleck, 1980; Lagasse and Baets, 1987]. Such approach inserts a lossy medium at the edges of the computational window to absorb the reflections at the boundary. However, this method is problem dependent, usually the absorption coefficient is set in between zero to some maximum value at the boundary node but if such coefficient is too large then itself will generate reflections. Also for a specific structure, various parameters of this

approach have to be chosen carefully in respect of the thickness of the lossy region, the value of the absorption coefficient and the functional shape.

The boundary condition associated with FD-BPM in here is known as 'transparent boundary condition' (TBC)[Hadley, 1991; Hadley, 1992a]. Such method is to approximate the wave near the boundary of the computational domain as a plane wave which satisfies:

$$\frac{\partial \phi}{\partial \rho} = -jk\phi \quad (2.54)$$

where  $\Phi$  is the field near the boundary,  $k$  is the transverse wave-vector and  $\rho$  is the distance in the direction normal to the boundary. In essence, this method simulates a non-existent boundary [Hadley, 1991; Hadley, 1992a] and that radiation is allowed to escape the problem region without significant reflection. This transparent boundary condition is more robust and problem independent than the absorbing boundary condition. However such boundary condition is not sufficient to suppress large radiation of the outgoing wave near the boundary.

Perfectly matched layer (PML) is a boundary condition that was developed by Berenger [Berenger, 1994; Berenger, 1996; Sacks *et al.*, 1995] as an alternative to the absorbing or transparent boundary conditions. Its aim is to synthesise an absorbing layer for the finite difference time domain (FDTD) method. In its original form, the field components are split into two sub-components, in doing so, it leads to non-Maxwell's equations, which finite elements cannot be applied to. Therefore, Pekel and Mittra [Perkel and Mittra, 1995a; Perkel and Mittra, 1995b] have introduced a new form of PML to solve the free space scattering problems. Such method does not split the field components and it also retaining the desired form of the Maxwell's equation for the finite element application. Obayya [Obayya *et al.*, 2000a] has also incorporated the PML in FE-BPM formulations.

### **2.6.3 PERFECTLY MATCHED LAYER (PML)**

In this chapter, the PML boundary condition is incorporated into the vectorial FE-BPM equations. The cross section of an arbitrarily shaped waveguide is shown in Fig. 2.5. The transverse direction is defined as  $x$  and  $y$ , where as  $z$  is the propagation

direction,  $\Omega$  corresponds as the computational domain region.  $H_x$  and  $H_y$  are the width and height of the computational domain in the  $x$  and  $y$  directions, respectively. Region  $\Omega_1$  and  $\Omega_2$  are the PML regions normally faced with  $x$  and  $y$  directions, respectively, where as  $\Omega_3$  corresponds to the four corners of the PML regions.

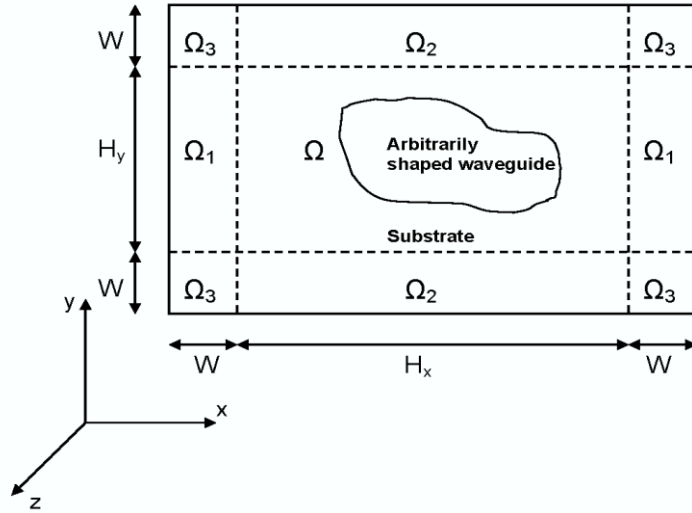


Fig. 2.5 An arbitrarily shaped waveguide with different PML regions.

Maxwell's curl equations with PML can take the form of:

$$\nabla' \times \mathbf{H} = j\omega \varepsilon_0 n^2 \mathbf{E} \quad (2.55)$$

$$\nabla' \times \mathbf{E} = -j\omega \mu_0 \mathbf{H} \quad (2.56)$$

where  $\mathbf{H}$  and  $\mathbf{E}$  are the magnetic and electric field vectors, respectively.

The square of the refractive index is  $n^2$  and  $\nabla'$  is the modified differential operator which is defined as:

$$\nabla' = x\alpha_x \frac{\partial}{\partial x} + y\alpha_y \frac{\partial}{\partial y} + z \frac{\partial}{\partial z} \quad (2.57)$$

where,

$$\alpha_t (t = x \text{ or } y) = \frac{1}{1 - j \frac{\sigma_e}{\omega \varepsilon_0 n^2}} = \frac{1}{1 - j \frac{\sigma_m}{\omega \mu_0}} \quad (2.58)$$

in which,  $\sigma_e$  and  $\sigma_m$  are the electric and magnetic conductivities of the PML, respectively. Equation (2.58) shows that the PML satisfies the impedance matching

condition with an adjacent medium in the computational domain with refractive index  $n$  and impedance  $\sqrt{\frac{\mu_0}{\varepsilon_0 n^2}}$ .

In the PML region,  $\alpha_x$  and  $\alpha_y$  are defined as:

1. In region  $\Omega$  (computation domain)

$$\alpha_x = 1 \quad \text{and} \quad \alpha_y = 1$$

2. In region  $\Omega_1$  (right or left region)

$$\alpha_x = \alpha_t \quad \text{and} \quad \alpha_y = 1$$

3. In region  $\Omega_2$  (top or bottom region)

$$\alpha_x = 1 \quad \text{and} \quad \alpha_y = \alpha_t$$

4. In region  $\Omega_3$  (four corners region)

$$\alpha_x = \alpha_t \quad \text{and} \quad \alpha_y = \alpha_t$$

In the PML regions, the electric conductivity is expressed as:

$$\sigma_e(\rho) = \sigma_{\max} \left[ \frac{\rho}{w} \right]^m \quad (2.59)$$

where  $\rho$  is the distance inside the PML region, which is measured from the interface of the computational domain and the PML section. The maximum value of the electric conductivity corresponds to  $\sigma_{\max}$  and  $m$  is the power of the conductivity profile, normally it is taken as the value of 2. For the conductivity profile, the theoretical reflection coefficient  $R$ , at the interface between the PML region and the computational domain is defined as [Huang *et al.*, 1996]:

$$R = \exp \left[ -2 \frac{\sigma_{\max}}{cn\varepsilon_0} \int_0^w \left[ \frac{\rho}{w} \right]^2 \partial\rho \right]^m \quad (2.60)$$

where  $c$  is the velocity of light in free space. By integrating equation (2.60),  $\sigma_{\max}$  can be given as:

$$\sigma_{\max} = \frac{3cn\varepsilon_0}{2d} \ln \left[ \frac{1}{R} \right] \quad (2.61)$$

The value of the theoretical coefficient  $R$  can be chosen and normally it is set to a very small value, the maximum electric conductivity,  $\sigma_{\max}$  can be calculated by using equation (2.61). In doing so, the electric conductivity profile,  $\sigma(\rho)$  and the PML parameters  $\alpha_x$  and  $\alpha_y$  will also be calculated for different PML regions. With these arrangements of PML in different regions, any nonphysical radiation wave will freely leave the computational domain.

## 2.6.4 WAVE EQUATIONS

To derive the vectorial wave equations, Maxwell's curl equations of (2.55) and (2.56) will be required. By taking the curl equation of (2.55) and substituting equation (2.56) into equation (2.55) gives:

$$\nabla' \times (n^{-2} \nabla' \times \mathbf{H}) - k_0^2 \mathbf{H} = 0 \quad (2.62)$$

where  $k_0$  is the free space wavenumber and it is given by:

$$k_0 = \omega \sqrt{\mu_0 \epsilon_0} = \frac{2\pi}{\lambda} \quad (2.63)$$

where  $\lambda$  is the free space wavelength.

The full vectorial wave equation shown in equation (2.62) that it consists of three components of the magnetic field vector,  $\mathbf{H}$ . This full vectorial wave equation can be reduced to two transverse components of  $H_x$  and  $H_y$  by the use of zero divergence condition, which is expressed as:

$$\nabla \cdot \mathbf{H} = 0 = \alpha_x \frac{\partial H_x}{\partial x} + \alpha_y \frac{\partial H_y}{\partial y} + \frac{\partial H_z}{\partial z} \quad (2.64)$$

By substituting equation (2.64) into equation (2.62) yields the following two coupled wave equations:

For  $H_x$  component,

$$\begin{aligned} 0 = & \frac{\partial}{\partial z} \left( n^{-2} \frac{\partial H_x}{\partial z} \right) + \alpha_y \frac{\partial}{\partial y} \left( n^{-2} \alpha_y \frac{\partial H_x}{\partial y} \right) + n^{-2} \alpha_x \frac{\partial}{\partial x} \left( \alpha_x \frac{\partial H_x}{\partial x} \right) + k_0^2 H_x \\ & + n^{-2} \alpha_x \frac{\partial}{\partial x} \left( \alpha_y \frac{\partial H_y}{\partial y} \right) - \alpha_y \frac{\partial}{\partial y} \left( n^{-2} \alpha_x \frac{\partial H_y}{\partial x} \right) \end{aligned} \quad (2.65)$$

Similarly for  $H_y$  component,

$$0 = \frac{\partial}{\partial z} \left( n^{-2} \frac{\partial H_y}{\partial z} \right) + \alpha_x \frac{\partial}{\partial x} \left( n^{-2} \alpha_x \frac{\partial H_y}{\partial x} \right) + n^{-2} \alpha_y \frac{\partial}{\partial y} \left( \alpha_y \frac{\partial H_y}{\partial y} \right) + k_0^2 H_y \\ + n^{-2} \alpha_y \frac{\partial}{\partial y} \left( \alpha_x \frac{\partial H_x}{\partial x} \right) - \alpha_x \frac{\partial}{\partial x} \left( n^{-2} \alpha_y \frac{\partial H_x}{\partial y} \right) \quad (2.66)$$

The refractive index in the direction of propagation is assumed to be slowly varying in deriving the wave equations of (2.65) and (2.66), in which  $\left( \frac{\partial n^{-2}}{\partial z} \right) = 0$ .

It is found that it is much easier to solve equations (2.65) and (2.66) than equation (2.62) because the number of unknown components are small and also zero divergence condition is automatically satisfied through the derivation, therefore it eliminates the occurrence of spurious solutions.

By assuming the wave travels along the  $+z$  direction, the fields can be separated as slowly-varying envelopes and a fast-oscillating phase term as:

$$\text{Let } \bar{H}_i = \bar{\phi}_i e^{-jn_0 k_0 z} \quad (2.67)$$

Equation (2.67) can be expressed as:

$$\begin{Bmatrix} H_x \\ H_y \end{Bmatrix} = \begin{Bmatrix} \phi_x \\ \phi_y \end{Bmatrix} \exp(-jn_0 k_0 z) \quad (2.68)$$

where  $n_0$  is a reference index of refraction,  $\Phi_x$  and  $\Phi_y$  are the slowly-varying envelopes of  $H_x$  and  $H_y$  components, respectively. In order to slowly-varying the envelopes in the  $+z$  direction,  $n_0$  should be chosen to the effective index of the guided mode(s) of the structure.

In the case of analysing the monomode waveguide,  $n_0$  can be set to the effective index of the fundamental mode. However, for the analysis of multimode waveguides, the effective indices of all guided modes have to be determined in order to set the value of  $n_0$ . In any case, for a better approximation, it is better to set  $n_0$  as the average value of the guide and substrate refractive indices.

By substituting equation (2.68) into equations (2.65) and (2.66) yields the following two coupled unidirectional wave equations:

$$\begin{aligned}
 0 = n^{-2} \frac{\partial^2 \phi_x}{\partial z^2} - 2jn_0 k_0 n^{-2} \frac{\partial \phi_x}{\partial z} + \alpha_y \frac{\partial}{\partial y} \left( n^{-2} \alpha_y \frac{\partial \phi_x}{\partial y} \right) + n^{-2} \alpha_x \frac{\partial}{\partial x} \left( \alpha_x \frac{\partial \phi_x}{\partial x} \right) \\
 + k_0^2 (1 - n^{-2} n_0^2) \phi_x + n^{-2} \alpha_x \frac{\partial}{\partial x} \left( \alpha_y \frac{\partial \phi_y}{\partial y} \right) - \alpha_y \frac{\partial}{\partial y} \left( n^{-2} \alpha_x \frac{\partial \phi_y}{\partial x} \right)
 \end{aligned} \tag{2.69}$$

$$\begin{aligned}
 0 = n^{-2} \frac{\partial^2 \phi_y}{\partial z^2} - 2jn_0 k_0 n^{-2} \frac{\partial \phi_y}{\partial z} + \alpha_x \frac{\partial}{\partial x} \left( n^{-2} \alpha_x \frac{\partial \phi_y}{\partial x} \right) + n^{-2} \alpha_y \frac{\partial}{\partial y} \left( \alpha_y \frac{\partial \phi_y}{\partial y} \right) \\
 + k_0^2 (1 - n^{-2} n_0^2) \phi_y + n^{-2} \alpha_y \frac{\partial}{\partial y} \left( \alpha_x \frac{\partial \phi_x}{\partial x} \right) - \alpha_x \frac{\partial}{\partial x} \left( n^{-2} \alpha_y \frac{\partial \phi_x}{\partial y} \right)
 \end{aligned} \tag{2.70}$$

## 2.7 BPM FINITE ELEMENTS FORMULATION

Equations (2.69) and (2.70) will be used to solve the slowly varying envelope by the application of the finite element method. First assume that the waveguide cross section shown in Fig. 2.5 is discretized into a patchwork of first order triangular elements.

By applying Galerkin's procedure to equations (2.69) and (2.70) leads to the following two equations:

$$\begin{aligned}
 0 = \int_e n^{-2} \frac{\partial^2 \phi_x}{\partial z^2} N_i ds - \int_e 2jn_0 k_0 n^{-2} \frac{\partial \phi_x}{\partial z} N_i ds + \int_e \alpha_y^2 \frac{\partial}{\partial y} \left( n^{-2} \frac{\partial \phi_x}{\partial y} \right) N_i ds \\
 + \int_e n^{-2} \alpha_x^2 \frac{\partial^2 \phi_x}{\partial x^2} N_i ds + \int_e k_0^2 (1 - n^{-2} n_0^2) \phi_x N_i ds \\
 + \int_e n^{-2} \alpha_x \alpha_y \frac{\partial^2 \phi_y}{\partial x \partial y} N_i ds - \int_e \alpha_x \alpha_y \frac{\partial}{\partial y} \left( n^{-2} \frac{\partial \phi_y}{\partial x} \right) N_i ds
 \end{aligned} \tag{2.71}$$

$$\begin{aligned}
0 = & \int_e n^{-2} \frac{\partial^2 \phi_y}{\partial z^2} N_i ds - \int_e 2jn_0 k_0 n^{-2} \frac{\partial \phi_y}{\partial z} N_i ds + \int_e \alpha_x^2 \frac{\partial}{\partial x} \left( n^{-2} \frac{\partial \phi_y}{\partial x} \right) N_i ds \\
& + \int_e n^{-2} \alpha_y^2 \frac{\partial^2 \phi_y}{\partial y^2} N_i ds + \int_e k_0^2 (1 - n^{-2} n_0^2) \phi_y N_i ds \\
& + \int_e n^{-2} \alpha_x \alpha_y \frac{\partial^2 \phi_x}{\partial x \partial y} N_i ds - \int_e \alpha_x \alpha_y \frac{\partial}{\partial x} \left( n^{-2} \frac{\partial \phi_x}{\partial y} \right) N_i ds
\end{aligned} \tag{2.72}$$

where  $N_i$  are the shape functions with  $i = 1, 2, 3$  over the first order triangular element,  $e$ , and  $\int_e (\cdot) ds$  is the integration over the element area.

Several assumptions have been made to derive equations (2.71) and (2.72). It has been assumed that the refractive index,  $n$ , and the PML  $\alpha_x$  and  $\alpha_y$  parameters are fixed to constant values within each element. Therefore, when working with the step index waveguides, the discontinuity of the refractive index and the associated interface boundary conditions will not be accounted for. But, using Green's theorem for integration by parts will result in line integrations around each element, which can be utilized to satisfy the following interface boundary conditions:

### Interface boundary conditions

- $E_z$  is continuous, in which,

$$E_z \propto n^{-2} \left( \frac{\partial \phi_y}{\partial x} - \frac{\partial \phi_x}{\partial y} \right)$$

- $n^{-2} \frac{\partial \phi_x}{\partial x}$  and  $n^{-2} \frac{\partial \phi_y}{\partial y}$  are discontinuous along the horizontal and vertical interfaces between two different media.

By considering the above interface boundary conditions and using the Green's theorem for integration by parts to equations (2.71) and (2.72) results in:

$$\begin{aligned}
 0 = & \int_e n^{-2} \frac{\partial^2 \phi_x}{\partial z^2} N_i ds - 2jn_0 k_0 \int_e n^{-2} \frac{\partial \phi_x}{\partial z} N_i ds - \int_e \alpha_y^2 n^{-2} \frac{\partial \phi_x}{\partial y} \frac{\partial N_i}{\partial y} ds \\
 & - \int_e \alpha_x^2 n^{-2} \frac{\partial \phi_x}{\partial x} \frac{\partial N_i}{\partial x} ds + \oint_{\Gamma_e} \alpha_x^2 n^{-2} \frac{\partial \phi_x}{\partial x} N_i n_x d\Gamma_e + \int_e k_0^2 (1 - n^{-2} n_0^2) \phi_x N_i ds \\
 & - \int_e \alpha_x \alpha_y n^{-2} \frac{\partial \phi_y}{\partial y} \frac{\partial N_i}{\partial x} ds + \oint_{\Gamma_e} \alpha_x \alpha_y n^{-2} \frac{\partial \phi_y}{\partial y} N_i n_x d\Gamma_e + \int_e \alpha_x \alpha_y n^{-2} \frac{\partial \phi_y}{\partial x} \frac{\partial N_i}{\partial y} ds
 \end{aligned} \tag{2.73}$$

$$\begin{aligned}
 0 = & \int_e n^{-2} \frac{\partial^2 \phi_y}{\partial z^2} N_i ds - 2jn_0 k_0 \int_e n^{-2} \frac{\partial \phi_y}{\partial z} N_i ds - \int_e \alpha_x^2 n^{-2} \frac{\partial \phi_y}{\partial x} \frac{\partial N_i}{\partial x} ds \\
 & - \int_e \alpha_y^2 n^{-2} \frac{\partial \phi_y}{\partial y} \frac{\partial N_i}{\partial y} ds + \oint_{\Gamma_e} \alpha_y^2 n^{-2} \frac{\partial \phi_y}{\partial y} N_i n_y d\Gamma_e + \int_e k_0^2 (1 - n^{-2} n_0^2) \phi_y N_i ds \\
 & - \int_e \alpha_x \alpha_y n^{-2} \frac{\partial \phi_x}{\partial y} \frac{\partial N_i}{\partial x} ds + \oint_{\Gamma_e} \alpha_x \alpha_y n^{-2} \frac{\partial \phi_x}{\partial x} N_i n_y d\Gamma_e + \int_e \alpha_x \alpha_y n^{-2} \frac{\partial \phi_x}{\partial x} \frac{\partial N_i}{\partial y} ds
 \end{aligned} \tag{2.74}$$

in which,  $n_x$  and  $n_y$  are the direction cosines between the normal to the element boundary  $\Gamma_e$  and  $x$  and  $y$  directions, respectively.  $\oint_{\Gamma_e} (\cdot) d\Gamma_e$  corresponds to the integration over the element boundary,  $\Gamma_e$ .

The line integrals in equation (2.73) and (2.74) are there for the interface boundary conditions, they are also responsible for the polarization dependence and coupling, therefore these integrals are mandatory for a full vectorial formulations.

Let the whole cross section of the computational window be divided into a number of triangles and approximate  $\Phi_x$  and  $\Phi_y$  as follow:

Over an element of  $e$  and in terms of shape functions,  $N_i$ , the transverse magnetic field envelopes can be expressed as:

$$\phi_{x(x,y,z)}^e = \sum_{i=1}^3 h_{xi}(z) N_{i(x,y)} \tag{2.75}$$

$$\phi_{y(x,y,z)}^e = \sum_{i=1}^3 h_{yi}(z) N_{i(x,y)} \tag{2.76}$$

in which,  $h_{xi}(z)$  and  $h_{yi}(z)$  are the element nodal values of the  $x$  and  $y$  components of the magnetic field, respectively.

By substituting Equations (2.75) and (2.76) into (2.73) and (2.74), and collecting the contributions from all elements results in:

$$[M] \frac{\partial^2 \{h_t\}}{\partial z^2} - 2jn_0k_0[M] \frac{\partial \{h_t\}}{\partial z} + ([K] - n_0^2k_0^2[M])\{h_t\} = \{0\} \quad (2.77)$$

where  $\{0\}$  is a column vector with all zero entries, and  $\{h_t\}$  is defined as the following:

$$\{h_t\} = \begin{Bmatrix} h_x(z) \\ h_y(z) \end{Bmatrix} = \sum_e \begin{Bmatrix} h_{x1} \\ h_{x2} \\ h_{x3} \\ h_{y1} \\ h_{y2} \\ h_{y3} \end{Bmatrix} \quad (2.78)$$

where  $h_x(z)$  and  $h_y(z)$  represent the nodal values of the  $x$  and  $y$  components of the magnetic field over the whole domain.

The global matrices  $[M]$  and  $[K]$  in equation (2.77) can be expressed as the summation of the corresponding element matrices:

$$[M]_{6 \times 6} = \sum_e [M_e] = \sum_e \begin{bmatrix} [M_{xx}]_{3 \times 3} & [0]_{3 \times 3} \\ [0]_{3 \times 3} & [M_{yy}]_{3 \times 3} \end{bmatrix} \quad (2.79)$$

$$[K]_{6 \times 6} = \sum_e [K_e] = \sum_e \begin{bmatrix} [K_{xx}]_{3 \times 3} & [K_{xy}]_{3 \times 3} \\ [K_{yx}]_{3 \times 3} & [K_{yy}]_{3 \times 3} \end{bmatrix} \quad (2.80)$$

in which,  $\sum_e$  stands for the contribution of all element matrices  $[M_e]$  and  $[K_e]$ . The calculations of the element matrices are shown in Appendix 2.

It is noted that the element matrix  $[K_e]$ , from equation (2.80) is responsible for coupling and polarization dependence issues. It is recognized that the inclusion of the line integrals in the matrices  $[K_{xx}]$  and  $[K_{yy}]$  make them unequal, and therefore polarization dependence is accounted for. As the matrices  $[K_{xy}]$  and  $[K_{yx}]$  are not zeros, the coupling between the polarization states is taken into account.

Although such formulation only considers two transverse components of the magnetic field but it is still being categorized as full-vectorial formulation. One advantage for such vectorial formulation is that the resulting global matrices  $[M]$  and  $[K]$  are sparse and therefore only nonzero elements values have to be stored and consequently, it reduced the computational cost greatly, unlike other full vectorial formulations based on transverse components, in which the resulting global matrices are dense matrices. This full vectorial formulation also has the ability to work as semi-vectorial formulation and scalar formulation, for instance, by neglecting some matrices liked the  $[K_{xy}]$  and  $[K_{yx}]$ , so that the formulation reduced to two decoupled wave equations for  $H_x$  and  $H_y$ , hence, the formulation became semi-vectorial.

The formulation shown in equation (2.77) represents the exact nonparaxial vectorial wave equation that needs to be solved in a step by step procedure in the  $z$ -direction. By neglecting the  $z$ -second derivative term, the formulation reduces to the approximate paraxial equation, in which this formulation is only valid for wave propagating very near to the axis of propagation,  $z$ . It is found that by using Pade' approach [Hadley, 1992b], a better approximation can be obtained. The equation (2.77) can be written as:

$$-2jn_0k_0[M]\frac{\partial\{h_i\}}{\partial z_{i+1}} = -\frac{([K]-n_0^2k_0^2[M])\{h_i\}}{1-\frac{1}{2jn_0k_0}\frac{\partial}{\partial z_i}} \quad (2.81)$$

By utilising the first order Pade' approximation (Pade'(1,0)) by putting  $i = 0$  in the recurrence Pade relation in equation (2.81) and that  $\frac{\partial}{\partial z_0} = 0$ , shows:

$$-2jn_0k_0[\tilde{M}]\frac{\partial\{h_i\}}{\partial z} + ([K]-n_0^2k_0^2[M])\{h_i\} = \{0\} \quad (2.82)$$

where

$$[\tilde{M}] = [M] + \frac{1}{4n_0^2k_0^2}([K]-n_0^2k_0^2[M]) \quad (2.83)$$

### 2.7.1 WIDE ANGLE APPROXIMATION

By replacing matrix  $[\tilde{M}]$  by  $[M]$  in equation (2.82), the paraxial equation can be easily obtained. Equation (2.82) is also called the 'wide angle equation', as this equation can trace waves propagating off the propagation axis more accurately than the paraxial equation. To solve equation (2.82) in a finite range of the  $z$ -domain, it has to be divided into sections each of a width  $\Delta z$ .

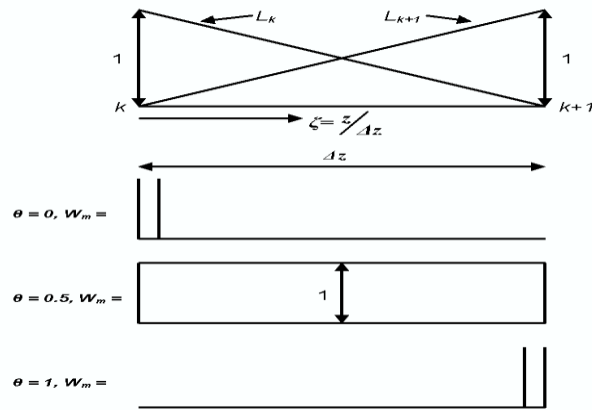


**Fig. 2.6** Shape functions and different cases of weighting functions for discretisation along the longitudinal  $z$ -axis.

Figure 2.6 shows that over the  $k^{\text{th}}$  section, the finite element method can also be used to approximate the field [Zienkiewicz, 1997] as :

$$\{h_t(\zeta)\} = L_k(\zeta)\{h_t(\zeta_k)\} + L_{k+1}(\zeta)\{h_t(\zeta_{k+1})\} \quad (2.84)$$

where  $\zeta$  is the local coordinate of the  $k^{\text{th}}$  section,  $\{h_t(\zeta_k)\}$  and  $\{h_t(\zeta_{k+1})\}$  are the column vectors containing the field nodal values over the whole cross section at  $k^{\text{th}}$  and  $(k+1)^{\text{th}}$  propagation steps, respectively, while  $L_k(\zeta)$  and  $L_{k+1}(\zeta)$  are the shape functions which can be expressed as:

$$L_k(\zeta) = 1 - \zeta \quad (2.85)$$

$$L_{k+1}(\zeta) = \zeta \quad (2.86)$$

Substituting the equations (2.84), (2.85) and (2.86) into equation (2.82) and applying Galerkin's method with weighting functions  $W_m$  gets the following equation:

$$[A]_k \{h_t\}_{k+1} = [B]_k \{h_t\}_k \quad (2.87)$$

where

$$[A]_k = -2jn_0k_0[\tilde{M}]_k + \theta\Delta z([K]_k - n_0^2k_0^2[M]_k) \quad (2.88)$$

$$[B]_k = -2jn_0k_0[\tilde{M}]_k + (\theta-1)\Delta z([K]_k - n_0^2k_0^2[M]_k) \quad (2.89)$$

where  $\Delta z$  is the propagation step size, subscripts  $k$  and  $k+1$  corresponds to the  $k^{\text{th}}$  and  $(k+1)^{\text{th}}$  propagation steps, respectively, and  $\theta$  is the scheme parameter given as:

$$\theta = \frac{\int_0^1 W_m \zeta d\zeta}{\int_0^1 W_m d\zeta} \quad (2.90)$$

Once the initial field is specified, the equation (2.88) can then be solved to find the field at the successive propagation steps.

The value of the scheme parameter,  $\theta$ , depends on the choice of the weighting function  $W_m$  shown in Fig. 2.6. The value of  $\theta$  decides the stability and the numerical losses of the propagation algorithm. It has been reported that for  $\theta \geq 0.5$ , the algorithm is going to be unconditionally stable [Zienkiewicz, 1997]. When  $\theta = 0.5$ , which it corresponds to the finite difference Crank-Nicolson algorithm, the algorithm will be stable and the propagating beam power is also conserved as well. However, as Crank-Nicolson algorithm is used, there will be some high frequency oscillations exist in the field distribution. One way to compensate this would be to use higher values of the scheme parameter,  $\theta$ , but such approach would result into some nonphysical numerical losses. The other method would be to employ PML boundary conditions in which, it would eliminate the appearance of high frequency oscillations within the field whenever Crank-Nicolson algorithm is used. Therefore it is found that the vectorial propagation algorithm proposed in this section is unconditionally stable when  $\theta$  is chosen to be 0.5 and that the power in the field is conserving as well.

## 2.8 POWER DEFINITION

In the analysis of optical devices, the propagating beam power is an important parameter to determine how much power is transmitted by the unit length of the optical waveguide device. Also, if the waveguide is bent, then the power losses of the bent section can be calculated and its losses can be minimised.

The power associated with a beam propagating in the +z direction is defined in terms of the Poynting's vector:

$$P = \frac{1}{2} R_e \left( \int E \times H^* \cdot \hat{z} d\Omega \right) = \frac{1}{2} R_e \left[ \int (E_x H_y^* - E_y H_x^*) d\Omega \right] \quad (2.91)$$

where,  $R_e$  means taking the real part, \* is defined as the complex conjugate,  $\hat{z}$  is the unit vector in the z-direction and that integration is carried out over the whole of the computational domain. For the Quasi-TE ( $E_x$ ) and Quasi-TM ( $E_y$ ) modes, these transverse electric field components can be given in terms of the magnetic field components as:

$$E_x = \frac{n_0 k_0}{\omega \epsilon_0} n^{-2} H_y \quad (2.92)$$

$$E_y = -\frac{n_0 k_0}{\omega \epsilon_0} n^{-2} H_x \quad (2.93)$$

Assuming that in deriving the  $E_x$  and  $E_y$  expressions, the second order derivatives with respect to the transverse coordinates,  $x$  and  $y$  can be neglected. Then by substituting the equations (2.92) and (2.93) into equation (2.91) gives:

$$P = \frac{n_0 Z_0}{2} \int n^{-2} \left( |H_x|^2 + |H_y|^2 \right) d\Omega \quad (2.94)$$

in which,  $Z_0 = \sqrt{\frac{\mu_0}{\epsilon_0}} = 377$  ohms or  $120\pi$  ohms, is the free space wave impedance. By

substituting equations (2.68), (2.75) and (2.76) into equation (2.94) gives:

$$P = \frac{n_0 Z_0}{2} \{h_t\}^T [M] \{h_t\} \quad (2.95)$$

where,  $\{h_t\}$  is the nodal values of the propagating field,  $[M]$  is the global matrix and  $T$  corresponds to the transpose of complex conjugate.

## 2.9 LEAST SQUARES BOUNDARY RESIDUAL (LSBR) METHOD

In the design of integrated optical devices, discontinuity problems in optical waveguides are important issues to overcome. These problems play a fundamental role in designing practical devices, such as, an isolated step discontinuity as found in the simple butt-joining of two waveguides of different widths, or as finite cascades of discontinuities found in the bending of an optical waveguide in an integrated optical directional coupler, or as found in the tapering of a channel waveguide for efficient coupling to an optical fibre and etc.

The LSBR method is a very powerful tool for the calculation of the discontinuity problem and such method is widely used in our simulation for the analysis of optical devices. In this thesis, the discontinuities in dielectric waveguides are accurately analysed using the LSBR developed by Rahman and Davies [El-Mikati and Davies, 1985; Rahman and Davies, 1988]. In this method, LSBR has to be used alongside the vectorial  $\mathbf{H}$ -field FEM [Rahman and Davies, 1984c] in order to calculate the power transfer from one waveguide section to another. The LSBR method considered here is found to be an alternative point-matching (and Galerkin) method of numerically solving scattering problems. It is found that LSBR method satisfies the boundary conditions more easily in the usual least-squares sense over the discontinuity interface. Unlike the point matching method, the LSBR [Davies, 1973; Brooke and Kharadly, 1976; Cullen and Yeo, 1987; Fernandez and Davies, 1988] is a rigorously convergence procedure free from the phenomenon of relative convergence. In this study it will be shown that LSBR method is an accurate and versatile numerical tool to obtain the power transfer between coupled waveguides.

## 2.10 LSBR FORMULATIONS

The LSBR method is a very useful and powerful numerical tool that can be used to analyse the discontinuity problems at an abrupt junction of two dielectric waveguides. Figure 2.7 illustrates how the discontinuity of two dielectric waveguide

is represented. Firstly, let's consider the vertical section of the discontinuity between two different waveguides, side I and side II, respectively, as shown in Fig. 2.7.a.

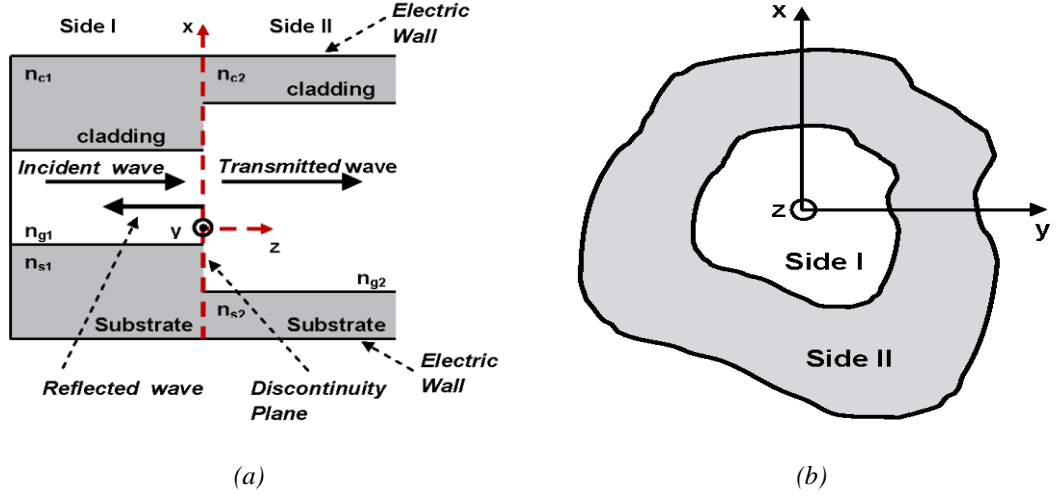


**Fig. 2.7** *Discontinuity at the junction of two dielectric waveguide. (a) Vertical section of the discontinuity between side I and side II. (b) Transverse cross section of the discontinuity between side I and side II.*

Assuming that an incoming wave is propagating through the guided medium from side I of the waveguide to the guided medium of the side II waveguide, it is thought that at the discontinuity junction (where two different waveguides are joined together), this interface (discontinuity plane) is excited by an incident wave of one mode from side I. Part of this incident wave is reflected back to side I waveguide, part of it is transmitted through to side II waveguide and part of it is radiated to the cladding and to the substrate.

Consider this in a mathematical term and suppose that  $E_t^{in}$  and  $H_t^{in}$  are the transverse components of the electric and magnetic fields of the incident wave, respectively. As mentioned, some of the incident wave is reflected back to the side I waveguide but due to the boundary conditions principle, many modes will be generated at the discontinuity plane and these modes can be guided or radiated modes in both sides of the discontinuity to satisfy its boundary conditions. Therefore, the total transverse electric and magnetic fields  $E_t^I$  and  $H_t^I$  in side I and  $E_t^{II}$  and  $H_t^{II}$  in side II at the discontinuity plane ( $z=0$ ), can be expressed in terms of the eigenvalue modes in side I and side II, respectively as:

$$E_t^I = E_t^{in} + \sum_{i=1}^{\infty} a_i E_{ii}^I \quad (2.96)$$

$$H_t^I = H_t^{in} - \sum_{i=1}^{\infty} a_i H_{ii}^I \quad (2.97)$$

$$E_t^{II} = \sum_{i=1}^{\infty} b_i E_{ii}^{II} \quad (2.98)$$

$$H_t^{II} = \sum_{i=1}^{\infty} b_i H_{ii}^{II} \quad (2.99)$$

It is now known that at the discontinuity plane, the modes generated may be propagating, radiating or evanescent to satisfy the boundary conditions. Equations (2.96) and (2.97) show that  $E_{ii}^I$  and  $H_{ii}^I$  represent the transverse field components of the  $i^{th}$  mode reflected from the discontinuity junction in side I and that  $a_i$  are the corresponding modal amplitudes of these reflected modes. Similarly for equations (2.98) and (2.99), instead of reflecting,  $E_{ii}^{II}$  and  $H_{ii}^{II}$  are the transverse field components of the  $i^{th}$  mode transmitted in side II and that  $b_i$  are the modal amplitudes of these transmitted modes. The  $a_i$  and  $b_i$  are also called the scattering coefficients and these values will be determined in the later section.

The aim of the LSBR method is to look for a stationary solution to satisfy the continuity conditions of the tangential fields in a least squares sense by minimising a functional, and by considering the fields in either side of the discontinuity junction, the functional can be defined as:

$$J = \int |E_t^I - E_t^{II}|^2 + \alpha \cdot Z_0^2 |H_t^I - H_t^{II}|^2 d\Omega \quad (2.100)$$

where,  $\alpha$  is the dimensionless weighting factor,  $Z_0$  is the free space wave impedance.

In order to obtain the approximate numerical solution of the problem (as in Equation (2.100)), the infinite expansions of Equations (2.96), (2.97), (2.98) and (2.99) are truncated, including all relevant propagating modes plus as many radiating and/or evanescent modes as convenient. By employing the LSBR method in the analysis, all the coefficients of reflection, transmission and radiation fields are determined in such a way that  $J$  becomes a minimum. Therefore equation (2.100) is minimised to the following:

$$\frac{\partial J}{\partial a_i} = 0, \quad \frac{\partial J}{\partial b_i} = 0 \quad \text{for } i = 1 \dots \infty \quad (2.101)$$

which results in a set of linear equation:

$$Cx = v \quad (2.102)$$

The solution of equation (2.102) gives  $\{x\}$ , which is the required approximate modal coefficient of  $a_i$  and  $b_i$ . These constitute one column of the scattering matrix which corresponds to the chosen incident mode. The parameter  $C$  in equation (2.102) represents a square matrix generated from the eigenvectors, and  $v$  is an array due to the incident mode. The elements of  $C$  matrix and  $v$  are given as:

$$C_{ij} = \langle E_{ii}, E_{ij} \rangle + \alpha \cdot Z^2 \langle H_{ii}, H_{ij} \rangle \quad (2.103)$$

$$v_i = \langle E_i^{in}, E_{ii} \rangle + \alpha \cdot Z^2 \langle H_i^{in}, H_{ii} \rangle \quad (2.104)$$

in which,  $i, j = 1, \dots, N$ , and the value of  $N$  is the total number of modes in side I and side II, and that the vectors  $E_t$  and  $H_t$  are made up of all the corresponding modal fields in both sides. The inner product involved in equations (2.103) and (2.104) is defined as:

$$\langle x_1, x_2 \rangle = \int x_1 \cdot x_2^* ds \quad (2.105)$$

where  $x_1$  and  $x_2$  are the two field vectors, the complex conjugate of  $x_2$  is represent by  $x_2^*$  and that the integration is carried out over the whole waveguide cross section.

In this section, the LSBR is outlined briefly and the application of such method will be given in more details in the next few chapters to analyse a relevant waveguide problems concerning power transfer between waveguides and in particular the unwanted polarization crosstalk in the polarization rotator.

## 2.11 APPLICATION OF LSBR METHOD BY USING FINITE ELEMENT MODAL SOLUTION OUTPUT

The vectorial  $\mathbf{H}$ -field FEM described earlier has become a versatile numerical tool for the analysis of microwave and optical waveguides. In order to analyse power transfer characteristics of coupled waveguides, the LSBR method can be used along with the vectorial  $\mathbf{H}$ -field FEM. It is found that by employing the penalty method in FEM, spurious solutions will be eliminated and this will improve the quality of the eigenvectors that FEM generated, which is a very important factor for the analysis of the discontinuity problems. By employing the finite element program on both of the

waveguides (side I and side II), the nodal values of the complete  $\mathbf{H}$ -field for each mode are obtained. By applying the Maxwell's equation, the  $\mathbf{E}$ -field over each element are calculated using these nodal  $\mathbf{H}$ -field vales. Next all the modal eigenvalues and eigenvectors of all the modes in both sides of the discontinuity that are generated by the vectorial  $\mathbf{H}$ -field method are then used as the input data to the LSBR method. The LSBR program reads all the input data and calculates the integral  $\mathbf{J}$  and minimizes the error criteria given by equation (2.100) with respect to each value of  $a_i$  and  $b_i$  for any given incidence by solving a homogeneous linear equation in (2.102). The solution generated by equation (2.102) gave a unknown column vector  $\{x\}$ , which consists of unknown reflected and transmitted coefficients of all the modes considered in the analysis.

The LSBR method has been applied on a wide range of discontinuity problems involving an abrupt change at the transverse plane between arbitrary guiding structures of uniform cross section, vertical shifts, horizontal misalignments, sudden changes of width or height and etc. LSBR method can also be used to find the optimum matching of the two waveguides by controlling the geometries and material properties of the guides. It is also found that the radiation loss from random fluctuations in waveguide geometry and refractive index can be minimised by choosing the optimum guide parameters. In doing so the resulting reflecting matrix and the transmission matrix give a complete understanding of the discontinuity problem which help to improve the design of optical devices.

## **2.12 FORMULATION OF LOSSES IN OPTICAL WAVEGUIDES**

The LSBR method can be applied to analyze the optical losses in the waveguide devices. When light wave is propagating through a guided medium in the optical waveguide devices, some optical power losses will occur. These losses can be propagation loss, coupling loss, electrode loading loss and waveguide bending loss. In particular for the propagating loss, normally it made up of three different additional losses such as, scattering loss, absorption loss and radiation loss. It is

found that the scattering loss is usually predominates in glass or dielectric waveguides, while the absorption loss is most important in semiconductors and other crystalline materials. Also radiation losses become more significant when waveguides are bent, where, photons can be scattered, absorbed or radiated, in which it leads to the reduction of the total power transmission. Therefore the intensity (power per area) at any point along the length of the waveguide is given as:

$$I(z) = I_0 e^{-\alpha z} \quad (2.106)$$

in which,  $I_0$  is the initial intensity at  $z = 0$ , and  $\alpha$  is the power attenuation coefficient.

The LSBR method is known to analyse the waveguide junction efficiently in order to calculate the power transfer from the input guide to the other waveguide. Normally the waveguide junction is described as a butt join or coupled with two optical waveguides. It is found that when a guided TE or TM mode is incident on the discontinuity plane between two waveguides, some of the incident wave (light) power is lost and such loss is called the 'insertion loss'. The LSBR method can also be used to calculate the power loss suffered by TE or TM mode by utilising the scattering coefficients. The insertion loss expressed in decibel (dB) is given as:

$$L = 10 \log_{10} \left( \sum_{i=1}^N |b_i|^2 \right) \quad (2.107)$$

where,  $b_i$  are the transmission coefficients of the  $i^{th}$  mode and  $N$  is the total number of modes considered.

The attenuation (dB) of an optical beam can be express as:

$$I_L = 10 \log_{10} \frac{P_{in}}{P_{out}} \quad (2.108)$$

in which,  $I_L$  is the insertion loss,  $P_{in}$  is the input power and  $P_{out}$  is the output power.

## 2.13 SUMMARY

The FEM based on the variational principle has been discussed in this chapter for solving optical waveguides programs. A brief overview of the method is also presented. The Maxwell's equations along with the boundary conditions, variational formulations of different scalar approximation method and vectorial methods are also discussed. In particular, the vector **H**-field based FEM is studied in great detail in which, the domain discretization, shape functions, natural boundary conditions and the formation of the element and global matrices are also evaluated. In order to eliminate the non-physical or spurious solution, the penalty function method is reviewed and discussion on the application of the penalty function method has also been studied.

Next the BPM based on the finite element technique has been presented. The incorporation of the PML boundary condition into the vectorial wave equations, in which the vectorial propagation algorithm can account for the polarisation dependence and coupling has also been shown. Such BPM is based on the transverse magnetic field components. The formulation for such method does not only consider the minimum number of components for a real vector formulation, but also, it satisfies the boundary condition at the interface and hence, automatically satisfies the zero divergence condition. Therefore the possibility for spurious solutions to propagate will not exist.

Finally, the LSBR is described for use to analyse the discontinuities in optical waveguides. It is described in this chapter that by using the scattering coefficients, the power transfer between two waveguides can be calculated in which the insertion loss is found by using the LSBR method.

The FEM along with the BPM and the LSBR presented here form the fundamental of the numerical works in the analysis of the optical waveguides problems. The application of these methods to characterise and optimise the performance of various waveguides and photonic devices will be presented in the subsequent chapters.

# 3

## Analysis of Bent Waveguides

### 3.1 INTRODUCTION

In the design of a PIC, most of the optical components used are assembled as basic elements which then are connected by using straight and bent waveguides. Bent waveguides are important building blocks used to interconnect non-collinear straight waveguides and input/output ports, and they are also used in the design of specialized components, such as ring resonators [Little *et al.*, 1997], arrayed waveguide filters [Zirngibl *et al.*, 1993], optical delay lines [Hayes, and Yap, 1993] and S-bend attenuators [Jiang *et al.*, 2006]. It is important to design a low-loss compact bend waveguide, such as an S-bend or a U-bend and to fold the guided wave sections to reduce the overall dimension of the PIC, which also reduces its fabrication cost. This procedure would also allow for a greater density of optical components onto the same overall ‘footprint’ of the PIC, in order to increase its functionality and the reliability of the sub-systems. Addressing these issues in this chapter, a rigorous study of various loss mechanisms in bent waveguides is presented.

Previous research has shown that the field distribution of the fundamental mode in a bent waveguide is different from that of the straight waveguide [Gambling *et al.*, 1978]. The radiation and transition losses between the straight and the bent

waveguide contribute to the propagation properties of a bent waveguide. As a result, the power loss in a bent waveguide will be higher, due to the conversion of the incident beam to the higher order modes. By introducing an offset [Pennings *et al.*, 1988; Subramaniam *et al.*, 1997; Rajarajan *et al.*, 2000b] for the input straight waveguide when coupled to a bent waveguide, the coupling or transition loss can be reduced. The unequal bending loss of the even and odd supermodes can also cause crosstalk in a directional coupler-based device [Powelson *et al.*, 1998]. Previously it has also been reported [Yeung *et al.*, 1988] that two polarized modes exchange power in bent waveguides causing polarization crosstalk. Bent waveguides are also be deliberately used in the design of compact polarization rotators [Van Dam *et al.*, 1996; Lui *et al.*, 1998; Little and Chu, 2000; Obayya *et al.*, 2001], which are important in the design of polarization-independent or polarization-diversity PICs, as they can be used to control the polarization state. Recent research has shown that hybrid optical modes exchange power between the polarization states if the modes are nearly phase-matched and have an enhanced overlap between them. However, to achieve power conversion, some forms of discontinuity such as bends, junctions or tapers should exist along the propagation direction. Therefore a polarization rotator may be made by using a number of uniform [Somasiri *et al.*, 2002] or curved [Obayya *et al.*, 2002] butt-coupled waveguide sections to transfer power between the two polarized modes. This emphasizes the importance of a rigorous investigation of the polarization rotation in bent waveguides and thus is the basis of this chapter.

Curved optical waveguides have attracted increasing interest in the design of compact PICs but, however, the rigorous analysis of such bent waveguides is a challenging problem. Marcatili [Marcatili, 1969] has developed an approximate solution for the eigenvalue equation, by dividing the waveguide cross-section into several regions and using field expansion and field matching at the interfaces in order to obtain the curvature loss. Another simplified formula has been introduced by Marcuse [Marcuse, 1976] by utilizing a similar field expansion and field matching, but its validity is limited for a single-mode weakly guided waveguide with a sufficiently large bending radius.

Subsequently, to study arbitrary bends, various numerical methods have been developed and used to simulate the light propagation in bent waveguides with the

aim of reducing the bending, transition and polarization losses. The conformal transformation [Heiblum and Harris, 1975] has been used widely to represent bent waveguides by converting a curved dielectric waveguide to its equivalent straight waveguide with a modified index profile. Following that, a modal solution approach is necessary to find the modal solutions of the fundamental and higher order modes in both straight and bent waveguides and for this the eigenmode expansion [Bienstman *et al.*, 2002], the method of lines [Gu *et al.*, 1989; Pregla, 1996], the finite difference method [Kim and Gopinath, 1996; Nesterov and Troppenz, 2003], the variational method [Wassmann, 1999], the matrix method [Thyagarajan *et al.*, 1987], the WKB analysis [Berglund and Gopinath, 2000], and the beam propagation method (BPM) [Baets and Lagasse, 1983; Subramaniam *et al.*, 1997; Rajarajan *et al.*, 2000*b*] have been used and also experimentally verified [Schermer and Cole, 2007].

The FEM has also been employed by using cylindrical coordinates with scalar [Yamamoto and Koshiha, 1993] and vector  $\mathbf{E}$ -field [Jedidi and Pierre, 2007] formulations and the equivalent anisotropic refractive index approach [Tsuji and Koshiha, 2004]. Compact bends or rings can be modeled as resonators with rotational invariance [Yamamoto and Koshiha, 1993; Prkna *et al.*, 2005], and using a cylindrical coordinate system [Kakihara *et al.*, 2006], which is expected to be more accurate when the bending radius is comparable to the waveguide dimensions. Although finite-difference time-domain approach can also be used [Vu *et al.*, 2008], this approach is more computer intensive than the modal solution or BPM approach used herein.

For this particular semiconductor waveguide (with a strong index contrast), as shown in Fig. 3.1, the modal fields are hybrid in nature due to a significant non-dominant field component existing around the dielectric interfaces. Therefore a full-vectorial approach is necessary and this has been used in this study to obtain modal solutions of straight and bent waveguides. The FEM based on the vector  $\mathbf{H}$ -field formulation (VFEM) [Rahman and Davies, 1984*c*] has been established as one of the most accurate and numerically efficient approaches to obtain the modal field profiles and propagation constants of the fundamental and higher order quasi-TE and TM modes. The full vectorial formulation is based on the minimization of the functional

[Rahman and Davies, 1984c] in terms of the nodal values of the full  $\mathbf{H}$ -field vector as described in Chapter 2 and equation (2.23).

The penalty function approach has also been incorporated to impose divergence-free condition of the magnetic field to reduce the appearance of spurious modes. This full-vectorial FEM modal solution may also be used to determine the beat lengths between the fundamental and the higher order modes and also the polarization beat length between the two quasi-TE and TM polarized fundamental modes.

The first step in the process is to transform the curved optical waveguide to an equivalent straight optical waveguide by using the conformal transformation method [Heiblum and Harris, 1975].

At the junction between a straight and a bent waveguide besides the incident mode, other higher order modes can also be generated to satisfy the necessary boundary conditions. In this study a powerful numerical approach, the Least Squares Boundary Residual (LSBR) method [Rahman and Davies, 1988] has been used, which rigorously satisfies the continuity of the tangential electric and magnetic fields at the junction interface, and obtains the modal coefficients of the transmitted and reflected modes at the discontinuity interface. The LSBR method looks for a stationary solution to satisfy the continuity conditions by minimizing the error energy functional,  $\mathbf{J}$ , as given by [Rahman and Davies, 1988] and in Chapter 2 and equation (2.100). The integration is carried out at the junction interface,  $\Omega$ , between the straight and bent guides.

The beam propagation method (BPM) [Obayya *et al.*, 2000a] is most widely used for the study of light propagation in optical waveguides, particularly through non-uniform and bent waveguides. Although a semi-vectorial BPM may yield polarization-dependent guiding properties, only a full-vectorial approach can identify the power coupling between the two polarization states. The finite element-based full-vectorial BPM (FEBPM) [Obayya *et al.*, 2000a] is used here to study the evolution of the optical beam in a bent waveguide for a given field excitation.

From Maxwell's two curl equations, the vector wave equation based on the magnetic field vector  $\mathbf{H}$  can be derived as [Obayya *et al.*, 2000a] and found in Chapter 2 and equation (2.64). In this work, after application of the conformal transformation, the 3-D curved waveguide is replaced by a simpler 3-D straight waveguide, butt-coupled to the input-section.

In order to calculate the radiation loss in a bent waveguide, in this study a rigorous boundary condition incorporating the Perfect Matched Layers (PML) [Berenger, 1994] has been introduced around the orthodox computational window.

## 3.2 ANALYSIS OF RIB WAVEGUIDE

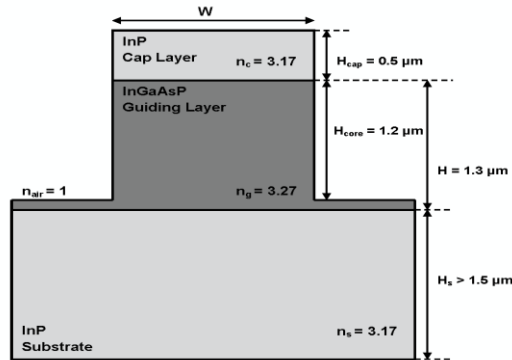


Fig. 3.1. Schematic cross-section of the bent optical waveguide.

The waveguide considered here for analysis is a symmetric rib waveguide. The schematic cross-section of the structure is shown in Fig. 3.1. Such structures can be fabricated by growing a  $1.3 \mu\text{m}$  ( $H$ ) thick indium gallium arsenide phosphide (InGaAsP) guiding layer on top of the indium phosphide (InP) substrate. Additionally a  $0.5 \mu\text{m}$  InP cap layer ( $H_{cap}$ ) can then be deposited on top of the InGaAsP guiding layer and subsequently a ridge can be etched with a core height ( $H_{core}$ ) of  $1.2 \mu\text{m}$ . The operating wavelength,  $\lambda$  for this analysis is considered to be  $1.55 \mu\text{m}$  and at this wavelength, the frequency dependent refractive indices of the InGaAsP and the InP layers are taken as 3.27 and 3.17, respectively. All other parameters are given in Fig. 3.1.

### 3.2.1 NUMERICAL ACCURACY

At first, accuracy of the  $\mathbf{H}$ -field based VFEM [Rahman and Davies, 1984c] method is tested with the other established methods. For that the numerical accuracy is assessed for a rib waveguide, shown in Fig. 3.2 (a), which was compiled by Hadley and Smith, 1995] is reported here, and further details are given below.

The waveguide considered here for simulation is shown in Fig. 3.2 (a). The structure was simulated by exploiting the existing one-fold symmetry and using the  $\mathbf{H}$ -field based VFEM. The effect of varying the mesh size on the effective index of the mode is shown in Fig. 3.2 (b).

The effective index,  $n_{eff}$  can be defined as:

$$n_{eff} = \frac{\beta_0}{k_0} \quad (3.1)$$

where  $\beta_0$  is the propagation constant of a given mode and  $k_0$  is the free space wavenumber, defined as:

$$k_0 = \omega(\varepsilon_0\mu_0)^{1/2} = \frac{2\pi}{\lambda} \quad (3.2)$$

In this case,  $\varepsilon_0$  is the free space permittivity,  $\mu_0$  is the free space permeability of the medium and  $\omega$  is the angular (radian) frequency. Variations of the  $n_{eff}$  of the fundamental TE mode is shown in Fig. 3.2 (b).

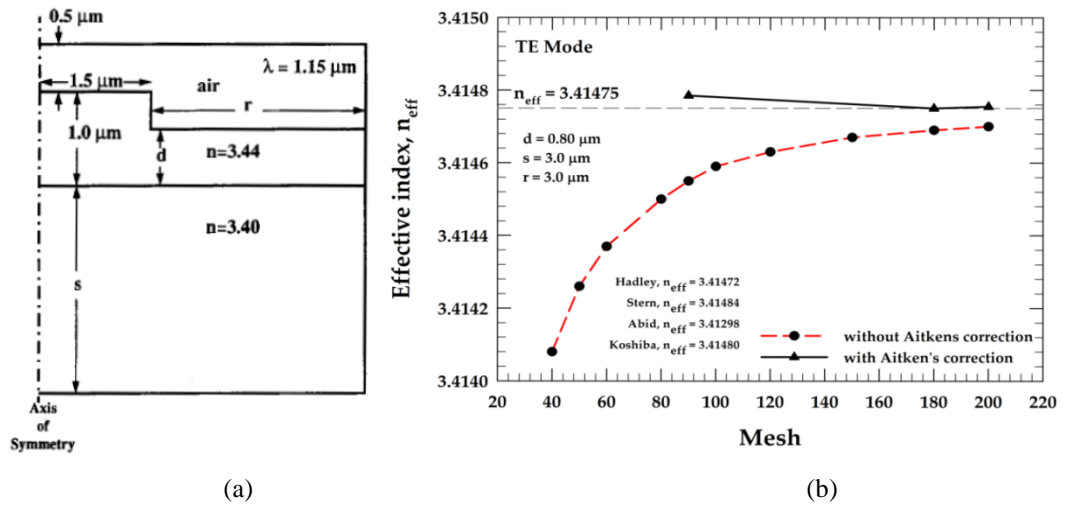
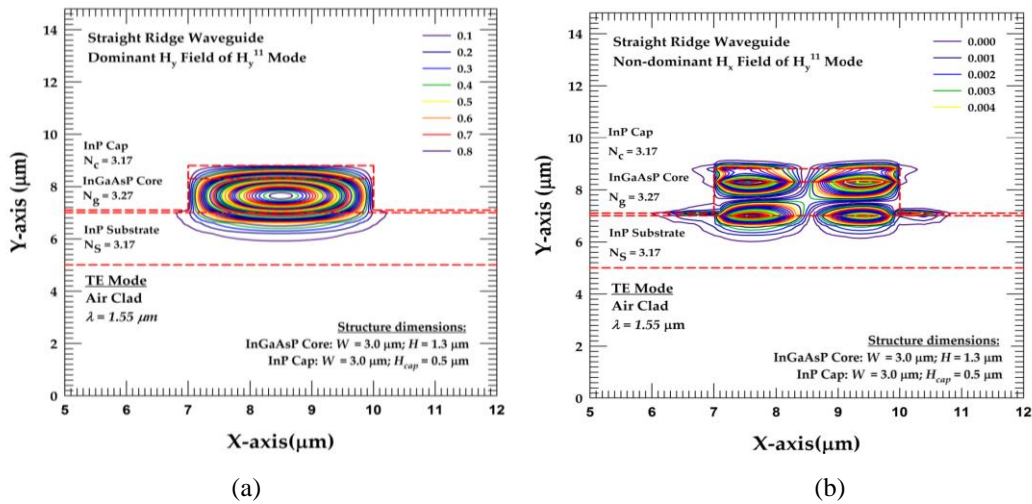


Fig. 3.2. (a) Schematic of the standard rib waveguide with a boundary condition at the left boundary, (b) the variations of  $n_{eff}$  with and without Aitkens correction as mesh is increasing.

It is known that for the finite difference method (FDM) or FEM solution, accuracy is increased as mesh refinement is carried out. Therefore in this case, Aitkens extrapolation (AE) [Rahman and Davies, 1985] can give the solution for very high mesh. It was extrapolated from 3 successive solutions when mesh was increased in a geometric ratio. In here the same number of mesh division have been used in both the transverse direction. It can be seen that, the  $n_{eff}$  values increase as mesh number is increased. It can also be observed that without the AE, the accuracy of the simulation results improves markedly. However, with the AE is employed, the  $n_{eff}$  was found to be converging to the value of 3.41475, which is in good agreement with values reported previously by Koshiba *et. al.*, Abid *et. al.*, Hadley *et. al.* and Stern *et. al.*

### 3.2.2 MODAL SOLUTION

In the first study, the  $\mathbf{H}$ -field based VFEM is used to obtain the modal solutions of the waveguide. In this approach, more than 20,000 first order triangular elements of different sizes have been used to represent the waveguide structure efficiently. The optical modes in semiconductor waveguides are highly hybrid in nature, where  $H_y$  and  $E_x$  components of the fundamental quasi-TE ( $H_y^{11}$ ) mode are the dominant field components. Whereas  $H_x$ ,  $H_z$ ,  $E_y$  and  $E_z$  are of the non-dominant components. Hence, both the dominant and non-dominant components of the quasi-TE modal field are presented here.



**Fig. 3.3.** (a) The dominant  $H_y$  field component and (b) the non-dominant  $H_x$  field component of the quasi-TE mode, with  $W = 3.0 \mu\text{m}$  and  $H = 1.3 \mu\text{m}$ .

The dominant  $H_y$  field component of the  $H_y^{11}$  mode in this straight rib waveguide is shown in Fig. 3.3 (a). Due to the stark refractive index contrast in both vertical and horizontal directions, the modal field is strongly confined at the centre of the waveguide. Moreover, due to a lower refractive index contrast between the InP and InGaAsP layers, the field slightly extends towards the upper cap and lower substrate regions. The non-dominant  $H_x$  field component of the  $H_y^{11}$  mode for the rib waveguide is shown in Fig. 3.3 (b). As the  $H_x$  field is related to the spatial derivative of the dominant  $H_y$  field, it clearly shows four peak values with alternate positive and negative signs and at the centre of the guide, an odd functional along the Y-axis and a nearly odd functional in the X-direction. The maximum magnitude of the  $H_x$  field

profile is very small and only about 0.006 times the maximum value of the dominant  $H_y$  field.

For the quasi-TM mode, the  $H_x$  field component of the  $H_x^{11}$  mode is dominant and the  $H_y$  field component is non-dominant (which were not shown here). Both these field components would show a similar contour plots like the quasi-TE mode. However it is noted in here that for this particular waveguide, the fundamental quasi-TE ( $H_y^{11}$ ) mode is more dominant with its higher  $n_{eff}$  value than its equivalent quasi-TM ( $H_x^{11}$ ) mode.

### 3.2.3 CHARACTERISTICS OF A RIB WAVEGUIDE

From the modal solutions of the quasi-TE and TM modes, the effective index of these modes, modal confinement, modal intensity (spot-size) and their birefringence characteristics, will be studied more thoroughly in this section.

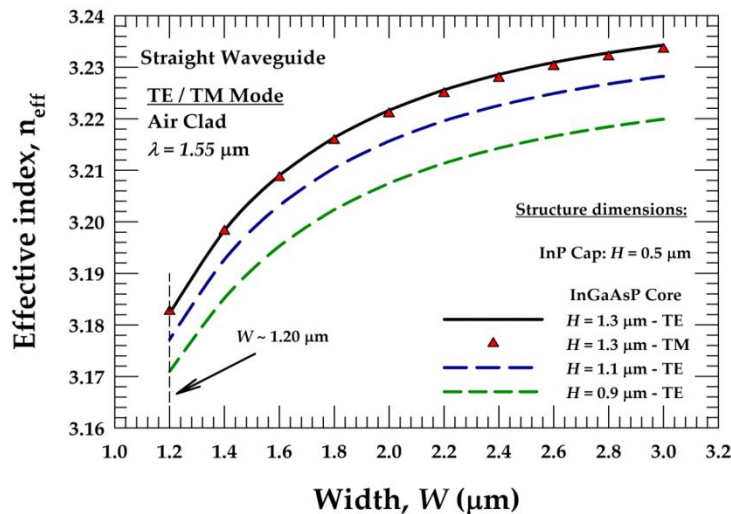


Fig. 3.4. Variations of the  $n_{eff}$  with  $W$  for different  $H$  for a straight waveguide.

Figure 3.4 shows the variation of the  $n_{eff}$  with the waveguide width,  $W$ . As the  $W$  increases, the fundamental TE and TM modes for  $H = 1.3 \mu\text{m}$  becomes more confined inside the core area, and hence, their  $n_{eff}$  increase and becoming more closely matched to the refractive index of the core region. By increasing the  $H$  of the waveguide, the proportion of the modal field leaking into the InP substrate reduces considerably. As a result, the phase velocity of the mode inside the core increases,

which results in higher  $n_{eff}$  of the mode. The cut-off width of the waveguide for all three different heights were observed to be or near to  $1.2 \mu\text{m}$ .

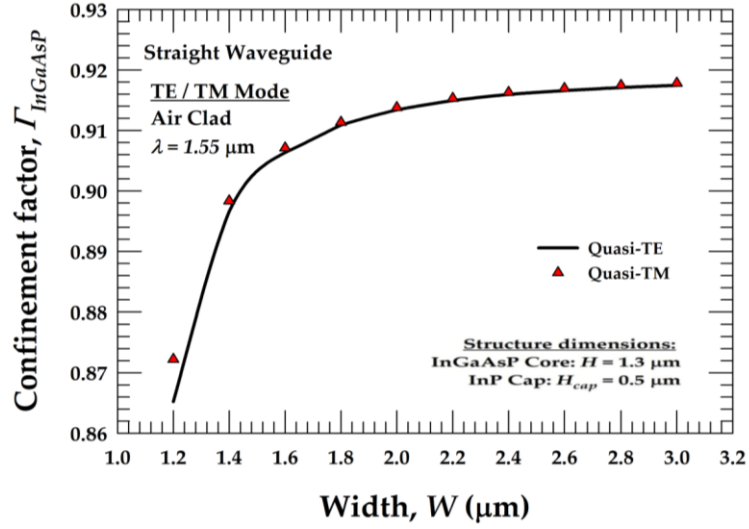


Fig. 3.5. Variations of the  $\Gamma_{InGaAsP}$  with  $W$  of quasi-TE and TM modes.

Figure 3.5 shows the variation of the optical confinement in the InGaAsP core ( $\Gamma_{InGaAsP}$ ) of the waveguide as a function of the  $W$ . The optical confinement in any area of the waveguide area normalized to the total power, can be obtained by integrating the Poynting vector, from the  $\mathbf{H}$ - and  $\mathbf{E}$ -fields.

It is given as below:

$$S_z = \iint_{\Omega} \{ \mathbf{E}^* \times \mathbf{H} \}_z dx dy \quad (3.3)$$

It is expected that as the waveguide dimension becomes large, most of the power would be confined in the InGaAsP core and that,  $\Gamma_{InGaAsP}$  would be close to 1.0. However, it can be noted that, the maximum power confinement in this case is closer to 0.92 as the core height is finite and the rest would either be leaked into the InP substrate or radiated into the InP cap-layer or into air cladding. It can be observed here that as  $W$  is reduced, the  $\Gamma_{InGaAsP}$  also reduces.

From the  $n_{eff}$  values of the quasi-TE and TM modes, the modal birefringence of the waveguide can be calculated. It is defined as the difference between the  $n_{eff}$  of the two fundamental polarizations states ( $n_{effTE} - n_{effTM}$ ). Although the value of the modal birefringence is very small for this waveguide, however this can have an effect on the polarization dependent performance of the PIC.

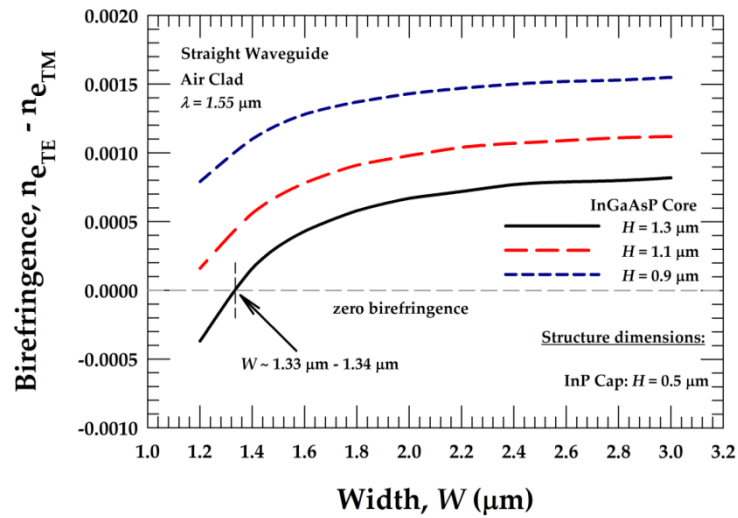


Fig. 3.6. Variations of the modal birefringene with  $W$  for different  $H$ .

Figure 3.6 shows the birefringence of the rib waveguide at three different sets of core height. When  $H$  is large (as  $H = 1.3 \mu\text{m}$ ) and  $W$  is small, it is possible to design a waveguide that the propagation constant of the fundamental quasi-TE and TM modes are the same and in which zero birefringence will be achieved. However when  $H$  is small, and as  $W$  is getting smaller, zero birefringence cannot be achieved as the mode of the waveguide will get closer to the refractive index of InP, where the mode reaches its cut-off condition. It is also shown that modal birefringence increases as  $W$  increases and then it saturates. It can be seen in here that the birefringence is zero when the waveguide's width and height are almost the same, in which polarization dependence can be eliminated.

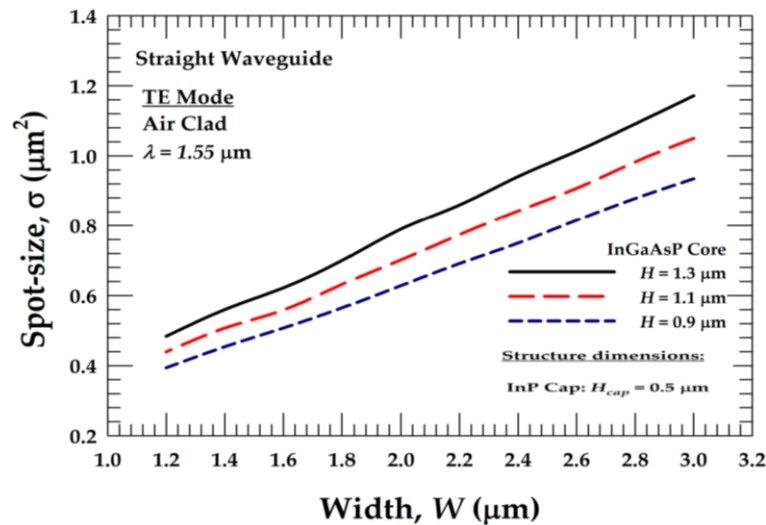


Fig. 3.7. Variations of  $\sigma$  with  $W$  for different  $H$ .

It is shown in Fig. 3.7 that as  $W$  increases, the modal spot-size,  $\sigma$  will also increase. Here the  $\sigma$  is defined as the area where the power density falls to  $1/e^2$  of its maximum power density. The  $\sigma$  of the mode when  $W = 3.0 \mu\text{m}$  and  $H = 1.3 \mu\text{m}$  has been calculated to be  $1.17\mu\text{m}^2$ . It is also shown that when  $H = 1.3 \mu\text{m}$ , its  $\sigma$  is higher than when  $H$  are at  $1.1 \mu\text{m}$  and  $0.9 \mu\text{m}$ , respectively.

### 3.3 FEATURES OF A BENT RIB WAVEGUIDE

For optical interconnect components, it is found that straight waveguides are useful and easy to couple them together for light to travel. However in the design of optical components, sometimes it is necessary to change the direction of light and to do this, waveguide with bends can be introduced. It is found that bending devices can be theoretically analysed by employing the conformal transformation method. The coordinate transformation allows a bent optical waveguide in the  $x$ -plane to be represented by an equivalent straight waveguide with a modified refractive index distribution,  $n^*(x,y)$  [Heiblum and Harris, 1975]

$$n^*(x,y) = n_m(x,y) \left(1 - \frac{x}{R}\right) \quad (3.4)$$

where  $n_m(x,y)$  is the original refractive index profile of the bent waveguide,  $n^*(x,y)$  is the equivalent index profile of a straight guide,  $R$  is the radius of the curvature and  $x$  is an arbitrary point of the waveguide from the axis of the transformation.

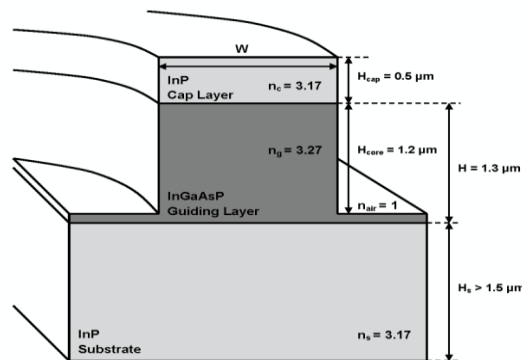
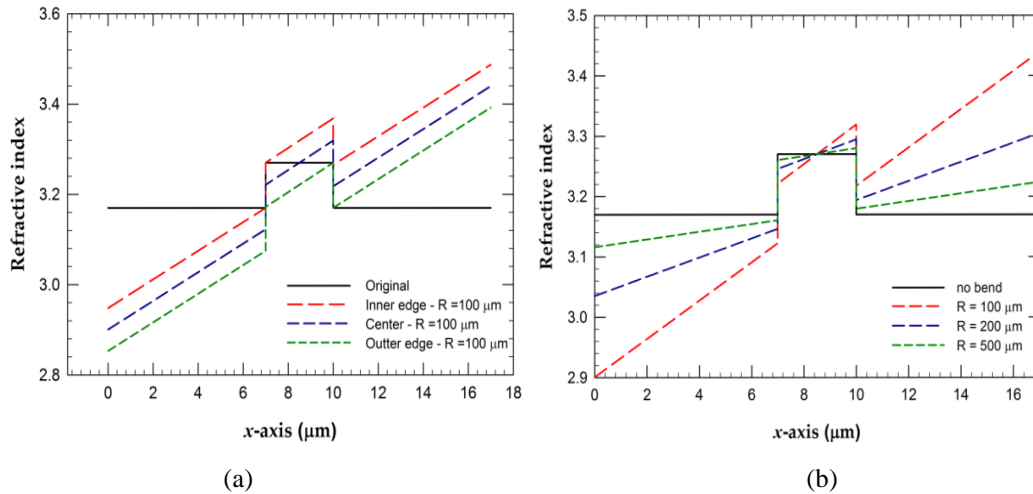


Fig. 3.8. Bend Orientations for the rib waveguide - left facet at bend radius,  $R$ .

Figure 3.8 illustrates the orientation of the bent rib waveguide. To further study the conformal transformation equation. Figure 3.9 (a) shows the effect on the

refractive index distribution when the transformation axis is taken at different locations. When the axis is taken as the outer edge of the waveguide, the modified refractive index distribution agreed well with the transformed index profile shown in [Smit and Pennings, 1993]. However most of the reports have considered the transformation axis at the centre of the waveguide [Baets and Lagasse, 1983] [Durniak and Love, 2007]. Therefore, it was decided in this work to employ the conformal transformation by taking the transformation axis at the centre of the waveguide. Figure 3.9 (b) shows the result of the refractive index distribution with three different radii. Although the original structure was symmetric along the vertical axis, however, after the transformation, symmetry along the transformation axis is destroyed, so the full waveguide needs to be considered for its modal solutions.



**Fig. 3.9.** (a) *Refractive index profile of the straight waveguide (solid) and refractive index due to bending (dashed line).* (b) *Refractive index profile due to bending with different radii.*

The dominant  $H_y$  field profile for the  $H_y^{11}$  (quasi-TE) mode is shown in Fig. 3.10 (a). In this case the modal field profile was obtained by using the VFEM after the conformal transformation equation (3.4) was applied to modify the equivalent index in the cross sectional plane of the rib waveguide. It clearly shows that the field in the core region shifts outward (right side) and therefore it is no longer symmetric. Due to a higher equivalent index on the right boundary, the power leaks out at the lower-right side as shown in Fig. 3.10 (a).

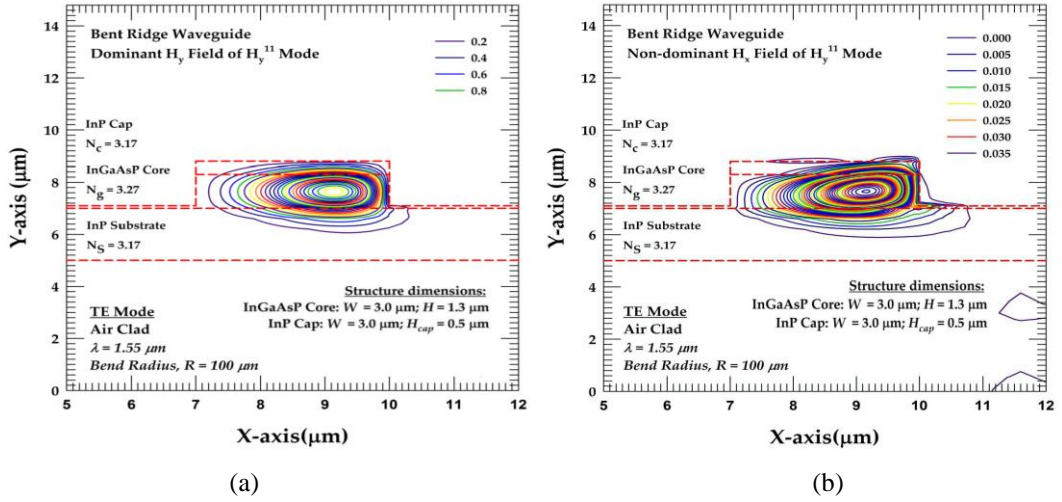


**Fig. 3.10.** (a) The dominant  $H_y$  field component and (b) the non-dominant  $H_x$  field component of the quasi-TE mode of a bent waveguide with  $R = 100 \mu\text{m}$ ,  $W = 3.0 \mu\text{m}$  and  $H = 1.3 \mu\text{m}$ .

The non-dominant  $H_x$  field component for  $H_y^{11}$  (quasi-TE) mode is also shown in Fig. 3.10 (b). It can be observed that the shape of the non-dominant  $H_x$  field is similar to that of the dominant  $H_y$  field. The magnitude of this non-dominant field in the bent waveguide is nearly 0.04 times than that of the dominant field. However, this magnitude is still significantly higher compared to the magnitude of the same field in a straight waveguide (which was 0.006). It also clearly shows that the field leaks out towards the lower-right corner. Similarly, for the quasi-TM  $H_x^{11}$  mode, both the dominant  $H_x$  and the non-dominant  $H_y$  field profiles are of similar shapes but these are not shown here. Since the dominant and non-dominant field profiles are similar in shape and the magnitude of the non-dominant component is higher in a bent waveguide, the overlap integral between the vector modal fields of the  $H_y^{11}$  and  $H_x^{11}$  modes is expected to be higher. As a result the power conversion between these two polarized modes will also be high.

The  $n_{eff}$  of this mode (bent guide with  $R = 100 \mu\text{m}$ ) is found to be 3.24346, which is higher than that of the straight waveguide. The higher  $n_{eff}$  is due to the shift of the modal field in the region where equivalent index is also higher. It is also found that the  $\sigma$  of this bent guide when  $W = 3 \mu\text{m}$  and  $H = 1.3 \mu\text{m}$  is found to be  $0.8145 \mu\text{m}^2$ , which is smaller than that of the straight waveguide as the field profile is more compact and shifted towards to the right as shown in Fig. 3.10 (a).

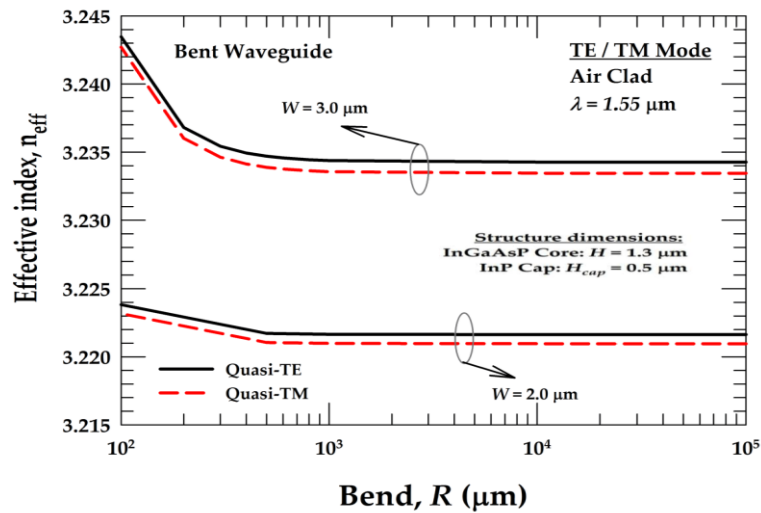


**Fig. 3.11.** Variations of the  $n_{eff}$  of quasi-TE and TM modes with the  $W$  for a bent waveguide.

Figure 3.11 shows the variation of the  $n_{eff}$  of the fundamental TE and TM modes with the bending radius,  $R$ , for  $W$  as  $3\ \mu\text{m}$  and  $2\ \mu\text{m}$ , respectively. As also shown in Fig. 3.11 is that as  $R$  decreases, the  $n_{eff}$  increases. It is also shown in here that  $n_{eff}$  of quasi-TE mode with bending is slightly higher than quasi-TM mode with bending for both  $W$  were shown. Furthermore, when  $W$  is  $3\ \mu\text{m}$ ,  $n_{eff}$  are much higher than that  $W$  of  $2\ \mu\text{m}$  as the waveguide area is much larger when  $W$  is  $3\ \mu\text{m}$ .

### 3.3.1 LEAKAGE LOSS/PROPAGATION LOSS

Next, to find the leakage loss of a bent rib waveguide, the FEBPM [Obayya *et al.* 2000a] is used. In this study, the fundamental  $H_y^{11}$  modal field profile of the straight guide with  $W = 3.0\ \mu\text{m}$  and  $H = 1.3\ \mu\text{m}$ , is used as the input field to launch into the FEBPM code [Obayya *et al.* 2000a], where the conformal transformation has also been used to represent a bent waveguide. The initial field (input field) of the quasi-TE mode of the straight waveguide propagates at a distance ( $z$ -direction) of  $5000\ \mu\text{m}$  through a bent waveguide ( $R = 100\ \mu\text{m}$ ). The propagation loss of the structure is calculated by using equation (2.108) outlined previously in Chapter 2.

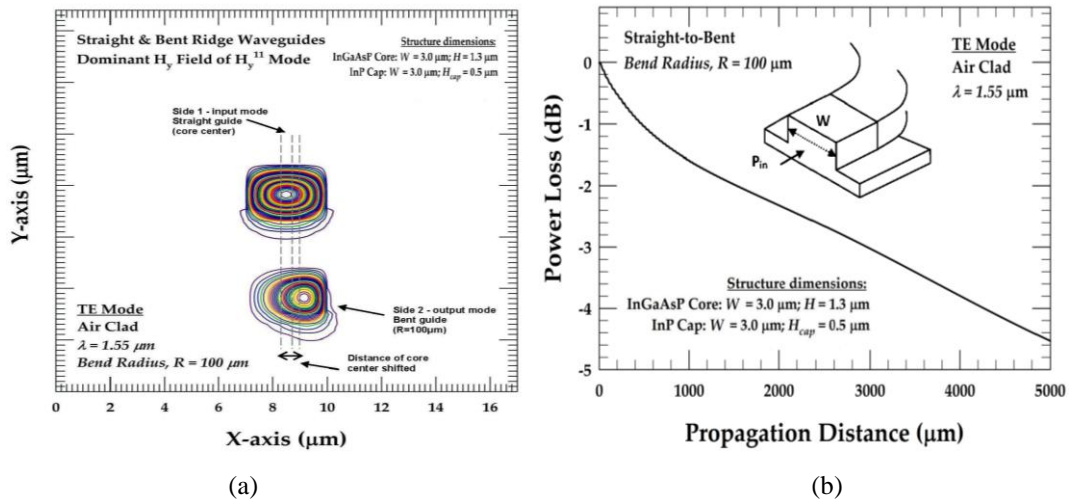


**Fig. 3.12.** (a) Illustration of how the straight waveguide is coupled with a bent waveguide with core waveguide  $W = 3.0 \mu\text{m}$  and  $H = 1.3 \mu\text{m}$ .  
 (b) Variation of power loss along the axial distance for a straight-to-bent waveguide with  $W = 3.0 \mu\text{m}$ ,  $H = 1.3 \mu\text{m}$  and  $R = 100 \mu\text{m}$ .

Figure 3.12 (a) illustrates the coupling between the dominant  $H_y$  field of quasi-TE mode of the straight and the bent waveguide. For the bent waveguide, the centre of the mode profile can be noticed to shift towards the right side compared to the straight waveguide. It should be noted that field profiles obtained by the mode solver and the BPM agree very well. The variation of the power loss for straight-to-bent waveguide along the propagation distance is shown in Fig. 3.12 (b). Initially, the rate of variation of the power loss is about 2.2 dB/mm obtained from the gradient of the line, at  $z = 0$ , when the guide contains both the fundamental and higher order modes. As the field propagates further down the bent waveguide, the rate of power loss is clearly seen to be reduced as the optical beam strips off the more lossy higher order modes and it mostly contains the fundamental mode in this location. It can be observed that the average loss value is about 0.74 dB/mm between the axial distances of 4000  $\mu\text{m}$  to 5000  $\mu\text{m}$ .

### 3.3.2 CALCULATION OF SPOT-SIZE IN BPM

The spot-size,  $\sigma$  has been defined previously in section 3.2.3 as the area where the power density falls to  $1/e^2$  of its maximum power density. The variation of the  $\sigma$  along the propagation distance is shown in Fig. 3.13 when a mode from the straight guide is launched into the bent guide.

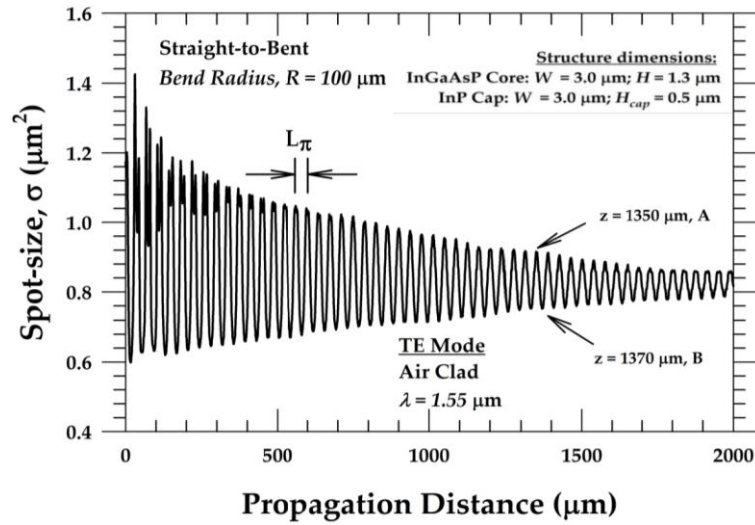


**Fig. 3.13.** Variation of the  $\sigma$  along the axial distance for a straight-to-bent waveguide with  $W = 3.0 \mu\text{m}$ ,  $H = 1.3 \mu\text{m}$  and  $R = 100 \mu\text{m}$ .

Rapid oscillations can be observed in the first  $1000 \mu\text{m}$  and as the propagation distance increases, the  $\sigma$  appears to show damped oscillations and settles at around  $0.82 \mu\text{m}^2$ . This saturation value is also very similar to the value of  $0.815 \mu\text{m}^2$  obtained by using the VFEM for a bent waveguide. The output field profile is not shown here but at  $z = 2000 \mu\text{m}$  it was observed to be similar to the modal field profile of the bent guide, which was shown in Fig. 3.10 (a). The periodic change of the  $\sigma$  has a beat length of  $20 \mu\text{m}$ . This period again clearly correlates with  $L_\pi = \pi / \Delta\beta = 19 \mu\text{m}$ , where  $\Delta\beta$  is the difference between the propagation constants of the  $H_y^{11}$  and  $H_y^{21}$  modes calculated by using the VFEM. The agreement between the beat length obtained by the FEM based modal solution and the BPM confirms the accuracy of both the approaches. This also suggests that at the junction of a straight-to-bent waveguide, the higher order  $H_y^{21}$  mode is also generated. The oscillations in the  $\sigma$  occurred because of the mode-beating between the fundamental mode and the higher order modes.

### 3.3.3 INVESTIGATION OF HIGHER ORDER MODES

It was described in previous section that higher order modes exist at the junction of a straight-to-bent waveguide. To investigate the nature and quantify the magnitudes of the higher order modes generated, a LSBR method [Rahman and Davies, 1988] has been used. Since the dominant mode in the bent guide is different from the input

field of the straight guide, the higher order modes are excited to satisfy the necessary boundary conditions.

The modal transmission coefficients of the  $H_y^{11}$  and  $H_y^{21}$  modes calculated by using the LSBR method are 0.89 and 0.38, respectively. This shows that although the fundamental  $H_y^{11}$  mode is dominant, the other modes also are excited and propagate along with the fundamental mode. The existence of  $H_y^{21}$  mode agrees with the periodic spot-size variation due to the mode beating between the  $H_y^{11}$  and  $H_y^{21}$  modes. It can be observed in Fig. 3.13 that when the propagation distance is more than the 500  $\mu\text{m}$ , the optical field mostly contains the  $H_y^{11}$  mode with a significantly attenuated  $H_y^{21}$  mode. On the other hand, a small amount of the  $H_y^{31}$  mode is also excited but being very close to its modal cut-off it leaks out very quickly, which correlates with the secondary peaks (shown in Fig. 3.13), which exist at an early stage, between a propagation distance of 0 and 400  $\mu\text{m}$ .

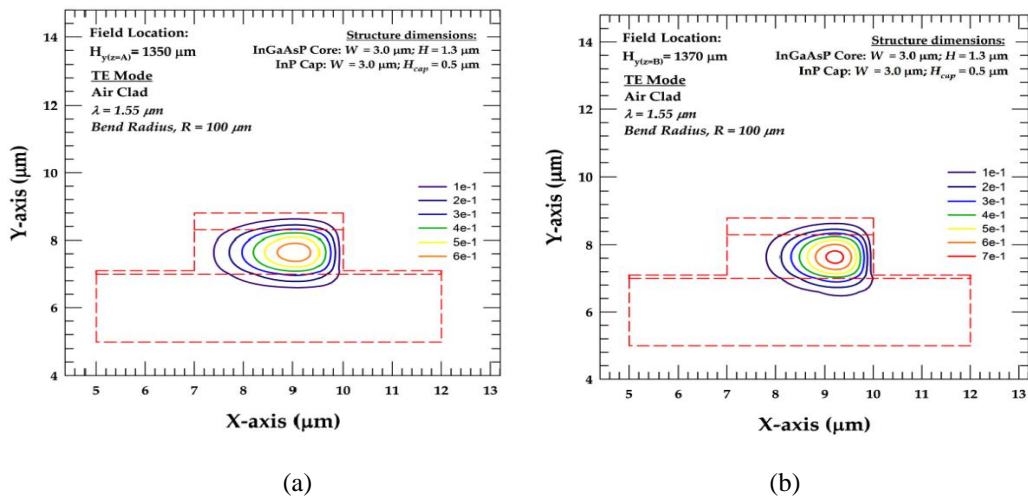


**Fig. 3.14.**  $H_y$  field profiles at two  $z$  propagation locations with  $W = 3.0 \mu\text{m}$ ,  $H = 1.3 \mu\text{m}$  and  $R = 100 \mu\text{m}$ . (a) At  $z = 1350 \mu\text{m}$ . (b) At  $z = 1370 \mu\text{m}$ .

To validate further the mode-beating exists, Fig. 3.14 (a) shows the bent  $H_y$  field profile at axial position A (at  $z = 1350 \mu\text{m}$ ) and Fig. 3.14 (b) shows the  $H_y$  field profile at axial position B (at  $z = 1370 \mu\text{m}$ ), as identified in Fig. 3.13. Although, they look very similar, but this change of  $\sigma$  is periodic. To study this subtle change further, the difference between the fundamental  $H_y$  field profiles at axial positions A (at  $z = 1350 \mu\text{m}$ ) and B (at  $z = 1370 \mu\text{m}$ ) is shown in Fig. 3.15, which clearly shows that this field profile is similar to that of the  $H_y^{21}$  mode in a bent guide mode as the field leaks out into the lower right-hand corner as well. This clearly illustrates that a

small magnitude of  $H_y^{21}$  mode and its periodic addition and subtraction from the fundamental mode causes periodic change in their  $\sigma$ . The existence of  $H_y^{21}$  mode from the BPM simulation illustrated here, and the calculation of its coefficient by the LSBR confirms the validity of both the approaches. This section clearly illustrates the usefulness of various approaches, namely the mode solver, junction analysis and the beam propagation method.

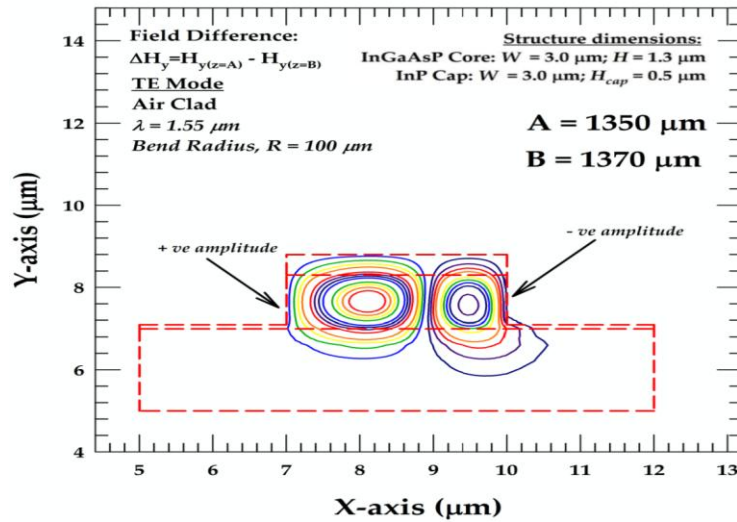


Fig. 3.15. Difference between two  $H_y$  field profiles at two locations with a phase reversal with  $W = 3.0 \mu\text{m}$ ,  $H = 1.3 \mu\text{m}$  and  $R = 100 \mu\text{m}$ .

### 3.3.4 POLARIZED POWER

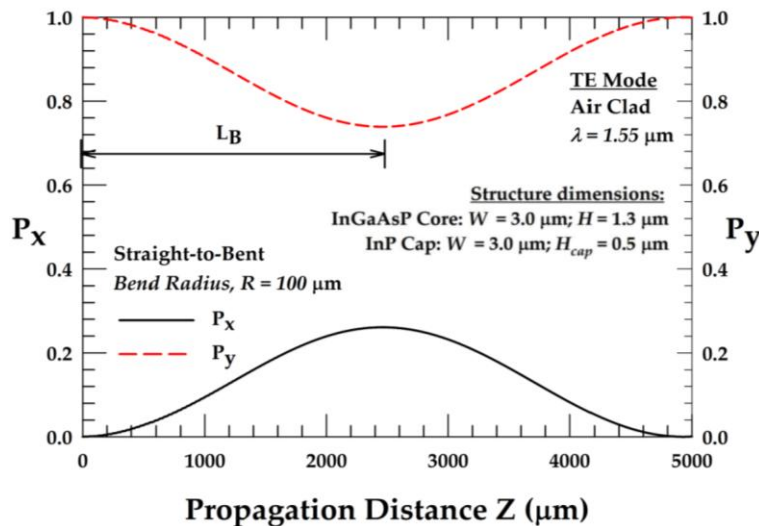


Fig. 3.16. Evolution of the y and x-polarized powers along the axial distance for straight-to-bent waveguide with  $W=3.0 \mu\text{m}$ ,  $H=1.3 \mu\text{m}$  and  $R=100 \mu\text{m}$ .

A bent waveguide is also known to exchange power between the two polarization states [Yeung *et al.* 1988]. A full-vectorial finite-element beam propagation program

(FEBPM) [Obayya *et al.* 2000a] with perfectly matched layer boundary conditions has been used here to find the TE-to-TM power conversion. The evolution of the quasi-TE and TM powers along the  $z$ -direction is shown in Fig. 3.16 for straight-to-bent waveguide coupling. In this case, since the quasi-TE ( $H_y^{11}$ ) mode was incident at the start of the bend waveguide ( $z = 0$ ), the  $H_x$ -polarized normalized power,  $P_x$ , is nearly zero and the  $H_y$ -polarized normalized power,  $P_y$ , is nearly 1. As the modes propagate along the bent, the maximum polarization conversion occurs at  $z = 2500 \mu\text{m}$ , which correlates well with the polarization-beat length  $L_B = \pi / |\beta_y - \beta_x|$ . This was obtained by using the VFEM, where  $\beta_y$  and  $\beta_x$  are the propagation constants of the fundamental  $H_y^{11}$  and  $H_x^{11}$  modes in the bent waveguide. Again, the strong correlation between the  $L_B$  value obtained from the modal solution and the periodic power conversion length obtained from the BPM confirms the accuracy and the validity of both the methods.

### 3.3.5 BENDING LOSS ANALYSIS

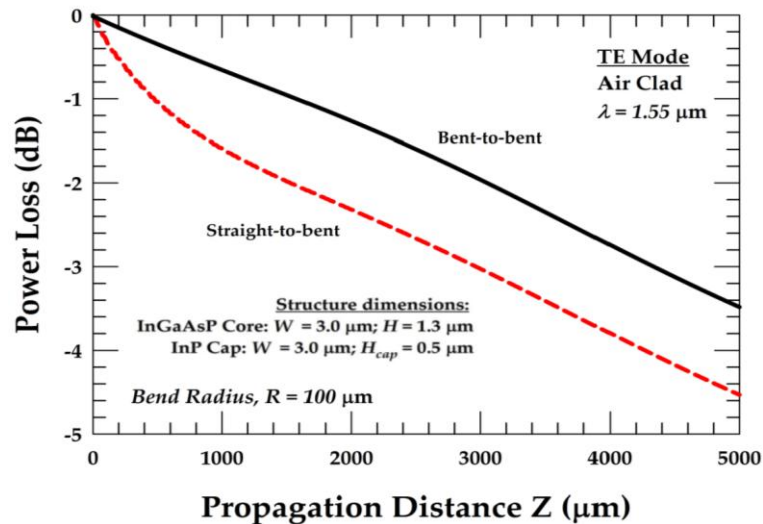


Fig. 3.17. Variations of power losses along the axial distance for bent-to-bent and straight-to-bent with  $W = 3.0 \mu\text{m}$ ,  $H = 1.2 \mu\text{m}$  and  $R = 100 \mu\text{m}$ .

In order to study the bending loss, the butt coupling between an imaginary bent-to-bent waveguide has been analysed. In this case the mode profile of the bent waveguide, obtained by using the VFEM [Rahman and Davies, 1984c] (after a conformal transformation of the input guide), is launched into the BPM code [Obayya *et al.* 2000a] representing the bent guide (also using the conformal transformation). The variation of the power loss along the propagation distance is

shown in Fig. 3.17 by a solid line. In this case, the power loss is less than that of the straight-to-bent waveguide coupling, since the loss in a straight-to-bent additionally includes the loss due to the field mismatch. For comparison, the loss for the straight-to-bent guide, as shown earlier in Fig. 3.12 (b), is also shown here by a dashed line. It can be observed that for  $z > 2$  mm, the slopes of both the curves are similar, because in the straight-to-bent case, the magnitudes of the higher order modes that remained beyond this position are very small and therefore the loss rates near the end are similar. As can be seen from the bent-to-bent graph, the rate of power loss of the pure  $H_y^{11}$  mode (of a bent guide) is nearly uniform, with a value of 0.68 dB/mm.

To quantify the overall loss, the loss value for the  $H_y^{21}$  mode was also obtained by launching this mode profile into the FEBPM code and this loss value found to be 10.61 dB/mm. For a straight-to-bent coupling, at the start in the bent section, modal coefficients of the excited  $H_y^{11}$  and  $H_y^{21}$  modes calculated by the LSBR were found to be 0.89 and 0.38 respectively. These values corresponded to the transmitted field contained 79% of the power in the  $H_y^{11}$  mode, 14% of the power in the  $H_y^{21}$  mode and the rest in the higher order radiating modes obtained by using the LSBR method. In the bent waveguide, the modal loss values of the  $H_y^{11}$  and  $H_y^{21}$  modes were calculated to be 0.68 dB/mm and 10.61 dB/mm, respectively. Their power fractions were also calculated to be 85% and 15%, respectively. For which the overall loss value was found to be 2.17 dB/mm. This value gives a good agreement with the loss value of 2.2 dB/mm shown previously in Fig. 3.12 (b) which also includes loss by other higher order modes. Again, this also confirms the validity and the accuracy of the 3 independent formulations, namely the modal analysis, the junction analysis and the BPM analysis, all based on the FEM. In all these cases, the fundamental  $H_y^{11}$  mode suffers the same bending loss; however, in the case of a straight-to-bent waveguide, nearly 21% power in the higher order guided and radiated modes are quickly loss. This is clearly shown in Fig. 3.17 as the additional 1.05 dB loss near the end, at  $z = 5$  mm.

For the bent-to-bent coupling, the  $\sigma$  along the propagation distance was constant, but this is not shown here. However, the constant value of  $0.824 \mu\text{m}^2$  obtained, agrees well with the  $\sigma$  value of  $0.82 \mu\text{m}^2$  calculated by using the VFEM for

a bent guide. In this case, since no higher order mode was excited, mode beating was not observed.

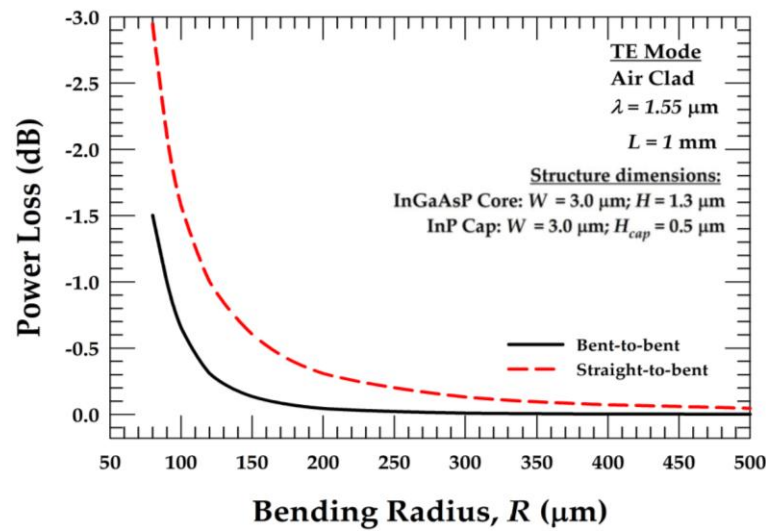


Fig. 3.18. Variations of power losses with  $R$ , for bent-to-bent and straight-to-bent waveguides with  $W = 3.0 \mu\text{m}$ ,  $H = 1.3 \mu\text{m}$ .

Power loss critically depends on the bending radius and the way the input and output sections are coupled. The variations of the total power loss values for a straight-to-bent and a bent-to-bent coupler with a 1 mm bent section are shown in Fig. 3.18. The total loss value for the straight-to-bent coupling is shown by a dashed line. On the other hand, for the bent-to-bent waveguide coupling, the loss values are shown by a solid line. It is shown here that, in both of these cases, as  $R$ , decreases, the loss value increases which also shows a higher loss for a straight-to-bent coupling. Here, the additional loss is due to the field mismatch at the discontinuity junction, which was previously discussed. It is worth mentioning here that the difference between the two sets also increases with the reduction of the bending radius. Since the more modified field profile in the bent guide increases the field mismatch loss.

### 3.3.6 ANALYSIS OF POLARIZATION CONVERSION AND CROSSTALK

It was also shown in Fig. 3.16 that such a bent waveguide suffers from the periodic exchange of power between the polarized modes. Often this can increase the polarization cross-talk in an optoelectronic system comprising bent sections. On the

other hand, such bent waveguides can be deliberately used to rotate the polarization state of an incoming signal. To illustrate the polarization conversion, the variation of the maximum polarization conversion with  $R$  is shown in Fig. 3.19. It can be clearly observed that as  $R$  decreases, the polarization conversion increases. However polarization conversions are similar for both the cases, whether the input waveguide is straight or bent. This suggests that the polarization conversion primarily depends on the bending radius. In order to keep the polarization cross-talk below an acceptable level, the maximum allowable  $R$  has to be designed carefully.

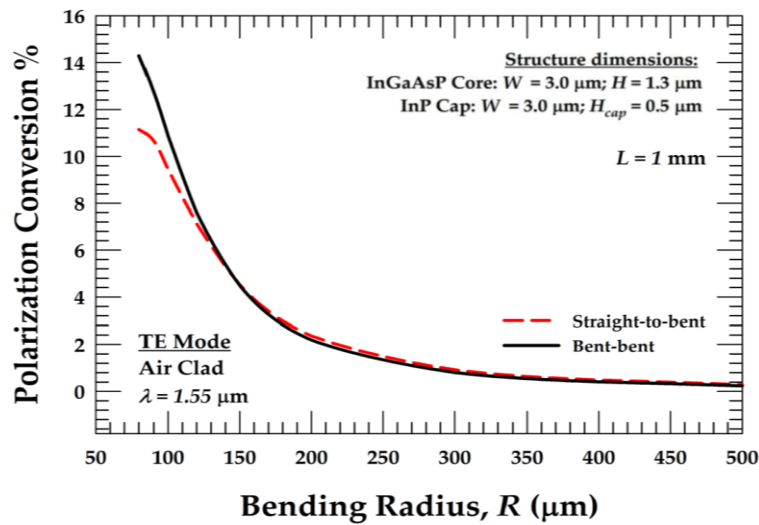


**Fig. 3.19.** Variations of the polarization conversions with  $R$ , for bent-to-bent and straight-to-bent with  $W = 3.0 \mu\text{m}$  and  $H = 1.3 \mu\text{m}$ .

In this case, the  $R$  should be larger than  $270 \mu\text{m}$  to keep the polarization cross-talk lower than  $-20 \text{ dB}$ . However, on the other hand for the design of a polarization rotator, the objective is to maximize the polarization conversion with minimum power loss. It may, however, be difficult to achieve 100% polarization conversion, using a single section polarization rotator design by reducing  $R$  appreciably, as in this case the power loss would also increase significantly. In such a case, several bend butt-coupled sections can be cascaded [Obayya *et al.*, 2002] with phase reversal at a regular interval equal to the polarization beat-length,  $L_B$ . However, most of the earlier work has only mentioned the normalized power conversion between the polarized modes (ignoring the power loss): our present study shows a significant power loss for compact bent sections, which cannot be ignored.

### 3.3.7 EFFECTS OF LATERAL SHIFT

In the discussion above it is shown that radiation loss primarily depends on the bending radius and the additional loss arises due to the mismatch between the fields on the both sides of a junction. Since it would not be possible in a practical case to excite the bent section by launching a field similar to that of the bent waveguide, several approaches have been reported to reduce such losses. One of these approaches is created by introducing a lateral shift between the straight and bent guides [Pennings *et al.*, 1988; Subramaniam *et al.*, 1997; Rajarajan *et al.* 2000b].

#### $\Delta x$ OFFSET

In this section, an offset is introduced where the input straight waveguide is shifted to the right when coupled to the bent waveguide in order to enhance the field matching (since the modal field of a bent guide shifts outwards). Figure 3.20 (a) shows how the fundamental  $H_y$  field of the  $H_y^{11}$  mode of both straight and bent waveguide are represented, when they are coupled together with a  $\Delta x$  offset. It can be noted that when the offset is at its optimum distance,  $\Delta x$ , the center core of the straight waveguide would have matched with the center core of the bent waveguide, hence they are in a similar position in horizontal axis, when the straight guide is shifted to the right by the optimum offset.

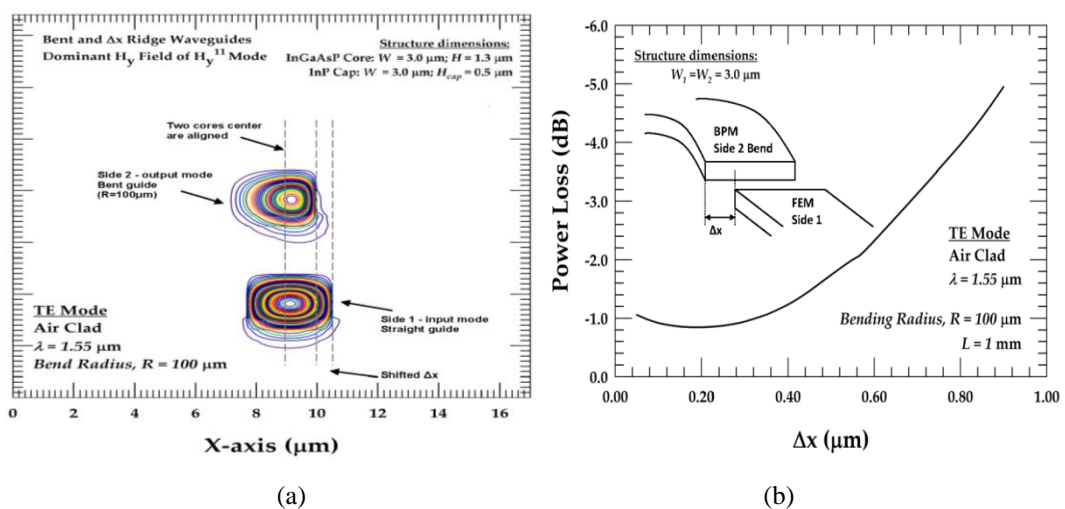


Fig. 3.20. (a) Illustration of modal field profiles when a straight waveguide is coupled to a bent waveguide with an offset,  $\Delta x$ , and (b) variations of the power loss for a straight-to-bent coupled waveguide with the waveguide offset,  $\Delta x$ .

Variation of the power loss at the junction with  $\Delta x$ , is shown in Fig. 3.20 (b). The inset diagram in Fig. 3.20 (b) also shows how this offset can be achieved. As  $\Delta x$  increases, the total loss initially reduces and reaches its minimum value before it starts to rise. The minimum loss is achieved when  $\Delta x = 0.19 \mu\text{m}$ , where the field matching is optimum and the minimum loss value is 0.84 dB. As mentioned earlier, this loss contains the bending loss of the fundamental mode, the higher order modes and also the loss due to the field mismatch between the two coupled waveguides.

By using the LSBR method [Rahman and Davies, 1988], the modal coefficients of the  $H_y^{11}$  and  $H_y^{21}$  modes were calculated to be 0.923 and 0.2706, respectively, when  $\Delta x = 0.19 \mu\text{m}$ . Therefore for this design optimization, the bent guide will contain about 85% of the power in the  $H_y^{11}$  and only 7.3% power in the  $H_y^{21}$  modes with the remaining power existing in higher order radiation modes. It is important to note that by introducing an offset to the waveguide, the polarization conversion reduces substantially.

## $\Delta w$ OFFSET

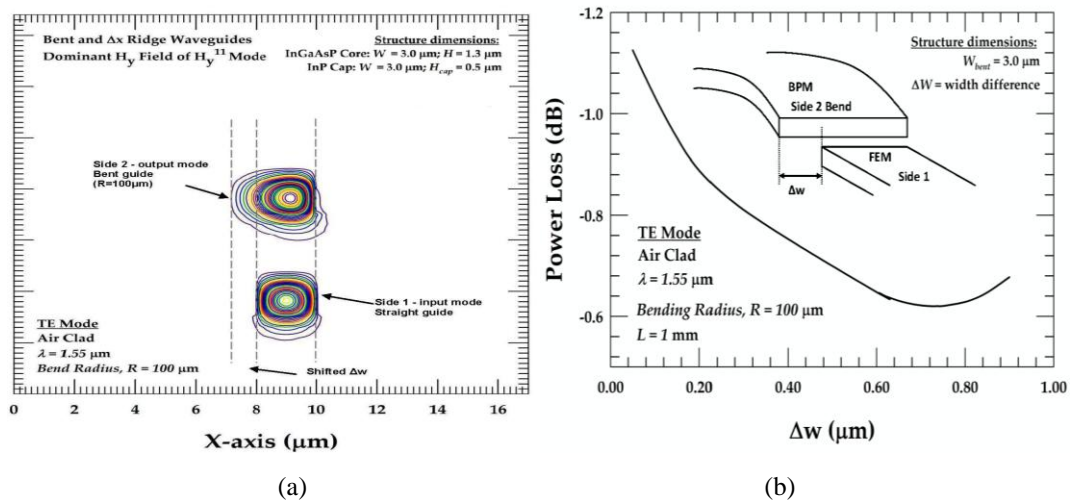


Fig. 3.21. (a) Illustration of modal field profiles when a straight waveguide is coupled to a bent waveguide with an offset,  $\Delta w$ , and (b) variations of the power loss for a straight-to-bent coupled waveguide with the  $\Delta w$  when the waveguide widths are equal.

It was shown in Fig. 3.10 (a) that the mode shape in a bent guide not only shifts outward but it also shrinks. To address this, an alternative offset method is analysed where the  $W$  of the input waveguide (straight guide) is reduced to improve the mode

matching. Figure 3.21 (a) shows how the fundamental  $H_y$  field of  $H_y^{11}$  mode of both straight and bent waveguide is represented when they are coupled together with an offset  $\Delta w$ . It can be noted that when the offset is at its optimum distance,  $\Delta w$ , the width of the input straight waveguide (which is shifted to the right side) would have matched with the bent waveguide. Hence the centre of the cores for both of these waveguides are in a similar position along the  $x$ -axis.

The inset diagram in Fig. 3.21 (b) also demonstrates how this particular offset was achieved. It can be observed in Fig. 3.21 (b) that as the width of the input waveguide decreases from  $3 \mu\text{m}$ , the width difference,  $\Delta w$  increases and the loss value decreases until it reaches its minimum, following which the loss value again increases. The optimum offset,  $\Delta w$  is found to be  $0.73 \mu\text{m}$  when the minimum loss value of  $0.619 \text{ dB}$  is attained. This shows the improvement due to the use of unequal waveguide is higher than that of using lateral offset for waveguides with identical width. It should be noted that most of the earlier work [Pennings *et al.*, 1988; Subramaniam *et al.*, 1997; Rajarajan *et al.* 2000b] reports only on the reduction of the transition loss by introducing an offset between the straight and curved section. However, this study shows for the first time, that by using waveguides of unequal width, the transition loss can also be reduced significantly.

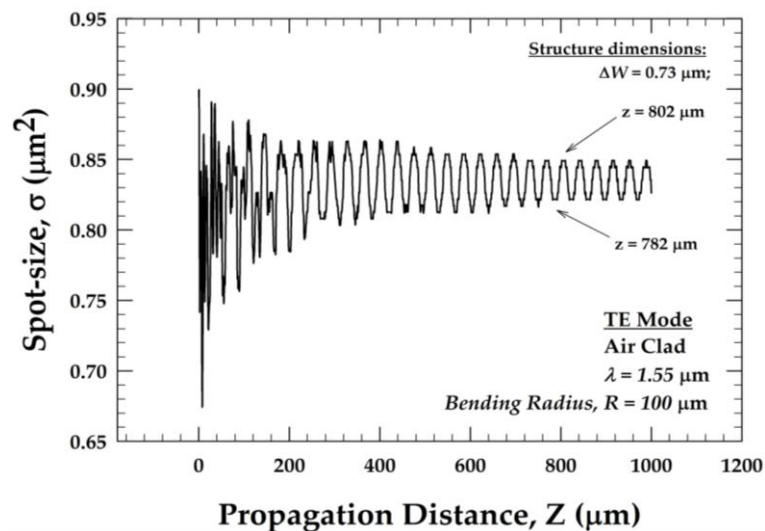
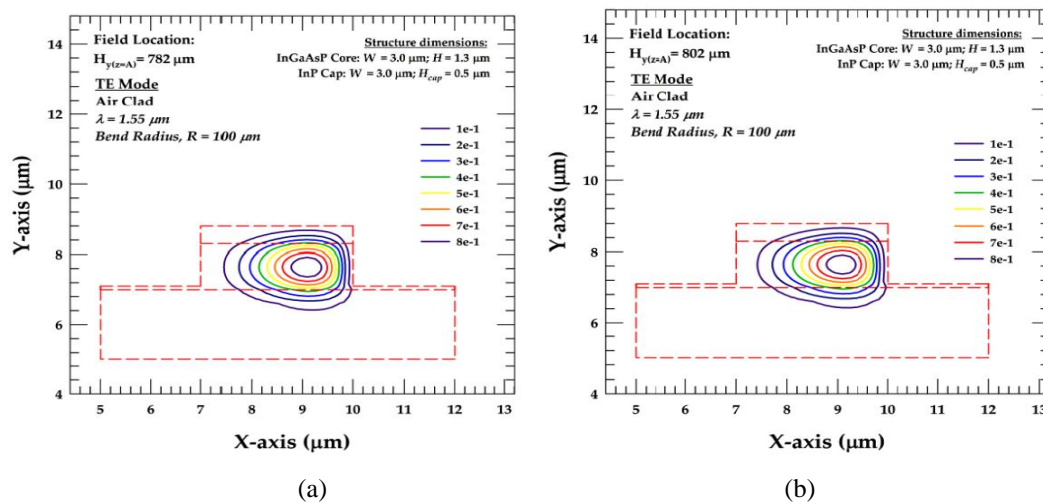


Fig. 3.22. Variations of the  $\sigma$  along the axial direction when an optimized value of  $\Delta w$  is used.

The variation of the  $\sigma$  for the straight-to-bent waveguide but with the width difference,  $\Delta w = 0.73 \mu\text{m}$ , is shown in Fig. 3.22. For this case, the coefficient for the  $H_y^{11}$  increases to  $0.977$  and that of the  $H_y^{21}$  mode reduces to only  $0.10$ , calculated by

using the LSBR method. It should be noted in here that in this case the power carried by the  $H_y^{21}$  mode is only 1% as compared to a significantly larger value of 14% when  $\Delta w = 0 \mu\text{m}$ . Figure 3.22 also clearly shows that  $\sigma$  varies around  $\pm 1.7\%$ , compared to more than  $\pm 12.6\%$  for  $\Delta w = 0$ , which was shown in Fig. 3.13. For many devices, the periodic pulsation of the  $\sigma$  also varies the local power density and this can bring detrimental nonlinear effects such as gain saturation or facet damage. It has also been observed that polarization conversion is only 0.4% when the optimized unequal waveguide width is used.

It is observed in Fig. 3.22 that the mode-beating,  $L_B$  is found to be  $20 \mu\text{m}$ . To illustrate that mode-beating exists, Fig. 3.23 (a) shows the bent  $H_y$  field profile at axial position A (at  $z = 782 \mu\text{m}$ ) and Fig. 3.23 (b) shows the  $H_y$  field profile at axial position B (at  $z = 802 \mu\text{m}$ ), as identified in Fig. 3.25.



**Fig. 3.23.**  $H_y$  field profiles at two  $z$  propagation locations with  $W = 3.0 \mu\text{m}$ ,  $H = 1.3 \mu\text{m}$  and  $R = 100 \mu\text{m}$ . (a) At  $z = 782 \mu\text{m}$ . (b) At  $z = 802 \mu\text{m}$ .

The difference between the fundamental  $H_y$  field profiles at the axial position A (at  $z = 782 \mu\text{m}$ ) and position B (at  $z = 802 \mu\text{m}$ ) where the  $H_y^{21}$  mode has gone through phase reversal, is shown in Fig. 3.24, which clearly shows that this field profile is similar to that of the  $H_y^{21}$  mode in a bent guide mode and it leaks out into the lower right-hand corner.

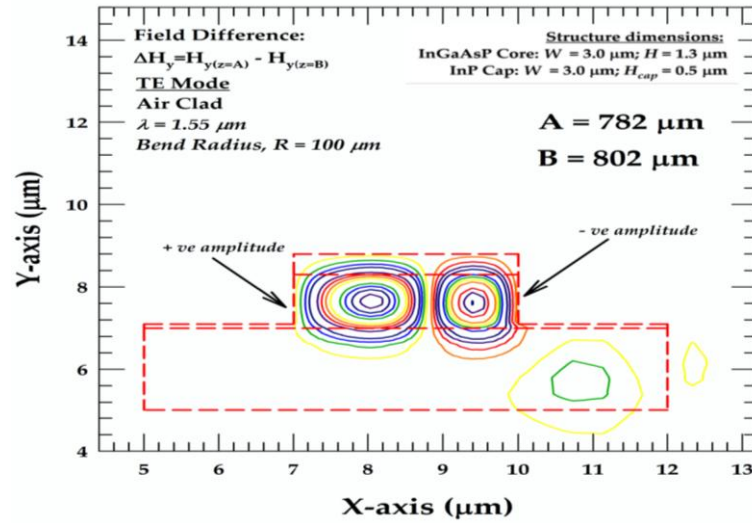


Fig. 3.24. Difference between two  $H_y$  field profiles at two locations with a phase reversal with  $W = 3.0 \mu\text{m}$ ,  $H = 1.3 \mu\text{m}$  and  $R = 100 \mu\text{m}$ .

For a specific design optimization, both the width change and offset can be incorporated simultaneously to reduce the bending loss, the transition loss, the mode beating and polarization conversion. Similarly, side trench [Rajaraman *et al.* 2000a] or index contouring by using multi-layers with a different refractive index profile [Tomljenovic *et al.*, 2003] can be used to increase the modal confinement in the outward side (here on the right side), to reduce the bending loss.

### 3.4 CHARACTERISTICS OF SLANTED WAVEGUIDE

In the previous section, the waveguide considered was a rib waveguide and for such waveguide the polarization conversion of TE mode to TM mode shown in Fig. 3.16 is small, with  $P_x$  at 24% at half-beat length found to be  $2500 \mu\text{m}$  when a straight waveguide was butt-coupled with a bent rib waveguide. In order to enhance the polarization conversion, a non-symmetrical rib waveguide with only one slanted side wall is considered here, in which such waveguide would increase the non-dominant field values of the quasi-TE and quasi-TM modes. Therefore by increasing the non-dominant field value, the hybridness (for TE mode - ratio of field value of  $H_x/H_y$  and for TM mode - the  $H_y/H_x$  ratio) of the waveguide would also increase, in which higher polarization conversion is possible.

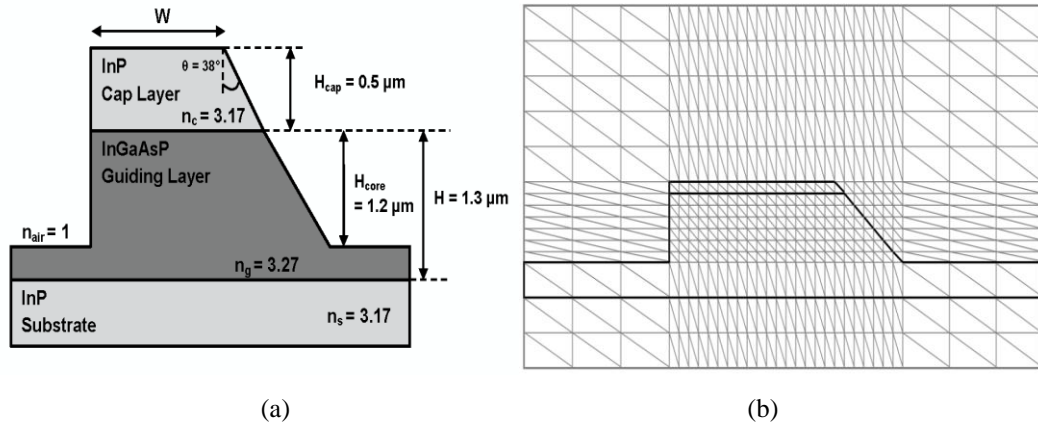


Fig. 3.25. (a) Schematic cross-section of the slanted rib waveguide, and (b) example of how the slanted waveguide is discretized.

The waveguide considered here is an asymmetric rib waveguide with a slanted side wall. The schematic cross-section of this slanted rib waveguide is shown in Fig. 3.25 (a). This structure can be fabricated by growing a  $1.3 \mu\text{m}$  ( $H$ ) thick InGaAsP guiding layer on top of the InP substrate. This is followed by depositing a  $0.5 \mu\text{m}$  InP cap layer ( $H_{cap}$ ) on top of the InGaAsP guiding layer and subsequently a ridge can be etched with a core height ( $H_{core}$ ) of  $1.2 \mu\text{m}$ . The right-sided slanted side wall can be formed by wet etching. It is found that the angle of this slanted wall with respect to the horizontal axis is naturally formed to be  $52^\circ$ , therefore, for the angle with respect to the vertical axis as shown in Fig. 3.25 (a),  $\theta$  is considered to be  $38^\circ$ . In the numerical simulations used, the width,  $W$ , is varied in order to understand its effect on modal field profiles and studying bending loss. The operating wavelength used in this analysis is  $1.55 \mu\text{m}$  and at this wavelength, the refractive indices of the InGaAsP and the InP layers are taken as 3.27 and 3.17, respectively. All other parameter values of the waveguide are given in Fig. 3.25 (a).

The finite element discretization of the slanted waveguide is shown in Fig. 3.25 (b). The waveguide is discretized on a  $200 \times 200$  mesh grid and with 80,000 first-order triangular elements. Each of these elements can be of various shapes and different sizes. Orientation of the triangles and sub-zones are taken in such a way that the slanted interface matches exactly with the sides of the adjacent elements. It should be noted here that, the FDM uses a staircase approximation and may not be satisfactory to evaluate polarization issues for such waveguides.

### 3.4.1 ANALYSIS OF SLANT AND A BENT SLANT WAVEGUIDE

Figure 3.26 (a) shows the variation of the  $n_{eff}$  with the  $W$  for the fundamental TE and TM modes for a straight slant (no bend) waveguide and a bent slant waveguide (that is bending to the left vertical computational wall). It can be noted in here that, as the  $W$  increases, the fundamental TE and TM modes will be more confined inside the core area, and hence, their  $n_{eff}$  increase. It is also shown in here that for quasi-TE mode, its  $n_{eff}$  is slightly higher than that of quasi TM mode when  $W$  is large.

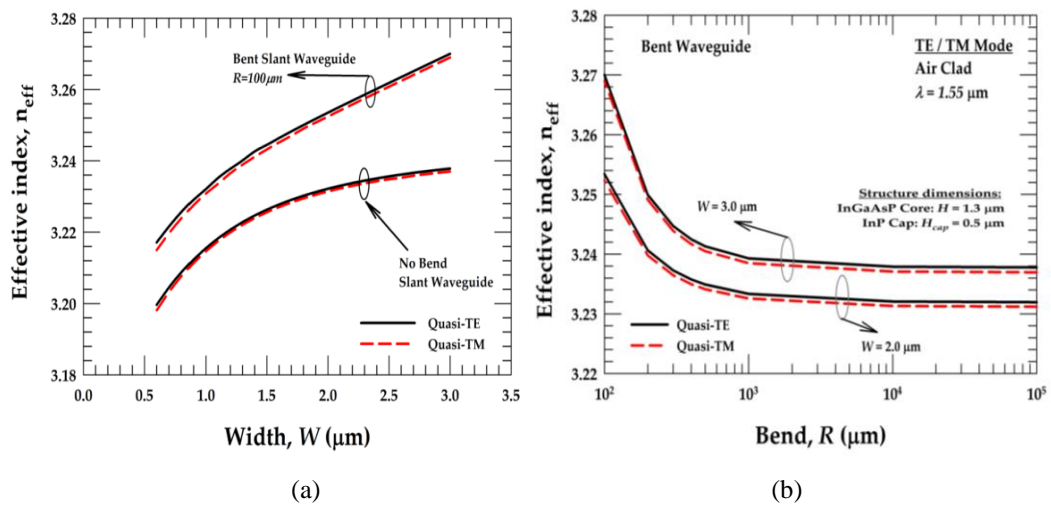


**Fig. 3.26.** (a) Variations of the  $n_{eff}$  of quasi-TE and TM modes with  $W$  for a straight slant and Bent slant ( $R=100\mu\text{m}$ ) waveguide. (b) Variations of the  $n_{eff}$  of quasi-modes with the bent radius of the slanted waveguide,  $R$  for different  $W$ .

The variations of the  $n_{eff}$ , with the bending radius,  $R$ , is shown in Fig. 3.26 (b) at two different waveguide widths. For a larger  $W$ , the  $n_{eff}$  of both the quasi-TE and TM modes can be noticed to higher than that of a narrow waveguide. This is due to a higher modal confinement of both the modes in a larger  $W$  waveguide.

The dominant  $H_y$  field profile of the  $H_y^{11}$  mode when  $W=1.2\mu\text{m}$  is shown in Fig. 3.27 (a), here, the field profile follows the shape of the slanted rib waveguide. The non-dominant  $H_x$  field profile is also shown in Fig. 3.27 (b) and it can be observed that the non-dominant field profile is very similar to that of the dominant field profiles of the  $H_x^{11}$  and  $H_y^{11}$  modes respectively. It can be noted in here that the maximum  $H_x$  value is 0.35, where the  $H_x$  value with vertical side wall is only 0.004

and that the  $H_x$  value for bent waveguide with vertical side wall is 0.035 as discussed earlier. Therefore the hybridness for the slant waveguide is substantially higher than other two waveguides (i.e. straight waveguide and straight-bent waveguide).

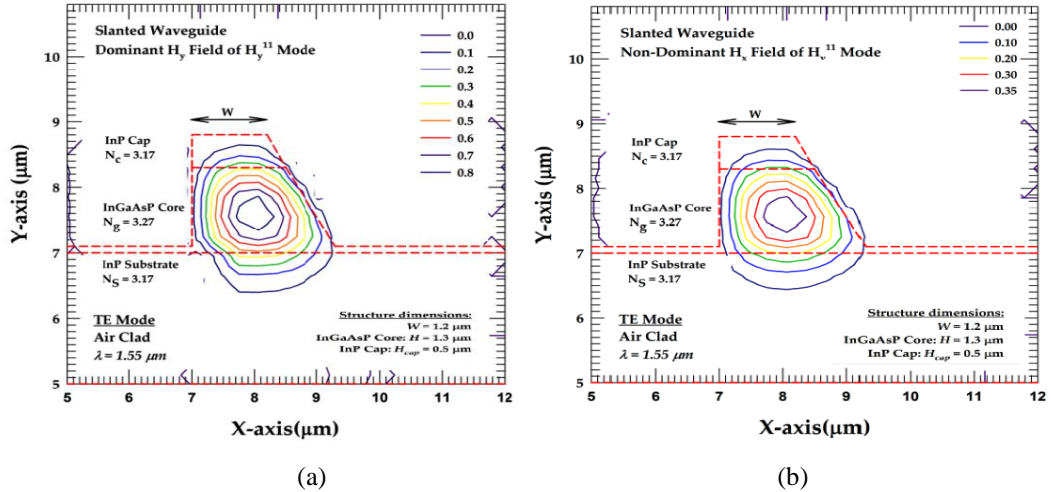


**Fig. 3.27.** (a) The dominant  $H_y$  field component and (b) the non-dominant  $H_x$  field component of quasi-TE mode of a slanted waveguide with  $W = 1.2 \mu\text{m}$  and  $H = 1.3 \mu\text{m}$

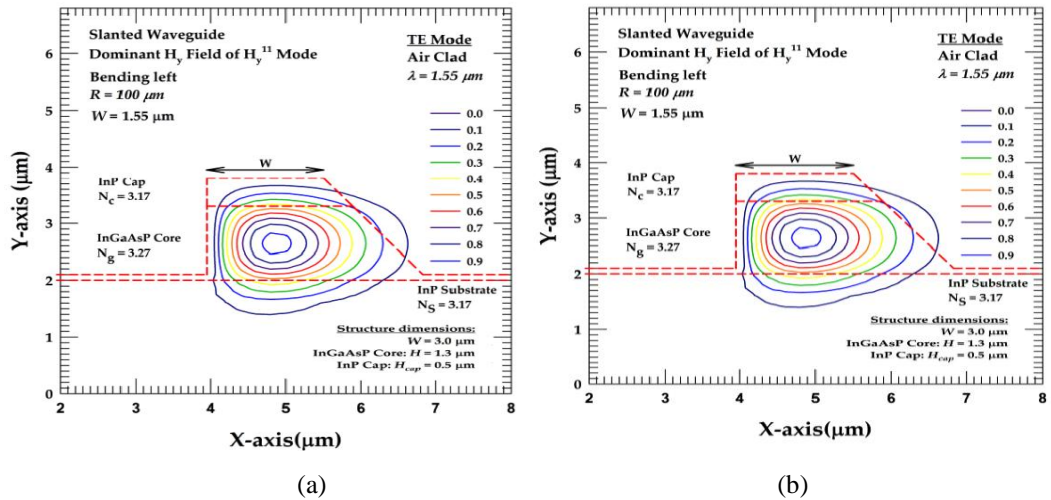


**Fig. 3.28.** (a) The dominant  $H_y$  field component and (b) the non-dominant  $H_x$  field component of quasi-TE mode of a bent slanted waveguide with  $R = 100 \mu\text{m}$  for  $W = 3.0 \mu\text{m}$  and  $H = 1.3 \mu\text{m}$ .

Figure 3.28 (a) shows the dominant component of  $H_y$  field of the  $H_y^{11}$  mode when  $W = 3.0 \mu\text{m}$  for a bent slanted waveguide with a bending radius,  $R = 100 \mu\text{m}$ . It can be observed that the field profile tends to extend outside the slanted side wall of the waveguide but it is more restricted to the left side of the vertical side wall and hence the field is getting more confined in the guiding region. For the non-dominant  $H_x$  field profile of the  $H_y^{11}$  mode, shown in Fig. 3.28 (b), it is similar to that of

dominant  $H_y$  field and its maximum  $H_x$  value is close to the  $H_y$  value and in this case they are 0.80 and 0.90, respectively. Therefore the hybridness for this bent slanted waveguide is higher than the slanted waveguide and much higher than a rib waveguide with vertical side wall, and it is found that such high hybridness can have a high polarization conversion.

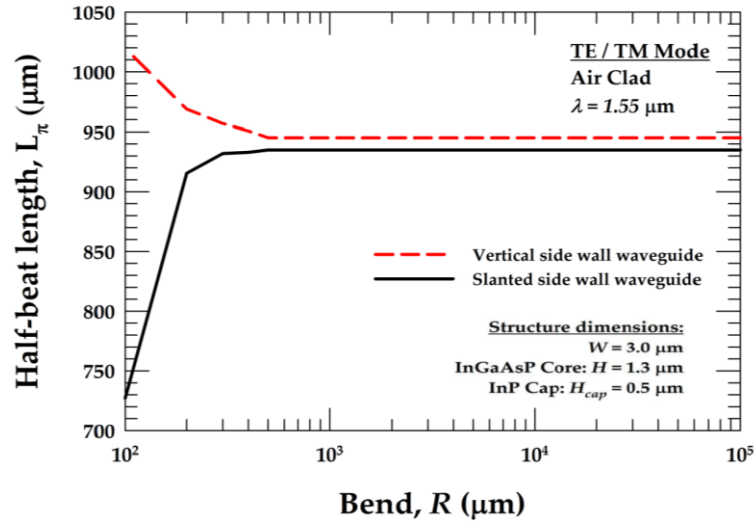
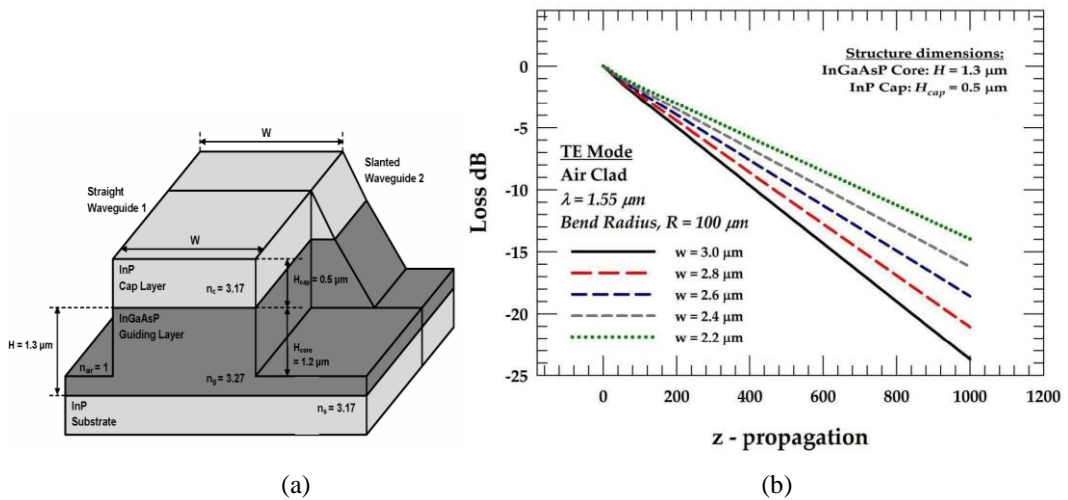


Fig. 3.29. Variations of the  $L_\pi$  of quasi- modes with the slanted waveguide  $W$  for a straight and Bent ( $R=100\mu\text{m}$ ) waveguide.

Next the effect of the  $R$  on  $L_\pi$  has been studied. To do so,  $W$  was kept constant at  $W = 3.0 \mu\text{m}$ , whilst  $R$ , was varied. The variation of  $L_\pi$  between the  $H_y^{11}$  and  $H_x^{11}$  modes as a function of the  $R$ , are shown in Fig. 3.29. The figure shows that, the  $L_\pi$  for the waveguide with the vertical wall is approximately 40% longer than the waveguide with the slanted wall, at a fixed  $R = 100 \mu\text{m}$ .

In order to illustrate the power loss of a bent slanted waveguide, the butt-coupling of the input rib waveguide with the bent slanted waveguide (in which both waveguides width are aligned) is consider here for further analysis. Figure 3.30 (a) shows the illustration of the butt-coupled waveguide. Initially, for the input rib waveguide, a VFEM is used to obtain the modal solution of the quasi-TE mode with  $W = 3.0 \mu\text{m}$ . It is then launched into the FEBPM code of a bent ( $R = 100 \mu\text{m}$ ) and slanted waveguide with  $W = 3.0 \mu\text{m}$  as an example.



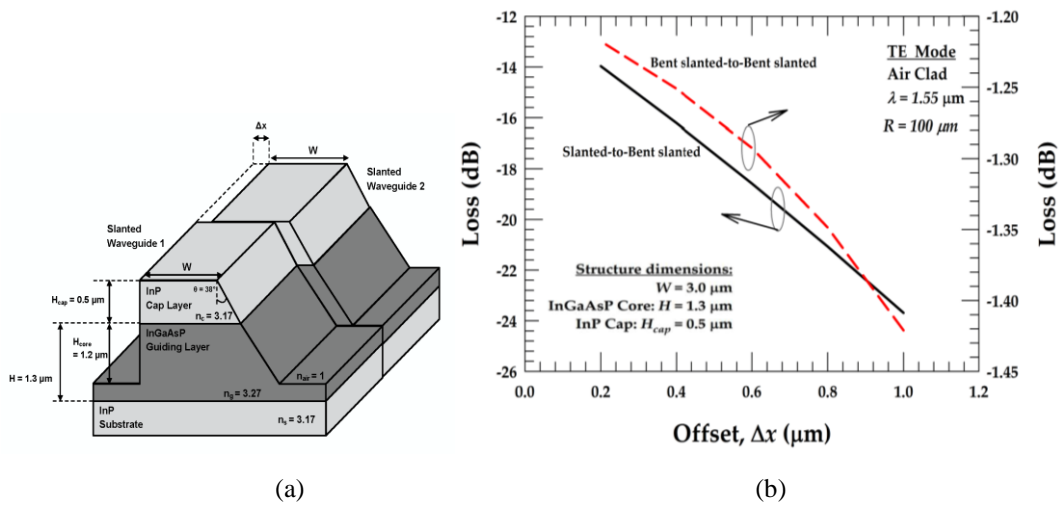
**Fig. 3.30.** (a) Butt-coupling of a rib waveguide with a bent slanted waveguide, and (b) the evolution of the power loss along the propagation direction of a butt-coupled straight waveguide to slant waveguide with bent ( $R=100\mu\text{m}$ ) with different  $W$ .

Figure 3.30 (b) shows the variation of the power loss for straight-to-bent waveguide along the propagation distance of over 1 mm. It can be observed that for  $W = 3.0 \mu\text{m}$ , the power loss is quite high (at 1 mm it is found to be about 23.69 dB). Initially, both the fundamental and higher order modes were propagated along the  $z$ -direction. As the field propagates further down the bent slanted waveguide, the optical beam strips off the more lossy higher order modes and leaving the fundamental mode as the dominant mode. It can be noted that as the  $W$  decreases, the power loss of the waveguide at 1 mm also decreases. At  $W = 2.2 \mu\text{m}$ , the waveguide power loss at 1 mm is 40% of the loss value calculated at  $W = 3.0 \mu\text{m}$ . It can be assumed that as the  $W$  decreases, the modal field of the input guide and the bent slanted waveguide are better aligned with each other at the butt-coupling junction. Hence, this reduces the propagation loss.

### 3.4.2 EFFECTS OF LATERAL OFFSETS ON LOSS

As described in the earlier section, an offset can be introduced to enhance the field mode matching. An offset can be described as the input straight waveguide that is shifted to the left when coupling to the bent slanted waveguide at the butt-junction to minimise the transmission loss.

Fig. 3.31 (a) shows that a  $\Delta x$  offset is used to shift the slanted input waveguide to the left when butt-coupled to another slanted waveguide with both waveguides  $W$  at  $3.0 \mu\text{m}$ . In here, two type of offset conditions had been investigated. Firstly, a slanted waveguide with no bend had been coupled to another slanted waveguide with  $R = 100 \mu\text{m}$ . It can be noted in Fig. 3.31 (b) that as  $\Delta x$  is increased the loss is increased also. Initially, when  $\Delta x$  is shifted 200 nm, the loss value is found to be about 14 dB, as  $\Delta x$  increased to 1000 nm, it is found that the loss is about 40% more. This indicates that the field modes of these two do not match with each other.



**Fig. 3.31.** (a) Butt-coupling of a (slanted) waveguide with a (bent) slanted waveguide, and (b) variations of the power loss with waveguide offset,  $\Delta x$  ( $\mu\text{m}$ ) for both Slanted-to-Bent slanted ( $R=100\mu\text{m}$ ) and Bent slanted-to-Bent slanted ( $R=100\mu\text{m}$ ) waveguide.

However, for the butt coupling between an imaginary bent-to-bent waveguide, the variation of the power loss along  $\Delta x$  at a propagation distance of  $1000 \mu\text{m}$  is shown in Fig. 3.31 (b) by a dash line (shown by the right y-axis). In this case, the power loss is much less than that of the straight-to-bent waveguide coupling. This is due to a higher modal field mismatch between a straight and a bent waveguide. It can be observed in here that for the bend-to-bend, the overall power loss is only about 1.21 dB, compared to 14 dB in a straight-to-bent waveguide, when  $\Delta x$  was taken to be  $200 \mu\text{m}$ .

### 3.4.3 EFFECTS OF BENDING ON POLARIZATION CONVERSIONS

In this study, the  $W$  was varied from  $2.5 \mu\text{m}$  to  $1.5 \mu\text{m}$  and the simulations have been carried out to observe the effect of  $W$  on the modal hybridness and the polarization conversion. Initially in Fig. 3.32 (a) the variations of  $n_{\text{eff}}$  of the modes as a function of  $W$  in a rib waveguide (no bend), a slanted rib waveguide and a slanted rib waveguide with a bending radius  $R = 200 \mu\text{m}$ , are shown. It can be observed in here that a rib waveguide with no bending has higher  $n_{\text{eff}}$  than both the slanted and bent slanted waveguide, as  $W$  of the waveguide is reduced.

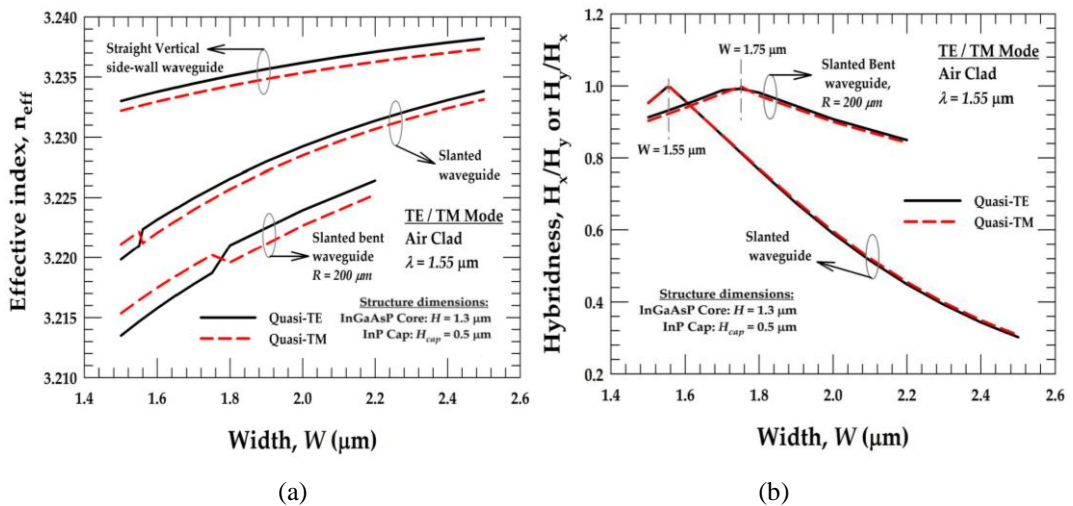


**Fig. 3.32.** (a) Variations of the  $n_{\text{eff}}$  of quasi-TE/TM modes for three different  $W$ .  
 (b) Variations of the Hybridness of quasi-TE/TM modes with the slanted waveguide  $W$  for a straight and Bent ( $R=200\mu\text{m}$ ) waveguide.

To achieve hybridness in any waveguide where there is a overlap between the vector field components of the quasi-TE and TM modes, the structure of the waveguide has to be asymmetric in some way. From figure 3.32 (b), it can be observed that the hybridness can be shifted by exploiting a bent waveguide. It can also be inferred that as the  $W$  decreases, the modal hybridness for different  $R$  in a slanted waveguide will be shifted towards to the hybridness for a slanted waveguide with no bend. This is also shown in Fig. 3.32 (b).

The TE to TM power conversion can be investigated by butt-coupled straight rib waveguide to a slanted waveguide with bend and the schematic of such a butt-coupled waveguide is illustrated in Fig. 3.33 (a). In here,  $W$  is kept constant at  $3.0$

$\mu\text{m}$  and that the width of the slanted waveguide with bend is set to  $W = 1.55 \mu\text{m}$ . Again the VFEM modal solution has been applied first and the resultant modal field profile of quasi-TE mode is launched in to the BPM code. For simulation purposes, different  $R$  of the slanted waveguide are used to investigate the effect of the polarization conversions.

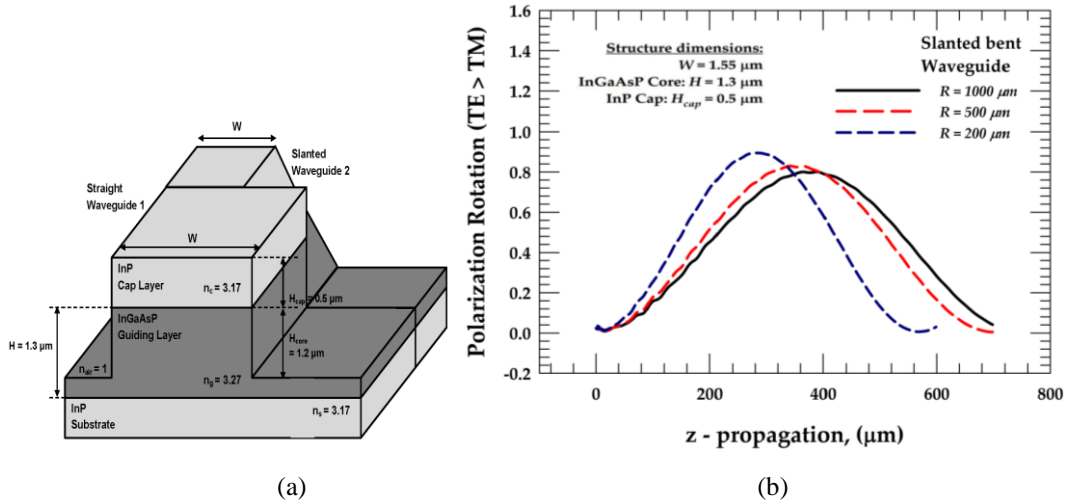


**Fig. 3.33.** (a) Butt-coupling of a rib waveguide with a (bent) slanted waveguide, and (b) variations of the polarization rotation along the slanted waveguide with different  $R$  when TE mode is incident.

It is expected that for larger  $W$  with a rising  $R$ , the modal field in the slanted waveguide (with bend) should be more confined in the core. For  $W = 1.55 \mu\text{m}$ , where the centre of the modal field in a slanted waveguide is nearly aligned with the core centre of the rib waveguide with  $W = 3.0 \mu\text{m}$ . The variations of the polarization rotation along the slanted waveguide with different  $R$  is shown in Fig. 3.33 (b). Initially, the input field is pure TE where at  $z = 0$ , the  $H_y$  polarized power,  $P_y$ , is nearly equal to one and that the  $H_x$  polarized power  $P_x$  is nearly zero. As the mode is propagating along the bent section of the slanted waveguide, the two polarized modes started to become out of phase, in which,  $P_x$  starts to increase and  $P_y$  starts to decrease. For  $R = 200 \mu\text{m}$ , the polarization rotation (when TE becomes TM) is at its highest with a maximum value of 0.90 at a distance  $L_\pi$  when  $z = 270 \mu\text{m}$ . Subsequently, the polarized power  $P_x$  starts to reduce. With the rise in  $R$  (in the case of  $R = 500 \mu\text{m}$ ), the device length,  $L_\pi$  is longer at  $z = 370 \mu\text{m}$  and that the power transfer from TE to TM will also be lower being at a maximum value of 0.80, when compared to shorter bending radius. It can also be noted in here that with  $W = 1.55 \mu\text{m}$ , polarization conversion will be at its maximum when  $R$  decreases

### **3.5 SUMMARY**

The rigorous full-vectorial modal solution, junction analysis and beam propagation methods have been used to study the bending loss, the transmission loss and the polarization conversion in a bent high index contrast semiconductor optical waveguide. It has been shown that by reducing the bending radius, the modal loss increases. Additionally, the transition (propagation) loss also increases as the mode shape significantly modifies in a bent waveguide. Rigorous full-vectorial characterization and design optimization of compact bent waveguides, to allow the highest degree of integration yet keeping the excess bending loss, transition loss, optical cross-talk, and polarization cross-talk within an acceptable limit are possible. It has also been shown here that by using a narrow input waveguide or an appropriate offset unit, the transition loss and polarization conversion can be reduced. For a specific PIC structure, both the narrow input waveguide and the appropriate offset can be introduced simultaneously and the numerical approaches presented here are suitable to carry out such optimisation by using the computationally efficient finite element-based approaches.

In a bent waveguide, the non-dominant field component is relatively large compared to that in a straight waveguide and its shape is also similar to that of the dominant field, so the overall integral between the two vector modal fields of the quasi-TE and TM modes is significantly higher. It is also shown that when the bending radius is reduced to design a compact PIC, the associated polarization conversion also increases significantly. However, by reducing the bending radius, a polarization rotator can be designed but it is also shown here that such devices suffer from a significant amount of power loss in the bent section. By incorporating single or several cascaded bent sections with vertical and with an optimized offset design or width difference, a compact and low-loss polarization rotator can be designed effectively.

By employing a slanted waveguide to couple with a straight waveguide, it is found in here that polarization conversion and higher hybridness can be achieved than the bent straight waveguide. It has also shown in here that by applying a bend

to a slanted waveguide, the polarization conversion efficiency can be significantly improved.

Overall, in this chapter, from the analysis of bent waveguides, the origin of higher order modes, the use of unequal guides and offsets on the coupling loss and polarization conversion and finally the use of slanted side in a bent waveguide to design polarization rotator are presented.

# 4

# Silicon Photonics Waveguides

## 4.1 INTRODUCTION

In recent years, there has been an increasing interest in the design of ultra-small and compact photonic devices. However most photonic devices have been fabricated using exotic materials, such as Gallium Arsenide (GaAs), Lithium Niobate ( $\text{LiNbO}_3$ ) and Indium Phosphide (InP) that are complicated to process and unless their critical material properties, such as their excellent electro-optic properties or emissive capabilities are explicitly needed, are excessively expensive to produce. A recent study [Lipson, 2005] has suggested that Silicon (Si) can be the material of choice to reduce the cost of fabrication and to increase the functionality of the components in building photonic integrated circuit (PIC). Si waveguides based on the silicon-on-insulator (SOI) platform are the most fundamental building blocks of many PIC systems, such as ring resonators [Vasalov and McNab, 2004], arrayed waveguide filters [Dai and He, 2006], modulators [Liao *et al.*, 2005] and lasers [Boyras and Jalali, 2004]. In photonic-based telecommunication systems, light is strongly confined in the Si waveguide because of the high refractive index contrast between the cladding and the core, and therefore, it allows for the waveguide core to be shrunk down to a submicron cross-section. It also permits the minimum bending radius of waveguides to be reduced, thus allowing an overall reduction in the dimensions of the PIC, which ultimately decreases the cost of Si photonics devices. Previous research [Yin *et al.*, 2007] has also shown that due to the strong electric

field in Si waveguides of small dimension, an ultra-high optical power density can be achieved in which the longitudinal field,  $E_z$  has a large effect on the waveguide nonlinearity.

For high index difference ( $\Delta n$ ) waveguides, the propagation/transmission loss is high, such loss usually contains the radiation loss and scattering loss. However, the high transmission loss is mainly due to the scattering loss. It is described that with  $\Delta n$  being high for the single-mode waveguide, the roughness of the sidewall results in transmission loss that scales with the square of the roughness amplitude [Payne and Lacey, 1994]. Scattering loss arises from the roughness of the side-wall interfaces associated with the fabrication process of waveguides. It can be reduced by using geometries that minimize the mode overlap with the rough sidewalls of the waveguide, in which the scattering loss reduces as the dimension of the waveguide is increased. This is due to the field mode is more confined and therefore smaller field will be at the interface. It is also described that TM loss may be lower to the TE loss as generally when the waveguide is fabricated; the horizontal layers are much smoother than the vertical side walls.

Typical scattering losses for a strip waveguide range from 0.2 to 5 dB/cm [Vlasov and McNab, 2004] and silicon slot waveguide can be higher. However, if oxidizing the vertical sidewalls [Sparacin, *et. al*, 2005] of the waveguide is employed during the fabrication process, scattering loss of as low as 0.8 dB/cm can be realised.

Scattering loss is generally estimated from the size of the roughness on the sidewall and the normalised field intensity at the interfaces [Tien, 1971]. In principle, FDTD can approximate the scattering loss, however such loss is difficult to calculate as the roughness of the sidewalls are often in the range of nanometre (which is beyond the mesh refinement used in the FDTD). However, if a flexible mesh can be used, as in the FEM, then this type of problem may be analysed more rigorously.

In this project, the calculation of scattering loss will not be included, nevertheless, the quoted scattering losses shown previously can be added to the calculated propagation/transmission losses in this thesis as an additional loss.

It is the aim of this chapter to provide a comprehensive review of the modal characteristics of the Si photonic waveguide. The **E** and **H** mode fields along with the Poynting vector of a Si strip waveguide with a nanoscale cross-section will be studied and shown in detail. The geometrical criteria of the Si photonic waveguide will be shown and the core dimension of the waveguide for single mode operation will also be shown in this chapter. Single mode condition is also a very important characteristic to design any function on a practical device. This is because most of the functional devices depend on the fundamental guided mode, therefore the single mode condition on a specific core thickness will be determined. In doing so, the hybridness, the effective area, the power confinements and the birefringence of the Si waveguide will also be studied for both air and SiO<sub>2</sub>-clad waveguides.

## 4.2 SILICON SLAB SOLUTION

It is well known that analytical modal solutions are not possible for an optical waveguide with two-dimensional confinement, however, analytical solution is possible for a planar (slab) waveguide by solving the transcendental equations developed by matching the field continuity at the two dielectric interfaces. Therefore to benchmark the FEM results, initially an analytical solution of a 3 layers slab waveguide was carried out to find the  $n_{eff}$  of a Si slab on top of a SiO<sub>2</sub> slab layer. It is assumed that  $W$  is infinite and that the thickness of the Si slab can be adjusted as necessary.

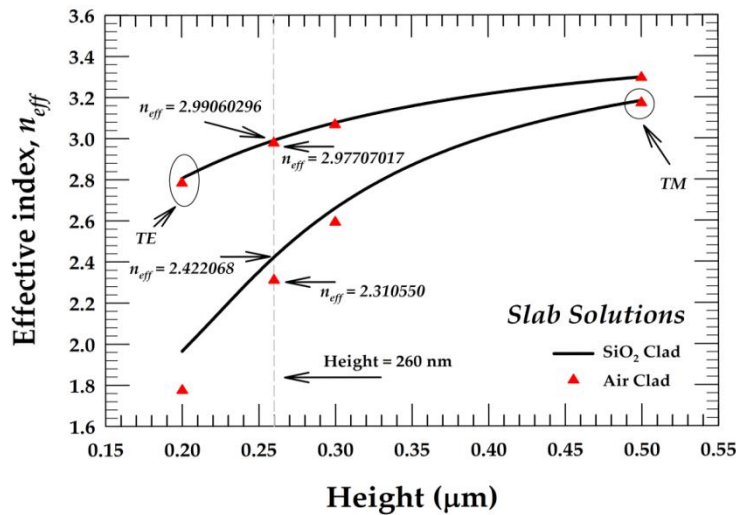


**Fig. 4.1.** Slab solutions for the variations of the  $n_{eff}$  of TE and TM modes with  $H$  for a Si slab waveguide.

Cladding	Thickness	TE		TM	
		Analytical	FEM	Analytical	FEM
Air	260nm	2.977095	2.977070	2.310551	2.310550
	300nm	3.066514	3.066492	2.592171	2.592170
	500nm	3.294015	3.294005	3.170643	3.170643
SiO <sub>2</sub>	260nm	2.990620	2.990603	2.422069	2.422068
	300nm	3.076448	3.076433	2.660336	2.660335
	500nm	3.297048	3.297041	3.182658	3.182658

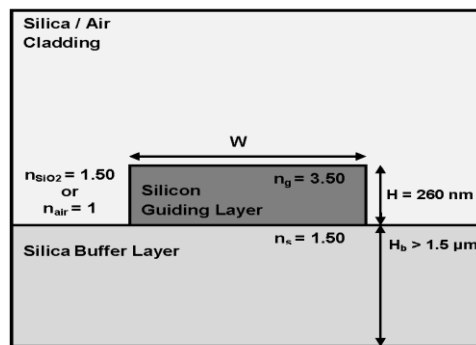
**Table 4.1.** Numerical comparison of analytical results with FEM results.

Figure 4.1 shows the variations of the  $n_{eff}$  of TE and TM modes with the waveguide  $H$ . It is also shown in Fig. 4.1 that as the thickness of the Si slab increases the  $n_{eff}$  of both TE and TM modes (in both air and SiO<sub>2</sub> clad waveguides) also increases. The  $n_{eff}$  of the TE mode was observed to be higher than the TM mode.

However the difference of TE and TM modes  $n_{eff}$  will narrow as the thickness of the Si slab increases.

The FEM results obtained and the calculated analytical results are also shown in Table. 4.1 for both air clad and SiO<sub>2</sub> clad planar waveguide. Both results shown an excellent agreement up to the fifth significant decimal of the  $n_{eff}$  values.

### 4.3 ANALYSIS OF STRIP WAVEGUIDE



*Fig. 4.2. Schematic cross-section of the Si strip waveguide.*

The structure considered here for a thorough investigation is a conventional silicon strip optical waveguide or Si photonic wire waveguide. Figure 4.2 shows the schematic cross-section this waveguide. Generally, these waveguides consist of a Si core with small rectangular cross-section, surrounded by either SiO<sub>2</sub> or air as a cladding layer. The structure can be fabricated by using a SOI (Silicon-On-Insulator) wafer on a Si substrate. A resist mask can be used on the surface of the Si layer and the Si waveguide core can be formed by etching down to the SiO<sub>2</sub> buffer layer by use of an Inductively Coupled Plasma (ICP) dry etcher. The Si core can then either be buried under a thick SiO<sub>2</sub> over-layer or surrounded with air. In this study, the thicknesses of the core waveguide is 260 nm ( $H$ ) and that of the lower SiO<sub>2</sub> buffer layer ( $H_b$ ) as 1.50  $\mu\text{m}$ . The refractive index of the rectangular Si core at 1.55  $\mu\text{m}$  wavelength is taken as 3.50. The refractive indices for the SiO<sub>2</sub> cladding or air cladding are set as 1.50 and 1.0, respectively.

## 4.4 MODAL FIELDS ANALYSIS

To begin with, simulations were carried out to determine the effect of the  $n_{eff}$  as a function of  $W$  with different  $H$  for Air clad waveguide. In this study, the  $\mathbf{H}$ -field based VFEM is used to obtain the modal solutions of such a waveguide. For this study, due to the availability of one-fold symmetry of the waveguide structure, only a half of the structure is considered and computational discretised using more than 80,000 irregular sized first order triangular elements. It is found that such simulation would take about 2 minutes CPU time on a dual-core Pentium processor computer running a Solaris platform.

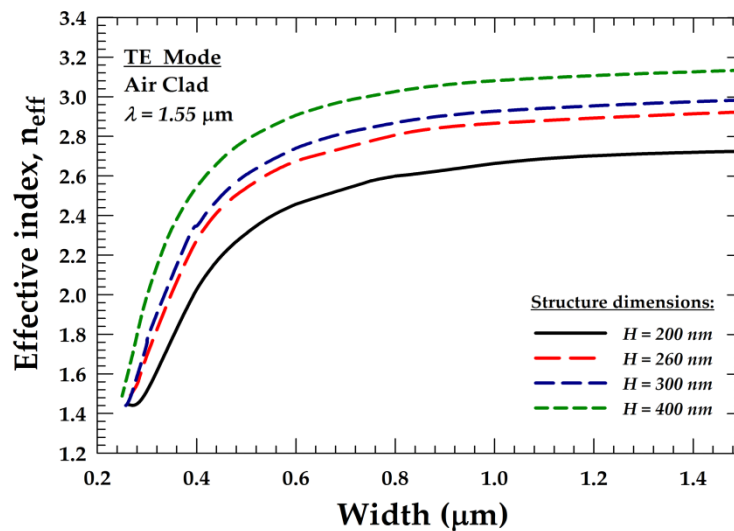


Fig. 4.3. Variations of the  $n_{eff}$  with  $W$ , for different quasi-TE modes.

Figure 4.3 shows the  $n_{eff}$  variation as  $W$  is varied from 1.5  $\mu\text{m}$  to nano-dimensions for various Si core heights. It is clearly seen that as  $H = 200$  nm and that  $W$  is reducing, its corresponding  $n_{eff}$  is reducing also. It can also be noted that when  $H = 200$  nm, it reaches its cut-off condition for the fundamental mode earlier than the other heights and that the cut-off width is at between 240 nm to 260 nm. As the behaviour of  $n_{eff}$  with  $W$  is determined, the thickness of 260 nm will be chosen to use as the Si core height for further analysis. The accuracy of the solution for the  $H_y^{11}$  mode was identified by using Aitken extrapolation [Rahman and Davies, 1985] to be better than 0.065%, when  $W = 500$  nm and  $H = 260$  nm.

### 4.4.1 MODAL H-FIELD PROFILES

In the analysis of modal  $\mathbf{H}$ -field profiles, for the  $\text{SiO}_2$  clad quasi-TE mode, the  $H_y$  field component is dominant, and  $H_x$  and  $H_z$  are the non-dominant components. The dominant  $H_y$  field component of the  $H_y^{11}$  mode is shown as an inset in Fig. 4.4 (a) for  $W = 300$  nm and  $H = 260$  nm.

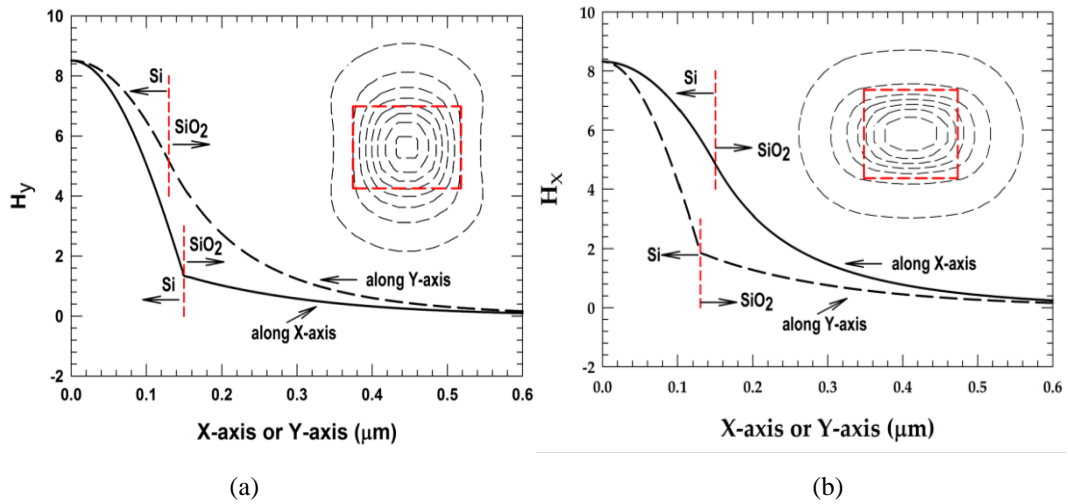


Fig. 4.4. (a) Variations of  $H_y$  for the  $H_y^{11}$  mode and (b) variations of  $H_x$  for the  $H_x^{11}$  mode along X-axis and Y-axis.

The field profile shown in Fig. 4.4 (a) clearly identifies the maximum intensity occurring at the center of the core. It is also shown that there is symmetry along the vertical and horizontal axes, and the mode extends considerably more into the top and bottom  $\text{SiO}_2$  cladding region. To illustrate its variation more clearly, the variation of the  $H_y$  field along the Y-axis is also shown by a dashed line in Fig. 4.4 (a). In this case, the  $H_y$  field is monotonically decreasing along the Y-axis and when  $Y = 0.13$   $\mu\text{m}$  (as  $H = 260$  nm), at the boundary between the Si and  $\text{SiO}_2$ , the magnitude of the  $H_y$  field is 60% of its maximum value. The variations of the  $H_y$  field along the X-axis is also shown by a solid line, which also decreases monotonically but with a rapid reduction inside the Si core until at the boundary interface, following which its slope reduces in the  $\text{SiO}_2$  cladding region. At the interface, (at  $X = 0.15$   $\mu\text{m}$ , as  $W = 300$  nm) the magnitude of the  $H_y$  field is only about 16% of its maximum value, which is significantly lower than field values at the upper and lower interfaces. In its contour plot it is clearly visible that the modal confinement in the horizontal direction is much stronger. The  $n_{\text{eff}}$ , of the  $H_y^{11}$  mode was found to be 2.00711 when  $W = 300$  nm.

Similarly, for the quasi-TM mode,  $H_x$  field component is dominant and that  $H_y$  and  $H_z$  are non-dominant components. It is found that when  $W = 300$  nm and  $H = 260$  nm, its  $n_{eff}$  is lower than the quasi-TE mode and that the  $n_{eff}$  of the  $H_x^{11}$  mode was found to be 1.873450. In its contour plot shown in Fig. 4.4 (b), it is clearly visible that the modal confinement in the vertical direction is much stronger. It is shown in Fig. 4.4 (b) that the variation of the  $H_x$  field along the X-axis is shown by a solid line and the  $H_x$  field is monotonically decreasing along the X-axis. It can be noted that when  $X = 0.15$   $\mu\text{m}$  ( $W = 300$  nm), the magnitude of the  $H_x$  field is 60% of its maximum value at the boundary between the Si and  $\text{SiO}_2$ . The variations of the  $H_x$  field along the Y-axis is also shown by a dashed line, which also decreases monotonically but with a rapid reduction inside the Si core until at the boundary interface, following which its slope reduces in the  $\text{SiO}_2$  region.

#### 4.4.2 ANALYSIS OF MODAL E-FIELD PROFILES

Once all the three components of the vector  $\mathbf{H}$ -field are obtained, Maxwell's  $\nabla \times \mathbf{H}$  equation is used to calculate the three components of the  $\mathbf{E}$ -field vector. The fundamental quasi-TE  $H_y^{11}$  mode contains all the three components of the electric field,  $E_x$ ,  $E_y$  and  $E_z$ : the  $E_x$  field is dominant, and the  $E_y$  and  $E_z$  field components are non-dominant. (The correlation between the  $\mathbf{E}$  and  $\mathbf{H}$  fields components were previously shown in Chapter 2)

Variations of the dominant  $E_x$  field along the X and Y-axes for the fundamental  $H_y^{11}$  mode are shown in Fig. 4.5 (a) for  $W = 300$  nm and  $H = 260$  nm. The variation of the  $E_x$  field along the Y-axis, shown here as a dashed-line, reduces monotonically from the center of the waveguide core and is continuous at the interface between Si/ $\text{SiO}_2$ , as required by the boundary condition. The  $\text{SiO}_2$  and Si interfaces are shown by two vertical dashed lines. However, the  $E_x$  field along the X-axis, shown here as a solid line, reduces more quickly in the core and at the Si/ $\text{SiO}_2$  interface increases abruptly with a step change in the ratio of  $(3.5/1.5)^2 = 5.44$  in the  $\text{SiO}_2$  region. Therefore the magnitude of the  $E_x$  field in the  $\text{SiO}_2$  region can be significantly higher than that in the core region and this behaviour is also shown in the 3D-contour of  $E_x$  field, this being shown as an inset in Fig. 4.5 (a).

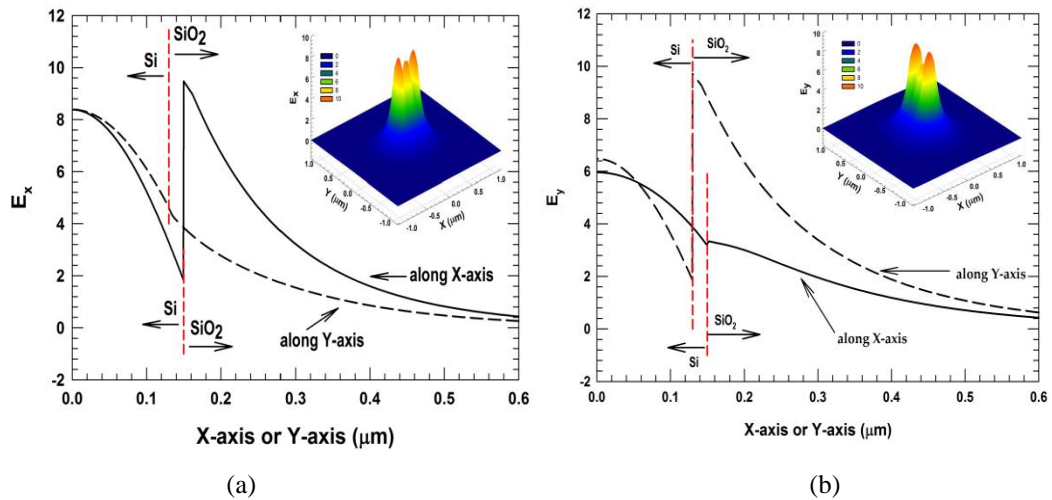


Fig. 4.5. (a) Variations of the  $E_x$  field for the  $H_y^{11}$  mode and (b) variations of the  $E_y$  field for the  $H_x^{11}$  mode along the X and Y-axes.

For quasi-TM mode the  $E_y$  field is dominant, and that the  $E_x$  and  $E_z$  field components are non-dominant components. It is shown in Fig. 4.5 (b) that when  $W = 300$  nm and  $H = 260$  nm, the variation of the  $E_y$  field along the X-axis reduces monotonically from the center of the waveguide core and with the boundary condition, it is continuous at the interface between Si/SiO<sub>2</sub> (when  $X = 0.15$  μm). However, for the  $E_y$  field along the Y-axis as shown here as a dashed line, the magnitude of  $E_y$  at the Si/SiO<sub>2</sub> interface increases abruptly with a step change in the ratio of  $(3.5/1.5)^2 = 5.44$  in the SiO<sub>2</sub> region which is similar to the dominant of  $E_x$  of quasi-TE mode. It is shown in here that such behaviour has higher magnitude of  $E_y$  field at the Si/SiO<sub>2</sub> interface than the core region along the Y-axis as this is also demonstrated in the 3D-contour of  $E_y$  field in Fig. 4.5 (b).

### 4.4.3 POYNTING VECTOR PROFILES ANALYSIS

From the full vectorial  $\mathbf{E}$  and  $\mathbf{H}$  fields, the Poynting Vector ( $S_z$ ) may be calculated. The contour of the  $S_z$  intensity distribution profile for the quasi-TE  $H_y^{11}$  mode is shown as an inset in Fig. 4.6 (a), where the core of the rectangular Si waveguide is also outlined by dashed lines. The variations of  $S_z$  along the X and Y-axes are also shown here. Variations of the  $S_z$  along the Y-axis are shown by a dashed-line, which clearly shows continuous power distribution at the interface. However, the variation of the  $S_z$  (along the X-axis is shown by solid line) reveals a small discontinuity step at the Si/SiO<sub>2</sub> interface which also decays more quickly in the Si core. It was

observed (but not shown here) that for a smaller  $W$ , the  $S_z$  discontinuity step can be even larger with a significant extension of the power intensity into the  $\text{SiO}_2$  cladding along the X-direction.

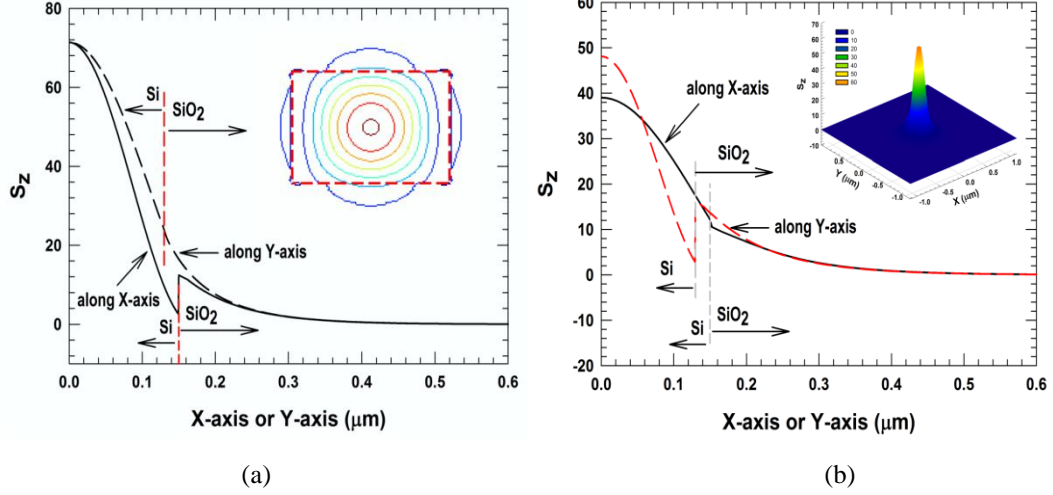


**Fig. 4.6.** (a) Variations of the  $S_z$  intensity for the  $H_y^{11}$  mode and (b) variations of the  $S_z$  intensity for the  $H_x^{11}$  mode along the X and Y-axes.

The variations of  $S_z$  along the X and Y-axes of the quasi-TM  $H_x^{11}$  mode is shown in Fig. 4.6 (b). Variations of the  $S_z$  along the Y-axis are shown by a dashed-line, which shows that there is a discontinuity step at the Si/SiO<sub>2</sub> interface. It can be noted in here that  $S_z$  has a maximum magnitude of 48 inside the Si core which then decays sharply inside the core than in the SiO<sub>2</sub> layer.

## 4.5 EFFECTIVE INDEX ANALYSIS

To begin with, simulations were carried out to determine the single-mode-to-multimode-transition of the strip waveguide by keeping  $H$  constant at 260 nm, while the  $W$  was decreased slowly from 3  $\mu\text{m}$  to nano-dimensions. In Fig. 4.7, variations of the  $n_{eff}$  as a function of  $W$  for the fundamental  $H_y^{11}$  and higher order  $H_y^{21}$ ,  $H_y^{31}$  and  $H_y^{41}$  quasi-TE modes are presented for the SiO<sub>2</sub>-cladding.

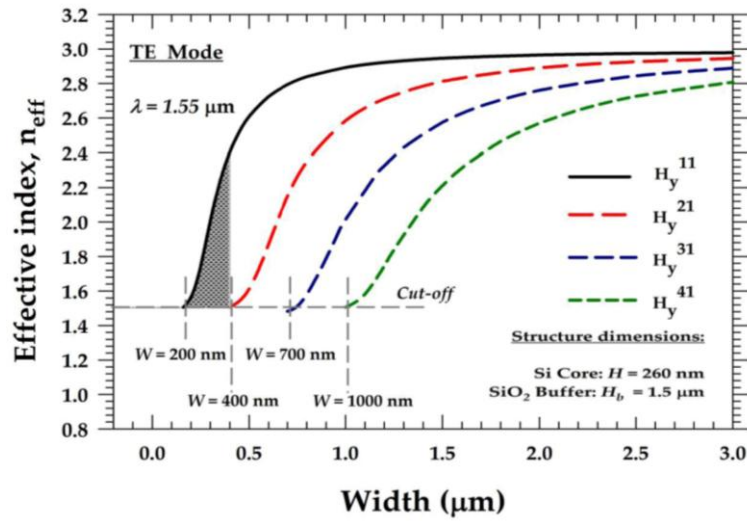


Fig. 4.7. The variations of  $n_{eff}$  with  $W$  for the  $H_y^{11}$ ,  $H_y^{21}$ ,  $H_y^{31}$  and  $H_y^{41}$  modes.

It can be observed that when  $W$  is large in comparison to  $H$ , the waveguide supports many modes and  $n_{eff}$  is closer to the  $n_{eff}$  of a slab guide with  $H = 260$  nm. As  $W$ , decreases,  $n_{eff}$  also decreases and gets closer to the refractive index of  $\text{SiO}_2$  where all the modes reach their cut-off. It is shown here that the cut-off widths for the  $H_y^{41}$ ,  $H_y^{31}$ ,  $H_y^{21}$  and  $H_y^{11}$  modes are 1000 nm, 700 nm, 400 nm and 200 nm, respectively. This simulation data generated suggests that the single-mode operation occurs when the waveguide width lies approximately between 200 nm to 400 nm for the operating wavelength,  $\lambda$  of 1550 nm with a height of 260 nm.

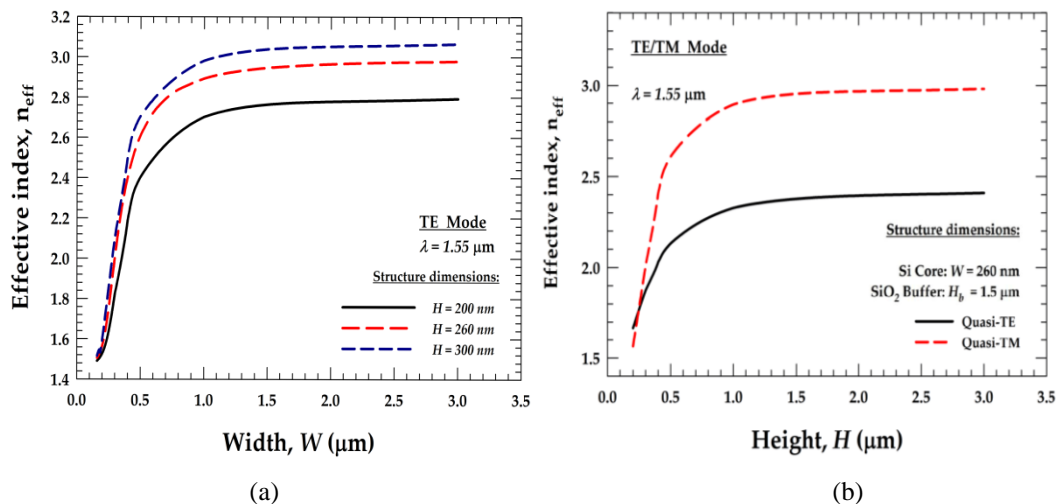


Fig. 4.8. The variations of  $n_{eff}$  (a) with  $W$  for quasi-TE modes with different  $H$ , (b) with  $H$  for quasi-TE and TM modes.

The heights of  $H = 200$  nm, 260 nm and 300 nm are used to investigate the effect of  $W$  on the strip waveguide. It is shown in Fig. 4.8 (a) that  $H = 200$  nm, the

$n_{eff}$  decreases as  $W$  decreases until it reaches its cut-off point. It can also be seen that when  $H = 200$  nm, it reaches its cut-off condition quickly than when  $H = 260$  nm and 300 nm.

The characteristics of the  $H$  is as important as the waveguide  $W$ , as  $H$  also dictates the cut-off condition of the mode. Figure 4.8 (b) shows the  $n_{eff}$  with  $H$  for quasi-TE and TM mode. It can be noticed in here that as  $W$  is smaller than  $H$ , the  $n_{eff}$  of the quasi-TM mode is higher than that of the quasi-TE mode. This can be observed as  $H$  is adjusted. As the  $H_x$  mode is the dominant mode of the waveguide, a larger waveguide  $H$  results in a significant overlap of the  $H_x^{11}$  field spreading vertically.

## 4.6 HYBRIDNESS ANALYSIS

Modes in optical waveguides with two-dimensional confinement are not truly TE or TM, but are hybrid in nature, which means that all the six components of the vector magnetic and electric fields are always present. For the quasi-TE  $H_y^{11}$  mode, the  $H_y$  component is the dominant and  $H_x$  and  $H_z$  each are non-dominant. The variations of the modal hybridness with  $W$  for the  $H_y^{11}$ ,  $H_y^{21}$ ,  $H_y^{31}$  and  $H_y^{41}$  modes are shown in Fig. 4.12. The modal hybridness in this case is defined as the ratio of the maximum value of non-dominant  $H_x$  field to the maximum value of dominant  $H_y$  field. This is an important parameter to calculate polarization cross-talk [Somasiri and Rahman, 2003] [Little *et al.*, 2005] and also in the design of polarization rotators [Rahman *et al.*, 2001].

The modal hybridness of the  $H_y^{11}$  mode is shown by a solid line in Fig. 4.9. A low hybridness can be observed for a wider waveguide, however as  $W$  is reduced, the hybridness reaches a maximum value, then slowly reduces as the fundamental  $H_y^{11}$  mode approaches its cut-off region. The maximum hybridness for the fundamental quasi-TE  $H_y^{11}$  mode is found to be 0.19 at  $W = 320$  nm. Furthermore, the hybridness variation of the higher order modes ( $H_y^{21}$ ,  $H_y^{31}$  and  $H_y^{41}$ ) are also similar to that of the fundamental mode.

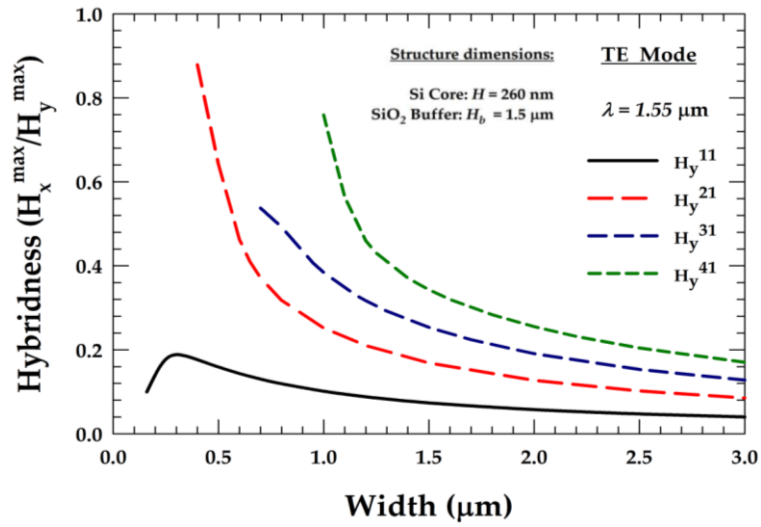


Fig. 4.9. The variations of hybridness with  $W$  for the  $H_y^{11}$ ,  $H_y^{21}$ ,  $H_y^{31}$  and  $H_y^{41}$  modes.

The variations of hybridness as a function of  $W$  for the TE mode of 3 different  $H$  is shown in Fig. 4.10 (a). It is shown in here that when  $W$  is small, hybridness will reach a higher maximum value as in the case when  $H = 200$  nm. It is also shown that as  $W$  reduces, the hybridness increases until it reaches its maximum value then starts to reduce as it approaches to its cut-off.

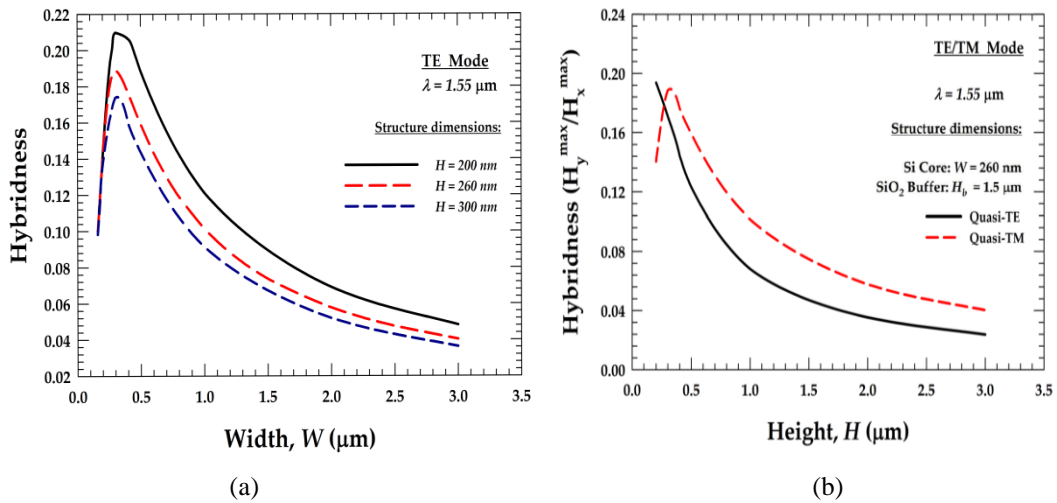


Fig. 4.10. The variations of hybridness, (a) with  $W$  for quasi-TE modes with different  $H$ , (b) with  $H$  for quasi-TE and TM modes.

The variation of the hybridness with the waveguide height,  $H$ , is shown in Fig. 4.10 (b). It can be seen that by reducing  $H$ , the hybridness can be further enhanced. An important aspect is that the hybridness of the  $H_x^{11}$  mode, shown by the dashed line is slightly higher than that of the  $H_y^{11}$  mode.

## 4.7 ANALYSIS OF EFFECTIVE AREA

Mode size area or effective area is an important design parameter for various applications and Fig. 4.11 shows the variation of the effective area ( $A_{eff}$ ) with the waveguide width for different quasi-TE modes. Following the second moment of intensity distribution (recommended by ISO Standard 11146), the definition of  $A_{eff}$  [ISO 11146, 2005] can be given by:

$$A_{eff} = \frac{\left( \iint_{\Omega} |E_t|^2 dx dy \right)^2}{\iint_{\Omega} |E_t|^4 dx dy} \quad (4.1)$$

where  $E_t$  is the transverse electric field vector and the integration is carried out over the whole cross-section of the waveguide,  $\Omega$ .

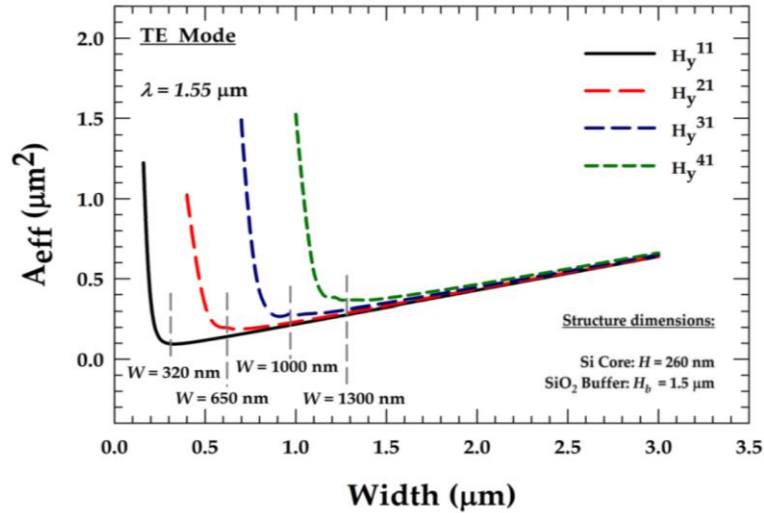
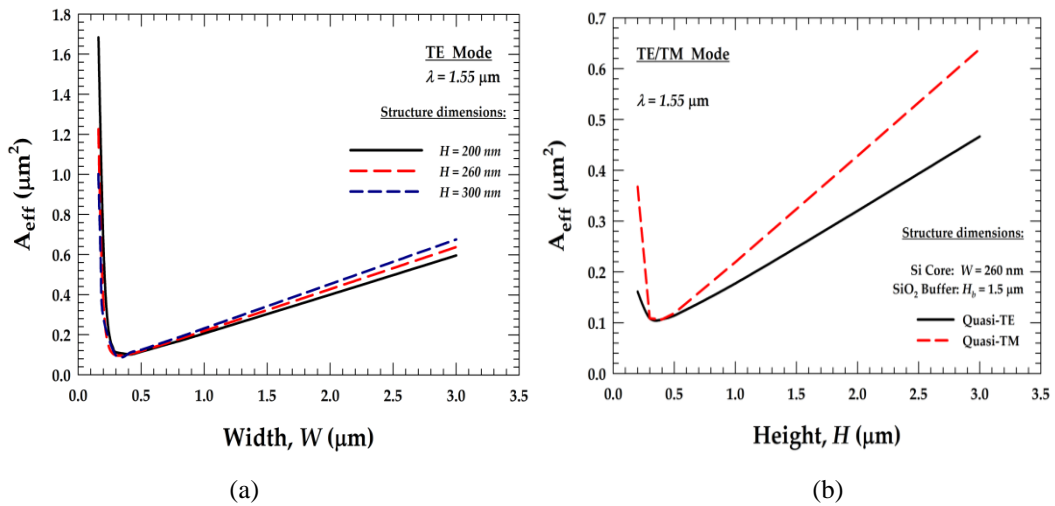


Fig. 4.11. Variations of the  $A_{eff}$  with  $W$  for the  $H_y^{11}$ ,  $H_y^{21}$ ,  $H_y^{31}$  and  $H_y^{41}$  modes.

It can be observed that as  $W$  reduces,  $A_{eff}$  reduces to a minimum value and any further reduction of  $W$ , results in the sudden rise in the  $A_{eff}$  as the mode approaches its cut-off. The minimum  $A_{min}$ , for the  $H_y^{11}$  mode is obtained as  $0.0956 \mu\text{m}^2$  when the value of  $W = 320 \text{ nm}$ , which means that the mode is more confined when the effective area is a minimum. Further rigorous simulations were carried out for the quasi-TE  $H_y^{21}$ ,  $H_y^{31}$  and  $H_y^{41}$  modes. It was found that the widths for the minimum  $A_{eff}$  values for the  $H_y^{21}$ ,  $H_y^{31}$  and  $H_y^{41}$  modes are  $650 \text{ nm}$ ,  $1000 \text{ nm}$  and  $1300 \text{ nm}$ , respectively. It can be noted that all the  $A_{eff}$  values are very similar when  $W$  is large but it is only slightly higher for the higher order modes.

Figure 4.12 (a) shows the evolutions of  $A_{eff}$  with  $W$  for different height,  $H$ . It was observed that as  $W$  decreases, its  $A_{eff}$  decreases until it reaches its minimum value and then starts to increase as it approaches its cut-off region. It can be noticed that for  $H = 300$  nm, its minimum  $A_{eff}$  is at  $0.096 \mu\text{m}^2$  at  $W$  around 300 nm. It was recorded that for  $H = 260$  nm and 200 nm the minimum  $A_{eff}$  was at  $W = 320$  nm and 400 nm, indicating that when the width is small, the respective  $H$  for the minimum  $A_{eff}$  will be large as the waveguide will reach its cut-off condition.



**Fig. 4.12.** Variations of the  $A_{eff}$ , (a) with  $W$ , for quasi-TE modes with different  $H$ , (b) with  $H$  for quasi-TE and TM modes.

The variations of  $A_{eff}$  with  $H$  for the fundamental quasi-TE and TM modes are shown in Fig. 4.12 (b). It can be clearly seen that for quasi-TM mode, the  $A_{eff}$  is higher than that of quasi-TE mode. It also shown that the  $A_{eff}$  for quasi-TM mode decreases to its minimum value when the waveguide height decreases and when  $H$  reduces further, it reaches its cut-off condition. The quasi-TE mode also follows the similar behaviour. In the case when  $H = 3.0 \mu\text{m}$ , the  $A_{eff}$  for the quasi-TM mode is  $0.66 \mu\text{m}^2$  and that it is  $0.47 \mu\text{m}^2$  for quasi-TE mode. It is a further evidence that the fundamental quasi-TM mode is more dominant than the quasi-TE mode when  $H$  is large.

## 4.8 CALCULATION OF POWER CONFINEMENTS

The variations of the  $\Gamma_{Si}$  with  $W$ , are shown in Fig. 4.13 for the  $H_y^{11}$ ,  $H_y^{21}$ ,  $H_y^{31}$  and  $H_y^{41}$  modes. The confinement factor in any particular area normalized to the total power, which is obtained by integrating the Poynting vector, from the  $\mathbf{H}$ - and  $\mathbf{E}$ -fields as given below:

$$S_z = \iint_{\Omega} \{\mathbf{E}^* \times \mathbf{H}\}_z dx dy \quad (4.2)$$

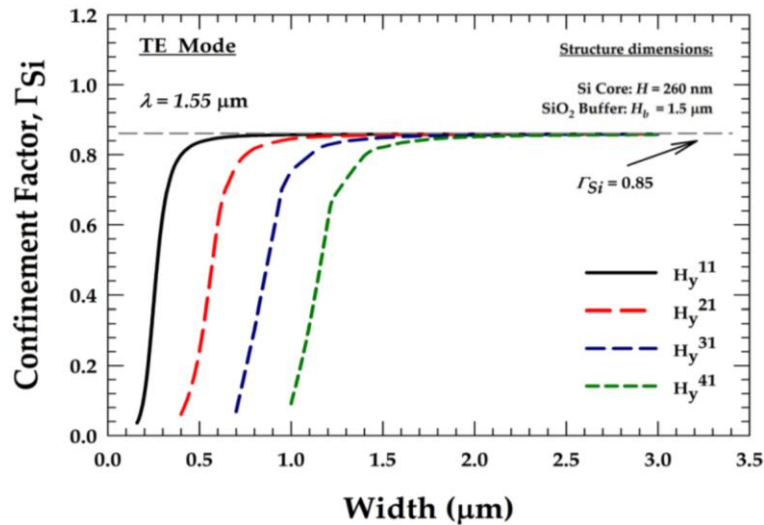
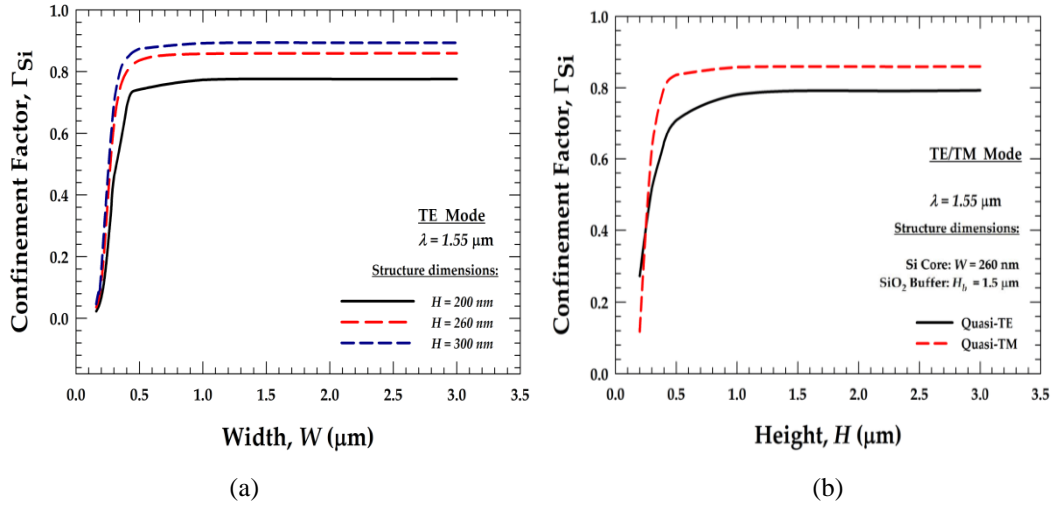


Fig. 4.13. Variations of  $\Gamma_{Si}$  with  $W$  for the  $H_y^{11}$ ,  $H_y^{21}$ ,  $H_y^{31}$  and  $H_y^{41}$  modes.

It is expected that as the waveguide dimension becomes large, most of the power would be confined in the Si core and that,  $\Gamma_{Si}$  would be close to 1.0. However, it can be noted that, the maximum  $\Gamma_{Si}$  in this case is closer to 0.85, because  $H$  was restricted to 260 nm. If the  $H$  of the core also becomes larger, then  $\Gamma_{Si}$  could approach 1.0. It can be observed here that as  $W$  is reduced, the  $\Gamma_{Si}$  also reduces. It can be also observed that although, for a wider waveguide, the  $\Gamma_{Si}$  for all the four modes shown here are similar, but for a narrower waveguide, the  $\Gamma_{Si}$  for the higher order modes are smaller.

Next the variations of the  $\Gamma_{Si}$  with the  $W$  for different heights are shown in Fig. 4.14 (a). It can be expected that if the  $H$  is large and the  $W$  starts to increase, the  $\Gamma_{Si}$  would be closer to 1.0. In the case of  $H = 300$  nm, the maximum  $\Gamma_{Si}$  is around 0.89 and it can also be assumed that the remaining normalized power (power confinement factor in  $\text{SiO}_2$ ),  $\Gamma_{SiO_2} = 0.11$ , would be contained in the  $\text{SiO}_2$  cladding.

For  $H = 200$  nm (thinner waveguide), the  $\Gamma_{Si}$  has dropped when compared to  $H = 300$  nm, and that only about 0.77 power confinement factor would be in the Si core and 0.23 in the SiO<sub>2</sub> cladding.



**Fig. 4.14.** Variations of the  $\Gamma_{Si}$  (a) with  $W$ , for quasi-TE modes with different  $H$ , (b) with  $H$  for quasi-TE and TM modes.

The investigation of the  $\Gamma_{Si}$  shown in Fig. 4.14 (b), yields that for the quasi-TM mode, most of the power would be confined in the Si core and for  $W = 260$  nm, the maximum  $\Gamma_{Si}$  is close to 0.85. If  $W$  also becomes large then the  $\Gamma_{Si}$  would be closer to 1.0. It can be observed here that, power is more confined in quasi-TM mode as the  $H$  is increased, hence  $\Gamma_{Si}$  in quasi-TM is higher than the  $\Gamma_{Si}$  in quasi-TE mode.

## 4.9 BIREFRINGENCE ANALYSIS

The next study in this work is to investigate the modal birefringence of such strip waveguide. For the design of optical photonics integrated circuits (PIC), light waves travelling inside the optical waveguide will have different propagation properties and will propagate at different velocities, and therefore suffers different losses. Thus it is essential to design PIC based on optical strip waveguide for it to be polarization independent. In this section, it will be shown that in a strip waveguide, it is possible to achieve zero birefringence with different waveguide dimension.

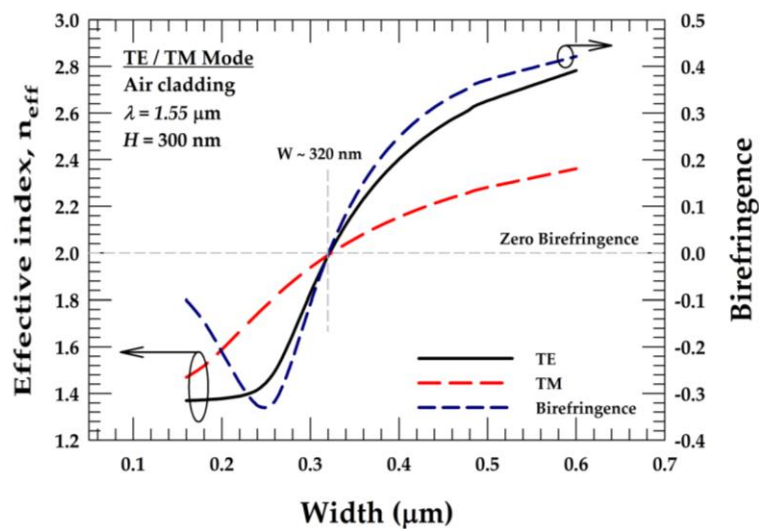


**Fig. 4.15** Variations of the  $n_{eff}$  of quasi-TE and TM modes and the birefringence with  $W$  for an air-clad Si strip waveguide with  $H = 300$  nm.

In the design of PIC, some Si guided-wave components may not be surrounded by SiO<sub>2</sub> cladding but be in air, in here the Si strip structure waveguide is surrounded with air, therefore, for the modal solutions, a one-fold symmetry with only a half of the structure is considered to apply into the vectorial simulations. Figure 4.15 shows the effect of birefringence and  $n_{eff}$  of quasi-TE and TM modes when the  $W$  is varied. Here, the modal birefringence is defined as the difference between the  $n_{eff}$  of the fundamental quasi-TE and TM modes. It can be observed in here by increasing  $W$ , the  $n_{eff}$  of the guided modes also increases. For  $W = 320$  nm, the  $n_{eff}$  of quasi-TE and TM mode is the same in which zero birefringence (shown as a dash-blue line) is achieved. It should be noted that with air-cladding, the waveguide is not symmetric along the  $y$ -axis. Hence for zero birefringence, the waveguide's  $W$  and  $H$  are different. The quasi-TM mode becomes more dominant as

the  $W$  decreases below the zero birefringence threshold of  $W = 300$  nm. Both the quasi-TE and TM modes were noticed to approach their respective cut-off conditions at  $W = 160$  nm.

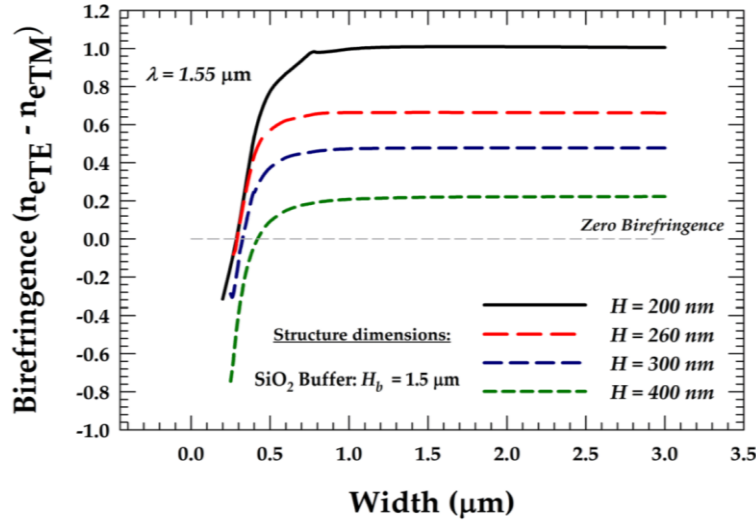


**Fig. 4.16** Variations of the modal birefringence with  $W$  for different  $H$  for an air-clad Si strip waveguide.

Figure 4.16 shows the variation of the modal birefringence caused by varying the  $W$ , at different values of the waveguide  $H$ . A negative modal birefringence can be observed for a narrow waveguide. However the birefringence increase with a wider waveguide. For example, for a waveguide with  $H = 200$  nm, the corresponding  $W$  to achieve zero birefringence is 280 nm. It was found that the widths for zero birefringence for  $H = 260$  nm, 300 nm and 400 nm are 290 nm, 320 nm and 420 nm, respectively. It can be described that for width beyond 500 nm, modal birefringence will be large when  $H$  is reduced but the width for zero birefringence will be small. Therefore it is possible to design a strip optical waveguide to eliminate the modal birefringence by optimising the waveguide geometries, in order to achieve polarization independence for various applications of PIC.

As described previously some Si guided-wave components may be surrounded by SiO<sub>2</sub> cladding and as well as be in air. Here the variations of their  $n_{eff}$  and the  $A_{eff}$  of the guided modes in these waveguides as a function of  $W$  are investigated. Figure 4.17 shows the variations of  $n_{eff}$  and  $A_{eff}$  for the fundamental H<sub>y</sub><sup>11</sup> mode with  $W$  for both air and SiO<sub>2</sub> cladding. It can be observed that when the

waveguide is covered with SiO<sub>2</sub> both the  $n_{eff}$  and the  $A_{eff}$  are slightly higher than that with the air-cladding.

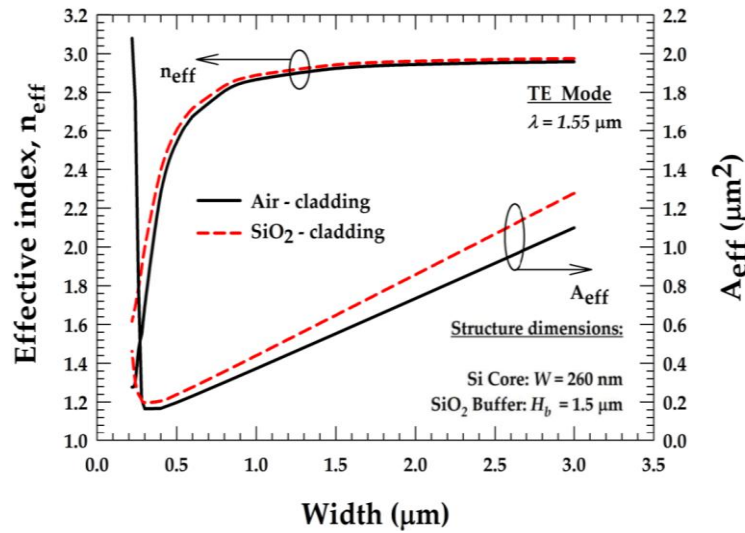


Fig. 4.17 Variations of the  $n_{eff}$  and  $A_{eff}$  with the  $W$  for SiO<sub>2</sub> or Air cladding for the  $H_y^{11}$  mode.

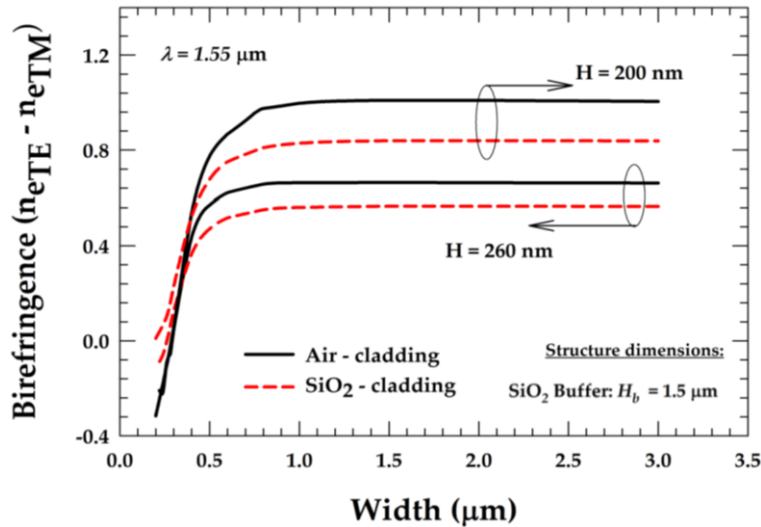


Fig 4.18 Variations of the modal birefringence with the  $W$  for the fundamental modes with SiO<sub>2</sub> or air cladding.

Finally, the variations of modal birefringence are shown in Fig. 4.18, for waveguide  $H$  of 200 nm and 260 nm. It is shown here that modal birefringence increases as  $W$  increases and then saturates. In an air-cladding waveguide, the modal birefringence is higher compared to a SiO<sub>2</sub> cladding waveguide. This is due to a stronger refractive index contrast between the Si core and the upper cladding material. It is important to note that the modal birefringence difference is larger when  $H$  is smaller. When the dimensions of the waveguide are the same, zero birefringence can be achieved with SiO<sub>2</sub> cladding.

## 4.10 SUMMARY

There is an impetus to develop low-cost photonic devices that can be furthered by exploiting the well-developed, low-cost CMOS technology. The higher index contrast,  $\Delta n$ , of Si also allows for smaller waveguides and compact bend designs which will allow more reliable PIC to be developed, with increased functionality. It is shown in this Chapter that for a Si waveguide with a strong index contrast, the single mode operation region is 200 nm to 400 nm, when the waveguide height is 260 nm and the operating wavelength is 1550 nm. Initially, accuracy of the FEM used here is benchmarked and convergence of solutions is discussed.

It is also discussed here that non-dominant field components are significantly higher, (often more than 50%), in which case the simpler scalar approaches often considered would be totally inadequate. It is also shown that, for this case ( $H = 260$  nm), the effective area not only is minimum, when  $W = 320$  nm, but also these values are similar for both the polarizations. In this case, the modal birefringence is also small and spot-size is near circular and could be a suitable dimension for many applications. However, it was also noted that, the modal hybridness was nearly its maximum value for this case.

In this study, the spatial variations of the components of the  $\mathbf{E}$  and  $\mathbf{H}$ -fields are shown, together with the  $S_z$  profile. The modal hybridness, the power confinement and the modal birefringence for silica and air-clad Si nanowires are also shown here. It should be noted that the performance of these highly birefringence guided-wave devices are polarization dependent. However, in the presence of slanted side walls and bends, there may be additional polarization conversion that occurs due to the presence of higher magnitude of the non-dominant field components and this can only be studied by using a rigorous full-vectorial approach, as was carried out in this work.

# 5

# Silicon Polarization Rotators

## 5.1 INTRODUCTION

As the telecommunication industry embraces higher optical transmission networks, the importance of minimizing the unexpected polarization rotation or polarization crosstalk to compensate the polarization mode dispersion (PMD) [Liu *et al.*, 1996] in an optical transmission network is of great interest in the design of polarization diversity photonics devices and PIC [Hilbk *et al.*, 1995]. It is also important to design such systems in integrated optics format rather than using separate fibre optics based components. Nowadays, PICs can improve reliability and reduce the size of complex devices by using fewer isolated components. However, so far there has not been a large-scale PIC commercially deployed [Yoo, 2009] because of the high development cost and poor flexibility associated with the fabrication processes of monolithically integrated subsystems. Recently, it has been suggested [Lipson, 2005] that Si with SOI technology can be considered to be a material choice for designing and integrating dense PIC and optoelectronic integrated circuit (OEIC) devices.

Si has already been well adapted to the complimentary-metal-oxide-semiconductor (CMOS) fabrication processes used commonly in the semiconductor industry. It is also found that when building optoelectronic devices, Si waveguides based on the SOI platform can also be used as building blocks in many Si PIC systems, such as nano-waveguides, compact bends, directional couplers, power splitters, ring resonators, arrayed waveguide filters, modulators, lasers and polarization rotators. Polarization rotators and polarization splitters can be used together to design polarization diversity OEICs. In this paper, the optimization of the design of a compact Si polarization rotator based on SOI technology is presented. This Si polarization rotator reported here has a relatively small footprint and has very low losses compared with the other polarization rotators so far reported, such as the single-section passive polarization rotator [Little and Chu, 2000].

In Si nanowire, the modal hybridness becomes more prominent as there is a high index contrast between the constituting materials. For the hybrid modes in a complex OEIC system, polarization is also a major issue because power can be exchanged between the polarization states in the presence of junctions, tapers, slanted side wall [Somasiri *et al.*, 2002], bends or other discontinuities. Therefore sometimes it is necessary to have a fixed degree of polarization state, such as a TE or a TM polarization state and it may also be necessary to rotate an incoming polarization state. It was reported that polarization rotation can be achieved by applying the electro-optic effect in LiNbO<sub>3</sub> [Alferness and Buhl, 1982] and InP [Schlak *et al.*, 1991]. However, it has also been suggested that a passive polarization converter [Mertens *et al.*, 1998] would be much preferred for use, because it would be much simpler to fabricate and to process. In particular, a passive polarization converter based on the use of asymmetrically periodic loaded rib waveguides had also been reported [Shani *et al.*, 1991], but such a converter has a relatively large device length. Therefore to minimize the device length and to reduce the excess loss, a single-section passive polarization rotator [Little and Chu, 2000] has been suggested, however, it required a complicated fabrication process, often due to its tilted [Deng *et al.*, 2005] or slanted sidewalls [Rahman *et al.*, 2001; Brooks *et al.*, 2006]. The Si polarization rotator proposed here shows a very compact design without a slanted side wall and it requires a less complex fabrication process. It is also compatible with more mature CMOS technology which is backed by the well-

established semiconductor industry. However, with the index contrast being high, the modes are hybrid in nature with all the six components of the  $\mathbf{E}$  and  $\mathbf{H}$ -fields, which requires a full-vectorial treatment.

The asymmetry of the Si nano-scale waveguide which consists of a trench section in the Si strip core waveguide is therefore been rigorously investigated in this work by using a  $\mathbf{H}$ -field VFEM [Rahman and Davies, 1984c] to calculate the propagation constant and the modal field profiles of the proposed waveguide structure and a Si strip waveguide. A Beam Propagation Method (BPM) [Obayya *et al.*, 2000a] can be used to calculate the power conversion between the two polarization states; however, the proposed structure consisting of only two discrete interfaces, the Least Squares Boundary Residual (LSBR) [Rahman and Davies, 1988] method would be more efficient to use to calculate the coefficients of the excited modes at the butt-coupled junctions and also to find the resulting polarization rotation. The half-beat length and polarization crosstalk along with the power loss in the proposed polarization rotator are presented in this chapter. Finally, different lateral offsets between the butt-coupled sections are also considered to further improve the design.

## 5.2 NUMERICAL APPROACH

The accurate calculation of the magnitudes of the non-dominant field components and their profiles for the fundamental quasi-TE and TM polarized modes are of great importance when designing a polarization rotator. In the design of a compact optical polarization rotator, a full VFEM is used to obtain the modal field profiles of the constituent waveguides. The VFEM is used because the modes in optical waveguide with a very strong index contrast are hybrid in nature. In this formulation, all the  $\mathbf{H}$ -field components are continuous across the dielectric interface. On the other hand, since the normal component of the  $\mathbf{E}$ -field is discontinuous around the interface, an equivalent  $\mathbf{E}$ -field based approach would be less satisfactory. As for the hybrid modes, a significant non-dominant field component exists around the dielectric interfaces and hence, the  $\mathbf{H}$ -field formulation can be used to treat such waveguides more rigorously. In the design process, it is necessary not only to increase the magnitude of the non-dominant field components but also for its profile to be optimized so that its overlap with the dominant field components can be enhanced to achieve the maximum polarization rotation. The full-vectorial formulation with penalty function used here was shown in Chapter 2. This full-vectorial FEM modal solution is also used to determine the polarization beat length between the quasi-TE and TM polarized fundamental modes.

A junction analysis approach is also used, as the proposed polarization rotator structure is composed of two butt-coupled uniform waveguide sections with only two discrete interfaces between them. A powerful numerical approach, LSBR method [Rahman and Davies, 1988] has been used, which rigorously satisfies the continuity of the tangential electric and magnetic fields at the junction interface in a least squares sense, and the modal coefficients of the transmitted and reflected modes at the discontinuity interface can be obtained. This particular LSBR method is used to look for a stationary solution to satisfy the continuity conditions by minimizing the error energy functional,  $\mathbf{J}$ , and the detail explanations of such error energy functional has been given previously in Chapter 2. The integration is carried out over the junction interface,  $\Omega$ , between the straight and the asymmetric Si waveguides.

### 5.3 SINGLE SECTION POLARIZATION ROTATOR

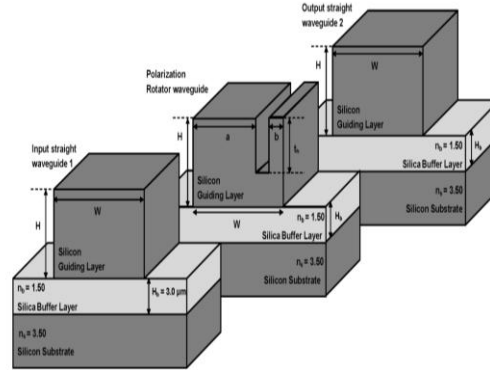


**Fig. 5.1.** Schematic diagram of the asymmetric polarization rotator butt-coupled to input and output of a SOI strip waveguide with waveguide dimensions.

Figure 5.1 shows a single-stage polarization rotator, which consists of two Si strip waveguides with straight side-walls, where both are butt coupled to a Si asymmetric strip polarization rotator waveguide in the middle. In the design of a polarization rotator, an asymmetric section which supports the highly hybrid modes of quasi-TE and TM, is sandwiched between two standard Si waveguides where the hybridness is small. When a quasi-TE (or quasi-TM) mode from a standard Si waveguide with its polarization angle at nearly zero degrees (or  $90^\circ$ ) is launched into the asymmetric section (which supports highly hybrid modes, e.g. M1 and M2, with polarization direction  $\pm 45^\circ$ ) then both of them are excited almost equally to satisfy the continuity of the  $\mathbf{E}_t$  and  $\mathbf{H}_t$  fields at that interface, and travels along the asymmetric sections.

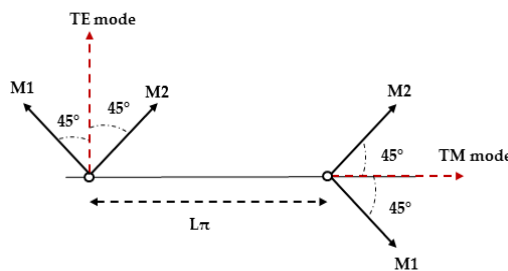


**Fig. 5.2.** Illustration of Polarization Rotation.

The half-beat length ( $L_\pi$ ) is a key parameter used in order to identify the optimum length of this asymmetrical section to achieve the maximum polarization rotation. The half-beat length is defined as  $L_\pi = \pi / \Delta\beta$ , where  $\Delta\beta$  is the difference between the propagation constants of the  $H_y^{11}$  and the  $H_x^{11}$  modes. After propagating a distance,  $L = L_\pi$ , the original phase condition between the highly polarized modes,

M1 and M2 would be reversed and the polarization state of the superimposed modes would be rotated by  $90^\circ$  as shown in Fig. 5.2. If a standard Si waveguide (with smaller modal hybridness) is placed at this position, this quasi-TM (or TE) mode would propagate in this waveguide without any further polarization rotation.

### 5.3.1 WAVEGUIDE STRUCTURE

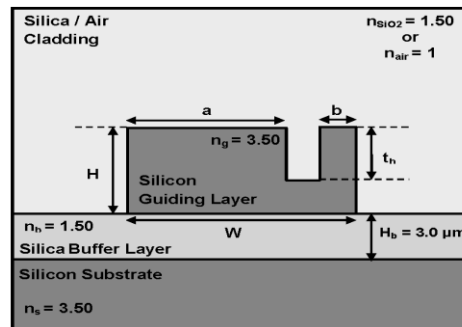


*Fig. 5.3. Schematic diagram of the Si asymmetric strip rotator.*

The structure under rigorous analysis is a Si asymmetric strip polarization rotator waveguide; the cross-section of this particular waveguide is also shown in Fig. 5.3. Such waveguide structure consists of a single-trench in the waveguide core and it can easily be fabricated by using a SOI wafer on a Si substrate. A single-trench photoresist mask can be used on the surface of the Si core and then etched down to the desired depth in the Si core waveguide. The Si core waveguide then either can be buried under a thick silica ( $\text{SiO}_2$ ) or covered by air or other polymers.

In the numerical simulations used, the structure is surrounded by air and initially,  $W$ , is varied in order to study its effect on modal field profiles and particularly the effect of polarization degeneration. In this analysis, the operating wavelength is considered to be  $1.55 \mu\text{m}$  and at this  $\lambda$ , the refractive index of the Si core is set as 3.5 and that of the  $\text{SiO}_2$  cladding and the  $\text{SiO}_2$  buffer layer is set as 1.5. The thickness of the Si core waveguide,  $H$ , is fixed as  $600 \text{ nm}$  and that  $1.50 \mu\text{m}$  of the lower  $\text{SiO}_2$  buffer layer is used. If a lower  $H$  was considered for the Si layer then the  $W$  required to bring polarization degeneration would have been also smaller and such that the waveguide would be more lossy. Hence, in this study, a greater  $H$  is deliberately considered, although if required alternative designs can also be

optimised. The thickness,  $t_h$ , and the width,  $t_w$ , of the trench waveguide section and the width,  $a$ , of the rotator waveguide section are varied to optimize the design, while the width,  $b$ , of the rotator waveguide section is set as 100 nm.

### 5.3.2 MODAL H-FIELD ANALYSIS

A full-vectorial Finite Element Method (FEM) is used in this study to obtain the modal solutions of the single-trench Si waveguide. In this analysis, due to the waveguide structure is asymmetric, therefore a full waveguide structure will be investigated and that more than 20,000 first order triangular elements have been employed to represent the waveguide structure. In this particular waveguide, for the quasi-TE ( $H_y^{11}$ ) mode, the  $H_y$  field component is dominant, and  $H_x$  and  $H_z$  are the non-dominant components. Similarly,  $H_x$  is the dominant field component of the quasi-TM ( $H_x^{11}$ ) mode and that  $H_y$  and  $H_z$  are the non-dominant field components.

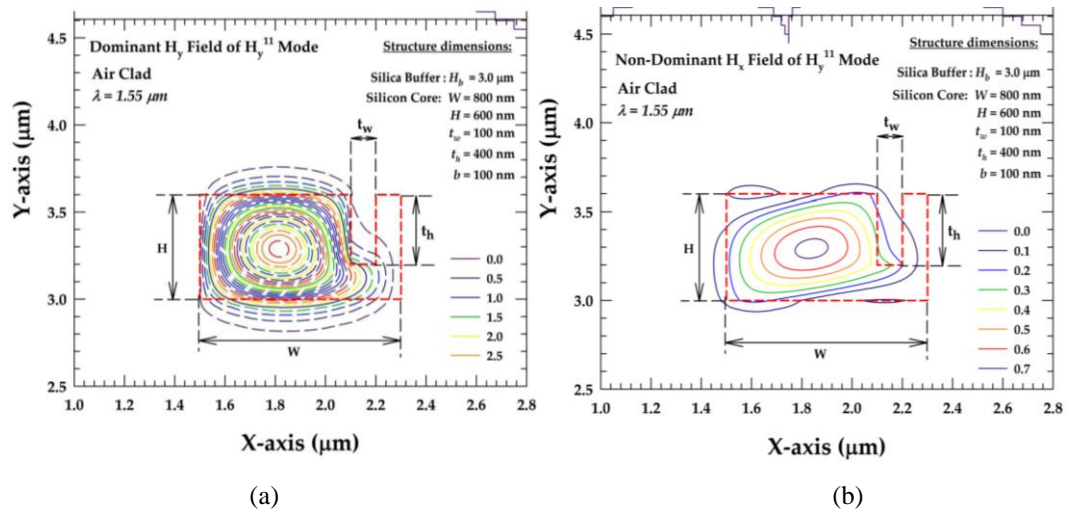


**Fig. 5.4.** Field profile of the (a) dominant  $H_y$  and (b) non-dominant  $H_x$  of the  $H_y^{11}$  mode with  $W=800\text{nm}$ ,  $H=600\text{nm}$ ,  $t_w=100\text{nm}$  and  $t_h=400\text{nm}$ .

The spatial profile of the dominant  $H_y$  field component of the quasi-TE mode is shown in Fig. 5.4 (a) for a larger guide as  $W = 800$  nm. The trench,  $t_w$ , of the structure is taken as 100 nm and the  $t_h$ , is taken as 400 nm and the overall Si core waveguide is surrounded with air, but if necessary, other materials such as  $\text{SiO}_2$  or polymer can also be considered. In this case, the modal hybridness was relatively small and the  $H_y$  field profile shows that the maximum optical intensity occurs near the geometrical-centre of the larger Si core region. However, due to the asymmetry

of the waveguide, the field profile is slightly asymmetric and it shows that the field extends more to the lower SiO<sub>2</sub> substrate region and also by a smaller amount into the air region.

The non-dominant H<sub>x</sub> field component of the quasi-TE mode is shown in Fig. 5.4 (b), and it is nearly similar in shape like that of the dominant H<sub>y</sub> mode. In this case, the maximum magnitude of the H<sub>x</sub> field profile is found to be about 25% of the maximum value of the dominant H<sub>y</sub> field. It should be noted that the non-dominant H<sub>x</sub> field profile for a Si strip without the trench section has a very small magnitude with the odd-like symmetry along the *y*-axis, however this is not shown here. However, this non-dominant H<sub>x</sub> field was observed previously for dimensions  $W = 300$  nm and  $H = 260$  nm, and this was shown earlier in Fig. 4.4 in Chapter 4.

## 5.4 ROTATOR SIMULATION RESULTS

In this section, the asymmetric polarization rotator with a trench is rigorously investigated. The width,  $W$  is an important parameter when designing a polarization rotator with the optimum performance for a specific height,  $H$ . The dimension of  $W$  is varied from 900 nm to 500 nm to analyse the effect on effective index, modal hybridness, effective area, power confinement in silicon or silica, modal birefringence and the polarization beat length.

### 5.4.1 CHARACTERISTIC OF POLARIZATION ROTATOR

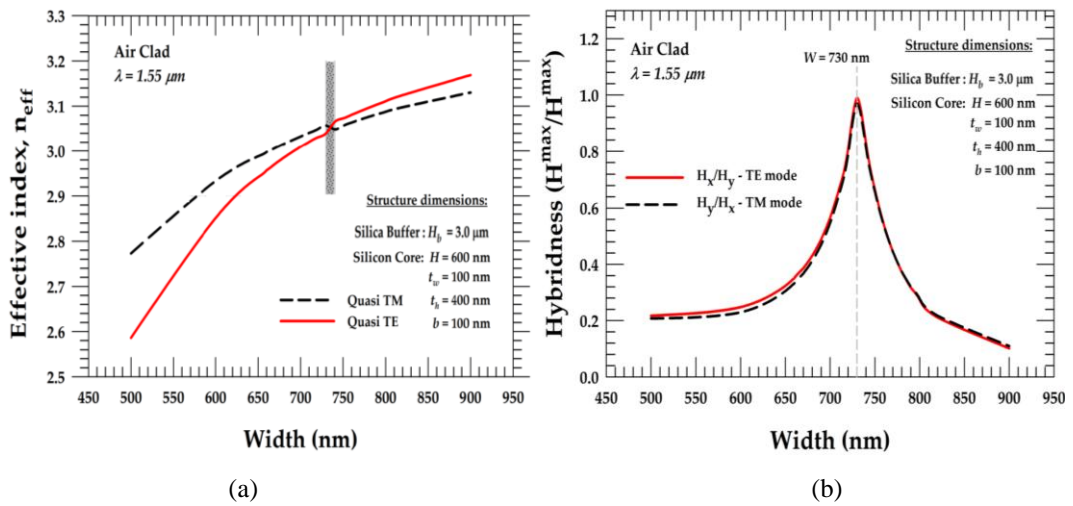


Fig. 5.5. (a) Variations of the  $n_{\text{eff}}$  and (b) variations of the hybridness with  $W$  for the quasi-TE and TM modes.

It is important however, in the design of a polarization rotator, to further enhance the modal hybridness of the asymmetric structure. In Fig. 5.5 (a), the variations of the  $n_{\text{eff}}$ , with  $W$  for the fundamental quasi-TE ( $H_y^{11}$ ) and TM ( $H_x^{11}$ ) modes are presented for the air cladding structure. In this case, as  $W$  is reduced, both  $t_w$  and  $b$  were kept constant at 100 nm. It can be observed that when  $W$  is large,  $n_{\text{eff}}$  is closer to the refractive index of the Si. As  $W$  decreases,  $n_{\text{eff}}$  also decreases and gets closer to the refractive index of  $\text{SiO}_2$  where a mode reaches its cut-off. However, it is shown here that the  $n_{\text{eff}}$  of the  $H_y^{11}$  mode crosses that of the  $H_x^{11}$  mode when  $W$  is between 730 nm and 740 nm, when the equivalent  $W$  is comparable to its  $H$  and these two polarized modes become degenerate. In fact, their  $n_{\text{eff}}$  values do not actually cross each other, but the modes rather transform from one dominant polarization state to the other in this region.

The effect of  $W$  on the modal hybridness is shown in Fig. 5.5 (b). In the case of the  $H_y^{11}$  mode, the modal hybridness is given by the ratio of the non-dominant  $H_x$  field (the maximum value) to the dominant  $H_y$  field (its maximum value) and it is shown here by a solid line. The modal hybridness of the  $H_x^{11}$  mode, calculated from the ratio of the maximum value of the  $H_y$  field to its  $H_x$  field, is also shown as a dashed line. It can be seen here that for both polarized modes, when  $W$  is reduced from 900 nm to 730 nm, the hybridness is increased. At  $W$  equal to 730 nm, their hybridness values reach their maximum of about one in which it indicates that magnitude of both the transverse field components are identical. Under this condition, the polarization directions are  $\pm 45^\circ$  with respect to the  $x$  and  $y$ -axes for the two polarized modes. For both the polarized modes it is also shown that as  $W$  reduces further, the hybridness decreases. The modal hybridness of the  $H_x^{11}$  mode also follows a similar trend to that of the  $H_y^{11}$  mode and its maximum hybridness also occurs at  $W=730$  nm.

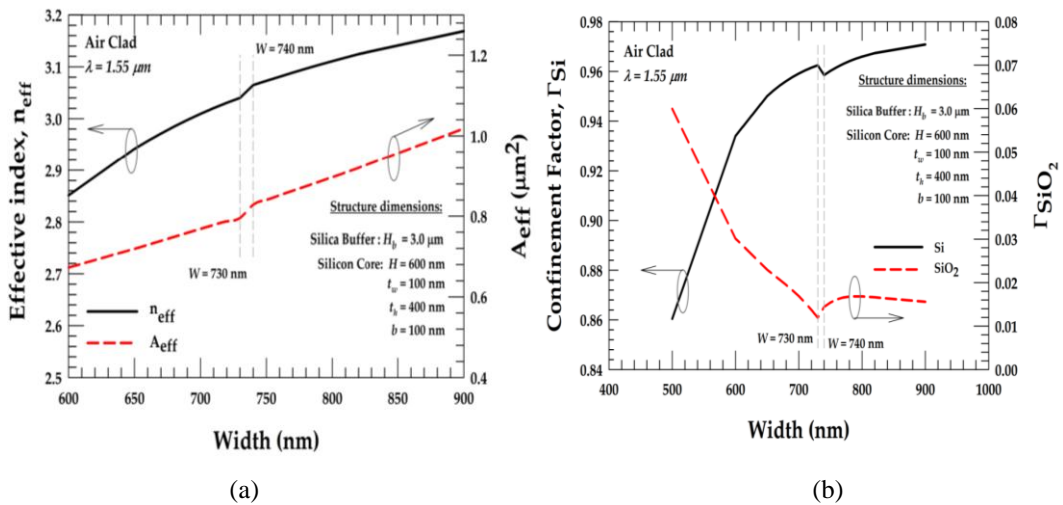


Fig. 5.6. (a) Variations of  $n_{\text{eff}}$  and  $A_{\text{eff}}$  with  $W$  and (b) variations of  $\Gamma_{\text{Si}}$  and  $\Gamma_{\text{SiO}_2}$  with  $W$  for the fundamental TE mode.

The variations of the  $A_{\text{eff}}$ , with the change of  $W$  is shown in Fig. 5.6 (a) along with the  $n_{\text{eff}}$  for the quasi-TE mode. It can be observed that as  $W$  increases, the  $A_{\text{eff}}$  also increases. It is also shown in here that the  $n_{\text{eff}}$  for a quasi-TE mode follows a similar trend to that of the  $A_{\text{eff}}$ . It can be seen that there is a slight discontinuity in its  $n_{\text{eff}}$  and  $A_{\text{eff}}$  variations near  $W \sim 730$  nm where TE and TM modes were degenerate. It can be noted that at  $W = 730$  nm where the hybridness is at its highest, the  $n_{\text{eff}}$  and  $A_{\text{eff}}$  are found to be 3.03999 and  $0.80 \mu\text{m}^2$ , respectively. For  $W = 740$  nm, the  $n_{\text{eff}}$  for quasi-TE mode is found to be 3.04857 and its respective  $A_{\text{eff}}$  is found to be  $0.83 \mu\text{m}^2$ .

It can be observed that in between  $W = 730$  nm and  $740$  nm, minimum modal birefringence is possible for such polarization rotator waveguide where the  $n_{eff}$  of quasi-TE mode and TM mode are close to each other.

The variations of the  $\Gamma_{Si}$  and the  $\Gamma_{SiO_2}$  with the change of  $W$  are shown in Fig. 5.6 (b) for the quasi-TE mode. It is shown in here that as  $W$  increases, most of the power would be confined in Si core and only a small amount of power would be remain in the  $SiO_2$  buffer layer. Here, for  $W = 730$  nm where the hybridness is the highest, the  $\Gamma_{Si}$  is of 0.96 and the  $\Gamma_{SiO_2}$  is about 0.01 and the rest would be in the air-clad including the air-slot region. It can be noticed that as  $W$  increases from  $730$  nm to  $740$  nm, there is a small step change of  $\Gamma_{Si}$  where the modes transform from one dominant polarization state to the other in this region. It can be observed that for such asymmetric polarization rotator, there is a strong confinement of light in the core waveguide as shown in Fig. 5.6 (b) and also demonstrated in the contour plot of the  $H_y$  dominant field mode in Fig. 5.4 (a).

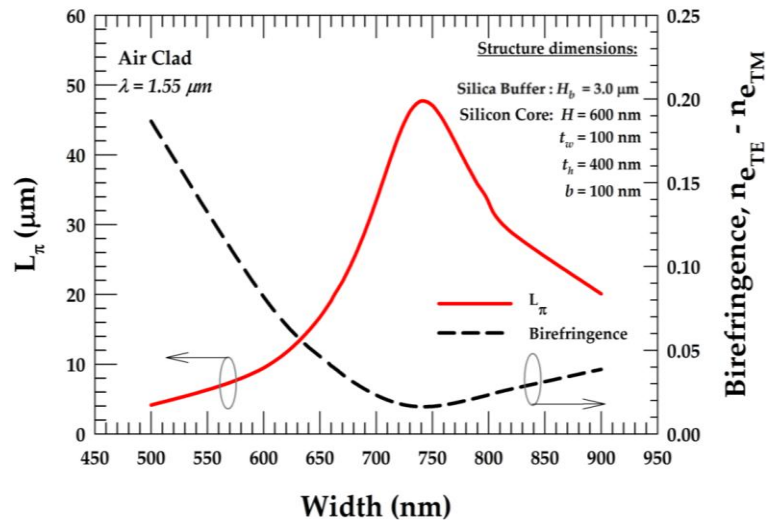
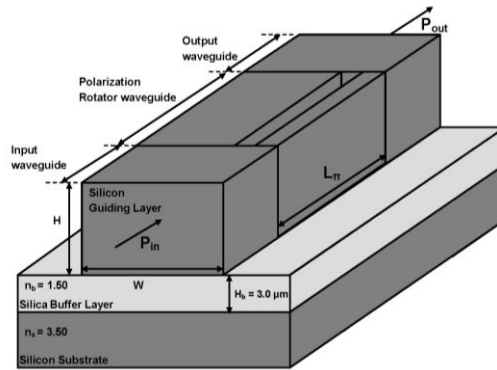


Fig. 5.7. Variations of  $L_{\pi}$  and birefringence with  $W$  for the fundamental TE mode.

The half-beat length ( $L_{\pi}$ ) is a key parameter used in order to identify the optimum length of the asymmetrical section to achieve the maximum polarization rotation. At the  $L_{\pi}$ , the phase mismatch between the two polarized modes,  $H_y^{11}$  and  $H_x^{11}$ , is also at its minimum. Figure 5.7 shows the variations of the  $L_{\pi}$  with the  $W$ . In Fig. 5.7, it is shown in here that  $L_{\pi}$  starts to increase when  $W$  increases until it reaches its maximum value, and then the  $L_{\pi}$  gradually reduces as  $W$  further increases. Therefore in this study, when the two modes are degenerate, their hybridness is about

1.0, their polarization angles are  $\pm 45^\circ$  and that  $L_\pi$  also reaches the maximum value of  $48 \mu\text{m}$ . Hence, the length of the central asymmetric section of the waveguide with the trench needs to be  $48 \mu\text{m}$ , which is reasonably short, compared to other designs reported so far [Kim *et al.*, 2009; Deng *et al.*, 2006]. It is also shown in Fig. 5.7 that the variations of the modal birefringence with the change of  $W$ , the minimum modal birefringence is found to be 0.01624 at  $W = 740 \text{ nm}$ .

## 5.4.2 POLARIZATION CONVERSION AND CROSS-TALK



*Fig. 5.8. Schematic diagram of the asymmetric polarization rotator butt-coupled to input and output of a SOI strip waveguide.*

In this section, the power conversion and the cross-talk is rigorously studied. It was shown in the previous section that the modes obtained from the polarization rotator waveguide are not pure TE or TM, but hybrid in nature. Moreover due to the asymmetric of the rotator waveguide, it is possible to achieve polarization conversion, where if a TE or TM is incident in from the input waveguide, it will excite both the hybrid modes at the junction between the input and rotator waveguides. Therefore, to understand the polarization conversion further, an input strip-waveguide is butt-coupled to the asymmetric polarization rotator waveguide as shown in Fig. 5.8.

As mentioned previously, the incoming TE (or TM)  $x$ - (or  $y$ -) polarized wave of a standard guide would excite two highly hybrid,  $\pm 45^\circ$  polarized modes in the asymmetric section. To quantify further in the analysis, the scattering coefficients (the excited modal coefficients),  $C_y$  and  $C_x$  of the two quasi-TE and TM modes, respectively, at the junction need to be obtained. In this study, a rigorous numerical

approach using the LSBR has been employed to obtain the modal coefficients at the discontinuity interface by enforcing the boundary conditions in a least squares sense.

In this example, the  $H_y^{11}$  mode of the vertical side-wall waveguide (without the trench section), where the modal hybridness is very small (but it was not neglected), is launched into the single-trench waveguide section which excites two highly hybrid modes to satisfy the necessary boundary conditions.

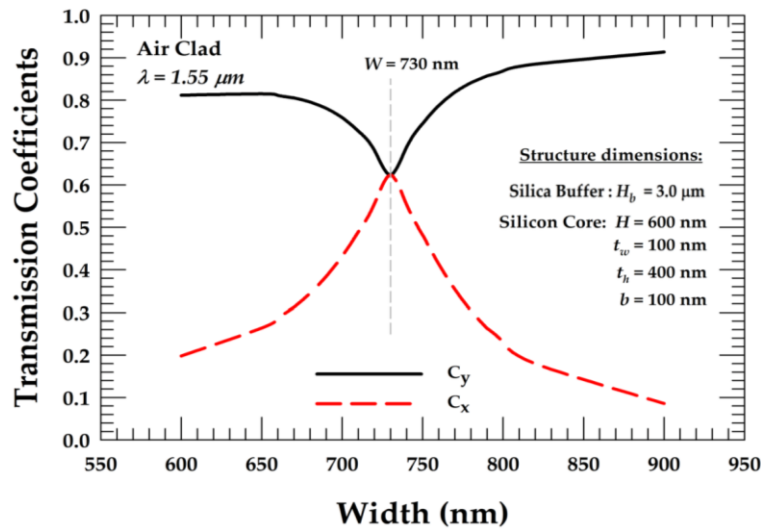


*Fig. 5.9. Variations of the transmitted modal coefficients  $C_x$  and  $C_y$ , with  $W$ , for the TE mode.*

The transmitted modal coefficients,  $C_y$  and  $C_x$  of the  $H_y^{11}$  and  $H_x^{11}$  modes, respectively, were calculated and the variations of these two modal coefficients with  $W$ , are shown in Fig. 5.9. It can be seen that as  $W$  reduces, the modal coefficient of the transmitted  $H_x^{11}$  polarized fundamental mode,  $C_x$ , reaches a maximum value of 0.6236 at  $W = 730$  nm and then reduces to 0.198 at  $W = 600$  nm where the hybridness is low. It is also shown that the modal coefficient of the transmitted quasi-TE polarized fundamental mode,  $C_y$ , reaches its minimum value of 0.6234 as  $W$  reduces to 730 nm where the hybridness is at its highest. For a system where 100% polarization rotation can be achieved without any power loss, these two values are expected to be equal to  $1/\sqrt{2}$ , indicating that each mode is carrying equal and half of the total power (50% of the total input optical power). Hence in this case, at the mode degeneracy condition, since the modal coefficient of both the modes are similar, the power carried by each of them is also similar and here the total power

loss is found to be only 1.09 dB, which is very small. Reflections from both the butt-coupled interfaces were small, with the reflection coefficient less than 2%.

As these two polarized modes travel along the single trench section waveguide, the polarization states of these two modes will be continuously rotated due to the phase difference between them. From the modal coefficients and their full vectorial field profiles, the polarization conversion can be calculated. At a distance  $L_\pi$ , the polarization state will be fully rotated, i.e. an incident TE mode will transform to a TM mode and this can be further guided unchanged in a butt-coupled standard Si waveguide with vertical side walls. The variations of the polarization conversion with  $W$ , is shown in Fig. 5.10 (a). The fraction of TE power converted to TM ( $P_x$ ) is shown by a solid line. The amount of TE power remain unconverted ( $P_y$ ) is shown by a dashed line. It can be clearly seen that, as  $W$  increases from 600 nm, the normalized power conversion of TE ( $P_y$ ), to TM ( $P_x$ ), reaches a maximum value of 0.9947 (almost 100% of the TE power is converted into TM power) at  $W = 730$  nm and then reduces as  $W$  increases further. With  $\pm 10$  nm tolerance from the maximum power conversion at the optimum width, the power conversion is found to be 0.9467 when  $W = 720$  nm and 0.9557 when  $W = 740$  nm and this shows that the polarization conversion only decreases by about 5% for a derivation of  $\pm 10$  nm from the desired optimum width.

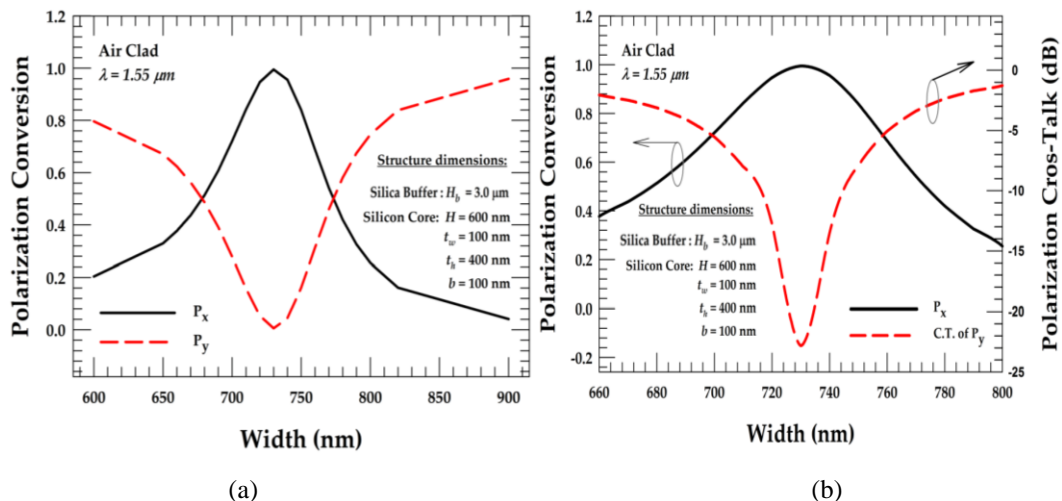


Fig. 5.10. (a) Variations of the polarization conversion and (b) variations of polarization cross-talk and polarization conversion with  $W$ .

Along the polarization rotator, the power  $P_y$  of the TE polarized mode is incident at the junction between two interfaces and most of the power will be

converted into TM polarized mode  $P_x$  at the end of this section. However there may remain some power from  $P_y$ : here this normalized residual power  $P_y$  is referred to as the polarization crosstalk. In this study, the polarization crosstalk is defined as the unwanted polarized power (in this case  $P_y$ ), normalized to the total input power, which remains at the end of the single-trench waveguide. The variation of the polarization crosstalk with  $W$  is shown in Fig. 5.10 (b), for  $W > 600$  nm. It can be observed in here that as  $W$  increases from 660 nm, polarization cross-talk starts to decrease and reaches a minimum value, as  $W$  starts to deviate away from  $W$  of the minimum cross-talk value, cross-talk starts to increase until it reaches a value of -1.275 dB at  $W = 800$  nm. It is again shown here that at this 730 nm optimum width, the crosstalk reaches a minimum value of -22.82 dB, a very low value. It can be observed that with  $\pm 10$  nm derivation from the optimum width, only 80% of polarization conversion (TE to TM) will occur and that the crosstalk values are found to be -13.54 dB and -12.73 dB when the widths are at 740 nm and 720 nm respectively.

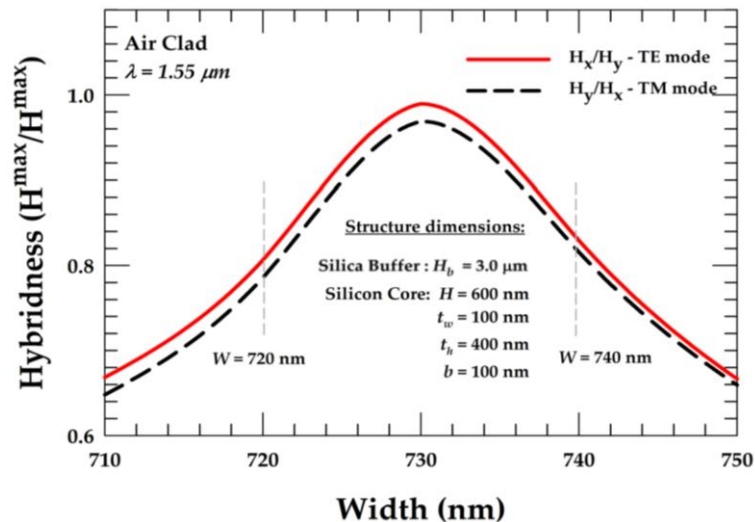
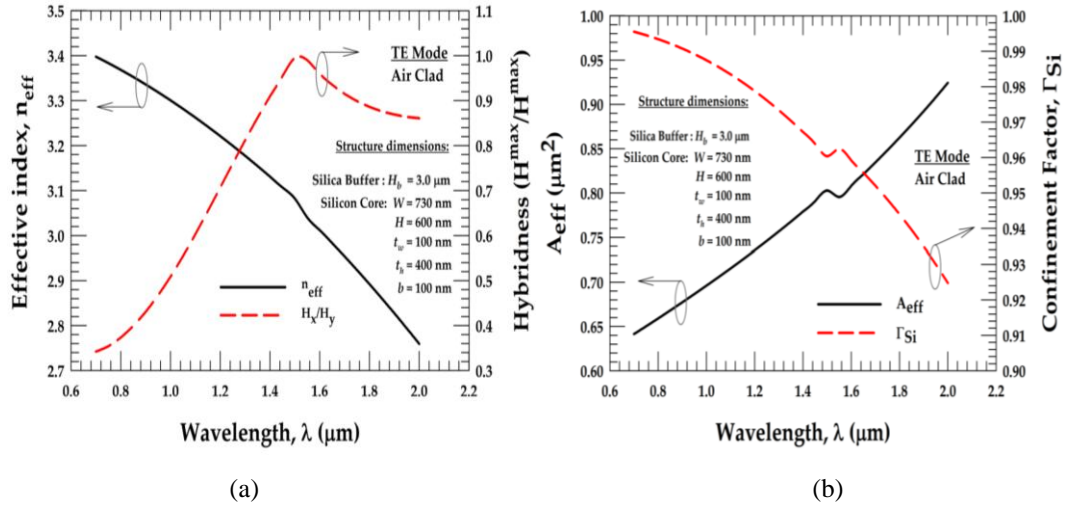


Fig. 5.11. Variations of the hybridness with  $W$ , from 710 nm to 750 nm for the fundamental TE and TM modes.

However with  $\pm 10$  nm derivation from the optimum width as shown in Fig. 5.11 for the variation of the hybridness with  $W$  for the quasi-TE mode. Its hybridness at the  $\pm 10$  nm derivation from the optimum width, are found to be 0.80 and 0.83 when the widths are at 720 nm and 740 nm respectively.



**Fig. 5.12.** (a) Variations of  $n_{eff}$  and hybridness and (b) variations of  $A_{eff}$ , and  $\Gamma_{Si}$  with  $\lambda$  for quasi-TE mode.

The  $L_{\pi}$  and the modal hybridness are also depend on the operating wavelength. The variations of the  $n_{eff}$  and the hybridness with  $\lambda$  for the quasi-TE mode with  $W = 730$  nm are shown in Fig. 5.12 (a). It can be observed that for the  $n_{eff}$ , it slowly reduces as  $\lambda$  increases. It can also be seen that hybridness increases as wavelength increases until the hybridness reaches its maximum value of 0.995 with the  $n_{eff} = 3.08215$  at  $\lambda = 1.50$   $\mu\text{m}$ . At this wavelength, 99 % of TE power is converted into TM power, however as  $\lambda$  increases further, the power conversion will then be reduced.

The variations of the  $A_{eff}$ , and  $\Gamma_{Si}$  with the  $\lambda$  are shown in Fig. 5.12 (b). It is shown in here that as  $\lambda$  increases, the power intensity of the waveguide contained in the Si core decreases. However, it is not the case for the  $A_{eff}$ , it can be seen that as  $\lambda$  increases, the  $A_{eff}$  of the waveguide also increases. It can be observed that there is a small step change in the  $\lambda$  region of 1.50  $\mu\text{m}$  and 1.55  $\mu\text{m}$ , it is found that at this region, the polarization state of the modes transform from one dominant polarization state to the other in which TE mode will be converted into TM mode.

When the operating length is changed from 1550 nm to 1450 nm, the resulting modal hybridness,  $L_{\pi}$ , polarization conversion and polarization cross-talk are found to be 0.94, 54  $\mu\text{m}$ , 94% and -11.83 dB, respectively and for  $\lambda = 1650$  nm, these values were 0.92, 39  $\mu\text{m}$ , 92% and -10.80 dB, respectively.

### 5.4.3 LATERAL OFFSET ANALYSIS

It was evident that the spatial field profiles of the straight section waveguide and the single trench polarization rotator waveguide are different; in particular the field profile of the single trench polarization rotator had a smaller width and was off-centre due to the presence of the trench. It has often been assumed by others (and also so far in the above section) that the input strip waveguide is of the same width as that of the polarization rotator waveguide section and their two vertical end side-walls are exactly aligned. However, it does not need to be, rather, by employing an offset, the fields in both sides of the junction can be matched even better. Therefore, the different lateral shifts between the guides are introduced to study the effect on the polarization rotation and also on the insertion loss.

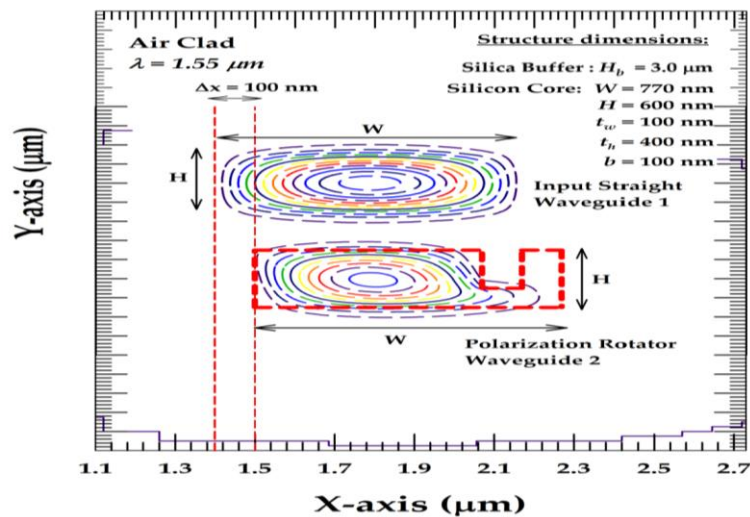


*Fig. 5.13. Illustrations of the performance of the straight-to-polarization rotator coupled waveguide with offsets,  $\Delta x = 100$  nm.*

To do so, first, an offset ( $\Delta x$ ) is introduced where the input straight side-wall waveguide is shifted to the left when coupling to the single-trench waveguide to enhance the field matching. In this example,  $W$  is taken as 770 nm,  $\Delta x$  is taken as 100 nm and it is shown in Fig. 5.13 how this  $\Delta x$  can be introduced. It can be observed that the location of the field maximum of the straight waveguide is now better aligned with that of the single-trench waveguide when  $\Delta x$  is introduced. In this case, the transmitted modal coefficients of the  $H_y^{11}$  and  $H_x^{11}$  modes were found to be 0.703 and 0.634, respectively, which yield 98.47% conversion with the polarization crosstalk value slightly deteriorated to reach a value of around -18.16 dB. However,

the loss in this case was found to be 0.47 dB, which represents a reduction of almost 50% in the power loss, when compared to the original design without  $\Delta x$ .

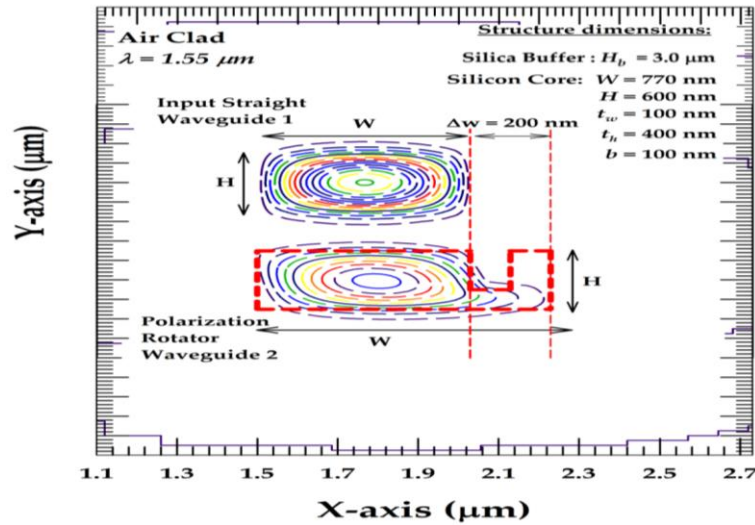


Fig. 5.14. Illustrations of the performance of the straight-to-polarization rotator coupled waveguide with offsets,  $\Delta w = 200$  nm.

An alternative offset ( $\Delta w$ ) method has also been studied, where the  $W$  of the input straight side-wall waveguide is reduced to improve the mode matching. Figure 5.18 shows how this particular  $\Delta w$  can be achieved. The width of the straight side-wall waveguide is reduced by  $\Delta w$ , with the single-trench waveguide width kept at 730 nm. It can be observed in Fig. 5.14 that although the straight side-wall is reduced by 200 nm to 530 nm, overall their field profiles match much better. Using the LSBR method, the transmitted modal coefficients of the  $H_y^{11}$  and  $H_x^{11}$  modes were found to be 0.698 and 0.681, respectively. The maximum polarization conversion of the TE to TM was found to be 99.42% (again a very high value) but the loss was found to be only 0.21 dB, a significantly smaller value when compared to the loss without  $\Delta w$  and with equal width at 730 nm. The crosstalk in this case was also found to be similar to the value of crosstalk when no lateral offset was applied, with its value at -22.38 dB.

## 5.5 SUMMARY

In this chapter, a compact polarization rotator based on an asymmetric Si nanowire has been presented. The rigorous full VFEM was used to characterize such structures with very strong modal hybridness. Such a compact asymmetric waveguide with its vertical side wall is easy to fabricate when compared to the other asymmetric polarization rotators with slanting side walls. It was found that more than 99% of polarization conversion can be obtained for a device length of 48  $\mu\text{m}$  in such a design with the power loss as 1.09 dB. However, such loss did not include the scattering loss described previously in Chapter 4 [Vlasov and McNab, 2004], therefore, an additional 0.02 dB loss have to be added (assuming 5 dB/cm loss on the waveguide) into this loss found for the polarization rotator. Therefore the power loss would be 1.11 dB. It is also shown that the power loss is only 0.21 dB by optimizing the offset between the sections, in which total power loss would be 0.23 dB.

This design compares favourably with the recent polarization rotator designs reported recently [Correia, et. al., 2003] [Watts and Haus, 2005] [Deng, et. al, 2006] [Holmes and Hutchings, 2006] [Augustin, et. al., 2007] [Feng, et. al, 2007] [Fukuda, et. al, 2008] [Wang and Dai, 2008]. In this case slightly larger Si dimensions are considered, in which most of the power was confined in the Si core for their conversion process and the propagation loss near the degeneration point would be reduced and also when a 100 nm slot is introduced, the slot mode would be avoided. The design approach used here avoids the slanted side wall and curved waveguide, such approach is more suitable to fabricate by using conventional CMOS technique but additional double etching steps would be required in the fabrication process. However, more specific system requirements may be obtained and optimized, including the effects of fabrication tolerances as required.

# 6

# Silicon Slot Waveguides

## 6.1 INTRODUCTION

In recent years, there has been a gradual increase of investment into the research of Si photonic technology based on SOI platform. With SOI technology, it is possible to develop Si based PIC systems that includes ring resonators, arrayed waveguide filters, hybrid silicon lasers, Mach-Zehnder interferometer silicon modulators, detectors and biosensors. There is the potential to reduce power consumption, size, and cost; also it can increase the functionality and reliability of the PIC. SOI is also said to be 100% compatible with complementary metal-oxide-semiconductor (CMOS) technology, which is already widely employed in the electronic industry. For SOI technology, PICs fabricated in Si can take the advantage of CMOS technology to develop and create next generation of low cost and high performance optoelectronic devices for both photonics and electronics. In Si photonics, most conventional waveguides are of strip and rib structures. In these waveguides, light is strongly concentrated in the high-index material, which can be the Si core, in which, light can confine in the cross-section of the Si core with dimensions of around 200 nm x 260 nm and with similar optical mode sizes.

Lately, one variant of such silicon waveguide, the slot-waveguides [Almeida *et al.*, 2004] has attracted considerable attention because of its ability to enhance the optical intensity in a low refractive index area. The slot-waveguide structure can

guide and confine light in a nano-scale low refractive index material (or in air) which is situated between the two strips of Si or similar high index material, at a scale that cannot be achieved by conventional strip or rib waveguides. The boundary condition at the dielectric interfaces demands tangential electric and magnetic fields to be continuous across the interface. It also demands normal component of  $\mathbf{B}$  to be continuous, but as permeability was considered to be constant (equal to 1) for all the dielectric materials, this component is also continuous. However, as permittivity is different across the dielectric interface, the continuity of the  $D_n$  would increase the  $E_n$ , the normal component of the electric-field ( $\mathbf{E}$ -field) in the low refractive index slot region than The  $E_n$  field in the high refractive index Si cores. As a result, ultra high optical power density can also be achieved in the slot region. Such high power intensity can be exploited for designing various non-linear devices such as the four wave mixing (FWM) in silicon waveguides. If the slots are placed vertically,  $E_x$  field would be normal to the interface and being the dominant component for the quasi-TE mode, this polarization would carry higher power in the slot region. On the other hand, if the slot is placed horizontally, the  $E_y$  field would be normal to the dielectric interfaces, and this being the dominant component of the quasi-TM mode, a higher power would be confined in the slot region for this polarization. Both the horizontal [Sun *et al.*, 2007] and vertical [Vivien *et al.*, 2008] type of slots waveguide have been reported, including the use of electro-optic [Ding *et al.*, 2010] or gain medium [Robinson *et al.*, 2008] in the slot area. It was also reported that, such waveguide's structure can be used for designing optical sensors [Dell'Olio *et al.*, 2007], in which the high power density in slot region can be exploited to get maximum interaction from the sensing medium. More recently electro-optic polymers were also used in a slot waveguide to design high speed electro-optic modulator [Leuthold *et al.*, 2009 and Preston *et al.*, 2009].

In this chapter, the characteristics of a Si slot waveguide with nano-scale cross section are thoroughly investigated. For analysing such a waveguide, an accurate and efficient VFEM is employed here to calculate the propagation constant and the full-vectorial electric and magnetic modal field profiles of the waveguide. Optimization of the power confinement and the power density in the slot area have also been carried out and presented here.

## 6.2 ANALYSIS OF THE VERTICAL SLOT WAVEGUIDE

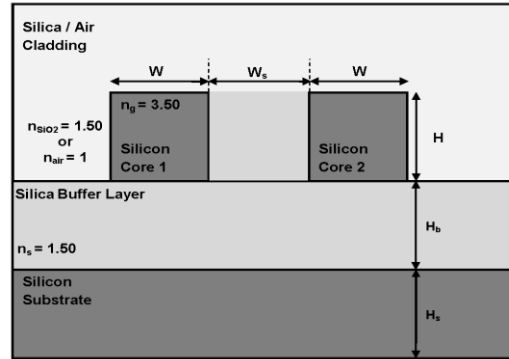


*Fig. 6.1. 2D Schematic cross-section of Si vertical slot nano-waveguide.*

The structure being considered here is a conventional Si slot optical waveguide. The 2D schematic cross-section of the Si slot nano-waveguide is shown in Fig. 6.1. This single slot waveguide is based on a low refractive index slot region between two high-index Si strip guides. The slot can be generally formed of low-index air or porous Si, nonlinear organic material, electro-optic polymer material or SiO<sub>2</sub> and the whole structure is then be covered by either SiO<sub>2</sub> or polymer if necessary. This waveguide can be fabricated by using a SOI wafer on a Si substrate. A resist mask with a slot can be used on the surface of the Si guiding layer and the selected surface Si layer may then be etched down to the SiO<sub>2</sub> layer (buffer layer) by inductively coupled plasma (ICP) dry etcher to form the two Si strip waveguides and the slot region simultaneously. Then the waveguide can either be buried under a thick SiO<sub>2</sub> or polymer layer or left surrounded with air. Such waveguide will be rigorously study in the later sections.

### 6.2.1 MODAL SOLUTION OF VERTICAL SLOT WAVEGUIDE

To the study of modal field profile of the Si slot waveguide (SSW) shown in Fig. 6.1, the **H**-field based VFEM has been used. For this study, the symmetric geometry of the structure has been exploited and only half of the structure is considered for simulation. The structure was discretized using more than 80,000 first order triangular elements.

For the quasi-TE mode, the  $H_y$  field component is dominant, and  $H_x$  and  $H_z$  are the non-dominant components. The dominant  $H_y$  field component of the  $H_y^{11}$  mode is shown in Fig. 6.2 (a) for a waveguide with width,  $W = 225$  nm and height,  $H = 220$  nm with the slot width,  $W_s = 50$  nm. The 3D contour plot of the  $H_y$ -field with one half of the structure is also shown in Fig. 6.2 (a) as an inset. The dashed-line showed in Fig. 6.2 (a) represents the boundary of the Si core.

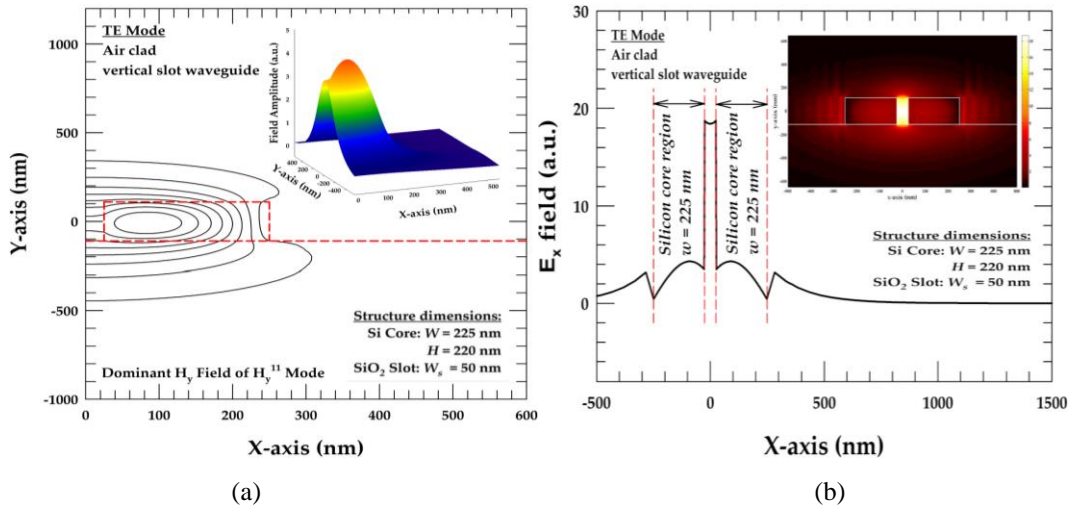


**Fig. 6.2.** (a) The dominant  $H_y$  field profile and (b) variations of the  $E_x$  field along the X axis for the  $H_y^{11}$  mode.

It can be seen in the figure that the field profile shows that the maximum intensity is not located exactly at the centre of the Si core. It is shown in here that the maximum intensity occurs close to the boundary between the Si waveguide and the SiO<sub>2</sub> slot, and when the separation is small, a strong  $H_y$  field exists in the low-index slot region. It can be observed that the field extends more into the SiO<sub>2</sub> buffer layer underneath when compared to the upper air cladding region with a low index. In the contour field plot, it can be seen that the main peak is in the Si core with a pronounced field magnitude in the slot area. It was noted that as  $W$ , increases, the mode gets better confined in the isolated strip waveguide, the coupling between the strips reduces and the dominant  $H_y$  field component is shifted toward to the center of the Si strip waveguide, similar to that of an isolated guide. When the width of the Si waveguide becomes very large, the field in the slot region will decrease, and particularly when width of the slot is also large, its maximum intensity will be concentrated at the centre of the two constituent Si strip waveguides.

The contour field profile for the  $E_x$  field of the quasi-TE mode is shown in Fig. 6.2 (b), where the Si core waveguide is also outlined by the dashed-lines. The  $E_x$  field along the X-axis, shows that at the Si/SiO<sub>2</sub> interface the field increases abruptly in the SiO<sub>2</sub> region. Therefore Fig. 6.2 (b) shows that there is a very strong  $E$ -field in the slot-separation region, compared to that in the Si strip regions.

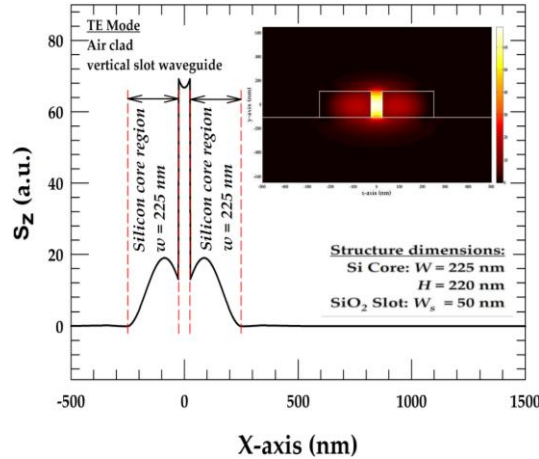
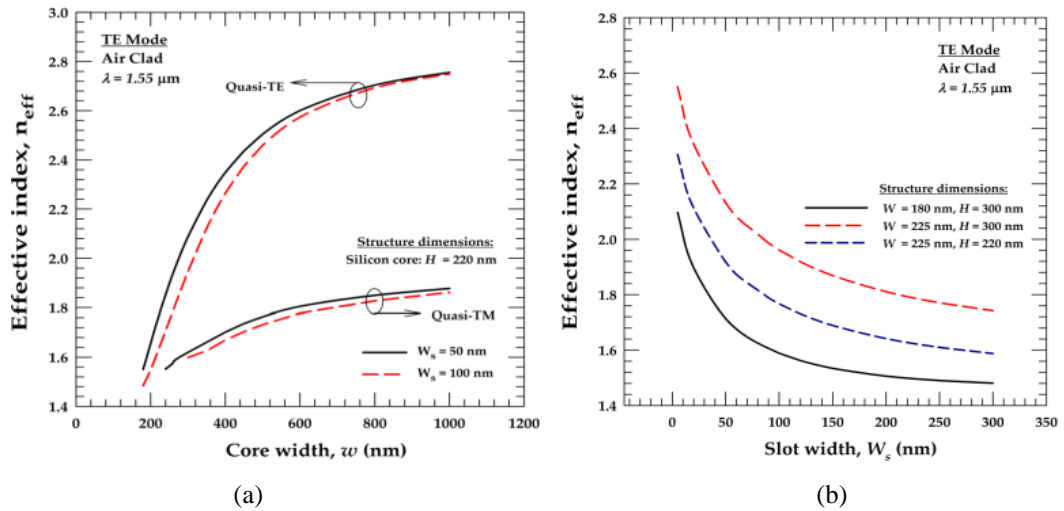


Fig. 6.3. Variations of the  $S_z$  field along the X axis for the  $H_y^{11}$  mode.

From the full vectorial  $\mathbf{E}$  and  $\mathbf{H}$  fields, the Poynting Vector ( $S_z$ ) may be calculated and Fig. 6.3 shows the contour of the  $S_z$  intensity profile. It is shown that the  $S_z$  intensity is primarily concentrated in the low index SiO<sub>2</sub> slot-separation region and it is much higher than that in the high index Si strips region. Such a high power in low-index cladding region, outside the high-index strip will allow access to a higher evanescent field, suitable for compact optical sensor design. It also shown that there is a small discontinuity step at the Si/SiO<sub>2</sub> interface and it decays more quickly in the Si core. The slot area can also be filled up by nonlinear or electro-optic materials to exploit the high power density in this area.

For a compact PIC design, it is necessary to reduce the height of the SSW to its acceptable minimum value. It was widely suggested that a silicon slab with 220 nm thickness would be able to guide light and that in industry, SOI with the height of 220 nm is already fabricated to use as industry standard for various devices. Subsequently in the this study, a SSW with height,  $H = 220$  nm is concentrated for a rigorous analysis

## 6.2.2 EFFECTS OF EFFECTIVE INDEX



**Fig. 6.4.** (a) Variations of  $n_{eff}$  with  $W$  for different  $W_s$  for quasi-TE and TM modes. (b) Variations of  $n_{eff}$  with  $W_s$  for different structure dimension for TE modes

Figure 6.4 (a) shows the variations of the effective index,  $n_{eff}$  with the width ( $W$ ) for the fundamental quasi-TE and TM modes for the air-cladding of the Si slot waveguides, with slot separation widths ( $W_s$ ) of 50 nm and 100 nm shown by solid and dashed-line, respectively. It is shown here that as the core width increases, the  $n_{eff}$  increases for both quasi-TE and TM modes. It can also be observed that for quasi-TE modes, the  $n_{eff}$  for both  $W_s$  are significantly higher than the quasi-TM modes. In which, for  $H = 220 \text{ nm}$ , both  $W_s$  wide waveguides are very much polarization dependence, therefore to eliminate the polarization dependence, a very wide core has to be used. It can be noted in here that for  $H = 220 \text{ nm}$ , quasi-TM modes reaches the cut-off condition for the core width much earlier than when  $H = 300 \text{ nm}$  shown in Fig. 6.4 (b).

## 6.2.3 POWER CONFINEMENT AND DENSITY VARIATIONS

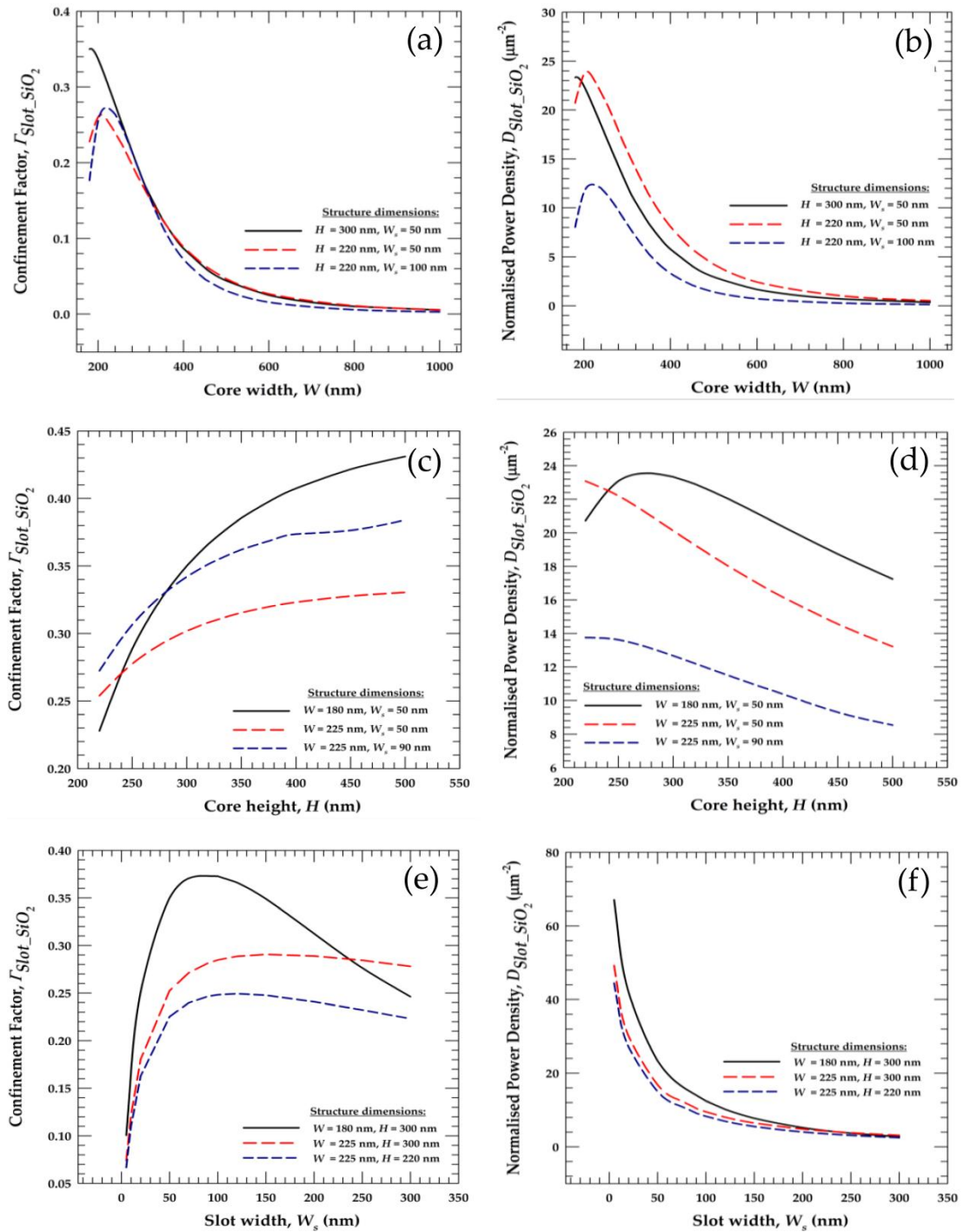


Fig. 6.5. Variations of confinement factor in slot,  $\Gamma_{\text{Slot\_SiO}_2}$ , and power density,  $D_{\text{Slot\_SiO}_2}$ , with different scenarios for the vertical slot waveguide .

The power confinement in silica slot is an important parameter to optimize for the design of various device applications when the slot area is completely filled with

electro-optic, non-linear or active materials. Therefore the variations of the power confinement in the silica slot region,  $\Gamma_{Slot\_SiO_2}$ , with the width,  $W$ , are shown in Fig. 6.5 (a) for quasi-TE modes for three different slot waveguide parameters. When the width of the Si strip,  $W$ , is large, the Si core is wide enough to confine the light in isolated Si waveguides. It can be observed that as the width,  $W$ , is reduced, the power confinement in the slot region increases, however, for a very smaller waveguide core, the  $\Gamma_{Slot\_SiO_2}$  reduces very rapidly. It is shown in here that maximum  $\Gamma_{Slot\_SiO_2}$  can be realized by using a thicker waveguide as this is shown by a solid line.

The variations of the confinement factor in the silica slot region,  $\Gamma_{Slot\_SiO_2}$ , for three different slot waveguide scenarios are shown in Fig. 6.5 (c). It is shown that as the core height,  $H$  of the waveguide increases; the  $\Gamma_{Slot\_SiO_2}$  also increases. For a narrow waveguide with a small  $W_s$  (as  $W = 180$  nm,  $W_s = 50$  nm) its reaches its cut-off height at  $H = 220$  nm faster than the other waveguide parameters.

Figure 6.5 (e) shows the variations of the  $\Gamma_{Slot\_SiO_2}$  with the slot width,  $W_s$ . It can be clearly seen in here that  $\Gamma_{Slot\_SiO_2}$  reaches a maximum value with  $W_s$  for a narrow and thicker waveguide ( $W = 180$  nm,  $H = 300$  nm)

The variations of the normalized power density,  $D_{Slot\_SiO_2}$  in the slot region with the width,  $W$ , for different slot waveguide parameters for the quasi-TE mode are shown in Fig. 6.5 (b). It is suggested that  $D_{Slot\_SiO_2}$  can be a very important parameter to optimize when designing a sensor application, in particular when the localized high power density is exploited, such as by applying a thin sensing layer in the slot region. It is shown in here that as  $W$  decreases, initially, the power density in the slot increases, reaches their maximum values and then rapidly decreases. It can be observed in Fig. 6.5 (b) that a high power confinement in the slot area can be achieved by utilizing a thicker waveguide

The variation of the  $D_{Slot\_SiO_2}$  with the core height is shown in Fig. 6.5 (d). It can be observed that for  $W = 180$  nm and  $W_s = 50$  nm, shown by a solid curve, initially  $D_{Slot\_SiO_2}$  increases as the height,  $H$  decreases and reaches a maximum value, however as the thickness of the waveguide is further reduced, the  $D_{Slot\_SiO_2}$  decreases. It can be seen that for a wider waveguide, as shown by a dashed-line for

the case of  $W = 225$  nm and  $W_s = 50$  nm, the  $D_{Slot\_SiO_2}$  in the slot region reaches its peak value at a lower waveguide thickness. However on the other hand, when the slot width,  $W_s$  is increased,  $D_{Slot\_SiO_2}$  is much lower, which is due to the increase of the slot area.

Finally the variations of the  $D_{Slot\_SiO_2}$  with the slot-separation,  $W_s$ , for the quasi-TE modes are shown in Fig. 6.5 (f). It is found that the mode is closer to the cut-off mode when the  $W_s$  become large. This is due to the fact that as the isolated mode gets weakly confined in the Si core in which the field mode spreads more outward of the Si core, and as a consequence, the power confinement in the slot region reaches its lowest value. However it can be observed that when  $W_s$  is reduced, more power is confined in the slot region, along with that, as the slot area is reduced, the  $D_{Slot\_SiO_2}$  increases exponentially. Maximization of the  $D_{Slot\_SiO_2}$  is important for sensing applications, where a thin layer of sensing medium would have a stronger effect. However, fabrication of a slot width below 100 nm is often not so easy and present fabrication process may also yield slant side wall angle, which can enhance the polarization cross-talk [Somasiri *et al.*, 2003].

### 6.3 ANALYSIS OF THE HORIZONTAL SLOT WAVEGUIDE

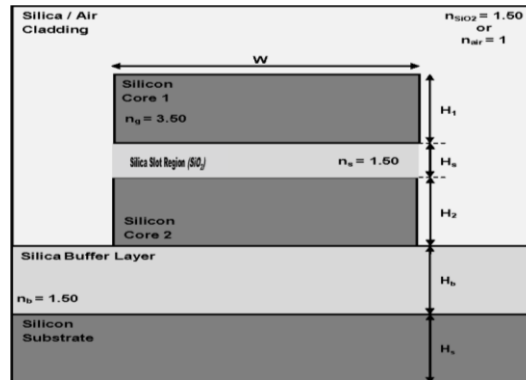


Fig. 6.6. 2D Schematic cross-section of Si horizontal slot nano-waveguide.

A single slot horizontal waveguide has also been investigated and reported here. The schematic for the single slot waveguide is shown in Fig. 6.6. In here, the dimensions of such waveguide are of widths,  $W = 350$  nm and  $\text{SiO}_2$  buffer layer of  $H_b = 1.5$   $\mu\text{m}$ . Initially, a height,  $H = 190$  nm are set for the two silicon cores ( $H_1$  and  $H_2$ ) with a fixed slot height,  $H_s = 100$  nm is considered. This single slot horizontal waveguide is based on a low refractive index,  $\text{SiO}_2$  slot sandwiched between two symmetric high-index Si core guides. The overall waveguide is then can be surrounded by either  $\text{SiO}_2$  or air. This particular waveguide can be fabricated by using a SOI wafer on a Si substrate. The horizontal low index slot can be fabricated by layered deposition or thermal oxidation [Almeida *et al.*, 2004]. It is described earlier that due to the high index contrast at the interface, the normal component of the  $\mathbf{E}$  field undergoes large discontinuity therefore enhancing the field in the slot region. By optimising the dimension of the waveguide structure, the maximum field confinement in the slot area can be achieved in which applications such as chemical and biochemical sensor can be designed to use with such structure.

### 6.3.1 MODAL ANALYSIS FOR QUASI-TM MODE

In the case of a horizontal slot waveguide, the  $E_y$  field is dominant. Therefore the contour plot of the  $E_y$  field for the  $H_x^{11}$  mode is shown in Fig. 6.7 (a), where the Si horizontal waveguide is also outlined. It is clearly shown that due to the large index contrast at interfaces, the normal electric field undergoes a large discontinuity, which results in a field enhancement in the low-index region (which in this case it is in the silica slot region), where the  $E_y$  field is located.

In this case, heights of the two Si layers were taken to be equal. For air-clad horizontal slot waveguide, the field profile is not symmetric along the vertical direction due to the structural asymmetry. However, if needed, the heights of the two Si layer can be unequal and optimized for any particular application.

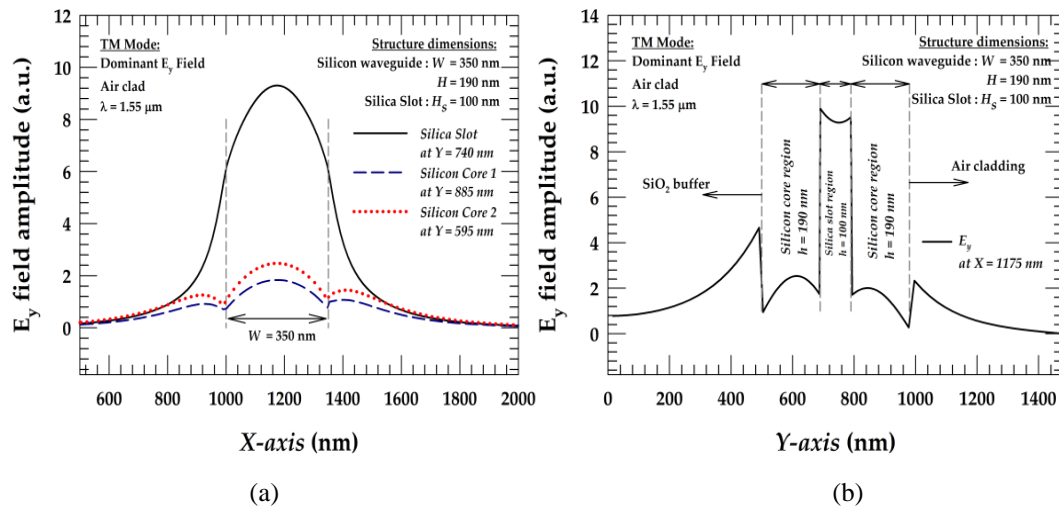


Fig. 6.7. Variations of  $E_y$  field along (a) X-axis or (b) Y-axis for the  $H_x^{11}$  mode.

The variations of the  $E_y$  field along the X-axis are shown in Fig. 6.7 (a), it can be observed that the  $E_y$  field is continuous at the interface between Si/Air along the centre of the Si core. It is also shown in here that the magnitude of  $E_y$  field (shown by a solid line) is the highest in the silica slot region which suggests that most of the  $E_y$  field is confined in this area. For the  $E_y$  field along the Y-axis as shown in Fig. 6.7 (b), it can be observed that the magnitude of  $E_y$  at the Si/SiO<sub>2</sub> interface increases abruptly with a step change in the ratio of  $(3.5/1.5)^2 = 5.44$  in the SiO<sub>2</sub> region.

The Poynting Vector ( $S_z$ ) intensity field profile is shown in Fig. 6.8. It is shown that the  $S_z$  intensity is primarily concentrated in the low index  $\text{SiO}_2$  slot-separation region and it is much higher than that in the high index Si core region. It is also shown that there is a discontinuity step at the Si/ $\text{SiO}_2$  interface.

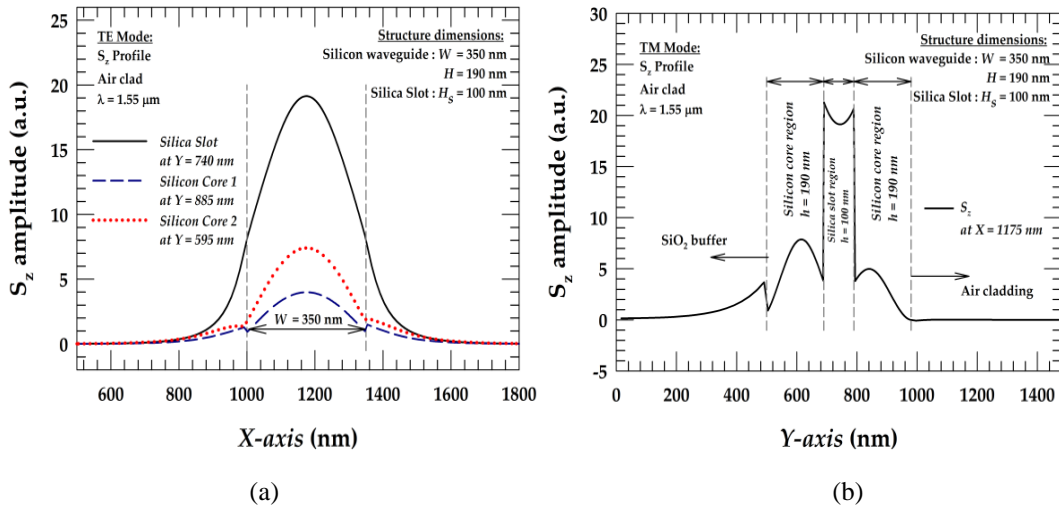
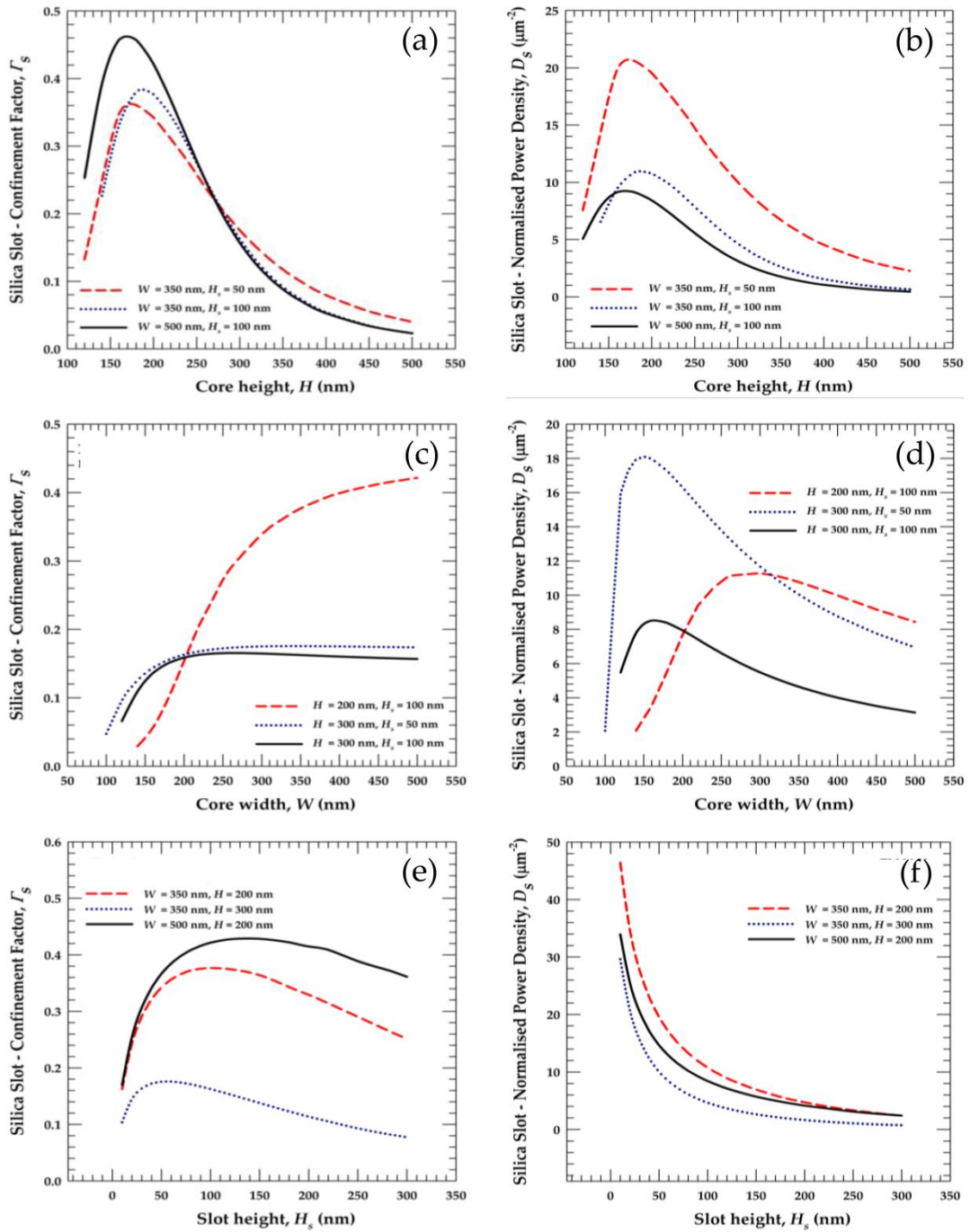


Fig. 6.8. Variations of  $S_z$  field profile along (a) X-axis or (b) Y-axis.

It can be seen in Fig. 6.8 (a) that most of the field intensity is inside the  $\text{SiO}_2$  slot area as show in the graph of the variations of the  $S_z$  intensity along the X-axis. It can also be observed that Fig. 6.8 (b) shows the  $S_z$  intensity along the Y-axis and it shows that the  $S_z$  is at its maximum inside the slot area. It can be noted that  $S_z$  has a normalised magnitude value of 20 inside the slot region.

## 6.3.2 EFFECTS OF POWER CONFINEMENT AND DENSITY



**Fig. 6.9.** Variations of confinement factor in slot,  $\Gamma_s$ , and power density,  $D_s$ , with different scenarios for the horizontal slot waveguide.

It is found that for the TM mode, the field is strongly coupled when the slot is small, therefore, power confinement in the slot region can be very high. The power confinement of the waveguide slot filled with  $\text{SiO}_2$  is shown in Fig. 6.9 (a) when the core height is varied. It is shown that the field will be better confined when

waveguide is wide and larger than its height. The power confinement in slot with the variations of core height,  $H$ , with different widths and slot heights are also shown in Fig. 6.9 (a). In here it is shown that when the thickness of the waveguide is small but with a larger width, as in the case of  $W = 350$  nm and  $H_s = 50$  nm (shown by a solid line), the power confinement in the slot is high.

Figure 6.9 (c) shows the variation of power confinement in the SiO<sub>2</sub> slot area with the core width for three different parameters. It can be observed that for  $H = 200$  nm and  $H_s = 100$  nm (shown by a dashed-line), it shows that as  $W$  increases, the power confinement in the slot increases. As the height of the waveguide is increased to 300 nm (shown by a solid line), power confinement will increase as  $W$  increases, at  $W = 200$  nm, power confinement in the slot area will remain constant as  $W$  is increased further, similar observation can be made for  $H = 300$  nm and  $H_s = 50$  nm (shown by a dotted line).

Figure 6.9 (e) shows the variation of power confinement in the SiO<sub>2</sub> slot area with the slot height for three different parameters. It can be observed that initially power confinement increases as the slot height,  $h_s$  increases and reaches a maximum value, however as the  $H_s$  is further increased, the power confinement in the slot area decreases. It can be seen that for a wider core waveguide with smaller  $H$  as in the case of  $W = 500$  nm and  $H = 200$  nm (shown by a solid line). It has a higher power confinement in the slot area, when the waveguide  $W$  is reduced to 350 nm (shown by a dashed-line), power confinement in the slot area is reduced. However for a narrower waveguide with a larger thickness as in the case of when  $W = 350$  nm and  $H = 300$  nm (shown by a dotted line), the power confinement in the slot area has reduced substantially.

The variation of power density in the SiO<sub>2</sub> slot area with the core height is shown in Fig. 6.9 (b). For core width,  $W = 350$  nm and slot height,  $H_s = 50$  nm (shown by a dashed-line) in particular, it will have a high power density in the slot region when the core height,  $H$ , is in the region between 150 nm to 200 nm, as  $H$  increases, the power density in the slot decreases, this can be exploited in the design of optical sensors or modulators (by incorporating electro-optic material inside the slot area).

The variation of power density in the SiO<sub>2</sub> slot area with the core width is shown in Fig. 6.9 (d). It can be observed that power density increases as the  $W$  decreases. For the core height,  $H = 300$  nm and slot height,  $H_s = 50$  nm (shown by a dotted line), it will have a high power density in the slot region when the core width,  $W$ , is at 150 nm. As the core is reduced, a sudden drop of power density can be noticed as the core width is approaching to the cut-off width for this fundamental quasi-TM mode. It can also be observed that, when the slot height is increased to 100 nm (shown by a solid line), the maximum power density is reduced approximately 40% of the from the maximum power density achieved by the waveguide with slot height as 50 nm (shown by a dotted line).

Figure 6.9 (f) shows the variation of power density in the SiO<sub>2</sub> slot area with the slot height. It can be seen that for a narrower Si core waveguide with a thinner height as in the case of Si core width,  $W = 350$  nm and height,  $H = 200$  nm (shown by a dashed-line), it will have a high power density in the slot region when the slot height,  $H_s$ , is below 50 nm, as  $H$  increases (shown by a dotted line), the power density in the slot decreases. It is also shown that for a wider Si core waveguide with a smaller height (shown by a solid line), power density will not be as high as the narrower Si core waveguide with a thinner height (shown by a dashed-line)

## **6.4 SUMMARY**

The **H**-field and **E**-field components of both vertical and horizontal slot waveguides along with their Poynting vector profile are shown in this Chapter. It is showed here that slot area with a lower refractive index, normal component of **E**-field increases significantly and as a consequence, the power density will be high. By introducing different geometry dimensions of the silicon waveguide, the performances on power confinement and power density in the slot area can be improved and optimized. Such a slot waveguide can be used to design very compact directional coupler and Mach-Zehnder based system or for polarization splitters or polarization rotators. Design of modulators or optical switches or second harmonic generation can also be considered by introducing a nonlinear material in the slot region.

# 7

## Conclusion and further work

This chapter draws conclusion from previous chapter and presents a proposal for further research.

### 7.1 CONCLUSION

This research focuses on designing and characterising the waveguides used for silicon photonics devices. The objectives set out at the beginning of the study have been successfully met and presented in this research. The fundamental of this research was based on using accurate and efficient numerical methods to rigorously characterise different types of optical waveguides for use in silicon photonics devices and study their propagation properties.

Firstly, Chapter 2 presented the basic and fundamental background of the numerical methods those were used in this research work. The numerical methods described here are the vector **H**-field Finite Element Method (VFEM), the Finite Element based Beam Propagation Method (BPM) and the Least Square Boundary Method (LSBR). Initially, the VFEM was described. This technique has been established as one of the most accurate and efficient numerically efficient approaches to obtain the modal field profiles and propagation constants of the fundamental and higher order quasi-TE and TM modes. It has been described in this chapter that for

optical waveguide analysis, the magnetic field vector  $\mathbf{H}$  is naturally continuous across the dielectric interfaces and the associated natural boundary condition is that of an electric wall, which is very convenient to implement in many practical waveguide problems. For this  $\mathbf{H}$ -field formulation, the domain discretization, shape functions, natural boundary conditions and the formation of the element and global matrices are also evaluated in this chapter. With this  $\mathbf{H}$ -field formulation, the appearance of spurious (non-physical) modes along with the real physical modes cannot not be avoided. Therefore in order to eliminate the non-physical or spurious solution, the penalty function method is employed into the formulation by imposing a constraint ( $\nabla \cdot \mathbf{H} = \mathbf{0}$ ). Such a modal solution method can also be applied to determine the initial field distribution profile for the analysis of the waveguide discontinuities by using the LSBR method or the BPM. The BPM based on the finite element technique has also been presented in this chapter. The incorporation of the perfectly matched layer boundary condition into the vectorial wave equations, in which the vectorial propagation algorithm can account for the polarisation dependence and coupling has also been shown. Such vectorial BPM is based on the transverse magnetic field components, which were used to simulate the evolution of a given initial field profile and to calculate the propagation power and propagation loss. Finally the LSBR method is described for use to analyse the discontinuities in optical waveguides. It is described in this chapter that by using the scattering coefficients, the power transfer between two waveguides can be calculated in which the insertion loss is found by using the LSBR method.

In the design of photonics integrated circuit (PIC), multiple optical components such as ring resonators, arrayed waveguide filters or laser are integrated into one single chip. In order to interconnect all the individual optical components, straight or/and bent waveguides have to be used. Chapter 3 looked at these straight and bent waveguides based on Indium Gallium Arsenide Phosphide (InGaAsP) on top of the Indium Phosphide (InP) substrate in detail. The study of the bending, insertion and bent propagation losses and polarization conversion in a high index contrast semiconductor optical waveguide was presented in this chapter. Initially, a typical rib waveguide with InP cap layer was analysed. It has been found in this chapter that for a rib waveguide with height of 1.3  $\mu\text{m}$ , zero birefringence is possible when the waveguide's width and height are almost the same. For curved optical

waveguides, the conformal transformation method has been employed to represent bent waveguides by converting a curved dielectric waveguide to its equivalent straight waveguide with a modified index profile. It has been shown that at the junction of a straight and bent waveguides, higher order modes and mode beating have been generated. By using the BPM, leakage loss of a bent waveguide can be found, it has been described in this chapter that the average loss value for the bent waveguide is about 0.74 dB/mm between the axial distances of 4000  $\mu\text{m}$  to 5000  $\mu\text{m}$ . It has been found that power do exchange between the two polarization states, therefore the polarization conversion, the power losses and the bending losses have been investigated. It has been shown that a reduction in the bending radius increases the modal loss and the associated transition loss also increases as the mode shape modifies significantly in the bent waveguide. By using both a narrower input guide and by introducing an appropriate offset, the transition losses and polarization conversion of the waveguide can be reduced.

Currently most large scaled PICs are fabricated using materials such as Gallium Arsenide (GaAs), Lithium Niobate ( $\text{LiNbO}_3$ ) and Indium Phosphide (InP). For optical system design, the cross-section of optical waveguide devices built by these materials are often in the micron dimensions. Nowadays, with the advances in technology and fabrication technique. It is possible to design and develop low-cost photonic devices that allowed for the waveguide core to be shrunk down to a submicron cross-section and such technology exists in the form of silicon (Si) photonics. Chapter 4 was devoted to a Si strip waveguide based on the silicon-on-insulator (SOI) platform. It has been described that Si strip waveguide is the most basic important building blocks used in many PIC systems. It has also been described that Si strip waveguide can be referred as Si nanowire. The aim of this chapter was to provide a novel comprehensive analysis defining the modal characteristics of a Si strip waveguide with a nanoscale cross-section, and in doing so, the effects of the critical size of such waveguide were also presented. In this chapter, the spatial variations of all the six components of the  $\mathbf{E}$  and  $\mathbf{H}$  fields were shown, together with the poynting vector profile. It has been shown that for a Si strip waveguide with a height of 260 nm, the single mode operation occurred when the waveguide width lied between the region of 200 nm to 400 nm for the wavelength of 1550 nm. The modal hybridness, the power confinement and the

modal birefringence for silica and air-clad Si nanowires were also shown here. It has also been shown that non-dominant field components are significantly higher, (often more than 50%), in which case the simpler scalar approaches would be totally inadequate. It was found that when  $H = 260 \text{ nm}$ , the effective area not only is minimum, when  $W = 320 \text{ nm}$ , but also these values are similar for both the polarizations.

In Chapter 5, a novel compact polarization rotator based on an asymmetric Si nanowire has been presented. The Si polarization rotator proposed here shown a very compact design which does not need a slanted side wall or a curved waveguide, and thus require a less complex fabrication process and compatible with mature CMOS technology which was backed by the well-established semiconductor industry. It has been described that modes in optical waveguides with two-dimensional confinement are hybrid in nature, with all the components of their  $\mathbf{E}$  and  $\mathbf{H}$  fields being present. It has been shown that this modal hybridness becomes more prominent as the index contrast increases, as in a Si nanowire. At the beginning of the chapter, the VFEM has been used to find the modal solutions followed by the LSBR method to calculate the scattering coefficients at the junction. The Si polarization rotator considered was based on the use of a single section asymmetrical silicon waveguide with a trench section butt-coupled between two standard input/output Si strip waveguides. It has been shown that it was important to design a polarization rotator waveguide that can rotate an incoming TE wave to the polarized TM wave. It was found that more than 99% of polarization conversion can be obtained for a compact device length of  $48 \mu\text{m}$  with a low power loss (which include an assume scattering loss) of 1.11 dB in such a design can be realised. It has also been shown that the total power loss was only 0.23 dB by optimizing the offset between the sections.

Chapter 6 focuses on the vertical and horizontal slot waveguides. The foundation of the Si slot waveguide was based on a strip waveguide and the basic fundamental of the Si strip waveguide was described in Chapter 4. In Chapter 6, the  $\mathbf{H}$ -field and  $\mathbf{E}$ -field components of both vertical and horizontal slot waveguides along with their Poynting vector profile are presented in this Chapter. It has been shown that slot area with a lower refractive index,  $|\mathbf{E}|$  increases significantly and that

power density will be high. It has been shown that for vertical slot waveguide, quasi-TE mode will yield higher power confinement and power density in the slot area. It has also been shown that for horizontal slot waveguide, quasi-TM was found to have higher power density and power confinement than the quasi-TE mode. By introducing different geometry dimensions of the Si waveguide, the performances on power confinement and power density in the slot area can be improved and optimized.

## **7.1 SUGGESTIONS FOR FURTHER WORK**

The Si slot waveguide (presented in Chapter 6) can be used as a compact directional coupler or Mach-Zehnder based systems or for polarization splitters or polarization rotators. By introducing a nonlinear material in the slot region of the waveguide (shown in Fig 6.1 or 6.27), modulators, optical switches and second or third harmonic generators can also be realised using this structure. It was reported that by employing erbium-doped low-index material in the optical fibre, amplification of light can be achieved at the telecommunication wavelength. A similar approach can be adopted for Si slot waveguide, in which using the doped material such as Er doped SiO<sub>2</sub> in the slot region, an amplifier based on Si slot waveguide can be designed.

Coupling a nano Si waveguide to an another PIC device or to a single mode fibre remains one of the major challenges in building nano-Si photonics devices. This is due to the mismatch of the core dimensions, for example, coupling to and from optical fibres that have a core dimension of typically around 8  $\mu\text{m}$ . It was shown in Chapter 4 that for a Si strip waveguide with a single mode operation condition, a cross-sectional dimension was found to be around 320 nm x 260 nm, therefore high coupling losses will exist with direct coupling of Si strip waveguide with the optical fibre. Various solutions have been proposed and demonstrated, one of which that can be considered for future work is the design of a spot-size converter incorporating a tapered Si core or an inverted tapered section. Another approach is to use Bragg gratings based couplers with Si waveguides, whereby exploiting the high index contrast of a Si waveguide, optical modes under the Bragg conditions in

Si waveguides can be strongly coupled. However such a technique is strongly polarisation sensitive and can only be applicable to polarisation dependent applications such as interconnects and sensors. A 2-dimensional Bragg grating can be considered to couple both TE and TM modes. The beam profile generated by Bragg grating coupler is not exactly a Gaussian mode therefore it is necessary to improve the beam shape. Apodized grating can be considered to improve the beam profile for better coupling but this requires multiple masking steps in the fabrication process. In order to reduce the masking steps, segment core waveguide section with different effective indices can be designed to be used so that fabrication of such grating can be made by using only one masking step.

Design of a PIC with a polarization diversity system that consists of polarization rotator and polarization splitter with Bragg grating spot-size converter for coupling input or output optical fibre can be considered. The polarization rotator can be based on the Si asymmetric strip polarization rotator with a single trench section presented in Chapter 5 and the polarization splitter can be based on the vertical slot waveguide described in Chapter 6 designed as a directional coupler. Both of these devices can be fabricated by using the CMOS technology with monolithic integration. So a polarization diversity system with improved coupling and any functional devices, such as amplifier, modulator or sensor can be considered for further detailed investigation.

# Appendix A

## Calculation of the Element Matrices in FEM

The elements matrices of  $[A]_e$  and  $[B]_e$  from equations 2.51 and 2.52 are evaluated here:

Equation 2.51 shown that:

$$[A] = \sum_{e=1}^n [A]_e = \sum_{e=1}^n \int_{\Omega} \varepsilon^{-1} [Q]^* [Q] \partial\Omega$$

Therefore

$$[A]_e = \varepsilon^{-1} \int_{\Omega} [Q]^* [Q] \partial\Omega$$

$$= \int_{\Omega} \varepsilon^{-1} \begin{bmatrix} -\beta^i [N]^T [N] + \frac{\partial [N]^T}{\partial y} \frac{\partial [N]}{\partial y} & -\frac{\partial [N]^T}{\partial y} \frac{\partial [N]}{\partial x} & j\beta [N]^T \frac{\partial [N]}{\partial x} \\ \frac{\partial [N]^T}{\partial x} \frac{\partial [N]}{\partial y} & -\beta^i [N]^T [N] + \frac{\partial [N]^T}{\partial x} \frac{\partial [N]}{\partial x} & j\beta [N]^T \frac{\partial [N]}{\partial y} \\ j\beta \frac{\partial [N]^T}{\partial x} [N] & j\beta \frac{\partial [N]^T}{\partial y} [N] & \frac{\partial [N]^T}{\partial y} \frac{\partial [N]}{\partial y} + \frac{\partial [N]^T}{\partial x} \frac{\partial [N]}{\partial x} \end{bmatrix} \partial\Omega \quad (A1.1)$$

Equation 2.52 shown that

$$[B] = \sum_{e=1}^n [B]_e = \sum_{e=1}^n \int_{\Omega} \mu [N]^T [N] \partial\Omega$$

Therefore

$$[B]_e = \mu \int_{\Omega} [N]^T [N] \partial\Omega$$

$$= \mu \int_{\Omega} \begin{bmatrix} [N]^T [N] & [0]^T [0] & [0]^T [0] \\ [0]^T [0] & [N]^T [N] & [0]^T [0] \\ [0]^T [0] & [0]^T [0] & [N]^T [N] \end{bmatrix} \partial\Omega \quad (A1.2)$$

The integration of the shape functions in equations A1.1 and A1.2 can be evaluated for a triangular element using the following relation:

$$\int_{\Omega} N_1^i N_2^j N_3^k \partial\Omega = \frac{i!j!k!2!}{(i+j+k+2)!} A_e \quad (\text{A1.3})$$

where  $A_e$  is the area of the triangular element.

Hence the following integrals can be obtained:

$$\int_{\Omega} N_1^2 \partial\Omega = \int_{\Omega} N_2^2 \partial\Omega = \int_{\Omega} N_3^2 \partial\Omega = \frac{A_e}{6} \quad (\text{A1.4})$$

$$\int_{\Omega} N_1 N_2 \partial\Omega = \int_{\Omega} N_2 N_3 \partial\Omega = \int_{\Omega} N_1 N_3 \partial\Omega = \frac{A_e}{12} \quad (\text{A1.5})$$

$$\int_{\Omega} \partial\Omega = A_e \quad (\text{A1.6})$$

Therefore from equation A1.1, some of the 9 x 9  $[A]_e$  elements matrix can be given as:

$$[A]_{e(1,1)} = \frac{1}{\varepsilon} \int_{\Omega} -j\beta N_1^2 + \left( \frac{\partial N_1}{\partial y} \right)^2 \partial\Omega = \frac{1}{\varepsilon} \left[ \frac{-\beta^2 A_e}{6} + c_1^2 A_e \right] \quad (\text{A1.7})$$

$$[A]_{e(1,2)} = \frac{1}{\varepsilon} \int_{\Omega} -j\beta N_1 N_2 + \frac{\partial N_1}{\partial y} \frac{\partial N_2}{\partial y} \partial\Omega = \frac{1}{\varepsilon} \left[ \frac{-\beta^2 A_e}{12} + c_1 c_2 A_e \right] \quad (\text{A1.8})$$

$$[A]_{e(1,4)} = \frac{1}{\varepsilon} \int_{\Omega} \frac{-\partial N_1}{\partial y} \frac{\partial N_1}{\partial x} \partial\Omega = \frac{1}{\varepsilon} c_1 b_1 A_e \quad (\text{A1.9})$$

From equation A1.2, some of the 9 x 9  $[B]_e$  elements matrix can also be given as:

$$[B]_{e(1,1)} = \mu \int_{\Omega} N_1^2 \partial\Omega = \mu \frac{A_e}{6} \quad (\text{A1.10})$$

$$[B]_{e(1,2)} = \mu \int_{\Omega} N_1 N_2 \partial\Omega = \mu \frac{A_e}{12} \quad (\text{A1.11})$$

$$[B]_{e(1,4)} = 0 \quad (\text{A1.12})$$

# Appendix B

## Calculation of the Element Matrices in BPM

The elements matrices of  $[M]_e$  and  $[K]_e$  from equations 2.79 and 2.80 are evaluated here:

Equation 2.79 shown that:

$$[M]_{6 \times 6} = \sum_e [M]_e = \sum_e \begin{bmatrix} [M_{xx}]_{3 \times 3} & [0]_{3 \times 3} \\ [0]_{3 \times 3} & [M_{yy}]_{3 \times 3} \end{bmatrix}$$

Therefore matrices  $[M_{xx}]$  and  $[M_{yy}]$  have the same forms as:

$$[M_{xx}] = [M_{yy}] = n^{-2} \begin{bmatrix} \int_e N_1^2 ds & \int_e N_1 N_2 ds & \int_e N_1 N_3 ds \\ \int_e N_2 N_1 ds & \int_e N_2^2 ds & \int_e N_2 N_3 ds \\ \int_e N_3 N_1 ds & \int_e N_3 N_2 ds & \int_e N_3^2 ds \end{bmatrix} \quad (\text{A2.1})$$

Equation 2.80 shown that:

$$[K]_{6 \times 6} = \sum_e [K]_e = \sum_e \begin{bmatrix} [K_{xx}]_{3 \times 3} & [K_{xy}]_{3 \times 3} \\ [K_{yx}]_{3 \times 3} & [K_{yy}]_{3 \times 3} \end{bmatrix}$$

Also the matrices  $[K_{xx}]$  and  $[K_{yy}]$  can be arranged in the form as:

$$[K_{xx}] = [K_u] + [K_{xx}]_{\Gamma_e} \quad (\text{A2.2})$$

$$[K_{yy}] = [K_u] + [K_{yy}]_{\Gamma_e} \quad (\text{A2.3})$$

where

$$\begin{aligned}
 [K_{\mu}] &= k_0^2 \begin{bmatrix} \int_e N_1^2 ds & \int_e N_1 N_2 ds & \int_e N_1 N_3 ds \\ \int_e N_2 N_1 ds & \int_e N_2^2 ds & \int_e N_2 N_3 ds \\ \int_e N_3 N_1 ds & \int_e N_3 N_2 ds & \int_e N_3^2 ds \end{bmatrix} - n^{-2} \alpha_y^2 \begin{bmatrix} \int_e N_{1y}^2 ds & \int_e N_{1y} N_{2y} ds & \int_e N_{1y} N_{3y} ds \\ \int_e N_{2y} N_{1y} ds & \int_e N_{2y}^2 ds & \int_e N_{2y} N_{3y} ds \\ \int_e N_{3y} N_{1y} ds & \int_e N_{3y} N_{2y} ds & \int_e N_{3y}^2 ds \end{bmatrix} \\
 &- n^{-2} \alpha_y^2 \begin{bmatrix} \int_e N_{1x}^2 ds & \int_e N_{1x} N_{2x} ds & \int_e N_{1x} N_{3x} ds \\ \int_e N_{2x} N_{1x} ds & \int_e N_{2x}^2 ds & \int_e N_{2x} N_{3x} ds \\ \int_e N_{3x} N_{1x} ds & \int_e N_{3x} N_{2x} ds & \int_e N_{3x}^2 ds \end{bmatrix}
 \end{aligned} \tag{A2.4}$$

where  $N_{ix}$  and  $N_{iy}$  denotes the  $x$  and  $y$  derivatives of the shape function  $N_i$ , respectively.

The matrices  $[K_{xx}]_{\Gamma_e}$  and  $[K_{yy}]_{\Gamma_e}$  are related to the line integrals and can be expressed as:

$$[K_{xx}]_{\Gamma_e} = n^{-2} \alpha_x^2 \begin{bmatrix} \oint_{\Gamma_e} N_1 N_{1x} n_x d\Gamma_e & \oint_{\Gamma_e} N_1 N_{2x} n_x d\Gamma_e & \oint_{\Gamma_e} N_1 N_{3x} n_x d\Gamma_e \\ \oint_{\Gamma_e} N_2 N_{1x} n_x d\Gamma_e & \oint_{\Gamma_e} N_2 N_{2x} n_x d\Gamma_e & \oint_{\Gamma_e} N_2 N_{3x} n_x d\Gamma_e \\ \oint_{\Gamma_e} N_3 N_{1x} n_x d\Gamma_e & \oint_{\Gamma_e} N_3 N_{2x} n_x d\Gamma_e & \oint_{\Gamma_e} N_3 N_{3x} n_x d\Gamma_e \end{bmatrix} \tag{A2.5}$$

$$[K_{yy}]_{\Gamma_e} = n^{-2} \alpha_y^2 \begin{bmatrix} \oint_{\Gamma_e} N_1 N_{1y} n_y d\Gamma_e & \oint_{\Gamma_e} N_1 N_{2y} n_y d\Gamma_e & \oint_{\Gamma_e} N_1 N_{3y} n_y d\Gamma_e \\ \oint_{\Gamma_e} N_2 N_{1y} n_y d\Gamma_e & \oint_{\Gamma_e} N_2 N_{2y} n_y d\Gamma_e & \oint_{\Gamma_e} N_2 N_{3y} n_y d\Gamma_e \\ \oint_{\Gamma_e} N_3 N_{1y} n_y d\Gamma_e & \oint_{\Gamma_e} N_3 N_{2y} n_y d\Gamma_e & \oint_{\Gamma_e} N_3 N_{3y} n_y d\Gamma_e \end{bmatrix} \tag{A2.6}$$

The matrices  $[K_{xy}]$  and  $[K_{yx}]$  can also be expressed:

$$[K_{xy}] = [K_1] - [K_2] + [K_{xy}]_{\Gamma_e} \tag{A2.7}$$

$$[K_{yx}] = [K_2] - [K_1] + [K_{yx}]_{\Gamma_e} \tag{A2.8}$$

where

$$[K_1] = n^{-2} \alpha_x \alpha_y \begin{bmatrix} \int_e N_{1y} N_{1x} ds & \int_e N_{1y} N_{2x} ds & \int_e N_{1y} N_{3x} ds \\ \int_e N_{2y} N_{1x} ds & \int_e N_{2y} N_{2x} ds & \int_e N_{2y} N_{3x} ds \\ \int_e N_{3y} N_{1x} ds & \int_e N_{3y} N_{2x} ds & \int_e N_{3y} N_{3x} ds \end{bmatrix} \quad (A2.9)$$

$$[K_2] = n^{-2} \alpha_x \alpha_y \begin{bmatrix} \int_e N_{1x} N_{1y} ds & \int_e N_{1x} N_{2y} ds & \int_e N_{1x} N_{3y} ds \\ \int_e N_{2x} N_{1y} ds & \int_e N_{2x} N_{2y} ds & \int_e N_{2x} N_{3y} ds \\ \int_e N_{3x} N_{1y} ds & \int_e N_{3x} N_{2y} ds & \int_e N_{3x} N_{3y} ds \end{bmatrix} \quad (A2.10)$$

$$[K_{xy}]_{\Gamma_e} = n^{-2} \alpha_x \alpha_y \begin{bmatrix} \oint_{\Gamma_e} N_1 N_{1y} n_x d\Gamma_e & \oint_{\Gamma_e} N_1 N_{2y} n_x d\Gamma_e & \oint_{\Gamma_e} N_1 N_{3y} n_x d\Gamma_e \\ \oint_{\Gamma_e} N_2 N_{1y} n_x d\Gamma_e & \oint_{\Gamma_e} N_2 N_{2y} n_x d\Gamma_e & \oint_{\Gamma_e} N_2 N_{3y} n_x d\Gamma_e \\ \oint_{\Gamma_e} N_3 N_{1y} n_x d\Gamma_e & \oint_{\Gamma_e} N_3 N_{2y} n_x d\Gamma_e & \oint_{\Gamma_e} N_3 N_{3y} n_x d\Gamma_e \end{bmatrix} \quad (A2.11)$$

$$[K_{yx}]_{\Gamma_e} = n^{-2} \alpha_x \alpha_y \begin{bmatrix} \oint_{\Gamma_e} N_1 N_{1x} n_y d\Gamma_e & \oint_{\Gamma_e} N_1 N_{2x} n_y d\Gamma_e & \oint_{\Gamma_e} N_1 N_{3x} n_y d\Gamma_e \\ \oint_{\Gamma_e} N_2 N_{1x} n_y d\Gamma_e & \oint_{\Gamma_e} N_2 N_{2x} n_y d\Gamma_e & \oint_{\Gamma_e} N_2 N_{3x} n_y d\Gamma_e \\ \oint_{\Gamma_e} N_3 N_{1x} n_y d\Gamma_e & \oint_{\Gamma_e} N_3 N_{2x} n_y d\Gamma_e & \oint_{\Gamma_e} N_3 N_{3x} n_y d\Gamma_e \end{bmatrix} \quad (A2.12)$$

The shape functions integrals included in the calculation of the element matrices  $[M]_e$  and  $[K]_e$  can be evaluated using the following relation:

$$\int_e N_1^i N_2^j N_3^k ds = \frac{i! j! k! 2!}{(i+j+k+2)!} A_e \quad (A2.13)$$

$$\int_{\Gamma_{12}} N_1^i N_2^j d\Gamma_e = \frac{i! j!}{(i+j+1)!} l_{12} \quad (A2.14)$$

where  $A_e$  is the area of the triangular element related to the nodal coordinates of the element, and  $\Gamma_{12}$  and  $l_{12}$  are the part and length of the element boundary connecting the nodes 1 and 2, respectively.

# Appendix C

## Author's Publications & Conferences Proceedings

### JOURNAL ARTICLES

Leung, D. M. H.; Kejalakshmy, N.; Rahman, B. M. A.; and Grattan, K. T. V.; ,  
“Rigorous Numerical Analysis and Characterization of a Silicon Vertical-Slot Nano-  
Waveguide,” *Journal of Nonlinear Optical Physics and Materials*, March 2012.

Leung, D. M. H.; Rahman, B. M. A.; Kejalakshmy, N.; and Grattan, K. T. V.; ,  
“Rigorous Full-Vectorial Solutions of Photonics Nanowires,” *Selected Topics in  
Quantum Electronics, IEEE Journal of* , vol.17, no.4, pp.952-959, July 2011.

Leung, D. M. H.; Rahman, B. M. A.; Kejalakshmy, N.; and Grattan, K. T. V.; ,  
“Characterization of silicon nanophotonic devices using the finite element method,”  
*Optical and Quantum Electronics, Springer Netherlands*, vol.42, no.8, pp.499-509,  
July 2011.

Leung, D. M. H.; Rahman, B. M. A.; and Grattan, K. T. V.; , “Numerical Analysis of  
Asymmetric Silicon Nanowire Waveguide as Compact Polarization Rotator,”  
*Photonics Journal, IEEE* , vol.3, no.3, pp.381-389, June 2011.

Leung, D. M. H.; Kejalakshmy, N.; Rahman, B. M. A.; and Grattan, K. T. V.; ,  
“Rigorous modal analysis of silicon strip nanoscale waveguides,” *Opt. Express*,  
vol.18, no.8, pp.8528-8539, April 2010.

Kejalakshmy, N.; Agrawal, A.; Aden, Y.; Leung, D. M. H.; Rahman, B. M. A.; and Grattan, K. T. V.; , “Characterization of silicon nanowire by use of full-vectorial finite element method,” *Appl. Opt.*, vol.49, no.16, pp.3173-3181, June 2010.

Rahman, B. M. A.; Leung, D. M. H.; Obayya, S. S. A.; and Grattan, K. T. V.; , “Numerical analysis of bent waveguides: bending loss, transmission loss, mode coupling, and polarization coupling,” *Appl. Opt.*, vol.47, no.16, pp.2961-2970, June 2008.

## CONFERENCE PROCEEDINGS

Rahman, B. M. A.; Leung, D. M. H.; Ahsan, S. N.; Koshy, K.; Tan, P.; and Grattan, K. T. V.; , “Light guidance through void: silicon slot waveguides and their rigorous characterization,” *Proc. SPIE* , SPIE Photonics West, USA, Jan. 2012.

Rahman, B. M. A.; Leung, D. M. H.; Kan, X. B.; Grattan, K. T. V.; and Kejalakshmy, N.; , “Optimizing the power confinement in silicon slot waveguides by use of Finite Element Method,” *Asia Communications and Photonics Conference and Exhibition (ACP)*, Shanghai China, Nov. 2011.

Rahman, B. M. A.; Leung, D. M. H.; and Grattan, K. T. V.; , “Rigorous characterization of silicon nanowires and slot waveguides,” *2011 SBMO/IEEE MTT-S INTERNATIONAL MICROWAVE AND OPTOELECTRONICS CONFERENCE*, Brazil, Oct. 2011.

Rahman, B. M. A.; Leung, D. M. H.; and Grattan, K. T. V.; , “Full-vectorial analysis on silicon nanowires and devices,” *8th International Symposium on Modern Optics and Its Applications (ISMOA)*, Bandung July 2011.

Rahman, B. M. A.; Leung, D. M. H.; Namassivayane, K.; Koshy, K.; Jiang, Z. J.; Law, A.; Ahmed H.; and Grattan, K. T. V.; , “Rigorous characterization of silicon nanowires and nanophotonic devices,” *Proc. SPIE* , SPIE Photonics West, USA, Jan. 2011.

Rahman, B. M. A.; Leung, D. M. H.; Kejalakshmy, N.; and Grattan, K. T. V.; ,  
“Rigorous numerical simulations of nanophotonic devices by use of the finite  
element method,” *PHOTONICS 2010 International Conference on fiber optics and  
photonics*, Indian Institute of Technology Guwahati, India, Dec. 2010.

Rahman, B. M. A.; Leung, D. M. H.; Tanvir, H.; Ashraf, M. A.; Kejalakshmy, N.;  
and Kabir, R.; , “Characterization of silicon nanowires,” *Electrical and Computer  
Engineering (ICECE), 2010 International Conference on Electrical and Computer  
Engineering*, pp.438-441, Dec. 2010.

Rahman, B. M. A.; Leung, D. M. H.; Kejalakshmy, N.; and Grattan, K. T. V.; ,  
“Finite element solutions of nanophotonics devices,” *International Conference of  
Numerical Analysis and Applied Mathematics 2010 (ICNAAM 2010)*, Greece, Sept.  
2010.

Rahman, B. M. A.; Leung, D. M. H.; Tanvir, H.; Ashraf, M. A.; Kejalakshmy, N.;  
Agrawal, A.; Kabir, R.; and Grattan, K. T. V.; , “Characterization of nanoscale  
silicon photonic devices,” in *Integrated Photonics Research, Silicon and  
Nanophotonics, OSA Technical Digest (CD) (Optical Society of America, 2010)*,  
paper IWH7, Integrated Photonics Research, Silicon and Nanophotonics (IPRSN),  
Monterey, Canada, July 2010.

Rahman, B. M. A.; Leung, D. M. H.; Tanvir, H.; Ashraf, M. A.; Kejalakshmy, N.;  
Kabir, R.; and Grattan, K. T. V.; , “Rigorous characterization of silicon nanowire for  
compact nanophotonic devices,” *Proc. SPIE 7719*, 77191A (2010); SPIE Photonics  
Europe 2010.

Rahman, B. M. A.; Leung, D. M. H.; Obayya, S. S. A.; and Grattan, K. T. V.; ,  
“Bending loss, transition loss, mode coupling, and polarization coupling in bent  
waveguides,” *Proc. SPIE 6996*, 69960O (2008); SPIE Photonics Europe 2008.

# References

- Ahmed, S., “Finite Element Method for Waveguide Problems,” *Electron. Lett.*, vol. **4**, pp. 381-389, 1968.
- Albares, D. J., and Soref, R. A., “Silicon-on-sapphire waveguides,” *Proc. SPIE: Integrated Optical Circuit Engineering IV*, vol. **704**, pp. 24 -25, 1987.
- Alferness, R. C., and Buhl, L. L., “High-speed waveguide electro-optic polarization modulator,” *Opt. Lett.*, vol. **7**, pp. 500-502, 1982.
- Almeida, V. R., Xu, Q., Barrios, C. A., and Lipson, M., “Guiding and confining light in void nanostructure,” *Opt. Lett.*, vol. **29**, pp. 1209-1211, 2004.
- Angkaew, T., Matsuhara, M., and Kumagai, N., “Finite-element analysis of waveguide modes: A novel approach that eliminates spurious modes,” *IEEE Trans. Microw. Theory Tech.*, vol. MTT-**35**, no. 2, pp. 117–123, 1987.
- Augustin, L. M., van der Tol, J. J. G., Geluk, E. J., Smit, M. K., “Short Polarization Converter Optimized for Active–Passive Integration in InGaAsP–InP,” *IEEE Photon. Technol. Lett.*, vol. **19**, no.20, pp.1673-1675, Oct. 2007.
- Baets R., and Lagasse, P. E., “Loss calculation and design of arbitrarily curved integrated-optic waveguides,” *J. Opt. Soc. Am.*, vol. **73**, pp. 177-182, 1983.
- Bardeen, J., and Brattain, W. H., “The Transistor, A Semi Conductor Triode,” *Phys. Rev.*, vol. **74**, pp. 230-231, 1948.
- Barrios, C. A., Almeida, V. R., Panepucci, R., and Lipson, M., “Electrooptic Modulation of Silicon-on-Insulator Submicrometer-Size Waveguide Devices,” *J. Lightwave Technol.*, vol. **21**, pp. 2332-, 2003.
- Bathe, K. J., *Finite Element Procedures in Engineering Analysis*, Englewood Cliffs, NJ, Prentice-Hall, 1982.
- Berenger, J. P., “A perfectly matched layer for the absorption of electromagnetic-waves,” *J. Computational Physics*, vol. **114**, no. 185, 1994.

- Berenger, J. P., "Three-dimensional perfectly matched layer for the absorption of electromagnetic waves," *J. Computational Physics*, vol. **127**, no. 363, 1996.
- Berglund, W., and Gopinath, A., "WKB analysis of bend losses in optical waveguides," *J. Lightw. Technol.*, vol. **18**, pp. 1161-1166, 2000.
- Berk, A., "Variational principles for electromagnetic resonators and waveguides," *IEEE Trans. Antennas Propag.*, vol. **4**, no.2, pp.104-111, April 1956.
- Bestwick, T., "ASOCTM-a silicon-based integrated optical manufacturing technology," *Electronic Components & Technology Conference*, 1998. 48th IEEE , vol., no., pp. 566-571, May 1998.
- Bienstman, P., Six, E., Roelens, M., Vanwolleghem, M., and Baets, R., "Calculation of bending losses in dielectric waveguides using eigenmode expansion and perfectly matched layers," *IEEE Photon. Technol. Lett.*, vol. **14**, pp. 164-166, Feb. 2002.
- Boyraz, O., and Jalali, B., "Demonstration of a silicon Raman laser," *Opt. Express*, vol. **12**, pp. 5269-5273, 2004.
- Brooke, G. H., and Kharadly, M. M. Z., "Step discontinuities on dielectric waveguides," *Electron. Lett.* , vol. **12**, no.18, pp. 473-475, Sep. 1976.
- Brooks, C., Jessop, P. E., Deng, H., Yevick, D. O., and Tarr, G., "Passive silicon-on-insulator polarization-rotating waveguides," *Opt. Eng.*, vol. **45**, 044603, 2006.
- Chan, S. P., Png, C. E., Lim, S. T., Reed, G. T., Passaro, V. M. N., "Single-mode and polarization-independent silicon-on-insulator waveguides with small cross section," *J. Lightwave Technol.*, vol. **23**, no. 6, pp. 2103- 2111, 2005.
- Chung, Y., and Dagli, N., "An assessment of finite difference beam propagation method," *IEEE J. Quantum Electron.*, vol. **26**, no.8, pp. 1335-1339, Aug 1990.
- Claps, R., Dimitropoulos, D., Han, Y., and Jalali, B., "Observation of Raman emission in silicon waveguides at 1.54  $\mu\text{m}$ ," *Opt. Express*, vol. **10**, pp. 1305-1313, 2002.

- 
- Cloutier, S. G., Kossyrev, P. A., and Xu, J., “Optical gain and stimulated emission in periodic nanopatterned crystalline silicon,” *Nat. Materials*, vol. **4**, pp. 887-891, 2005.
  - Clough, R. W., “The finite element method in plane stress analysis,” *Proc. 2nd ASCE Conf. on Electronic Computation*, Pittsburgh, Pa., Sept 1960.
  - Correia, D., da Silva, J. P., Hernandez-Figueroa, H. E., , “Genetic algorithm and finite-element design of short single-section passive polarization converter,” *IEEE Photon. Technol. Lett.*, vol.**15**, no.7, pp.915-917, July 2003.
  - Cortesi, E., Namavar, F., and Soref, R.A., “Novel silicon-on-insulator structures for silicon waveguides,” *SOS/SOI Technology Conference, 1989., 1989 IEEE*, pp.109, 1989.
  - Courant, R., “Variational methods for the solution of problems of equilibrium and vibrations,” *Bull. Amer. Math. Soc*, vol. **49**, pp. 1, 1943.
  - Cullen, A. L., and Yeo, S. P., “Using the least-squares boundary residual method to model the symmetrical five-port waveguide junction,” *IEE Proc. H Microw. Antennas Propag.*, vol. **134**, no.2, pp. 116-124, April 1987.
  - Dai, D., and He, S., “Ultrasmall overlapped arrayed-waveguide grating based on Si nanowire waveguides for dense wavelength division multiplexing,” *IEEE J. Sel. Topics Quantum Electron.*, vol. **12**, pp. 1301-1305, 2006.
  - Danielsen, P., “Two-dimensional propagating beam analysis of an electrooptic waveguide modulator,” *IEEE J. Quantum Electron.*, vol. **20**, no.9, pp. 1093- 1097, Sep 1984.
  - Davies, J. B., “A Least-Squares Boundary Residual Method for the Numerical Solution of Scattering Problems,” *IEEE Trans. Microw. Theory Tech.*, vol. **21**, no.2, pp. 99- 104, Feb 1973.
  - Davies, J. B., Fernandez, F. A., and Philippou, G. Y., “Finite Element Analysis of All Modes in Cavities with Circular Symmetry,” *IEEE Trans. Microw. Theory Tech.*, vol. **30**, no.11, pp.1975-1980, Nov. 1982.
  - Davies, J. B., *The finite element method, in Numerical techniques for microwave and millimeter-wave passive structures*, Edited by T. Itoh, NY, Wiley, pp. 33-132, 1989.
  - Dell'Olio, F., and Passaro, V. M., “Optical sensing by optimized silicon slot waveguides,” *Opt. Express*, vol. **15**, pp. 4977-4993, 2007.

- Deng, H., Yevick, D. O., Brooks, C., and Jessop, P. E., “Design Rules for Slanted-Angle Polarization Rotators,” *J. Lightw. Technol.*, vol. **23**, pp. 432-445, 2005.
- Deng, H., Yevick, D. O., Brooks, C., and Jessop, P. E., “Fabrication tolerance of asymmetric silicon-on-insulator polarization rotators,” *J. Opt. Soc. Am.*, vol. **23**, pp. 1741-1745, 2006.
- Ding, R., Baehr-Jones, T., Kim, W., Xiong, X., Bojko, R., Fedeli, J., Fournier, M., and Hochberg, M., “Low-loss strip-loaded slot waveguides in Silicon-on-Insulator,” *Opt. Express*, vol. **18**, pp. 25061-25067, 2010.
- El-Mikati, H. A., and Davies, J. B., “Coupling to an endfaced multi-clad optical fibre from a misaligned gaussian beam or a separated multi-clad fibre,” *Opt. Quant. Electron.*, vol. **17**, no. 5, pp. 297-309, 1985.
- English, W. J., and Young, F. J., “An E Vector Variational Formulation of the Maxwell Equations for Cylindrical Waveguide Problems,” *IEEE Trans. Microw. Theory Tech.*, vol. **19**, no.1, pp. 40- 46, Jan 1971.
- Fang, A. W., Park, H., Cohen, O., Jones, R., Paniccia, M. J., and Bowers, J. E., “Electrically pumped hybrid AlGaInAs-silicon evanescent laser,” *Opt. Express*, vol. **14**, no. 20, pp. 9203-9210, 2006.
- Feit, M. D., and Fleck, Jr. J. A., “Light propagation in graded-index optical fibers,” *Appl. Opt.*, vol. **17**, pp. 3990-3998, 1978.
- Feit, M. D., and Fleck, Jr. J. A., “Computation of mode properties in optical fiber waveguides by a propagating beam method,” *Appl. Opt.*, vol. **19**, pp. 1154-1164 1980.
- Feng, N., Sun, R., Michel, J., and Kimerling, L., “Low-loss compact-size slotted waveguide polarization rotator and transformer, ” *Opt. Lett.*, vol. **32**, pp. 2131-2133, 2007.
- Fernandez, F. A., and Davies, J. B., “Least-squares boundary residuals solution of microstrip step discontinuities,” *Electron. Lett.*, vol. **24**, pp. 640-, 1988.
- Fernandez, F. A., Davies, J. B., Zhu, S., and Lu, Y., “Sparse matrix eigenvalue solver for finite element solution of dielectric waveguides,” *Electron. Lett.*, vol. **27**, no.20, pp.1824-1826, 26 Sept. 1991.

- 
- Friedrich, E.E.L., Oberg, M.G., Broberg, B., Nilsson, S., and Valette, S., “Hybrid integration of semiconductor lasers with Si-based single-mode ridge waveguides,” *J. Lightw. Technol.*, vol. **10**, no. 3, pp. 336-340, 1992.
  - Fukuda, H., Yamada, K., Tsuchizawa, T., Watanabe, T., Shinojima, H., and Itabashi, S., “Polarization rotator based on silicon wire waveguides,” *Opt. Express*, vol. **16**, pp. 2628-2635, 2008.
  - Gambling, W. A., Matsumura, H., and Ragdale, C. M., “Field deformation in a curved single-mode fibre,” *Electron. Lett.*, vol. **14**, pp. 130-132, Mar. 1978.
  - Gardes, F. Y., Reed, G., Emerson, N., and Png, C., “A sub-micron depletion-type photonic modulator in Silicon On Insulator,” *Opt. Express*, vol. **13**, pp. 8845-8854, 2005.
  - Goodman, J. W., Leonberger, F. J., Kung, S. Y., Athale, R. A., “Optical interconnections for VLSI systems,” *Proc. IEEE*, vol. **72**, no. 7, pp. 850-866, 1984.
  - Gu, J., Besse, P., and Melchior, H., “Novel method for analysis of curved optical rib-waveguides,” *Electron. Lett.*, vol. **25**, pp. 278-280, Feb. 1989.
  - Hadley, G. R., “Transparent boundary condition for beam propagation,” *Opt. Lett.*, vol. **16**, pp. 624-626, 1991.
  - Hadley, G. R., “Multistep method for wide-angle beam propagation,” *Opt. Lett.*, vol. **17**, pp. 1743-1745, 1992a.
  - Hadley, G. R., “Transparent boundary condition for the beam propagation method,” *IEEE J. Quantum Electron.*, vol. **28**, no.1, pp. 363-370, Jan 1992b.
  - Hadley, G. R., “Wide-angle beam propagation using Padé approximant operators,” *Opt. Lett.*, vol. **17**, pp. 1426-1428, 1992c.
  - Hano, M., “Finite-Element Analysis of Dielectric-Loaded Waveguides,” *IEEE Trans. Microw. Theory Tech.*, vol. **32**, no.10, pp. 1275- 1279, Oct 1984.
  - Hattori, H. T., Seassal, C., Touraille, E., Rojo-Romeo, P., Letartre, X., Hollinger, G., Viktorovitch, P., Di Cioccio, L., Zussy, M., Melhaoui, L. E., and Fedeli, J. M., “Heterogeneous integration of microdisk lasers on silicon strip waveguides for optical interconnects,” *IEEE Photon. Technol. Lett.*, vol. **18**, no.1, pp.223-225, 2006.

- Hayata, K., Misawa, A., and Koshihara, M., "Split-step finite-element method applied to nonlinear integrated optics," *J. Opt. Soc. Am. B*, vol. **7**, pp. 1772-1784, 1990.
- Hayes, R. R., and Yap, D., "GaAs spiral optical waveguides for delay-line applications," *J. Lightw. Technol.*, vol. **11**, pp. 523-528, Mar. 1993.
- Heiblum, M., and Harris, J. H., "Analysis of curved optical waveguides by conformal transformation," *IEEE J. Quantum Electron.*, vol. **11**, pp. 75-83, Feb. 1975.
- Hendow, S. T., and Shakir, S. A., "Recursive numerical solution for nonlinear wave propagation in fibers and cylindrically symmetric systems," *Appl. Opt.*, vol. **25**, pp. 1759-1764, 1986.
- Hermansson, B., Yevick, D., and Danielsen, P., "Propagating beam analysis of multimode waveguide tapers," *IEEE J. Quantum Electron.*, vol. **19**, no.8, pp. 1246- 1251, Aug 1983.
- Hilbk, U., Hermes, T., Meissner, P., Jacumeit, C., Stentel, R., and Unterborsch, G., "First system experiments with a monolithically integrated tunable polarization diversity heterodyne receiver OEIC on InP," *IEEE Photon. Technol. Lett.*, vol. **7**, pp. 129-131, 1995.
- Holmes, B. M., Hutchings, D. C., "Realization of novel low-loss monolithically integrated passive waveguide mode converters," *IEEE Photon. Technol. Lett.*, vol.**18**, no.1, pp.43-45, Jan. 2006.
- Huang, W. P., Xu, C. L., Chu, S. T., and Chaudhuri, S. K., "A vector beam propagation method for guided-wave optics," *IEEE Photon. Technol. Lett.*, vol. **3**, no.10, pp.910-913, Oct. 1991a.
- Huang, W. P., Xu, C. L., and Chaudhuri, S. K., "A vector beam propagation method based on  $\mathbf{H}$  fields," *IEEE Photon. Technol. Lett.*, vol. **3**, no.12, pp. 1117-1120, Dec 1991b.
- Huang, W. P., Xu, C. L., and Chaudhuri, S. K., "A finite-difference vector beam propagation method for three-dimensional waveguide structures," *IEEE Photon. Technol. Lett.*, vol. **4**, no.2, pp. 148-151, Feb 1992a.
- Huang, W. P., Xu, C. L., Chu, S. T., and Chaudhuri, S. K., "The finite-difference vector beam propagation method: analysis and assessment," *J. Lightw. Technol.*, vol. **10**, no.3, pp. 295-305, Mar 1992b.

- 
- Huang, W. P., and Xu, C. L., “A wide-angle vector beam propagation method,” *IEEE Photon. Technol. Lett.*, vol. **4**, no.10, pp. 1118-1120, Oct 1992c.
  - Huang, W. P., and Xu, C. L., “Simulation of three-dimensional optical waveguides by a full-vector beam propagation method,” *IEEE J. Quantum Electron.*, vol. **29**, no.10, pp. 2639-2649, Oct 1993.
  - Huang, W. P., Xu, C. L., Lui, W., and Yokoyama, K., “The perfectly matched layer (PML) boundary condition for the beam propagation method,” *IEEE Photon. Technol. Lett.*, vol. **8**, no.5, pp. 649-651, May 1996.
  - ISO 11146, “Laser and laser related equipment – Test methods for laser beam widths, divergence and beam propagation ratios,” *International Organization for Standardization*, Geneva, Switzerland, 2005.
  - Jalali, B., Paniccia, M., and Reed, G., “Silicon photonics,” *IEEE Microw. Mag.*, vol. **7**, no. 3, pp.58-68, 2006.
  - Jedidi, R., and Pierre, R., “High-order finite-element method for the computation of bending loss in optical waveguides,” *J. Lightw. Technol.*, vol. **25**, pp. 2618-2630, Sep. 2007.
  - Jiang, X., Qi, W., Zhang, H., Tang, Y., Hao, Y., Yang, J., and Wang, M., “Loss crosstalk 1x2 thermo-optic digital optical switch with integrated S-bend attenuator,” *IEEE Photon. Technol. Lett.*, vol. **18**, pp. 610-612, Feb. 2006.
  - Jokerst, N. M., Brooke, M. A., Cho, S., Thomas, M., Lillie, J., Kim, D., Ralph, S., and Dennis, K., “Integrated planar lightwave bio/chem OEIC sensors on Si CMOS circuits,” *Proc. SPIE*, vol. **5730**, pp. 226–233, 2005.
  - Kakihara, K., Kono, N., Saitoh, K., and Koshiba, M., “Full-vectorial finite element method in cylindrical coordinate system for loss analysis of photonic wire bends,” *Opt. Express*, vol. **14**, pp. 11128-11141, 2006.
  - Kang, Y., Liu, H., Morse, M., Paniccia, M. J., Zadka, M., Litski, S., Sarid, G., Pauchard, A., Kuo, Y., Chen, H., Zaoui, W. S., Bowers, J. E., Beling, A., McIntosh, D. C., Zheng, X., and Campbell, J. C., “Monolithic germanium/silicon avalanche photodiodes with 340 GHz gain–bandwidth product,” *Nat. Photonics*, vol. **3**, pp. 59-63, 2009.
  - Kao, K. C., and Hockham, G. H., “Dielectric fibre surface waveguides for optical frequencies,” *Proc. IEE*, vol. **113**, no. 7, pp. 1151-1158, 1966.

- Kapron, F. P., Keck, D. B., and Maurer, R. D., “Radiation losses in glass optical waveguides,” *Appl. Phys. Lett.*, vol. **17**, pp. 423-425, 1970.
- Kato, K., and Tohmori, Y., “PLC hybrid integration technology and its application to photonic components,” *IEEE J. Sel. Topics Quantum Electron.*, vol. **6**, no.1, pp.4-13, 2000.
- Kim, S., and Gopinath, A., “Vector analysis of optical dielectric waveguide bends using finite-difference method,” *J. Lightw. Technol.*, vol. **14**, pp. 2085-2092, Sep. 1996.
- Kim, S. H., Takei, R., Shoji, Y., and Mizumoto, T., “Single-trench waveguide TE-TM mode converter,” *Opt. Express*, vol. **17**, pp. 11267-11273, 2009.
- Koch, T. B., Davies, J. B., and Wickramasinghe, D., “Finite element/finite difference propagation algorithm for integrated optical device,” *Electron. Lett.*, vol. **25**, no.8, pp. 514-516, 13 April 1989.
- Koch, T. B., Davies, J. B., Fernandez, F. A. and Maerz, R., “Computation of wave propagation in integrated optical devices using z-transient variational principles,” *IEEE Trans. Magn.*, vol. **27**, no.5, pp. 3876- 3879, Sep 1991.
- Konrad, A., “Vector Variational Formulation of Electromagnetic Fields in Anisotropic Media,” *IEEE Trans. Microw. Theory Tech.*, vol. **24**, no.9, pp. 553- 559, Sep 1976.
- Konrad, A., “High-Order Triangular Finite Elements for Electromagnetic Waves in Anisotropic Media,” *IEEE Trans. Microw. Theory Tech.*, vol. **25**, no.5, pp. 353- 360, May 1977.
- Koshiha, M., Hayata, K., and Suzuki, M., “Approximate scalar finite element analysis of anisotropic optical waveguides,” *Electron. Lett.*, vol. **18**, pp. 411–413, May 1982.
- Koshiha, M., Hayata, K., and Suzuki, M., “Vectorial finite-element method without spurious solutions for dielectric waveguide problems,” *Electron. Lett.*, vol. **20**, no.10, pp.409-410, May 10 1984.
- Koshiha, M., Hayata, K., and Suzuki, M., “Improved Finite-Element Formulation in Terms of the Magnetic Field Vector for Dielectric Waveguides,” *IEEE Trans. Microw. Theory Tech.*, vol. **33**, no.3, pp. 227-233, Mar 1985a.

- 
- Koshiha, M., Hayata, K., and Suzuki, M., “Finite-Element Formulation in Terms of the Electric-Field Vector for Electromagnetic Waveguide Problems,” *IEEE Trans. Microw. Theory Tech.*, vol. **33**, no.10, pp. 900- 905, Oct 1985*b*.
  - Koshiha, M., Hayata, K., and Suzuki, M., “Vector **E**-field finite-element analysis of dielectric optical waveguides,” *Appl. Opt.*, vol. **25**, pp. 10-11, 1986.
  - Kriezis, E. E., Pantelakis, P., Antonopoulos, C. S., and Papagiannakis, A. G., “Full vector beam propagation method for axially dependent 3-D structures,” *IEEE Trans. Magn.*, vol. **33**, no.2, pp. 1540-1543, Mar 1997.
  - Lagasse, P. E., and Baets, R., “Application of propagating beam methods to electromagnetic and acoustic wave propagation problems: A review,” *Radio Sci.*, 22(7), pp. 1225–1233, 1987.
  - Leuthold, J., Freude, W., Brosi, J. M., Baets, R., Dumon, P., Biaggio, I., Scimeca, M. L., Diederich, F., Frank, B., and Koos, C., “Silicon Organic Hybrid Technology—A Platform for Practical Nonlinear Optics,” *Proc. IEEE*, vol. **97**, no.7, pp. 1304-1316, July 2009.
  - Liao, L., Samara-Rubio, D., Morse, M., Liu, A., Hodge, D., Rubin, D., Keil, U. D., and Franck, T., “High speed silicon Mach-Zehnder modulator,” *Opt. Express*, vol. **13**, pp. 3129-3135, 2005.
  - Lin, C., Kobrinski, H., Frenkel, A., and Brackett, C. A., “Wavelength-tunable 16 optical channel transmission experiment at 2 Gbit/s and 600 Mbit/s for broadband subscriber distribution,” *Electron. Lett.*, vol. **24**, no. 19, pp. 1215-1216, 1988.
  - Lipson, M., “Guiding, Modulating, and Emitting Light on Silicon-Challenges and Opportunities,” *J. Lightw. Technol.*, vol. **23**, pp. 4222- 4238, 2005.
  - Little, B. E., Chu, S. T., Haus, H. A., Foresi, J., and Laine, J. P., “Microring resonator channel dropping filters,” *J. Lightw. Technol.*, vol. **15**, pp. 998-1005, June 1997.
  - Little, B. E., and Chu, S. T., “Theory of polarization rotation and conversion in vertically coupled microresonators,” *IEEE Photon. Technol. Lett.*, vol. **12**, pp. 401-403, Apr. 2000.

- Liu, J. L., Shi, Y., Wang, F., Lu, Y., Gu, S. L., Zhang, R., and Zheng, Y. D., “Study of dry oxidation of triangle-shaped silicon nanostructure,” *Appl. Phys. Lett.*, vol. **69**, pp. 1761-1763, 1996.
- Liu, P. L., and Li, B. J., “Study of form birefringence in waveguide devices using the semivectorial beam propagation method,” *IEEE Photon. Technol. Lett.*, vol. **3**, no.10, pp. 913-915, Oct. 1991.
- Liu, P. L., and Li, B. J., “Semivectorial beam-propagation method for analyzing polarized modes of rib waveguides,” *IEEE J. Quantum Electron.*, vol. **28**, no.4, pp. 778-782, Apr 1992.
- Liu, P. L., Yang, S. L., and Yuan, D. M., “The semivectorial beam propagation method,” *IEEE J. Quantum Electron.*, vol. **29**, no.4, pp.1205-1211, Apr 1993.
- Lui, W. W., Hirono, T., Yokoyama, K., and Huang, W. P., “Polarization rotation in semiconductor bending waveguides: A coupled-mode theory formulation,” *J. Lightw. Technol.*, vol. **16**, pp. 929-936, May 1998.
- Mabaya, N., Lagasse, P. E., and Vandenbulcke, P., “Finite-element analysis of optical waveguides,” *IEEE Trans. Microwave Theory Tech.*, vol. MTT-**29**, pp. 600–605, June 1981.
- Maiman, T. H., “Stimulated optical radiation in ruby,” *Nature*, vol. **187**, pp. 493-494, 1960.
- Marcatili, E. A. J., “Bends in optical dielectric guides,” *Bell Syst. Tech. J.*, vol. **48**, pp. 2103-2132, Sep. 1969.
- Marcuse, D., “Curvature loss formula for optical fibers,” *J. Opt. Soc. Am.*, vol. **66**, pp. 216-220, Mar. 1976.
- Mertens, K., Scholl, B., and Schmitt, H. J., “Strong polarization conversion in periodically loaded strip waveguides,” *IEEE Photon. Technol. Lett.*, vol. **10**, pp. 1133-1135, 1998.
- Miller, D. A. B., “Optical interconnects to silicon,” *IEEE J. Sel. Topics Quantum Electron.*, vol. **6**, no. 6, pp. 1312–1317, 2000.
- Miller, S. E., “Integrated optics: an introduction,” *Bell Syst. Tech. Journal*, vol. **48**, pp. 2059-2069, 1969.
- Monat, C., Seassal, C., Rojo-Romeo, P., Letartre, X., Regreny, P., Gendry, M., Viktorovitch, P., Hollinger, G., Jalaguier, E., Pocas, S., and Aspar, B.,

- 
- “InP membrane-based microlasers on silicon wafer: microdisks vs photonic crystal cavities,” *Proc. IEEE, 2001 International Conference on Indium Phosphide and Related Materials*, pp. 603-606, Nara, Japan, 2001.
- Montanari, E., Selleri, S., Vincetti, L., and Zoboli, M., “Finite-element formulation for full-vectorial propagation analysis in three-dimensional optical waveguides,” *IEEE Photon. Technol. Lett.*, vol. **9**, no.9, pp. 1244-1246, Sept. 1997.
  - Montanari, E., Selleri, S., Vincetti, L., and Zoboli, M., “Finite-element full-vectorial propagation analysis for three-dimensional z-varying optical waveguides,” *J. Lightw. Technol.*, vol. **16**, no.4, pp. 703-714, Apr 1998.
  - Moore, G. E., “Cramming more Components onto Integrated Circuits,” *Electronics*, vol. **38**, no. 8, pp.114-117, 1965.
  - Nesterov, A., and Troppenz, U., “A plane-wave boundary method for analysis of bent optical waveguides,” *J. Lightw. Technol.*, vol. **21**, pp. 2434-2437, 2003.
  - Neyer, A., Mevenkamp, W., Thylén, L., and Lagerstrom, B., “A beam propagation method analysis of active and passive waveguide crossings,” *J. Lightw. Technol.*, vol. **3**, no.3, pp. 635- 642, Jun 1985.
  - Niiyama, A., and Koshiha, M., “Three-Dimensional Beam Propagation Analysis of Nonlinear Optical Fibers and Optical Logic Gates,” *J. Lightw. Technol.*, vol. **16**, pp. 162- , 1998.
  - Obayya, S. S. A., Rahman, B. M. A., and El-Mikati, H. A., “New full-vectorial numerically efficient propagation algorithm based on the finite element method,” *J. Lightw. Technol.*, vol. **18**, no.3, pp. 409-415, Mar 2000a.
  - Obayya, S. S. A., Rahman, B. M. A., and El-Mikati, H. A., “Full-vectorial finite-element beam propagation method for nonlinear directional coupler devices,” *IEEE J. Quantum Electron.*, vol. **36**, no.5, pp. 556-562, May 2000b.
  - Obayya, S. S. A., Rahman, B. M. A., Grattan, K. T. V., and El-Mikati, H. A., “Improved design of a polarization converter based on semiconductor optical waveguide bends,” *Appl. Opt.*, vol. **40**, pp. 5395-5401, Oct. 2001.
  - Obayya, S. S. A., Rahman, B. M. A., Grattan, K. T. V., and El-Mikathi, H. A., “Analysis of polarisation rotation in cascaded optical waveguide bends,” *IEE Proc. Optoelectronics*, vol. **149**, pp. 75-80, Apr. 2002.

- Park, H., Fang, A. W., Kodama, S., and Bowers, J. E., “Hybrid silicon evanescent laser fabricated with a silicon waveguide and III-V offset quantum wells,” *Opt. Express*, vol. **13**, pp. 9460-9464, 2005.
- Pavesi, L., Dal Negro, L., Mazzoleni, C., Franzo, G., and Priolo, F., “Optical gain in silicon nanocrystals,” *Nature*, vol. **408**, pp. 440–444, 2000.
- Pekel, U., and Mittra, R., “An application of the perfectly matched layer (PML) concept to the finite element method frequency domain analysis of scattering problems,” *IEEE Microw. Guided Wave Lett.*, vol. **5**, no.8, pp. 258-260, Aug 1995a.
- Pekel, U., and Mittra, R., “A finite-element-method frequency-domain application of the perfectly matched layer (PML) concept,” *Microw. Opt. Technol. Lett.*, vol. **9**, pp. 117–122, 1995b.
- Pennings, E. C. M., Manhoudt, G. H., and Smit, M. K., “Low-loss bends in planar optical ridge waveguides,” *Electron. Lett.*, vol. **24**, pp. 998-999, Aug. 1988.
- Powelson, J. C., Feng, W., Lin, S., Feuerstein, R. J., and Tomic, D., “Crosstalk of passive directional couplers,” *J. Lightw. Technol.*, vol. **16**, pp. 2020-2027, Nov. 1998.
- Pregla, R., “The method of lines for analysis of dielectric waveguide bends,” *J. Lightw. Technol.*, vol. **14**, pp. 634-639, Apr. 1996.
- Preston, K., Manipatruni, S., Gondarenko, A., Poitras, C. B., and Lipson, M., “Deposited silicon high-speed integrated electro-optic modulator,” *Opt. Express*, vol. **17**, pp. 5118-5124, 2009.
- Prkna, L., Hubalek, M., and Ctyroky, J., “Field modelling of circular microresonators by film mode matching,” *IEEE J. Sel. Topics Quantum Electron.*, vol. **11**, pp. 217-223, 2005.
- Rahman, B. M. A., and Davies, J. B., “Finite-Element Analysis of Optical and Microwave Waveguide Problems,” *IEEE Trans. Microw. Theory Tech.*, vol. **32**, no.1, pp. 20- 28, Jan 1984a.
- Rahman, B. M. A., and Davies, J. B., “Penalty Function Improvement of Waveguide Solution by Finite Elements,” *IEEE Trans. Microw. Theory Tech.*, vol. **32**, no.8, pp. 922- 928, Aug 1984b.

- 
- Rahman, B. M. A., and Davies, J. B., “Finite-element solution of integrated optical waveguides,” *J. Lightw. Technol.*, vol. **2**, no.5, pp. 682- 688, Oct 1984c.
  - Rahman, B. M. A., and Davies, J. B., “Vector-H finite element solution of GaAs/GaAlAs rib waveguides,” *IEE Proc. J Optoelectron.*, vol. **132**, pp. 349-353, 1985.
  - Rahman, B. M. A., and Davies, J. B., “Analysis of optical waveguide discontinuities,” *J. Lightw. Technol.*, vol. **6**, no.1, pp. 52-57, Jan 1988.
  - Rahman, B. M. A., Obayya, S. S. A., Somasiri, N., Rajarajan, M., Grattan, K. T. V., and El-Mikathi, H. A., “Design and characterization of compact single-section passive polarization rotator,” *J. Lightw. Technol.*, vol. **19**, pp. 512-519, 2001.
  - Rajarajan, M., Obayya, S. S. A., Rahman, B. M. A., Grattan, K. T. V., and El-Mikathi, H. A., “Design of compact optical bends with a trench by use of finite element and beam propagation methods,” *Appl. Opt.*, vol. **33**, pp. 4946-4953, Sep. 2000a.
  - Rajarajan, M., Obayya, S. S. A., Rahman, B. M. A., Grattan, K. T. V., and El-Mikathi, H. A., “Characterization of low-loss waveguide bends with offset optimisation for compact photonic integrated circuits,” *IEE Proc. Optoelectron.*, vol. **147**, pp. 382-388, Dec. 2000b.
  - Reddy, J. N., *An Introduction to the Finite Element Method*, McGraw-Hill Inc., NY, 1984.
  - Reed, G. T., and Knights, A. P., “Silicon Photonics: An Introduction” Ch. 4, pp. 97-103, Wiley, 2004.
  - Reed, G. T., Mashanovich, G., Gardes, F. Y., and Thomson, D. J., “Silicon optical modulator,” *Nat. Photonics*, vol. 4., pp. 518-526, 2010.
  - Robinson, J. T., Preston, K., Painter, O., and Lipson, M., “First-principle derivation of gain in high-index-contrast waveguides,” *Opt. Express*, vol. **16**, pp. 16659-16669, 2008.
  - Rolland, C., Mak, G., Fox, K. E., Adams, D. M., Springthorpe, A. J., Yevick, D., and Hermansson, B., “Analysis of strongly guiding rib waveguide S-bends: theory and experiment,” *Electron. Lett.*, vol. **25**, no.18, pp. 1256-1257, 31 Aug. 1989.

- Rong, H., Jones, R., Liu, A., Cohen, O., Hak, D., Fang, A., and Paniccia, M., “A continuous-wave Raman silicon laser,” *Nature*, vol. **433**, pp. 725–728, 2005.
- Saarinen, J. J., Sipe, J. E., Weiss, S. M., and Fauchet, P. M. “Optical sensors based on resonant porous silicon structures,” *Opt. Express*, vol. **13**, no. 10, pp. 3754–3764, 2005.
- Sacks, Z. S., Kingsland, D. M., Lee R., and Lee, J. F., “A perfectly matched anisotropic absorber for use as an absorbing boundary condition,” *IEEE Trans. Antennas Propag.*, vol. **43**, no. 12, pp. 1460-1463, 1995.
- Sasaki, J., Itoh, M., Tamanuki, T., Hatakeyama, H., Kitamura, S., Shimoda, T., and Kato, T., “Multiple-chip precise self-aligned assembly for hybrid integrated optical modules using Au-Sn solder bumps,” *IEEE Trans. Adv. Packag.*, vol. **24**, no.4, pp.569-575, 2001.
- Schlak, M., Weinert, C. M., Albrecht, P., and Nolting, H. P., “Tunable TE/TM-mode converter on (001)-InP-substrate,” *IEEE Photon. Technol. Lett.*, vol. **3**, pp. 15-16, 1991.
- Schermer, R. T., and Cole, J. H., “Improved bend loss formula verified for optical fiber by simulation and experiment,” *IEEE J. Quantum Electron.*, vol. **43**, pp. 899-909, Oct. 2007.
- Shani, Y., Alferness, R., Koch, T., Koren, U., Miller, B. I., and Young, M. G., “Polarization rotation in asymmetric periodic loaded rib waveguides,” *Appl. Phys. Lett.*, vol. **59**, pp. 1278-1280, 1991.
- Somasiri, N., Rahman, B. M. A., and Obayya, S. S. A., “Fabrication tolerance study of a compact passive polarization rotator,” *J. Lightw. Technol.*, vol. **20**, pp. 751-757, Apr. 2002.
- Somasiri, N., and Rahman, B. M. A., “Polarization crosstalk in high index contrast planar silica waveguides with slanted sidewalls,” *J. Lightw. Technol.*, vol. **21**, pp. 54- 60, 2003.
- Soref, R. A., and Lorenzo, J. P., “All-Silicon Active and Passive Guided-Wave Components for  $\lambda = 1.3$  and  $1.6 \mu\text{m}$ ,” *IEEE J. Quantum Electron.*, vol. **22**, pp. 873–879, 1986.
- Soref, R., and Bennett, B., “Electrooptical effects in silicon,” *IEEE J. Quantum Electron.*, vol. **23**, no.1, pp. 123-129, 1987.

- 
- Soref, R. A., Namavar, F., and Lorenzo, J. P., "Optical waveguiding in a single-crystal layer of germanium silicon grown on silicon," *Opt. Lett.*, vol. **15**, pp. 270-272, 1990.
  - Subramaniam, V., De Brabander, G. N., Naghski, D. H., and Boyd, J. T., "Measurement of mode field profiles and bending and transition losses in curved optical channel waveguides," *J. Lightw. Technol.*, vol. **15**, pp. 990-997, June 1997.
  - Sun, R., Dong, P., Feng, N., Hong, C., Michel, J., Lipson, M., and Kimerling, L., "Horizontal single and multiple slot waveguides: optical transmission at  $\lambda = 1550$  nm," *Opt. Express*, vol. **15**, pp. 17967-17972, 2007.
  - Svedin, J. A. M., "A numerically efficient finite-element formulation for the general waveguide problem without spurious modes," *IEEE Trans. Microw. Theory Tech.*, vol. **37**, no.11, pp.1708-1715, Nov 1989.
  - Thyagarajan, K., Shenoy, M. R., and Ghatak, A. K., "Accurate numerical method for the calculation of bending loss in optical waveguides using a matrix approach," *Opt. Lett.*, vol. **12**, pp. 296-298, 1987.
  - Thylén, L., "The beam propagation method: an analysis of its applicability," *Opt. Quantum Electron.*, vol. **15**, pp. 433- 439, 1983.
  - Thylén, L., Wright, E. M., Stegeman, G. I., Seaton, C. T., and Moloney, J. V., "Beam-propagation method analysis of a nonlinear directional coupler," *Opt. Lett.*, vol. **11**, pp. 739-741, 1986.
  - Tomljenovic-Hanic, S., Love, J. D., and Ankiewicz, A., "Effect of additional layers on bend loss in buried channel waveguides," *IEE Proc. Optoelectron.*, vol. **150**, pp. 259-265, June 2003.
  - Tsuchizawa, T., Yamada, K., Watanabe, T., Fukuda, H., Nishi, H., Shinojima, H., and Itabashi, S., "Si photonics platform and its fabrication," *The 5th International Symposium on Advanced Science and Technology of Silicon Materials (JSPS Si Symposium)*, 2008.
  - Tsuji, Y., and Koshiba, M., "A finite element beam propagation method for strongly guiding and longitudinally varying optical waveguides," *Lightwave Technology, Journal of*, vol. **14**, no.2, pp. 217-222, Feb 1996.

- Tsuji, Y., Koshihara, M., and Tanabe, T., “A wide-angle beam propagation method based on a finite element scheme,” *Magnetics, IEEE Transactions on*, vol. **33**, no.2, pp. 1544-1547, Mar 1997a.
- Tsuji, Y., Koshihara, M., and Shiraishi, T., “Finite element beam propagation method for three-dimensional optical waveguide structures,” *J. Lightw. Technol.*, vol. **15**, no.9, pp. 1728-1734, Sep 1997b.
- Tsuji, Y., and Koshihara, M., “Complex modal analysis of curved optical waveguides using a full-vectorial finite element method with perfectly matched layer boundary conditions,” *Electromagnetics*, vol. **24**, pp. 39-48, Jan. 2004.
- Turner, J. L., Clough, R. W., Martin, H. C., and Topp, L. J., “Stiffness and deflection analysis of complex structures,” *I. Aero. Sci*, vol. **23**, pp. 805-825, 1956.
- Van Dam, C., Spiekman, L. H., van Ham, F. P. G. M., Groen, F. H., van der Tol, J. J. G. M., Moerman, I., Pascher, W. W., Hamacher, M., Heidrich, H., Weinert, C. M., and Smit, M. K., “Novel compact polarization converters based on ultra short bends,” *IEEE Photon. Technol. Lett.*, vol. **8**, pp. 1346-1348, Oct. 1996.
- Vivien, L., Marris-Morini, D., Griol, A., Gylfason, K. B., Hill, D., Alvarez, J., Sohlström, H., Hurtado, J., Bouville, D., and Cassan, E., “Vertical multiple-slot waveguide ring resonators in silicon nitride,” *Opt. Express*, vol. **16**, pp. 17237-17242, 2008.
- Vlasov, Y., and McNab, S., “Losses in single-mode silicon-on-insulator strip waveguides and bends,” *Opt. Express*, vol. **12**, pp.1622-1631, 2004.
- Vu, N. H., Hwang, I. K., and Lee, Y. H., “Bending loss analyses of photonic crystal fibers based on the finite-difference time-domain method,” *Opt. Lett.*, vol. **33**, pp. 119-121, 2008.
- Wang, Z., and Dai, D., “Ultrasmall Si-nanowire-based polarization rotator, ” *J. Opt. Soc. Am. B*, vol. **25**, pp. 747-753, 2008.
- Wassmann, F., “Modal field analysis of circularly bent single-mode fibers,” *J. Lightw. Technol.*, vol. **17**, pp. 957-968, 1999.
- Watts, M., and Haus, H., “Integrated mode-evolution-based polarization rotators, ” *Opt. Lett.* Vol. **30**, pp. 138-140, 2005.

- 
- Yamamoto, T., and Koshiha, M., “Numerical analysis of curvature loss in optical waveguides by the finite-element method,” *J. Lightw. Technol.*, vol. **11**, pp. 1579-1583, Oct. 1993.
  - Yamauchi, J., Ando, T., and Nakano, H., “Beam-propagation analysis of optical fibres by alternating direction implicit method,” *Electron. Lett.*, vol. **27**, no.18, pp. 1663-1665, 29 Aug. 1991.
  - Yamauchi, J., Shibayama, J., and Nakano, H., “Modified finite-difference beam propagation method based on the generalized Douglas scheme for variable coefficients,” *IEEE Photon. Technol. Lett.*, vol. **7**, no.6, pp. 661-663, Jun 1995.
  - Yeung, C., Rozzi, T., and Cerri, G., “Cross polarisation coupling in curved dielectric rib waveguides,” *IEE Proc. Optoelectron.*, vol. **135**, pp. 281-284, Jun. 1988.
  - Yevick, D., and Thylén, L., “Analysis of gratings by the beam-propagation method,” *J. Opt. Soc. Am.* vol. **72**, pp. 1084-1089, 1982.
  - Yevick, D., and Glasner, M., “Analysis of Forward Wide-Angle Light-Propagation in Semiconductor Rib Wave-Guides and Integrated-Optic Structures,” *Electron. Lett.*, vol. **25**, no. 23, pp. 1611-1613, 1989a.
  - Yevick, D., and Hermansson, B., “Split-step finite difference analysis of rib waveguides,” *Electron. Lett.*, vol. **25**, no.7, pp. 461-462, 30 March 1989b.
  - Yevick, D., and Hermansson, B., “Efficient beam propagation techniques,” *IEEE J. Quantum Electron.*, vol. **26**, no.1, pp. 109-112, Jan 1990.
  - Yin, L., Lin, Q., and Agrawal, G. P., “Soliton fission and supercontinuum generation in silicon waveguides,” *Opt. Lett.*, vol. **32**, pp. 391-393, 2007.
  - Yoo, S. J. B., “Future prospects of silicon photonics in next generation communication and computing systems,” *Electron. Lett.*, vol. **45**, pp. 584-588, 2009.
  - Young, T. P., “Design of integrated optical circuits using finite elements,” *IEE Proc. A*, vol. **135**, no.3, pp.135-144, March 1988.
  - Zienkiewicz, O. C., *The finite element method*, McGraw-Hill, UK, 1977.
  - Zirngibl, M., Joyner, C. H., Stulz, L. W., Gaiffe, Th., and Dragone, C., “Polarization independent 8x8 waveguide grating multiplexers on InP,” *Electron. Lett.*, vol. **29**, pp. 201-202, Jan. 1993.